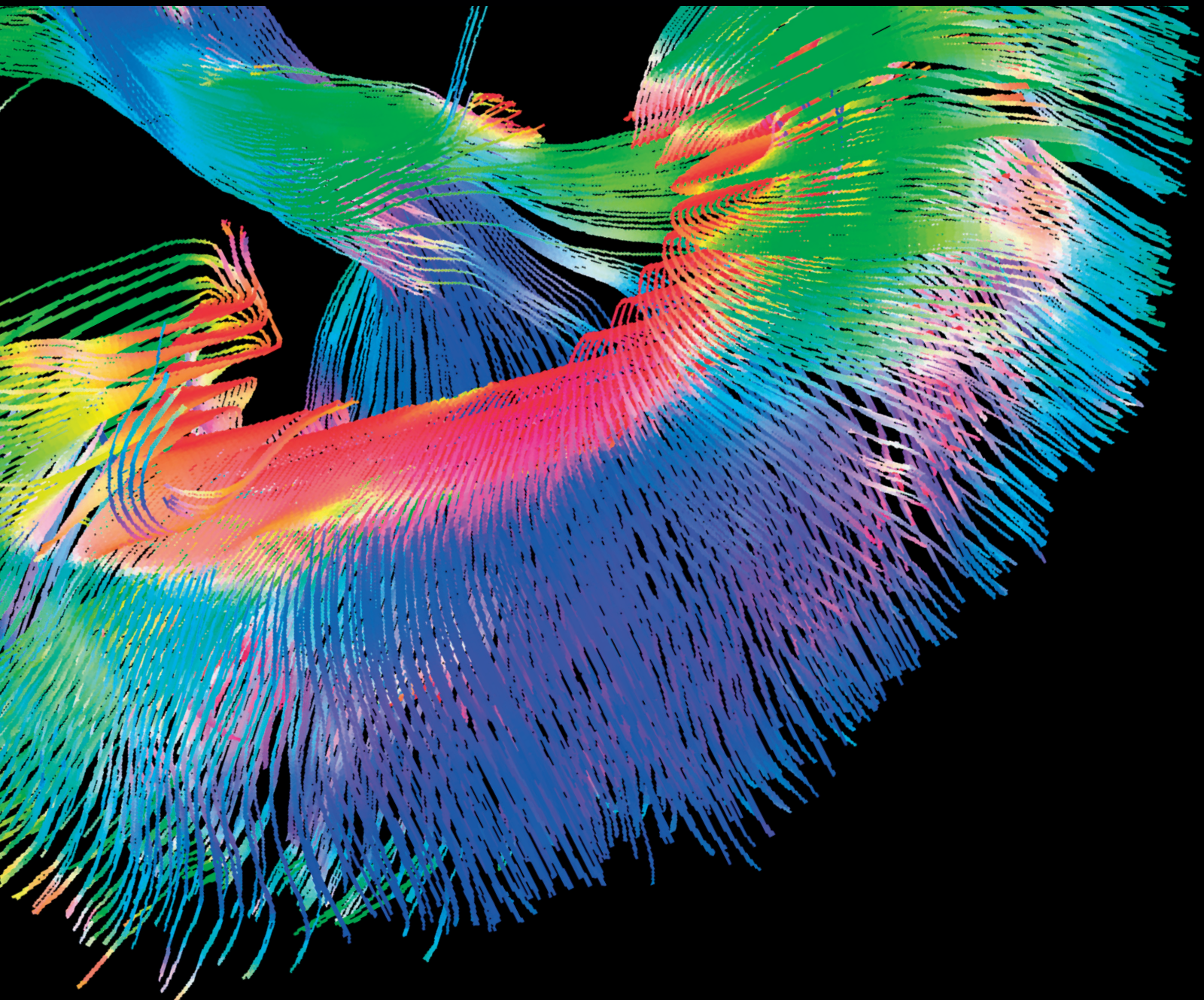


Contrast Media & Molecular Imaging

# Molecular Imaging in Targeted Therapeutics

Lead Guest Editor: Yuebing Wang

Guest Editors: Zhen Cheng, Shuang Liu, and Guoqiang Shao





---

# **Molecular Imaging in Targeted Therapeutics**

Contrast Media & Molecular Imaging

---

## **Molecular Imaging in Targeted Therapeutics**

Lead Guest Editor: Yuebing Wang

Guest Editors: Zhen Cheng, Shuang Liu, and Guoqiang Shao



---

Copyright © 2018 Hindawi. All rights reserved.

This is a special issue published in “Contrast Media & Molecular Imaging.” All articles are open access articles distributed under the Creative Commons Attribution License, which permits unrestricted use, distribution, and reproduction in any medium, provided the original work is properly cited.

## Editorial Board

Ali Azhdarinia, USA  
Peter Bannas, Germany  
Giorgio Biasiotto, Italy  
André L. B. de Barros, Brazil  
Dinesh K. Deelchand, USA  
Paul Edison, UK  
Michael J. Evans, USA  
Samer Ezziddin, Germany  
Guillermina Ferro-Flores, Mexico  
Filippo Galli, Italy  
María L. García-Martín, Spain

Alexander R. Haug, Germany  
Hao Hong, USA  
Alexey P. Kostikov, Canada  
Françoise Kraeber-Bodéré, France  
Kuo-Shyan Lin, Canada  
Gaurav Malviya, UK  
Barbara Palumbo, Italy  
Giancarlo Pascali, Australia  
Maria Joao Ribeiro, France  
Laurent M. Riou, France  
Anne Roivainen, Finland

Pedro Rosa-Neto, Canada  
Giuseppe Rubini, Italy  
Barbara Salvatore, Italy  
Ralf Schirmacher, Canada  
Giorgio Treglia, Switzerland  
Reza Vali, Canada  
Mattia Veronese, UK  
Changning Wang, USA  
Habib Zaidi, Switzerland  
Luc Zimmer, France

## Contents

### **Molecular Imaging in Targeted Therapeutics**

Yuebing Wang , Zhen Cheng , Shuang Liu, and Guoqiang Shao   
Editorial (2 pages), Article ID 3236829, Volume 2018 (2018)

### **Investigation on the Neural Mechanism of Hypnosis-Based Respiratory Control Using Functional MRI**

Yanjun Liu , Wenjian Qin, Rongmao Li, Shaode Yu , Yini He , and Yaoqin Xie   
Research Article (11 pages), Article ID 8182542, Volume 2018 (2018)

### **Differential Diagnosis between Low-Grade and High-Grade Astrocytoma Using System A Amino Acid Transport PET Imaging with C-11-MeAIB: A Comparison Study with C-11-Methionine PET Imaging**

Ryuichi Nishii , Tatsuya Higashi , Shinya Kagawa, Maya Arimoto, Yoshihiko Kishibe, Masaaki Takahashi, Shigeki Yamada, Masaaki Saiki, Yoshiki Arakawa, Hiroshi Yamauchi, Chio Okuyama, Masato Hojo, Toshihiro Munemitsu, Masahiro Sawada, Masato Kobayashi, Keiichi Kawai, Shigeki Nagamachi, Toshinori Hirai, and Susumu Miyamoto  
Clinical Study (9 pages), Article ID 1292746, Volume 2018 (2018)

### **The Place of PET to Assess New Therapeutic Effectiveness in Neurodegenerative Diseases**

Anne-Claire Dupont , Bérenger Largeau , Denis Guilloteau, Maria Joao Santiago Ribeiro, and Nicolas Arlicot  
Review Article (15 pages), Article ID 7043578, Volume 2018 (2018)

### **Multimodality Molecular Imaging-Guided Tumor Border Delineation and Photothermal Therapy Analysis Based on Graphene Oxide-Conjugated Gold Nanoparticles Chelated with Gd**

Xibo Ma, Yushen Jin, Yi Wang, Shuai Zhang, Dong Peng, Xin Yang, Shoushui Wei, Wei Chai, Xuejun Li , and Jie Tian   
Research Article (14 pages), Article ID 9321862, Volume 2018 (2018)

### **Investigation of Newly Prepared Biodegradable <sup>32</sup>P-chromic Phosphate-poly lactide-co-glycolide Seeds and Their Therapeutic Response Evaluation for Glioma Brachytherapy**

Guoqiang Shao, Yuebing Wang , Xianzhong Liu, Meili Zhao, Jinhua Song, Peiling Huang, Feng Wang , and Zizheng Wang   
Research Article (11 pages), Article ID 2630480, Volume 2018 (2018)

### **Preparation of <sup>68</sup>Ga-PSMA-II with a Synthesis Module for Micro PET-CT Imaging of PSMA Expression during Prostate Cancer Progression**

Yuebing Wang , Guoqiang Shao, Jianping Wu, Can Cui, Shimin Zang, Fan Qiu, Ruipeng Jia , Zizheng Wang , and Feng Wang   
Research Article (9 pages), Article ID 8046541, Volume 2018 (2018)

### **Evans Blue Dye: A Revisit of Its Applications in Biomedicine**

Linpeng Yao , Xing Xue, Peipei Yu, Yicheng Ni , and Feng Chen   
Review Article (10 pages), Article ID 7628037, Volume 2018 (2018)

**Thyroid Cancer Detection by Ultrasound Molecular Imaging with SHP2-Targeted Perfluorocarbon Nanoparticles**

ZhongQian Hu , Bin Yang, Tiankuan Li, and Jia Li 

Research Article (7 pages), Article ID 8710862, Volume 2018 (2018)

**One-Step  $^{18}\text{F}$ -Labeling of Estradiol Derivative for PET Imaging of Breast Cancer**

Hongbo Huang, Ke Li, Gaochao Lv, Guiqing Liu, Xueyu Zhao, Qingzhu Liu, Shanshan Wang, Xi Li,

Ling Qiu , and Jianguo Lin 

Research Article (9 pages), Article ID 5362329, Volume 2018 (2018)

**Comparing the Differential Diagnostic Values of  $^{18}\text{F}$ -Alfatide II PET/CT between Tuberculosis and Lung Cancer Patients**

Xiaoqing Du, Yu Zhang, Liping Chen, Baoming Mi, Qingjun You, Yuping Xu, Donghui Pan, Weixing Wan, Min Yang, and Chunjing Yu 

Clinical Study (6 pages), Article ID 8194678, Volume 2018 (2018)

**Synthesis and Bioevaluation of Iodine-131 Directly Labeled Cyclic RGD-PEGylated Gold Nanorods for Tumor-Targeted Imaging**

Yingying Zhang, Yongxue Zhang, Lianglan Yin, Xiaotian Xia, Fan Hu, QingYao Liu, Chunxia Qin, and Xiaoli Lan

Research Article (10 pages), Article ID 6081724, Volume 2017 (2018)

## Editorial

# Molecular Imaging in Targeted Therapeutics

Yuebing Wang <sup>1</sup>, Zhen Cheng <sup>2</sup>, Shuang Liu,<sup>3</sup> and Guoqiang Shao <sup>4</sup>

<sup>1</sup>Department of Biochemistry, School of Medicine, Nankai University, Tianjin 300071, China

<sup>2</sup>Molecular Imaging Program at Stanford (MIPS), Canary Center at Stanford for Cancer Early Detection, Department of Radiology and Bio-X Program, School of Medicine, Stanford University, Stanford, CA 94305, USA

<sup>3</sup>School of Health Sciences, Purdue University, 550 Stadium Mall Drive, West Lafayette, IN 47907, USA

<sup>4</sup>Department of Nuclear Medicine, Nanjing First Hospital, Nanjing Medical University, Nanjing 210006, China

Correspondence should be addressed to Yuebing Wang; wangyuebing@nankai.edu.cn and Guoqiang Shao; guoqiangshao@163.com

Received 6 August 2018; Accepted 7 August 2018; Published 5 September 2018

Copyright © 2018 Yuebing Wang et al. This is an open access article distributed under the Creative Commons Attribution License, which permits unrestricted use, distribution, and reproduction in any medium, provided the original work is properly cited.

With the rapid development of precision medicine, targeted therapy of tumors has made great advances. However, tumors of the same type were found to harbor different molecular alterations such as specific receptor, transporter, and cell expression levels before and even during the targeted therapy. Molecular imaging allows mapping of disease markers *in vivo* and understanding of disease biology. It promotes targeted therapy by therapeutic effect prediction, early response evaluation, and therapeutic regimen determination in preclinical and clinical settings. Molecular imaging technologies are being recognized as one of the most valuable tools in the field of precision medicine, which will make individual treatment decisions for better patient outcome care.

In this special issue, we focus on the recent advances of molecular imaging for targeted treatment strategies in precision medicine. Two review articles and nine original research articles are published in this special issue. The topics included synthesized targeting probes: PET, SPECT, MR, ultrasound, fluorescence, photoacoustics, and multimodal imaging.

L. P. Yao et al. reviewed the features of even blues and their potential applications in biomedicine. They pointed out that radiolabeled even blue and its derivatives will play an important role in clinical imaging of tumor lesions, evaluation of lymphatic disorders, and development of long-acting therapeutics. In the other review paper, A. C. Dupont et al. summarized the current inputs of PET in the assessment of therapeutic effectiveness in neurodegenerative diseases connected by common pathophysiological mechanisms.

In addition, they discussed the opportunities for PET imaging to drive more personalized neuroprotective and therapeutic strategies.

Smart targeting probes were designed by the researchers in this special issue. Y. Y. Zhang et al. developed a smart nanoprobe named [<sup>131</sup>I] GNR-PEG-cRGD, which can be used for angiogenesis-targeted SPECT/CT imaging. This nanoprobe possesses a remarkable capacity for highly efficient photothermal conversion in the near-infrared region, suggesting its potential as a multifunctional theragnostic agent. Z. Q. Hu et al. designed NPs-SHP2 nanoparticles, which had high specificity to thyroid tumors *in vitro* and *in vivo*. Moreover, NPs-SHP2 could be activated by LIFU irradiation to enhance ultrasound molecular imaging in thyroid cancer model. In the study by X. B. Ma et al., GO-AuNS-DOTA-Gd was prepared and its physicochemical properties indicated that this probe could act as an efficient photosensitizer for photothermal therapy. Additionally, GO-AuNS-DOTA-Gd can be used for precisely delineating the tumor margin from normal tissues based on multimodality molecular imaging.

A new tracer [<sup>18</sup>F] AmBF<sub>3</sub>-TEG-ES was prepared by H. B. Huang et al. They showed that [<sup>18</sup>F] AmBF<sub>3</sub>-TEG-ES would be a potential PET imaging agent for the diagnosis of estrogen-dependent tumors. Similarly, X. Q. Du et al. investigated the differential diagnostic value of <sup>18</sup>F-Alfatide II PET/CT between tuberculosis and lung cancer patients. Moreover, they analyzed the angiogenesis in sarcoidosis and chronic inflammations.

R. Nishii et al. also focus on PET imaging. They demonstrated that MeAIB-PET could provide better assessments for detecting malignant type brain tumors. In a differential diagnosis between low-grade and high-grade astrocytoma, MeAIB-PET is a useful diagnostic imaging tool, especially in evaluations using the T/N ratio.

Y. J. Liu et al. observed that positive neural correlations of respiratory amplitude were shown in anterior lobe and insula, while they were negative in prefrontal cortex and sensorimotor areas. Their findings revealed the involvement of cognitive, executive control, and sensorimotor processing in hypnosis for respiratory control.

G. Q. Shao et al. published two articles in this special issue. In one of the papers, they synthesized a novel  $^{32}\text{P}$ -CP-PLGA seeds which can control the release of entrapped  $^{32}\text{P}$ -CP particles. Their results demonstrated that  $^{32}\text{P}$ -CP-PLGA seeds are very promising for glioma brachytherapy, and  $^{68}\text{Ga}$ -3PRGD2 imaging shows great potential for early response evaluation of  $^{32}\text{P}$ -CP-PLGA seeds brachytherapy. In the other paper, they demonstrated that the  $^{68}\text{Ga}$ -PSMA-11 PET-CT imaging could invasively evaluate PSMA expression during PCa progression and tumor growth with % ID/cm<sup>3</sup> (based on functional volume) as an important index. Low-dose 2-PMPA preadministration might be a choice to decrease kidney uptake of  $^{68}\text{Ga}$ -PSMA-11.

### **Conflicts of Interest**

The editors declare that they have no conflicts of interest.

### **Acknowledgments**

We are very grateful to all the authors for submitting their manuscripts to the special issue “Molecular Imaging in Targeted Therapeutics” as well as the professional reviewers for providing their helpful comments and suggestions. We thank the reviewers and authors for their time and efforts.

*Yuebing Wang  
Zhen Cheng  
Shuang Liu  
Guoqiang Shao*

## Research Article

# Investigation on the Neural Mechanism of Hypnosis-Based Respiratory Control Using Functional MRI

Yanjun Liu <sup>1,2</sup> Wenjian Qin,<sup>1,3</sup> Rongmao Li,<sup>1</sup> Shaode Yu <sup>1,3</sup> Yini He <sup>4</sup>  
and Yaoqin Xie <sup>1</sup>

<sup>1</sup>Institute of Biomedical and Health Engineering, Shenzhen Institutes of Advanced Technology, Chinese Academy of Sciences, Shenzhen 518055, China

<sup>2</sup>Shenzhen Deep Bay Innovation Co., Ltd., Shenzhen 518055, China

<sup>3</sup>Shenzhen College of Advanced Technology, University of Chinese Academy of Sciences, Shenzhen 518055, China

<sup>4</sup>Key Laboratory for NeuroInformation of Ministry of Education, School of Life Science and Technology, University of Electronic Science and Technology of China, Chengdu 610054, China

Correspondence should be addressed to Yaoqin Xie; yq.xie@siat.ac.cn

Received 27 December 2017; Revised 26 April 2018; Accepted 16 May 2018; Published 2 July 2018

Academic Editor: Yuebing Wang

Copyright © 2018 Yanjun Liu et al. This is an open access article distributed under the Creative Commons Attribution License, which permits unrestricted use, distribution, and reproduction in any medium, provided the original work is properly cited.

Respiratory control is essential for treatment effect of radiotherapy due to the high dose, especially for thoracic-abdomen tumor, such as lung and liver tumors. As a noninvasive and comfortable way of respiratory control, hypnosis has been proven effective as a psychological technology in clinical therapy. In this study, the neural control mechanism of hypnosis for respiration was investigated by using functional magnetic resonance imaging (fMRI). Altered spontaneous brain activity as well as neural correlation of respiratory motion was detected for eight healthy subjects in normal state (NS) and hypnosis state (HS) guided by a hypnotist. Reduced respiratory amplitude was observed in HS (mean  $\pm$  SD: 14.23  $\pm$  3.40 mm in NS, 12.79  $\pm$  2.49 mm in HS,  $p = 0.0350$ ), with mean amplitude deduction of 9.2%. Interstate difference of neural activity showed activations in the visual cortex and cerebellum, while deactivations in the prefrontal cortex and precuneus/posterior cingulate cortex (PCu/PCC) in HS. Within these regions, negative correlations of neural activity and respiratory motion were observed in visual cortex in HS. Moreover, in HS, voxel-wise neural correlations of respiratory amplitude demonstrated positive correlations in cerebellum anterior lobe and insula, while negative correlations were shown in the prefrontal cortex and sensorimotor area. These findings reveal the involvement of cognitive, executive control, and sensorimotor processing in the control mechanisms of hypnosis for respiration, and shed new light on hypnosis performance in interaction of psychology, physiology, and cognitive neuroscience.

## 1. Introduction

Respiratory control is one of the most essential parts for dose distribution management during radiotherapy, especially for lung and liver tumors. Conventional technologies of respiration control during radiotherapy include stable-respiration training before treatment, gating technology that coincides with the treatment in breath cycle [1], assistant visual system by showing standard respiration waveform to guide patients to breathe regularly, and real-time tumor tracking by implanting metallic or radio frequency fiducials [2, 3]. These methods may prolong treatment time for gating,

feel uncomfortable for patient, and even cause potential complications. In this study, hypnosis is introduced for respiratory control during radiotherapy without any side effects.

Many clinical evidences have proven that hypnosis is effective and safe in pain reduction [4], emotional stress reduction [4, 5], which can be applied for treating depression [6], sleeping disorders [7], and anxiety [8], and other psychological therapy. Relative studies using electroencephalogram (EEG) [9, 10] and functional magnetic resonance imaging (fMRI) [11–16] demonstrate the existence of neural brain activity in response to hypnotic suggestion. Additionally, respiration works in its neural regulation. Tiny

variation in respiration (breathing rate or depth) and breath-holding attribute to the change of arterial level of carbon dioxide (CO<sub>2</sub>) therefore leading to increased cerebral blood flow (CBF) and blood oxygen level-dependent (BOLD) signal [17–21]. Similarly, an fMRI study of hyperventilation suggested that changed level of arterial CO<sub>2</sub> comes with the BOLD signal [22]. Conversely, the chemoreflex triggered by the changing concentration of CO<sub>2</sub> has an influence on respiratory variability (changing the breathing rate and depth) in return [23, 24]. It forms a chemoreflex-mediated feedback cycle among respiration, CO<sub>2</sub>, CBF, and BOLD signal [20]. These studies provide the basis for investigation of neural mechanism of respiration control during radiotherapy.

As we know, lower amplitude of respiration is helpful for precise dose delivery, which can increase dose rate for tumor target, while protecting the organ at risk (OAR) from dose radiation. Our previous study has demonstrated that hypnosis can effectively reduce respiration amplitude and increase respiration stability [25]. In this study, we furthermore explore the mechanisms of hypnosis for respiratory control by using resting-state fMRI. The temporal variation [26] and signal synchronization [27, 28] of BOLD signal were detected to investigate the correlative relationship between neural activity and respiratory motion.

## 2. Materials and Methods

*2.1. Experimental Design.* A wide distribution of physiological difference of eight volunteers (Table 1) without history of neurological disorder participated in the hypnosis experiment. Intrasubject design was used, which consisted of two sections for every volunteer, corresponding to normal state (NS) and hypnosis state (HS), respectively. In the NS section, the volunteers were lying quietly in MRI, stayed awake with eyes closed and without any thinking activities. The NS section lasted about 10 minutes. In the HS section, the volunteers were guided into hypnosis by hypnotists to lead them into psychologically stable and comfortable state. The period of HS section lasted about 30–40 minutes. During both sections, the following three images for every subject were scanned: the structural coronal section of thoracic-abdomen, BOLD functional image, and structural T1 image of the brain. The structural thoracic-abdomen images were applied for analysis of respiratory motion, and the brain images (BOLD-fMRI and T1) were applied for analysis of spontaneous brain activities during hypnosis. It is noted that all of the volunteers are hypnotists themselves, and all of them are suitable for hypnosis.

*2.1.1. Ethical Statement.* All methods were carried out in accordance with relevant guidelines and regulations. The experiment was approved by the Institutional Review Board of Shenzhen Institutes of Advanced Technology, Chinese Academy of Sciences. The informed consent was written in an approval document. Informed consent of the experiment was obtained from all subjects. Informed consent for publication of identifying information/images in an online open-access publication was obtained from all subjects.

TABLE 1: Demographic characteristics of eight healthy volunteers.

	Mean $\pm$ SD	Range
Age (year)	33 $\pm$ 9	23–47
Gender (female/male)	6/2	/
Height (cm)	166 $\pm$ 12	155–185
Weight (kg)	66 $\pm$ 21	52–105

SD = standard deviation.

*2.2. Data Acquisition and Preprocessing.* All of the data were acquired through a 3.0T SIEMENS MRI machine system. The scanning settings were as follows. Structural thoracic-abdomen parameters: repetition time and echo time (TR/TE) = 4.25/1.97 ms, slice thickness = 5 mm, flip angle (FA) = 30°, field of view (FOV) = 350 mm  $\times$  350 mm, matrix = 128  $\times$  128, and frequency = 3 Hz. Functional image-scanning parameters: TR/TE = 2000/30 ms, slice thickness = 4 mm, FA = 90°, FOV = 220 mm  $\times$  220 mm, and matrix = 64  $\times$  64. T1 image-scanning parameters: TR/TE = 2000/9.2 ms, slice thickness = 4 mm, FA = 130°, FOV = 230 mm  $\times$  130 mm, and matrix = 320  $\times$  182.

The functional image processing was performed by RESTplus\_V1.2 ([www.restfmri.net](http://www.restfmri.net)), SPM8 ([www.fil.ion.ucl.ac.uk/spm](http://www.fil.ion.ucl.ac.uk/spm)), and data analysis toolkits for resting state fMRI, running on MATLAB platform. The pre-processing procedures included time points removal (the first five time points were removed to avoid the unstable operation in the beginning of scan), slice timing, head motion correction, spatial normalization (by using T1 image unified segmentation [29], normalized to Montreal Neurological Institute (MNI) space, resampled to 3 mm  $\times$  3 mm  $\times$  3 mm), spatial smooth (smoothed with 4 mm full-width at half-maximum Gaussian kernel), linear drift trends removal, nuisance covariates regression (including head motion parameters, global mean signal, white matter signal, and cerebrospinal fluid signal), and temporal filter (0.01–0.1 Hz).

*2.3. Respiratory Motion Analysis.* The MRI image of thoracic-abdomen section in coronal view was used to extract respiration data. The distance from thoracic diaphragm to the top of the lung was defined as respiration length (Figure 1(a)). The influence of cardiac motion was regressed out by frequency depression of 1 Hz. The amplitude fluctuated during respiratory motion, which formed a respiratory motion curve (Figure 1(b)). To evaluate the characteristics of respiratory motion, amplitude and tail-end of respiration were identified. For each volunteer, these indicators were calculated for both NS and HS to analyze interstate differences of respiratory motion.

*2.3.1. Respiration Amplitude.* Respiration amplitude evaluates the variation of respiration length. As demonstrated in Figure 1(b), in a single cycle, the amplitude is the averaged value from the peak to its two adjacent troughs ( $a_k$  and  $b_k$ ). For each volunteer, the respiration amplitude is defined as the weighted average of the amplitudes of all cycles, as follows:

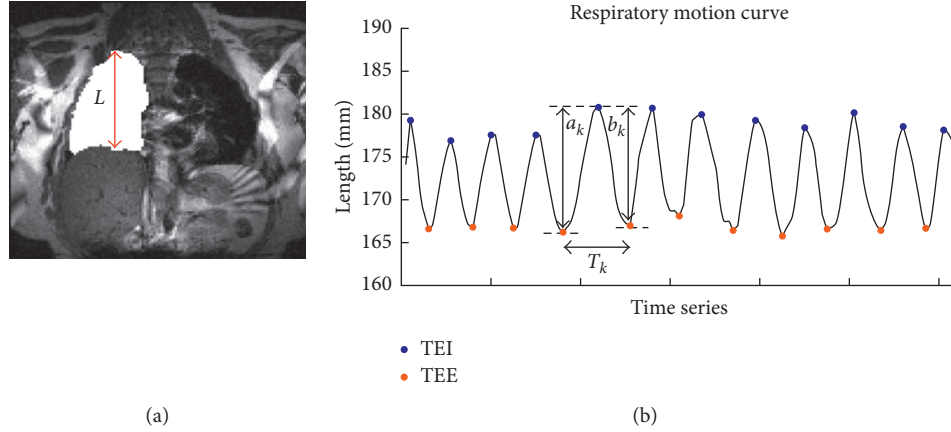


FIGURE 1: Characteristics of respiratory motion. (a) MRI image of thoracic-abdomen section in coronal view.  $L$  indicates respiration length, the distance from thoracic diaphragm to the top of the lung. (b) Sample of respiration curve. TEI = tail end of inspiration; TEE = tail end of expiration.

$$A = \sum_{k=1}^K w_k \cdot \frac{a_k + b_k}{2}, \quad (1)$$

where  $A$  is the averaged respiration amplitude of the volunteer,  $K$  is the total number of respiratory cycle,  $w_k$  is the weight of  $k$ th cycle to the entire respiration curve, and  $\sum_{k=1}^K w_k = 1$ .

In addition, we define amplitude deduction AD as follows:

$$AD = -\frac{A^{HS} - A^{NS}}{A^{NS}} \times 100\%, \quad (2)$$

where  $A^{NS}$  indicates the amplitude in NS,  $A^{HS}$  indicates the amplitude in HS, positive AD represents decreased amplitude in HS, and negative AD represents increased amplitude in HS.

**2.3.2. Tail End of Respiration.** Tail end of respiration includes tail end of inspiration (TEI) and tail end of expiration (TEE), corresponding to the peak and trough in the respiratory motion curve (Figure 1(b)). For each volunteer, TEI/TEE averages all of the peaks/troughs.

$$\begin{aligned} TEI &= \frac{1}{K} \sum_{k=1}^K P_k, \\ TEE &= \frac{1}{K} \sum_{k=1}^K Q_k, \end{aligned} \quad (3)$$

where  $P_k$  is the peak position of  $k$ th cycle and  $Q_k$  is the trough position of  $k$ th cycle.

**2.4. Analysis of Spontaneous Brain Activity.** To analyze the spontaneous brain activity in NS and HS, three voxel-wise measurements were calculated: fractional amplitude of low frequency fluctuation (fALFF), regional homogeneity (ReHo), and degree centrality (DC). Low frequency fluctuation is thought to reflect spontaneous brain activity [30, 31]. Fractional ALFF is defined as the ratio of the power of the low frequency band (0.01–0.1 Hz) to the power of the entire detectable (0–0.25 Hz) frequency band [26]. ReHo calculates Kendall's coefficient concordance to evaluate the local signal

synchronization by analyzing the similarity of time series of the chosen voxel with its neighboring voxels [27]. In this paper, ReHo was calculated by the synchronization of a voxel with its 26 neighboring voxels. DC is a voxel-wise measurement to estimate the global functional connectivity density between a voxel with all other voxels within the mask [28]. In this study, DC was calculated by summing up the number of voxels whose correlation coefficient with the target voxel reached a given threshold ( $r = 0.25$ ). Additionally, the fALFF/ReHo/DC value of each voxel was converted to the Z-value by Fisher's Z transformation (through subtracting the global-brain mean value and then dividing by the global standard deviation) for standardization.

**2.5. Statistical and Correlative Analysis.** For the respiratory motion analysis, individual level and group level of interstate differences were identified by a two sample  $t$ -test ( $p < 0.05$ ) and paired  $t$ -test ( $p < 0.05$ ), respectively. Interstate difference of neural activity was identified by a paired  $t$ -test ( $p < 0.005$ , AlphaSim multiple comparison correction) within a grey matter mask on fALFF/ReHo/DC maps of two states. Afterwards, the clusters showing significant difference were taken as regions of interest (ROIs) for the Pearson correlative analysis between respiratory motion (amplitude, TEI, TEE) and neural activity. ROI signals of fALFF/ReHo/DC were extracted by averaging all of the within-ROI voxels. Moreover, to examine the correlation between neural activity and respiratory motion comprehensively, voxel-wise correlation within the grey matter mask of two states was calculated and compared, regressing out the covariates of demographic characteristics in Table 1. For both NS and HS, the threshold of the correlation maps were set at  $r > 0.5$ , and the survival voxels of two states were combined as a mask to compare the interstate difference of neural correlation.

## 3. Results

### 3.1. Characteristics of Respiratory Motion

**3.1.1. Amplitude.** As demonstrated in Figure 2(a), group level amplitude in NS was  $14.23 \pm 3.40$  mm (mean  $\pm$  SD) and

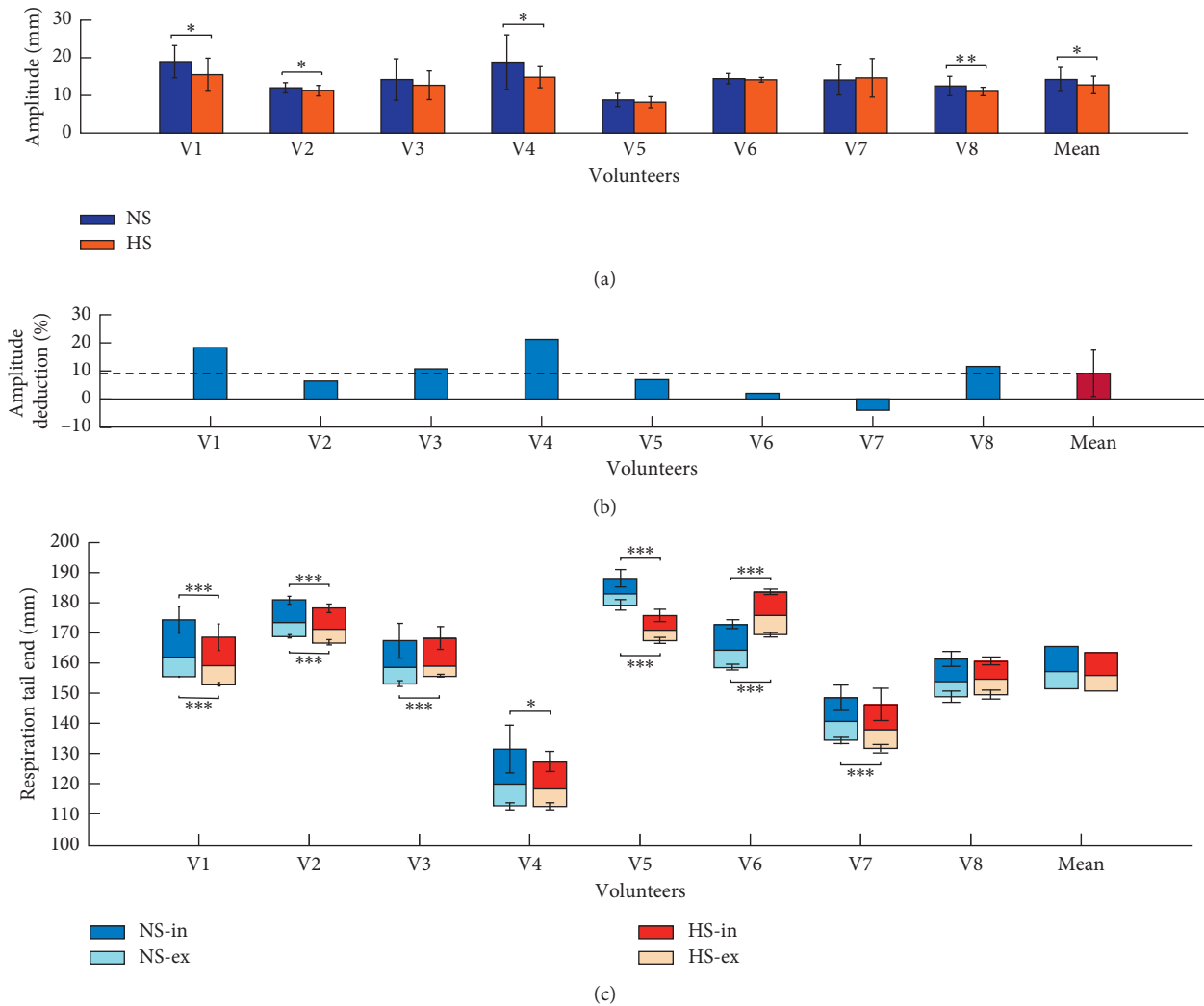


FIGURE 2: Amplitude and tail end of respiration in normal state (NS) and hypnosis state (HS). (a) Amplitudes. (b) Amplitude deduction in HS comparing to NS. (c) Tail end of inspiration (in) and expiration (ex). V1, V2, . . . , V8 were noted for individual volunteers. Statistical significance notation: \*  $p < 0.05$ , \*\*  $p < 0.005$ , and \*\*\*  $p < 0.0005$ .

in HS was  $12.79 \pm 2.49$  mm. Significant lower amplitude was observed in HS in comparison with NS ( $p = 0.0350$ ). Seven out of eight volunteers were observed with reduced amplitude in HS, and the mean amplitude deduction was 9.2% (Figure 2(b)). However, the unique one with increased mean amplitude in HS showed no significant ( $p = 0.6394$ ) higher values (V7 in Figure 2(a)). These results indicated that hypnosis had an effect on respiratory control.

**3.1.2. Tail End of Respiration.** Tail end of inspiration (TEI) and tail end of expiration (TEE) are the highest and the lowest respiration positions, respectively (Figure 1(b)). In this paper, the boundary line (BL) between inspiration and expiration was defined as the averaged respiration amplitude of the entire respiratory motion curve. In HS, the mean TEI/BL/TEE across all volunteers was 163.45/155.81/150.65 mm, and all of them were lower than the results (165.49/156.89/151.26 mm) in NS (Figure 2(c)). Although no significant interstate difference of TEI ( $p = 0.4020$ ), BL ( $p = 0.6573$ ), and TEE ( $p = 0.7910$ ) was

observed in the group level, significant difference was demonstrated in individual volunteers (Figure 2(c)).

**3.2. Interstate Difference of Neural Activity.** The resultant statistical T-maps (voxel  $p < 0.005$ , AlphaSim-corrected without smoothness estimate, cluster size  $> 324$  mm<sup>3</sup>, and grey matter mask) showed that there existed interstate difference in fALFF/ReHo/DC between NS and HS (Table 2; Figure 3). In HS, decreased fALFF was observed in the left inferior parietal lobule (IPL). As for ReHo, increased ReHo was observed in the left cerebellum anterior lobe (CAL) and right calcarine, while it was decreased in the left dorsolateral superior frontal gyrus (SFG), the left precuneus/posterior cingulate cortex (PCu/PCC), the left triangular part of inferior frontal gyrus, the and middle frontal gyrus (IFGtri/MFG). DC was increased in the bilateral calcarine and right cerebellum posterior lobe (CPL), whereas it was decreased in the left PCu/cuneus, left medial orbital of prefrontal cortex, and left MFG.

TABLE 2: Clusters showing interstate fALFF/ReHo/DC difference.

Brain region	Brodmann area	Cluster size (mm <sup>3</sup> )	Peak MNI coordinates	Peak T value
<i>Interstate fALFF difference</i>				
L-IPL	40	324	-48 -45 42	-5.65
<i>Interstate ReHo difference</i>				
L-CAL	/	324	-24 -36 -39	10.73
R-calcarine	18	459	15 -78 3	6.56
L-SFGdor	9	378	-15 42 48	-8.80
L-PCu/PCC	23/30	702	0 -51 21	-7.39
L-IFGtri/MFG	45/46	351	-39 30 27	-6.46
<i>Interstate DC difference</i>				
R-calcarine	18/17	1566	18 -75 9	12.14
R-CPL	/	486	33 -63 -24	8.36
L-calcarine	17	891	-15 -75 12	7.47
L-PCu/cuneus	23	378	-9 -63 24	-7.37
L-MPFCorb	11	351	-3 63 -12	-7.11
L-MFG	46	432	-39 39 30	-6.90

fALFF = fractional amplitude of low frequency fluctuation; ReHo = regional homogeneity; DC = degree centrality; MNI = Montreal Neurological Institute; L = left hemisphere; R = right hemisphere; IPL = inferior parietal lobule; CAL = cerebellum anterior lobe; SFGdor = dorsolateral superior frontal gyrus; PCu = precuneus; PCC = posterior cingulate cortex; IFGtri = triangular part of inferior frontal gyrus; MFG = middle frontal gyrus; CPL = cerebellum posterior lobe; MPFCorb = medial orbital of prefrontal cortex. Positive/negative T-value indicates increased/decreased activity in hypnosis state.

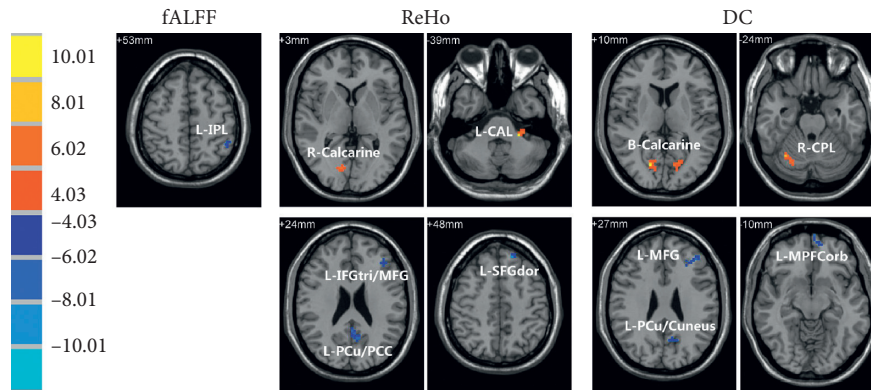


FIGURE 3: Statistical T-maps of interstate neural activity differences. The color-bar shows the statistical T-value for all maps. Red/blue indicates increased/decreased activity in hypnosis state, respectively. The threshold of T-maps are set at  $p < 0.005$ , AlphaSim-corrected, cluster size  $> 324 \text{ mm}^3$ . fALFF = fractional amplitude of low frequency fluctuation; ReHo = regional homogeneity; DC = degree centrality; L = left hemisphere; R = right hemisphere; IPL = inferior parietal lobule; CAL = cerebellum anterior lobe; SFGdor = dorsolateral superior frontal gyrus; PCu = precuneus; PCC = posterior cingulate cortex; IFGtri = triangular part of inferior frontal gyrus; MFG = middle frontal gyrus; CPL = cerebellum posterior lobe; MPFCorb = medial orbital of prefrontal cortex.

**3.3. Correlative Analysis of Neural Activity and Respiratory Motion.** The significant correlations ( $p < 0.05$ ) are demonstrated between brain activity (Table 2; Figure 3) and respiratory motion in Figure 4. Positive correlation ( $r = 0.78$ ,  $p = 0.024$ ) was observed between ReHo deduction and amplitude deduction in the left PCu/PCC (Figure 4(a)), while no significant correlation was observed between ReHo and amplitude in HS ( $r = 0.72$ ,  $p = 0.0433$  in NS;  $r = 0.33$ ,  $p = 0.4179$  in HS). Similarly, there was no significant correlation between ReHo and TEI/TEE in left the IFGtri/MFG (Figure 4(b)). Oppositely, in HS, negative correlations between DC and TEI/TEE ( $r = -0.81$ ,  $p = 0.0158$  for TEI;  $r = -0.80$ ,  $p = 0.0173$  for TEE) were observed in the left PCu/cuneus, as compared with insignificant positive correlations in NS (Figure 4(c)). Negative correlations of DC and TEI/TEE were both observed in the right calcarine in HS (Figure 4(d)).

The voxel-wise correlation maps between neural activity and respiratory motion, within the combined mask of correlation maps (threshold at  $r > 0.5$ ) of two states, were further threshold with state-disparity of correlation coefficient over 1 and cluster size over 80 voxels ( $2160 \text{ mm}^3$ ). The state-disparity of correlation coefficient (the correlation coefficient in HS minus that of NS) over 1 accounted for opposite correlations of two states. The brain regions of the surviving voxels and the correlation coefficients are shown in Figure 5 and Table 3. In HS, positive correlations between amplitude and neural activity were observed in the CAL, middle cingulate cortex (MCC), cuneus, fusiform gyrus, and insula, and negative correlations were observed in the anterior cingulate cortex (ACC), prefrontal cortex (PFC), and precentral gyrus (PreC). However, these correlations of the corresponding brain regions were reversed in NS (Table 3). The results of TEI and TEE were mostly consistent with each other. Different from

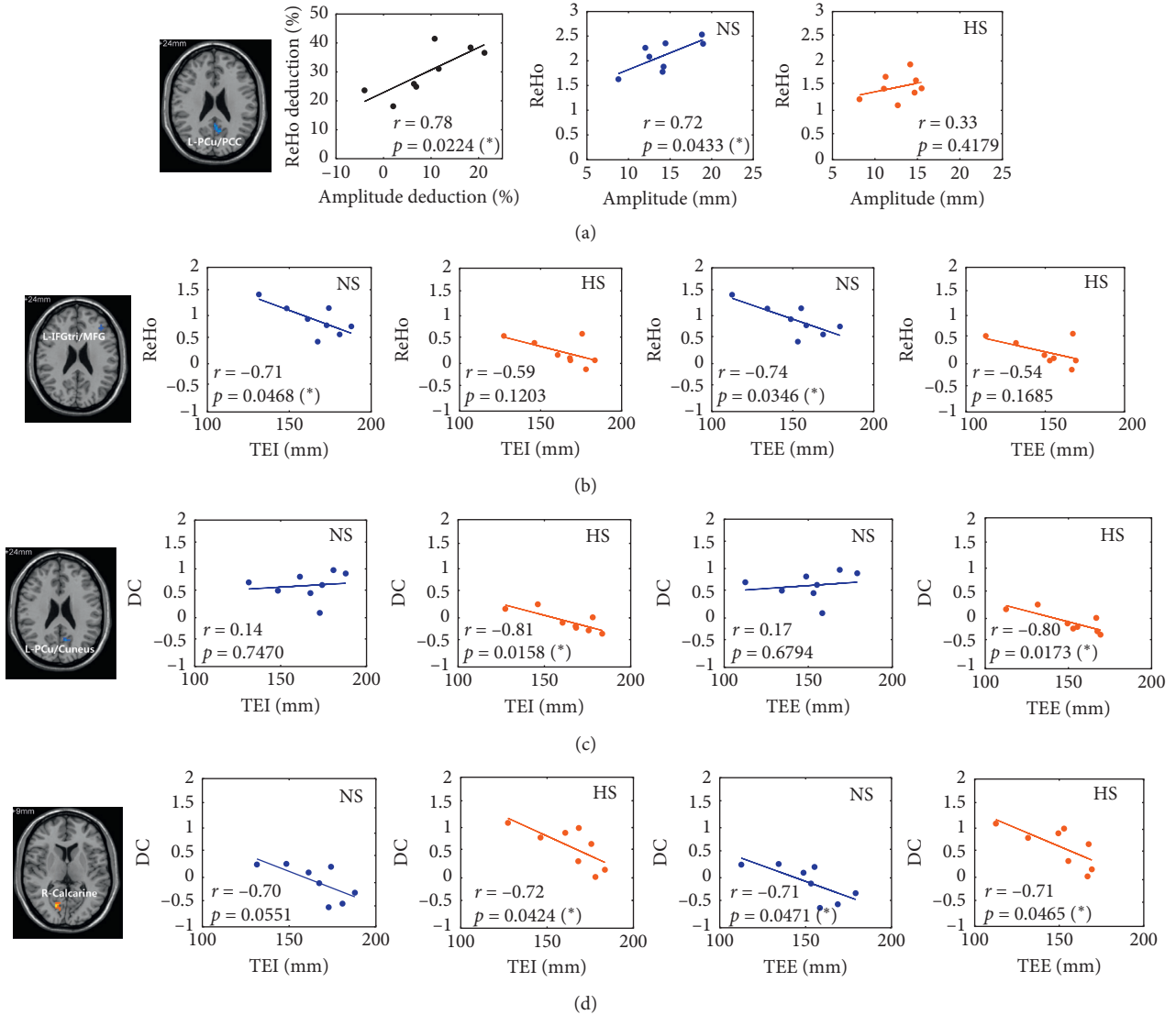


FIGURE 4: Correlation of neural activity and respiratory motion in brain regions showing interstate neural activity difference. (a) Correlation of ReHo and respiration in the left precuneus/posterior cingulate cortex (L-PCu/PCC). (b) Correlation of ReHo and respiration in the left triangular part of inferior frontal gyrus and middle frontal gyrus (L-IFGtri/MFG). (c) Correlation of DC and respiration in the left precuneus/cuneus (L-PCu/cuneus). (d) Correlation of DC and respiration in right calcarine. ReHo = regional homogeneity; DC = degree centrality; NS/HS = normal/hypnosis state; TEI/TEE = tail end of inspiration/expiration.

NS, in HS, positive correlations between ReHo/DC and TEI/TEE were observed in the CAL, supramarginal gyrus (SMG), PFC, and insula, while negative correlations were observed in the CPL, MCC, supplementary motor area (SMA), PreC, postcentral gyrus (PostC), fusiform gyrus, and thalamus (Table 3; Figure 5).

## 4. Discussion

**4.1. Hypnosis for Respiratory Control.** In this study, hypnosis is intended to be applied for respiratory control without side effects in radiotherapy. Following hypnotic guidance with individual-customized content, volunteers feel peaceful and stay in a more stable and comfortable state of respiration. In our results, reduced amplitude of respiratory motion was

observed in HS (Figures 2(a) and 2(b)), which is consistent with our previous study [25]. Respiratory motion may induce fluctuation of dose distribution during radiotherapy, especially for lung and liver tumors. Tumor fluctuates in pace with respiratory motion. Therefore, reduction of respiratory amplitude is instrumental to suppress tumor motion, thus increasing dose rate for tumor target, meanwhile protecting organ at risk (OAR) from dose radiation. Moreover, as a clinical auxiliary method, hypnosis may help patients get into an inner peaceful state with less dependency on self-control during treatment, which is beneficial to treatment. These demonstrations suggest that hypnosis is an efficient alternative for respiratory control in radiotherapy.

In radiotherapy, planning target volume (PTV) covers the area of tumor motion, indicating that less scope and

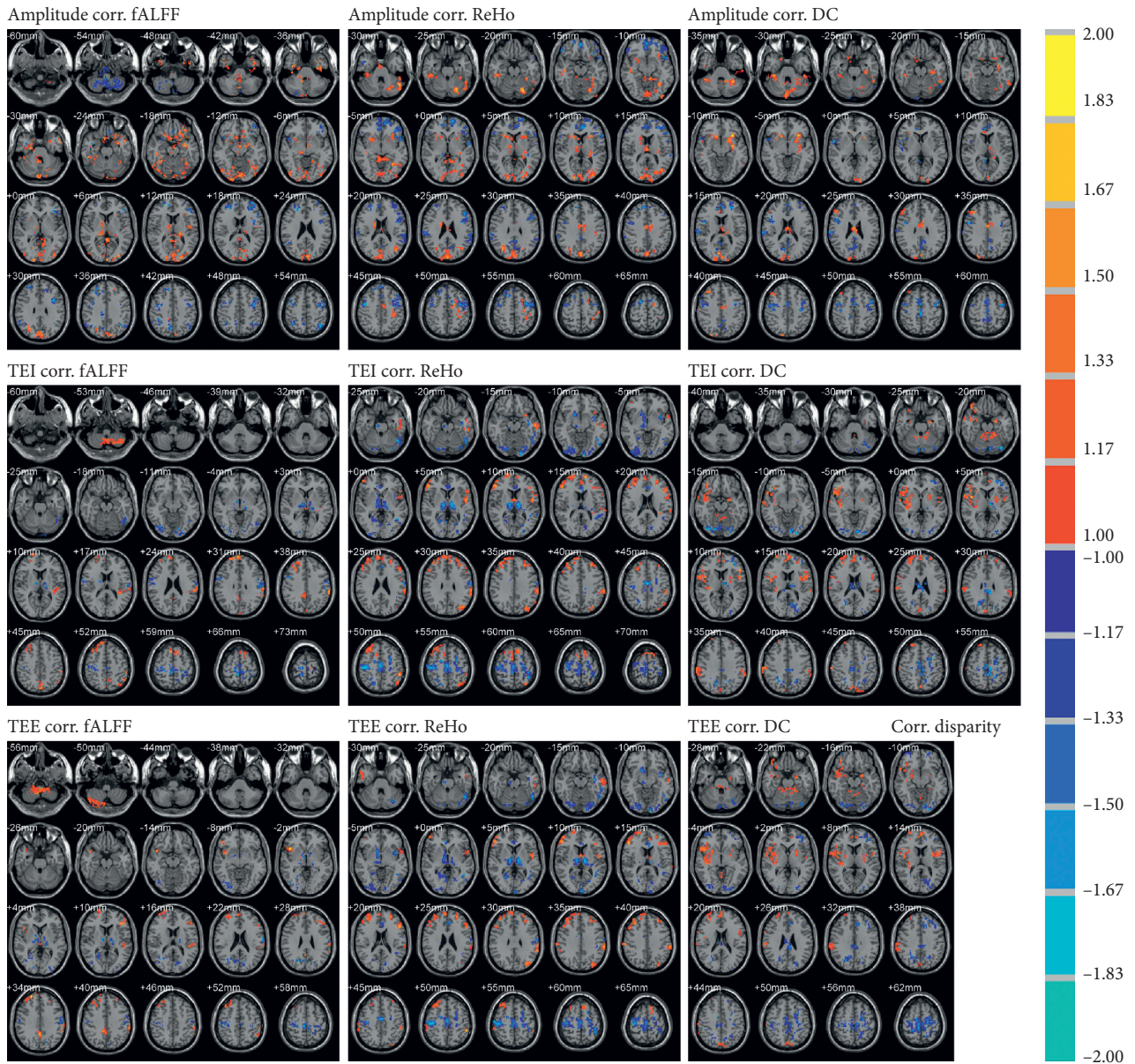


FIGURE 5: Interstate difference of voxel-wise correlation (corr.) between neural activity and respiratory motion, within combined mask of correlation maps of two states threshold at  $r > 0.5$ , and state-disparity of correlation coefficient over 1 and cluster size over 80 voxels ( $2160 \text{ mm}^3$ ). The value of color-bar indicates coefficient in hypnosis state minus that in normal state. Red overlap indicates positive correlation in hypnosis state and negative in normal state, while blue indicates the negative correlation in hypnosis state and positive in normal state. TEI/TEE = tail end of inspiration/expiration; fALFF = fractional amplitude of low frequency fluctuation; ReHo = regional homogeneity; DC = degree centrality.

more stability of tumor motion are beneficial to more accurate PTV along with less dose. To accomplish this target, gating technology is recommended to be employed in radiotherapy by delivering radiation dose during the deepest of expiration in every respiratory period. Therefore, stable cycles and stability of TEE are critical for gating technology. However, given the prolonged treatment time of this technology and practical difficulties of operation, gating technology is not widely applied to radiotherapy. Instead, continuous dose radiation covering the area of tumor motion throughout the radiation-treatment procedure is a more stable and safe choice. In this case, reduced amplitude of

respiration is crucial for radiotherapy. However, not all patients are adaptive to respiratory control by hypnosis. In this study, volunteers are all healthy; therefore, clinical trials of hypnosis are needed to examine its availability. Before it is applied to clinical treatment, sufficient pretrainings and evaluation of respiratory motion should be guaranteed to ensure its effectiveness and safety for the patient.

4.2. Neural Analysis of Hypnosis for Respiratory Control. Neural mechanisms of hypnosis have been explored for years, regarding its function of consciousness, cognitive processing,

TABLE 3: Brain regions showing significant interstate difference of voxel-wise correlation between neural activity and respiratory motion.

	fALFF				ReHo				DC			
	Brain regions	Voxels	NS-r	HS-r	Brain regions	Voxels	NS-r	HS-r	Brain regions	Voxels	NS-r	HS-r
Amplitude	B-CAL	103	-0.62	0.59	B-MCC	155	-0.64	0.54	B-CAL/fusiform	250	-0.52	0.66
	B-fusiform	319	-0.64	0.61	B-cuneus/fusiform	1037	-0.56	0.66	B-MCC	198	-0.61	0.61
	B-cuneus	1064	-0.63	0.60	L-CAL	113	-0.60	0.61	B-cuneus	213	-0.64	0.58
	B-CPL	404	0.47	-0.70	L-insula	99	-0.53	0.67	L-insula/Put	215	-0.68	0.61
	B-MFG/SFG	533	0.60	-0.64	R-caudate/thalamus	242	-0.60	0.59	R-caudate	98	-0.63	0.56
	B-PreC	235	0.65	-0.59	B-MPFC/ACC	599	0.60	-0.66	B-SMA/PreC/PostC	945	0.67	-0.58
	B-IPL	285	0.65	-0.56	B-SMG	188	0.58	-0.59	B-ACC	102	0.57	-0.67
	B-CAL	124	-0.70	0.47	L-PreC	709	0.59	-0.64	B-PCu/PCC	221	0.51	-0.65
	R-MFG/SFG	265	-0.64	0.55	B-PFC	1052	-0.64	0.55	B-CAL	139	-0.53	0.59
	B-PCu/PCC	150	-0.57	0.62	L-SMG	159	-0.66	0.62	B-SMG	195	-0.61	0.59
TEI	L-SMG	219	-0.62	0.60	L-insula	124	-0.63	0.56	B-PFC	248	-0.75	0.42
	B-fusiform	205	0.66	-0.53	B-thalamus	485	0.63	-0.65	B-insula/Put	887	-0.56	0.65
	B-thalamus	160	0.70	-0.53	B-fusiform	494	0.66	-0.56	B-cuneus	102	-0.54	0.61
	B-SMA/PostC/PreC	534	0.56	-0.68	B-ACC	112	0.51	-0.71	R-fusiform/CPL	525	0.60	-0.60
	B-CPL/CAL	241	-0.70	0.50	B-MCC/PostC/PreC	1249	0.61	-0.66	B-SMA/PreC/MCC	1325	0.58	-0.65
	B-PFC	323	-0.64	0.54	B-LG	316	0.62	-0.58	R-PCu	128	0.62	-0.59
	L-IPL	144	-0.64	0.59	B-PFG	881	-0.63	0.57	B-CAL	191	-0.57	0.55
	B-PCu/PCC	85	-0.69	0.58	B-SMG	207	-0.65	0.58	B-amygdala/Put/insula	855	-0.56	0.65
	R-insula	97	-0.58	0.68	B-thalamus	439	0.66	-0.61	R-SMG	115	-0.63	0.54
	B-SMA/PostC/PreC	412	0.58	-0.64	B-PostC/PreC	1201	0.65	-0.60	B-MPFC/R-MFG	169	-0.73	0.44
B-thalamus	167	0.67	-0.54	B-ACC	104	0.60	-0.63	B-CPL	514	0.64	-0.56	
R-fusiform	105	0.71	-0.50	B-CPL/fusiform	402	0.66	-0.52	B-SMA/PreC/MCC	1443	0.60	-0.64	
				B-LG	214	0.68	-0.49	L-MFG	221	0.66	-0.55	

Paired *t*-test of correlation coefficients of two states across voxels show significant interstate difference ( $p < 0.000001$ ) for every cluster. TEI/TEE = tail end of inspiration/expiration; fALFF = fractional amplitude of low frequency fluctuation; ReHo = regional homogeneity; DC = degree centrality; NS-r/HS-r = correlation coefficient in normal/hypnosis state; L/R/B = left/right/bilateral; LG = lingual gyrus; PCu = precuneus; CAL/CPL = cerebellum anterior/posterior lobe; ACC/MCC/PCC = anterior/middle/posterior cingulate cortex; MPFC/PFC = (medial) prefrontal cortex; SFG/MFG/IFG = superior/middle/inferior frontal gyrus; PreC/PostC = precentral/postcentral gyrus; SMA = supplementary motor area; SMG = supramarginal gyrus; IPL = inferior parietal lobule; Put = putamen; fusiform = fusiform gyrus.

emotional regulation, attentional processing, executive control, and clinical stress/pain processing. Experimental results of interstate difference of neural activity demonstrated that alterations in HS were mostly located in the occipital cortex, cerebellum, and prefrontal cortex (Table 2; Figure 3). Moreover, results of ReHo and DC were consistent with each other. ReHo and DC are both measurements to evaluate signal synchronization or functional connectivity, where the former reflects regional synchronization and the later represents global synchronization.

In our results, activations were observed in the occipital cortex and cerebellum. The occipital cortex is known as the visual cortex, associated with visual processing. However, no visual-related task was induced during hypnosis experiment. A possible explanation is that it formed a picture in volunteers' minds when following hypnotic guidance. Increased neural activity in the cerebellum was also observed. The cerebellum involves in the function of motor control, perceptual processes, and sensory perception [32, 33] and takes part in the charge of interoceptive processing [34] and emotional processing [35]. Moreover, the anterior lobe and posterior lobe associate with different functions, corresponding to sensorimotor CAL [33] and cognitive CPL [36]. In our results, neural activity in the anterior lobe and posterior lobe of the cerebellum were both demonstrated to be increased. The above results indicate that visual, sensorimotor, and cognitive processings are involved in hypnosis.

Contrary to the occipital cortex and cerebellum, decreased activity was demonstrated in the prefrontal cortex and PCu/PCC. The prefrontal cortex involves in complex cognitive behavior [37] and various subregions' response for different functions. Deactivations of the prefrontal cortex contained MPFC and dorsolateral prefrontal cortex (DLPFC). Both MPFC and PCu/PCC are critical parts of the default mode network (DMN), which activates in task-deprived state and deactivates in task-evoked state [38]. On the other hand, DLPFC is well known for its executive task-induced role in executive control processing [34] and attentional processing [39, 40]. Contrary to our results, activation in MPFC has been observed in strong emotional arousal [41]. Consistently, disrupting DLPFC activity is observed in subjective response to hypnotic suggestion [42]. Decreased activity in both DMN regions and executive control regions may imply modulation of emotion and executive processing in hypnosis.

**4.3. Neural Correlation of Respiratory Motion.** A great number of studies have been working on the neural correlations between hypnosis and psychological performance. However, the neural correlations between hypnosis and physiology are rarely studied. In this study, we examined the correlation between neural activity and physiological performance (respiratory motion) during hypnosis. Within the brain regions showing significant interstate differences, significantly negative correlations were observed between DC and respiratory motion in the visual cortex in HS (Figures 4(c) and 4(d)), while correlations were insignificant in PCu/PCC (Figure 4(a)) and DLPFC (Figure 4(b)). Activation in the visual cortex implies visual processing during HS; however, negative neural correlation of amplitude in visual cortex may indicate that less in-mind visual interruption helps for

amplitude reduction. Insignificantly positive neural respiration in critical role of DMN (PCu/PCC), together with insignificantly negative results in critical role of executive control network (DLPFC), supports the breakout of the default brain state and arouse of executive brain in hypnosis for respiration control, which are identified through respiratory characteristics. Therefore, neural correlation of respiratory motion is an informative way to explore the potential mechanism of hypnosis for respiration control.

Although indicative correlation results showed interstate difference in some brain regions, identification of these regions was not so much convincing in terms of multiple comparison corrections which were carried out without smoothing estimation when clustering the statistical maps [43]. To make up this shortcoming, whole brain voxel-wise correlation was further examined. It was demonstrated that, in HS (opposite to the results of NS), positive correlations between neural activity and respiratory amplitude were observed in CAL, MCC, fusiform gyrus, and insula, while negative correlations were observed in ACC, PCu/PCC, prefrontal cortex, and sensorimotor area (PreC/PostC/SMA) (Figure 5; Table 3). Increased neural activity (Figure 3; Table 2) and positive-neural-respiratory correlation in the cerebellum, together with decreased neural activity (Figure 3; Table 2) and negative neural-respiratory correlation of amplitude in PCu/PCC, emphasize the consistent involvement of these regions during hypnosis for respiratory control. MCC and ACC are both cingulate regions associated with cognitive processing [44, 45]. However, inconsistent results of their correlations of brain activity and respiratory motion may reveal their different neurophysiological functional roles in hypnosis. During hypnotic intervention, negative neural-respiratory correlations in sensorimotor areas (PreC/PostC/SMA) reveal the involvement of motor and sensory processing [46] during hypnosis for respiratory control. Interestingly, MPFC and DLPFC were observed with positive correlation between neural activity and TEE/TEI, while there was a negative correlation between neural activity and respiration amplitude (Figure 5; Table 3). The prefrontal cortex is suggested to be involved in the involuntariness in response to hypnotic suggestion [47]. These results further implicate that the prefrontal cortex plays a critical role during hypnosis for respiratory control.

Positive correlations were shown in both respiratory amplitude and TEE/TEI (Figure 5; Table 3). Studies observed with insula activation suggest that the insula is associated with awareness [48], self-representation, and emotional processing [49]. Additionally, the SMG, fusiform gyrus, and thalamus are robust brain areas that showed significant correlation between fALFF/ReHo/DC and TEE/TEI (Figure 5; Table 3). The SMG is part of Wernicke's area associated with semantic representation [50]. Positive correlation observed between brain activity in the SMG and respiratory motion during hypnotic intervention may result from hypnotic voice guidance from the hypnotist. The fusiform gyrus is a functionally defined region in visual face recognition [51, 52]; however, this function is not relevant to our study. We hypothesized that the fusiform gyrus works together with the default mode network and executive control network during hypnotic intervention for respiratory control, similar to its role in facilitating social

motivation with large-scale networks [53]. Hypnosis participates in the regulation of consciousness [13], and a clinical study suggests that lesions in thalamus may affect the level of consciousness [54]. Therefore, negative correlation results of the thalamus may indicate a kind of altered state of consciousness during hypnosis.

Hypnosis has been focused on its psychological aspect in many studies, whereas we highlight its physiological effects of respiratory control in this study. As a psychological intervention, hypnosis is not only for respiratory control, but also attenuates the pain of patients during radiotherapy. Our results suggest the involvement of cognitive processing, emotional regulation, sensorimotor processing, and executive control processing in hypnosis for respiratory control. Though significant results are observed, however, small sample size and individual specificity of hypnotic contents may miss other potential relations. Therefore, adequate patient cases are needed for further understanding the neural and molecular mechanisms of hypnosis for respiration control.

## 5. Conclusion

In conclusion, this study examined the effect of hypnosis on respiration control and investigated spontaneous brain activity by measuring fALFF/ReHo/DC as well as the correlation between neural activity and respiratory motion. Reduced respiratory motion amplitude and stable respiratory cycle were observed in hypnosis with relaxation suggestion. Increased brain activity was observed in the visual cortex and cerebellum, while it was decreased in the prefrontal cortex and PCu/PCC. Positive neural correlations of respiratory amplitude were shown in the anterior lobe and insula, while they were negative in the prefrontal cortex and sensorimotor areas. These findings reveal the involvement of cognitive, executive control, and sensorimotor processing in hypnosis for respiratory control.

## Conflicts of Interest

The authors declare that there are no conflicts of interest regarding the publication of this article.

## Authors' Contributions

YanJun Liu and Wenjian Qin contributed equally to this work.

## Acknowledgments

This work was supported in part by grants from National Key Research and Develop Program of China (2016YFC0105102), Leading Talent of Special Support Project in Guangdong (2016TX03R139), Shenzhen Key Technical Research Project (JSGG20160229203812944), Science Foundation of Guangdong (2017B020229002, 2015B020233004, and 2014A030312006), Shenzhen Basic Technology Research Project (JCYJ20170818160306270), and Beijing Center for Mathematics and Information Interdisciplinary Sciences.

## References

- [1] R. Wagman, E. Yorke, E. Ford et al., "Respiratory gating for liver tumors: use in dose escalation," *International Journal of Radiation Oncology, Biology, and Physics*, vol. 55, no. 3, pp. 659–668, 2003.
- [2] T. R. Willoughby, P. A. Kupelian, J. Pouliot et al., "Target localization and real-time tracking using the Calypso 4D localization system in patients with localized prostate cancer," *International Journal of Radiation Oncology, Biology, and Physics*, vol. 65, no. 2, pp. 528–534, 2006.
- [3] R. D. Wiersma, W. Mao, and L. Xing, "Combined kV and MV imaging for real-time tracking of implanted fiducial markers," *Medical Physics*, vol. 35, no. 4, pp. 1191–1198, 2008.
- [4] S. J. Chester, K. Stockton, A. De Young et al., "Effectiveness of medical hypnosis for pain reduction and faster wound healing in pediatric acute burn injury: study protocol for a randomized controlled trial," *Trials*, vol. 17, no. 1, p. 223, 2016.
- [5] J. B. Schnur, I. Kafer, C. Marcus et al., "Hypnosis to manage distress related to medical procedures: A meta-analysis," *Contemporary Hypnosis*, vol. 25, no. 3-4, pp. 114–128, 2008.
- [6] B. S. McCann and S. J. Landes, "Hypnosis in the treatment of depression: considerations in research design and methods," *International Journal of Clinical and Experimental Hypnosis*, vol. 58, no. 2, pp. 147–164, 2010.
- [7] L. J. Owens, K. G. France, and L. Wiggs, "Behavioural and cognitive-behavioural interventions for sleep disorders in infants and children: a review," *Sleep Medicine Reviews*, vol. 3, no. 4, pp. 281–302, 1999.
- [8] D. C. Hammond, "Hypnosis in the treatment of anxiety- and stress-related disorders," *Expert Review of Neurotherapeutics*, vol. 10, no. 2, pp. 263–273, 2010.
- [9] T. Hinterberger, J. Schonher, and U. Halsband, "Analysis of electrophysiological state patterns and changes during hypnosis induction," *International Journal of Clinical and Experimental Hypnosis*, vol. 59, no. 2, pp. 165–179, 2011.
- [10] M. P. Jensen and T. Adachi, "Brain oscillations, hypnosis, and hypnotizability," *American Journal of Clinical Hypnosis*, vol. 57, no. 3, pp. 230–253, 2015.
- [11] P. Maquet, M. E. Faymonville, C. Degueldre et al., "Functional neuroanatomy of hypnotic state," *Biological Psychiatry*, vol. 45, no. 3, pp. 327–333, 1999.
- [12] T. Egner, G. Jamieson, and J. Gruzeliier, "Hypnosis decouples cognitive control from conflict monitoring processes of the frontal lobe," *Neuroimage*, vol. 27, no. 4, pp. 969–978, 2005.
- [13] D. A. Oakley and P. W. Halligan, "Hypnotic suggestion and cognitive neuroscience," *Trends in Cognitive Sciences*, vol. 13, no. 6, pp. 264–270, 2009.
- [14] D. A. Oakley and P. W. Halligan, "Hypnotic suggestion: opportunities for cognitive neuroscience," *Nature Reviews Neuroscience*, vol. 14, no. 8, pp. 565–576, 2013.
- [15] Y. Takarada and D. Nozaki, "Hypnotic suggestion alters the state of the motor cortex," *Neuroscience Research*, vol. 85, pp. 28–32, 2014.
- [16] G. De Benedittis, "Neural mechanisms of hypnosis and meditation," *Journal of Physiology Paris*, vol. 109, no. 4–6, pp. 152–164, 2015.
- [17] P. A. Robbins, J. Conway, D. A. Cunningham et al., "A comparison of indirect methods for continuous estimation of arterial PCO<sub>2</sub> in men," *Journal of Applied Physiology*, vol. 68, no. 4, pp. 1727–1731, 1990.
- [18] A. Kastrup, G. Krüger, G. H. Glover et al., "Regional variability of cerebral blood oxygenation response to hypercapnia," *Neuroimage*, vol. 10, no. 6, pp. 675–681, 1999.

- [19] E. Rostrup, I. Law, M. Blinkenberg et al., "Regional differences in the CBF and BOLD responses to hypercapnia: a combined PET and fMRI study," *Neuroimage*, vol. 11, no. 2, pp. 87–97, 2000.
- [20] R. M. Birn, J. B. Diamond, M. A. Smith et al., "Separating respiratory-variation-related fluctuations from neuronal-activity-related fluctuations in fMRI," *Neuroimage*, vol. 31, no. 4, pp. 1536–1548, 2006.
- [21] K. Murphy, R. M. Birn, and P. A. Bandettini, "Resting-state fMRI confounds and cleanup," *Neuroimage*, vol. 80, pp. 349–359, 2013.
- [22] S. Posse, L. J. Kemna, B. Elghahwagi et al., "Effect of graded hypo- and hypercapnia on fMRI contrast in visual cortex: Quantification of T<sub>2</sub> changes by multiecho EPI," *Magnetic Resonance in Medicine*, vol. 46, no. 2, pp. 264–271, 2001.
- [23] M. Modarreszadeh and E. N. Bruce, "Ventilatory variability induced by spontaneous variations of PaCO<sub>2</sub> in humans," *Journal of Applied Physiology*, vol. 76, no. 6, pp. 2765–2775, 1994.
- [24] J. G. Van Den Aardweg and J. M. Karemaker, "Influence of chemoreflexes on respiratory variability in healthy subjects," *American Journal of Respiratory and Critical Care Medicine*, vol. 165, no. 8, pp. 1041–1047, 2002.
- [25] R. Li, J. Deng, and Y. Xie, "Control of respiratory motion by hypnosis intervention during radiotherapy of lung cancer I," *BioMed Research International*, vol. 2013, Article ID 574934, 8 pages, 2013.
- [26] Q. H. Zou, C. Z. Zhu, Y. Yang et al., "An improved approach to detection of amplitude of low-frequency fluctuation (ALFF) for resting-state fMRI: Fractional ALFF," *Journal of Neuroscience Methods*, vol. 172, no. 1, pp. 137–141, 2008.
- [27] Y. Zang, T. Jiang, Y. Lu et al., "Regional homogeneity approach to fMRI data analysis," *Neuroimage*, vol. 22, no. 1, pp. 394–400, 2004.
- [28] R. L. Buckner, J. Sepulcre, T. Talukdar et al., "Cortical hubs revealed by intrinsic functional connectivity: mapping, assessment of stability, and relation to Alzheimer's disease," *Journal of Neuroscience*, vol. 29, no. 6, pp. 1860–1873, 2009.
- [29] J. Ashburner and K. J. Friston, "Unified segmentation," *Neuroimage*, vol. 26, no. 3, pp. 839–851, 2005.
- [30] B. Biswal, F. Zerrin Yetkin, V. M. Haughton et al., "Functional connectivity in the motor cortex of resting human brain using echo-planar MRI," *Magnetic Resonance in Medicine*, vol. 34, no. 4, pp. 537–541, 1995.
- [31] M. D. Fox and M. E. Raichle, "Spontaneous fluctuations in brain activity observed with functional magnetic resonance imaging," *Nature Reviews Neuroscience*, vol. 8, no. 9, pp. 700–711, 2007.
- [32] O. Baumann, R. J. Borra, J. M. Bower et al., "Consensus paper: the role of the cerebellum in perceptual processes," *Cerebellum*, vol. 14, no. 2, pp. 197–220, 2015.
- [33] K. Kansal, Z. Yang, A. M. Fishman et al., "Structural cerebellar correlates of cognitive and motor dysfunctions in cerebellar degeneration," *Brain*, vol. 140, pp. 707–720, 2017.
- [34] W. W. Seeley, V. Menon, A. F. Schatzberg et al., "Dissociable intrinsic connectivity networks for salience processing and executive control," *Journal of Neuroscience*, vol. 27, no. 9, pp. 2349–2356, 2007.
- [35] M. Adamaszek, F. D'Agata, R. Ferrucci et al., "Consensus paper: cerebellum and emotion," *Cerebellum*, vol. 16, no. 2, pp. 552–576, 2017.
- [36] J. D. Schmahmann, "The role of the cerebellum in cognition and emotion: personal reflections since 1982 on the dysmetria of thought hypothesis, and its historical evolution from theory to therapy," *Neuropsychology Review*, vol. 20, no. 3, pp. 236–260, 2010.
- [37] Y. Yang and A. Raine, "Prefrontal structural and functional brain imaging findings in antisocial, violent, and psychopathic individuals: a meta-analysis," *Psychiatry Research–Neuroimaging*, vol. 174, no. 2, pp. 81–88, 2009.
- [38] M. E. Raichle, A. M. MacLeod, A. Z. Snyder et al., "A default mode of brain function," *Proceedings of the National Academy of Sciences*, vol. 98, no. 2, pp. 676–682, 2001.
- [39] T. P. Zanto, M. T. Rubens, A. Thangavel et al., "Causal role of the prefrontal cortex in top-down modulation of visual processing and working memory," *Nature Neuroscience*, vol. 14, no. 5, pp. 656–661, 2011.
- [40] A. Gazzaley and A. C. Nobre, "Top-down modulation: bridging selective attention and working memory," *Trends in Cognitive Sciences*, vol. 16, no. 2, pp. 129–135, 2012.
- [41] E. Vermetten and J. D. Bremner, "Functional brain imaging and the induction of traumatic recall: a cross-correlational review between neuroimaging and hypnosis," *International Journal of Clinical and Experimental Hypnosis*, vol. 52, no. 3, pp. 280–312, 1997.
- [42] Z. Dienes and S. Hutton, "Understanding hypnosis meta-cognitively: RTMS applied to left DLPFC increases hypnotic suggestibility," *Cortex*, vol. 49, no. 2, pp. 386–392, 2013.
- [43] A. Eklund, T. E. Nichols, and H. Knutsson, "Cluster failure: why fMRI inferences for spatial extent have inflated false-positive rates," *Proceedings of the National Academy of Sciences*, vol. 113, no. 28, pp. 7900–7905, 2016.
- [44] G. Bush, P. Luu, and M. Posner, "Cognitive and emotional influences in anterior cingulate cortex," *Trends in Cognitive Sciences*, vol. 4, no. 6, pp. 215–222, 2000.
- [45] A. J. Shackman, T. V. Salomons, H. A. Slagter et al., "The integration of negative affect, pain and cognitive control in the cingulate cortex," *Nature Reviews Neuroscience*, vol. 12, no. 3, pp. 154–167, 2011.
- [46] W. K. Yoo, S. H. You, M. H. Ko et al., "High frequency rTMS modulation of the sensorimotor networks: Behavioral changes and fMRI correlates," *Neuroimage*, vol. 39, no. 4, pp. 1886–1895, 2008.
- [47] J. F. Kihlstrom, "Neuro-hypnotism: prospects for hypnosis and neuroscience," *Cortex*, vol. 49, no. 2, pp. 365–374, 2013.
- [48] A. D. Craig, "How do you feel—now? The anterior insula and human awareness," *Nature Reviews Neuroscience*, vol. 10, no. 1, pp. 59–70, 2009.
- [49] M. Burgmer, H. Kugel, B. Pfeleiderer et al., "The mirror neuron system under hypnosis - Brain substrates of voluntary and involuntary motor activation in hypnotic paralysis," *Cortex*, vol. 49, pp. 437–445, 2013.
- [50] D. Bzdok, G. Hartwigsen, A. Reid et al., "Left inferior parietal lobe engagement in social cognition and language," *Neuroscience and Biobehavioral Reviews*, vol. 68, pp. 319–334, 2016.
- [51] N. Kanwisher, J. McDermott, and M. M. Chun, "The fusiform face area: a module in human extrastriate cortex specialized for face perception," *Journal of Neuroscience*, vol. 17, no. 11, pp. 4302–4311, 1997.
- [52] T. I. Brown, M. R. Uncapher, T. E. Chow et al., "Cognitive control, attention, and the other race effect in memory," *PLoS One*, vol. 12, no. 3, Article ID e0173579, 2017.
- [53] A. V. Utevsky, D. V. Smith, J. S. Young et al., "Large-scale network coupling with the fusiform cortex facilitates future social motivation," *ENEURO*, vol. 4, pp. 1–12, 2017.
- [54] H. K. Moe, K. G. Moen, T. Skandsen et al., "The influence of traumatic axonal injury in thalamus and brainstem on level of consciousness at scene or admission: a clinical magnetic resonance imaging study," *Journal of Neurotrauma*, vol. 35, no. 7, pp. 975–984, 2017.

## Clinical Study

# Differential Diagnosis between Low-Grade and High-Grade Astrocytoma Using System A Amino Acid Transport PET Imaging with C-11-MeAIB: A Comparison Study with C-11-Methionine PET Imaging

Ryuichi Nishii <sup>1,2,3</sup>, Tatsuya Higashi <sup>1,3</sup>, Shinya Kagawa,<sup>3</sup> Maya Arimoto,<sup>4</sup> Yoshihiko Kishibe,<sup>3</sup> Masaaki Takahashi,<sup>3</sup> Shigeki Yamada,<sup>5</sup> Masaaki Saiki,<sup>6</sup> Yoshiki Arakawa,<sup>7</sup> Hiroshi Yamauchi,<sup>3</sup> Chio Okuyama,<sup>3</sup> Masato Hojo,<sup>8</sup> Toshihiro Munemitsu,<sup>8</sup> Masahiro Sawada,<sup>8</sup> Masato Kobayashi,<sup>9</sup> Keiichi Kawai,<sup>10</sup> Shigeki Nagamachi,<sup>2,11</sup> Toshinori Hirai,<sup>2</sup> and Susumu Miyamoto<sup>7</sup>

<sup>1</sup>Department of Molecular Imaging and Theranostics, National Institute of Radiological Sciences (NIRS), QST, 4-9-1 Anagawa, Inage-ku, Chiba 263-8555, Japan

<sup>2</sup>Department of Radiology, Faculty of Medicine, University of Miyazaki, 5200 Kihara Kiyotake-cho, Miyazaki 889-1692, Japan

<sup>3</sup>Division of PET Imaging, Shiga Medical Center Research Institute, 5-4-30 Moriyama, Moriyama, Shiga 524-8524, Japan

<sup>4</sup>Department of Diagnostic Imaging and Nuclear Medicine, Graduate School of Medicine, Kyoto University, 54 Shogoin Kawahara-cho, Sakyo-ku, Kyoto 606-8507, Japan

<sup>5</sup>Department of Neurosurgery, Rakuwakai Otowa Hospital, 2 Otowachinjicho, Yamashina-ku, Kyoto 607-8062, Japan

<sup>6</sup>Department of Radiology, Japanese Red Cross Otsu Hospital, 1-1-35 Nagara, Otsu, Shiga 520-8511, Japan

<sup>7</sup>Department of Neurosurgery, Graduate School of Medicine, Kyoto University, 54 ShogoinKawahara-cho, Sakyo-ku, Kyoto 606-8507, Japan

<sup>8</sup>Department of Neurosurgery, Shiga Medical Center, 5-4-30 Moriyama, Moriyama, Shiga 524-8524, Japan

<sup>9</sup>Wellness Promotion Science Center, Institute of Medical, Kanazawa University, 5-10-80 Kodatsuno, Kanazawa, Ishikawa 920-0942, Japan

<sup>10</sup>Graduate School of Health Sciences, College of Medical, Pharmaceutical and Health Sciences, Kanazawa University, 5-10-80 Kodatsuno, Kanazawa, Ishikawa 920-0942, Japan

<sup>11</sup>Department of Radiology, Faculty of Medicine, Fukuoka University, 7-45-1 Nanakuma, Jonan-ku, Fukuoka 814-0180, Japan

Correspondence should be addressed to Tatsuya Higashi; [higashi.tatsuya@qst.go.jp](mailto:higashi.tatsuya@qst.go.jp)

Received 29 December 2017; Accepted 6 May 2018; Published 20 June 2018

Academic Editor: Guoqiang Shao

Copyright © 2018 Ryuichi Nishii et al. This is an open access article distributed under the Creative Commons Attribution License, which permits unrestricted use, distribution, and reproduction in any medium, provided the original work is properly cited.

**Introductions.** [*N*-methyl-C-11] $\alpha$ -Methylaminoisobutyric acid (MeAIB) is an artificial amino acid radiotracer used for PET study, which is metabolically stable in vivo. In addition, MeAIB is transported by system A neutral amino acid transport, which is observed ubiquitously in all types of mammalian cells. It has already been shown that MeAIB-PET is useful for malignant lymphoma, head and neck cancers, and lung tumors. However, there have been no reports evaluating the usefulness of MeAIB-PET in the diagnosis of brain tumors. The purpose of this study is to investigate the efficacy of system A amino acid transport PET imaging, MeAIB-PET, in clinical brain tumor diagnosis compared to [*S*-methyl-C-11]-L-methionine (MET)-PET. **Methods.** Thirty-one consecutive patients (male: 16, female: 15), who were suspected of having brain tumors, received both MeAIB-PET and MET-PET within a 2-week interval. All patients were classified into two groups: Group A as a benign group, which included patients who were diagnosed as low-grade astrocytoma, grade II or less, or other low-grade astrocytoma ( $n = 12$ ) and Group B as a malignant group, which included patients who were diagnosed as anaplastic astrocytoma, glioblastoma multiforme (GBM), or recurrent GBM despite prior surgery or chemoradiotherapy ( $n = 19$ ). PET imaging was performed 20 min after the IV injection of MeAIB and MET, respectively. Semiquantitative analyses of MeAIB and MET uptake using SUVmax and tumor-to-contralateral

normal brain tissue ( $T/N$ ) ratio were evaluated to compare these PET images. ROC analyses for the diagnostic accuracy of MeAIB-PET and MET-PET were also calculated. *Results.* In MeAIB-PET imaging, the SUVmax was  $1.20 \pm 1.29$  for the benign group and  $2.94 \pm 1.22$  for the malignant group ( $p < 0.005$ ), and the  $T/N$  ratio was  $3.77 \pm 2.39$  for the benign group and  $16.83 \pm 2.39$  for the malignant group ( $p < 0.001$ ). In MET-PET, the SUVmax was  $3.01 \pm 0.94$  for the benign group and  $4.72 \pm 1.61$  for the malignant group ( $p < 0.005$ ), and the  $T/N$  ratio was  $2.64 \pm 1.40$  for the benign group and  $3.21 \pm 1.14$  for the malignant group (*n.s.*). For the analysis using the  $T/N$  ratio, there was a significant difference between the benign and malignant groups with MeAIB-PET with  $p < 0.001$ . The result of ROC analysis using the  $T/N$  ratio indicated a better diagnosis accuracy for MeAIB-PET for brain tumors than MET-PET ( $p < 0.01$ ). *Conclusions.* MeAIB, a system A amino acid transport-specific radiolabeled agents, could provide better assessments for detecting malignant type brain tumors. In a differential diagnosis between low-grade and high-grade astrocytoma, MeAIB-PET is a useful diagnostic imaging tool, especially in evaluations using the  $T/N$  ratio. *Clinical trial registration.* This trial was registered with UMIN000032498.

## 1. Introduction

Positron emission tomography (PET) imaging with amino acid analogs has been focused greatly on clinical applications, as it targets increased amino acid transport by tumors [1, 2]. Especially for detecting brain tumors, PET studies with amino acid analogs have been developed [3, 4] to overcome the drawbacks of F-18 FDG (FDG) PET, such as physiological uptake by the brain [5, 6].

As methionine, an essential sulfur amino acid, is necessary for the growth and development of cells, radiolabelled [*S*-methyl-C-11]-L-methionine (MET), mainly transported by system L amino acid transporters [7, 8], has been clinically used as a tumor-seeking agent for PET imaging for several decades [9]. MET-PET images can visualize not only the population and activity of amino acid transport but also metabolic events inside the body, such as active cell membrane transport, cellular protein synthesis, polyamine synthesis, and *trans*-methylation reactions [10, 11]. However, MET-PET is known to have several drawbacks when diagnosing tumors. MET is unstable *in vivo* due to the aminotransfer reaction [10] and is excreted into the bile and intestines. In addition, MET-PET shows faint physiological uptake in the brain, strong physiological uptake in the liver and bone marrow, and uptake in certain types of inflammatory changes [12, 13].

[*N*-methyl-C-11] $\alpha$ -Methylaminoisobutyric acid (MeAIB) is an artificial amino acid radiotracer used for PET study, which is metabolically stable *in vivo* [14]. Although MET is transported mainly by system L neutral amino acid transport, MeAIB is transported by system A neutral amino acid transport, which is observed ubiquitously in all types of mammalian cells [11, 15]. It has already been shown that MeAIB is useful for amino acid uptake measurements in skeletal muscle and for the diagnosis of malignant lymphoma and head and neck cancers [14, 16, 17]. We have also been investigating system A amino acid PET molecular imaging with MeAIB to detect tumors and have reported its usefulness in the differential diagnosis of pulmonary and mediastinal mass lesions [18] and prostate cancer [19] in clinical practice.

However, there have been no reports evaluating the usefulness of MeAIB-PET in the diagnosis of brain tumors.

The purpose of this study is to investigate the efficacy of system A amino acid transport PET imaging, MeAIB-PET, in clinical brain tumor diagnosis compared to MET-PET.

## 2. Materials and Methods

*2.1. Patient Characteristics.* From March 2009 to December 2011, 31 consecutive patients (male: 16, female: 15), who were suspected of having brain tumors, received both MeAIB-PET and MET-PET within a 2-week interval. Patients' ages ranged from 5 to 71 years with a mean age of  $44.2 \pm 18.5$ , as shown in Table 1. Inclusion criteria for the study were as follows: (1) patients were suspected of having an intraaxial brain tumor (newly detected or recurrent lesions 6 months or more after successful treatment) by CT and MRI (both were performed as routine clinical studies), (2) each patient gave written informed consent and received MeAIB-PET and MET-PET, and (3) results were confirmed pathologically, or by clinical follow-up more than 6 months after the PET studies. Exclusion criteria were as follows: (1) patients with extra-axial tumors such as tumors of the meninges, pituitary tumors, pineal parenchymal tumors, or cranial nerve schwannomas, (2) patients with metastatic brain tumors or lymphoma, and (3) patients who refused to receive MeAIB-PET or MET-PET. Of the 52 patients who received MeAIB-PET with suspected brain tumors from March 2009 to December 2011, 31 patients were included in the present study, while the others were excluded because of the exclusion criteria. According to final diagnosis after surgery or biopsy, all patients who met the criteria were classified into the following two groups: Group A (benign), which included patients who were diagnosed as low-grade astrocytoma, grade II including a case of recurrent grade II glioma or less, or other low-grade astrocytomas ( $n = 12$ ; ranging from 5 to 46 years, mean age  $32.2 \pm 10.0$  years; seven males and five females); Group B (malignant), which included patients who were diagnosed as anaplastic astrocytoma, glioblastoma multiforme (GBM), or recurrent GBM despite prior surgery or chemoradiotherapy ( $n = 19$ ; ranging from 14 to 71 years, mean age  $56.7 \pm 16.8$  years; nine males and ten females).

This prospective clinical study was approved by our institutional review boards, the Human Study Committee (approval number: #36-04, March 25, 2009) and by the Committee for the Clinical Use of Short-Half Life Radioactive Materials (approval number: #2008-01, November 28, 2008). All enrolled patients or their parents if the patient was under 20 years old received explanations, and then they provided written informed consent regarding this study.

TABLE 1: Patient characteristics.

Total ( $n = 31$ )	
Age (years)	
Mean $\pm$ SD	44.2 $\pm$ 18.5
Median	44
Range	5–71
Male : female	16 : 15
Group A (benign) ( $n = 12$ )	
Age (years)	
Mean $\pm$ SD	32.2 $\pm$ 10.0
Median	33.5
Range	5–46
Male : female	7 : 5
Diagnosis	
Astrocytoma grade II or less/low-grade glioma	11
Brain stem glioma	1
Group B (malignant) ( $n = 19$ )	
Age (years)	
Mean $\pm$ SD	56.7 $\pm$ 16.8
Median	60
Range	14–71
Male : female	9 : 10
Diagnosis	
Glioblastoma multiforme	7
Glioblastoma multiforme, recurrence	10
Anaplastic astrocytoma, grade 3	2

2.2. *Radiotracers.* Production of MeAIB followed a previously described procedure [18]. The radiosynthesis method was based on that proposed by Nagren et al. [20]. Chemicals and solvents were of analytical grade and purchased commercially. [ $^{11}\text{C}$ ]MeOTf was bubbled into the reactor of an automated remotely controlled synthesizer module C-11-BII (SHI, Tokyo, Japan) filled with 1 mg of methyl  $\alpha$ -aminoisobutyrate hydrochloride (6.5 mmol) dissolved in 0.4 ml of methanol/acetone (1/1, v/v) and 3.2  $\mu\text{l}$  of 2,2,6,6,*N*-pentamethyl-piperidine (PMP) at  $-20^\circ\text{C}$ . Then, the reactor was heated to  $80^\circ\text{C}$  for 1 min. After cooling to  $25^\circ\text{C}$ , 400  $\mu\text{l}$  of 2 M NaOH was then loaded into the reactor. After heating the mixture for 3 min at  $60^\circ\text{C}$ , the hydrolyzed product was diluted with 0.5 ml of HPLC eluent and subsequently transferred to a preparative radio HPLC system consisting of a preparative HPLC pump (PU-980, JASCO), an automated flow-detector-controlled injection system with a 2 ml injection loop, a semipreparative HPLC column (hydrophilic interaction chromatography: HILIC column, Nacalai Tesque,  $250 \times 10 \text{ mm}^2$ ,  $5 \mu\text{m}$ ; mobile phase: MeCN/10 mM  $\text{CH}_3\text{COONH}_4$ , 4/1, v/v; flow: 8 ml/min), a UV detector (254 nm), and an NaI(Tl) radioactivity detector. The product-containing fraction was then diluted with 10 ml of isotonic saline. The radiochemical purity of the MeAIB was more than 99%.

MET was synthesized based on the method described in a previous report [21], by the reaction of C-11 methyltriflate with an aqueous solution of L-homocysteine thiolactone in a Sep-Pak tC18 cartridge, followed by purification with ion-exchange cartridges. The radiochemical purity of MET was also more than 99%.

2.3. *PET Study.* All patients were examined with a whole-body PET scanner, GE Advance (GE Healthcare, Waukesha, WI, USA), or with a whole-body PET/CT scanner, Siemens

TABLE 2: SUVmax and  $T/N$  ratios of MeAIB- and MET-PET study in patients with brain tumors.

Diagnosis		MeAIB		MET	
		SUVmax	$T/N$ ratio	SUVmax	$T/N$ ratio
<i>Group A (benign group)</i>					
1	Low-grade glioma	0.58	3.22	1.98	1.78
2	Astrocytoma grade II	2.83	8.09	2.83	1.35
3	Low-grade glioma	0.24	1.64	1.80	1.04
4	Glioma grade II	0.15	1.25	3.03	2.37
5	Low-grade glioma	0.62	1.11	3.13	1.82
6	Low-grade glioma	0.85	2.07	3.89	2.54
7	Brain stem glioma	3.40	4.86	3.03	1.89
8	Glioma grade II, rec.	3.49	6.13	1.96	2.68
9	Low-grade glioma	0.32	4.00	4.82	4.38
10	Low-grade glioma	0.4	6.67	2.19	3.22
11	Low-grade glioma	1.34	4.96	4.08	6.07
12	Low-grade glioma	0.12	1.20	3.41	2.54
Ave.		1.20	3.77	3.01	2.64
<i>Group B (malignant group)</i>					
13	GBM	4.81	32.07	5.82	4.44
14	GBM, rec.	2.95	14.89	3.49	3.45
15	GBM, rec.	2.94	26.72	3.63	3.67
16	GBM, rec.	2.33	8.96	5.39	2.51
17	GBM, rec.	2.84	12.91	5.54	2.55
18	GBM, rec.	2.83	15.00	4.27	3.30
19	GBM	1.60	4.00	3.10	1.24
20	GBM	2.89	22.23	6.47	3.87
21	GBM, rec.	4.51	25.10	6.14	3.23
22	GBM, rec.	2.89	17.00	3.40	2.91
23	GBM	2.81	17.56	6.07	6.07
24	GBM	5.85	15.81	4.57	3.41
25	GBM, rec.	1.22	17.43	1.46	1.76
26	GBM, rec.	4.58	21.73	5.90	2.71
27	GBM, rec.	2.83	15.00	4.27	3.30
28	GBM	2.89	22.23	7.82	4.68
29	Anaplastic astrocytoma	1.95	10.26	5.94	4.01
30	Anaplastic astrocytoma	1.73	7.86	2.18	1.79
31	GBM	1.43	13.00	4.27	2.12
Ave.		2.94	16.83	4.72	3.21

True Point Biograph 16 (Siemens/CTI, Erlangen, Germany). All subjects received an intravenous injection of MeAIB ( $513.6 \pm 65.6 \text{ MBq}$ ) or MET ( $533.9 \pm 35.0 \text{ MBq}$ ). Brain PET/CT images were acquired 20 min after the radiotracer injection in 1 bed position in both study. Emission images were acquired for 5 min per bed position. The data were reconstructed using the ordered subsets expectation-maximization method using eight subsets, two iterations, and an array size of  $256 \times 256$ . For the attenuation correction of PET/CT fusion images, the CT component was performed according to a standard protocol with the following parameters: 140 kV; 50 mAs; tube rotation time, 0.5 s per rotation; slice thickness, 5 mm; and gap, 2 mm. An E-software workstation (Siemens, Nashville, TN, USA) was used to construct PET/CT fusion images.

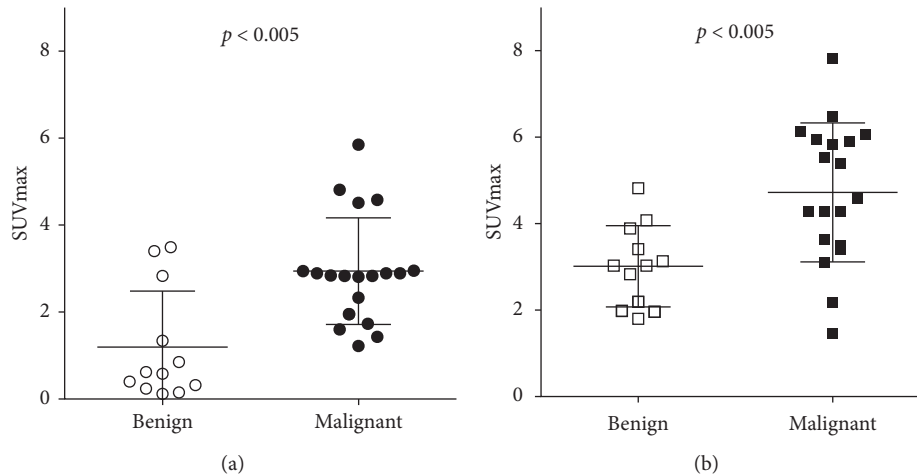


FIGURE 1: Comparison between benign and malignant groups by SUVmax of the lesions in MeAIB-PET (a) and MET-PET (b).

**2.4. Image Analysis.** PET images were interpreted and analyzed by two experienced nuclear medicine physicians with all the available clinical information, and then a final diagnosis was made in agreement. All PET images were fused with the MRI of each subject using the PMOD software, version 3.1 (PMOD; Zürich, Switzerland). We manually placed an irregular region of interest (ROI) on the coregistered MRI image of each patient, and then these ROIs were transferred to the PET image for the interpretation and calculation of the uptake of each radiotracer. The maximum standardized uptake value (SUVmax) was calculated for semiquantitative analysis of MeAIB and MET uptake by the lesion. The tumor-to-contralateral normal brain tissue ( $T/N$ ) ratio was determined by dividing the tumor SUVmax by the SUVmean of the contralateral hemisphere.

**2.5. Statistics.** All values are expressed as mean  $\pm$  SD. All the statistical analyses were performed using statistical software, JMP version 12 (SAS Institute, Cary, NC, USA), in which  $p$  values  $< 0.05$  were considered to be statistically significant. A comparison between each group was analyzed with the Wilcoxon score for the unpaired data.

### 3. Results

**3.1. Characteristics of Patients and Lesions.** Final diagnosis was confirmed pathologically by surgical resection, stereotactic biopsy, or by follow-ups of at least more than 6 months. In the benign group of 12 patients, there were 11 astrocytoma grade II or less and one brain stem glioma. In the malignant group of 19 patients, there were 7 with newly diagnosed GBM, 10 with recurrent GBM, and 2 with anaplastic astrocytoma (Table 1).

**3.2. Visual and Semiquantitative Analysis of MeAIB and MET Uptake.** Table 2 summarizes the SUVmax and  $T/N$  ratio of MeAIB- and MET-PET in all patients. In MeAIB-PET imaging, the average SUVmax was  $1.20 \pm 1.29$  for the benign group and  $2.94 \pm 1.22$  for the malignant group ( $p < 0.005$ ),

and the average  $T/N$  ratio was  $3.77 \pm 2.39$  for the benign group and  $16.83 \pm 2.39$  for the malignant group ( $p < 0.001$ ). In MET-PET, the average SUVmax was  $3.01 \pm 0.94$  for the benign group and  $4.72 \pm 1.61$  for the malignant group ( $p < 0.005$ ), and the average  $T/N$  ratio was  $2.64 \pm 1.40$  for the benign group and  $3.21 \pm 1.14$  for the malignant group (*n.s.*).

The average SUVmax of tumors with MeAIB-PET was significantly lower than that with MET-PET. However, MeAIB uptake in the tumors by the malignant group and the benign group showed significant statistical differences with  $p < 0.005$  (Figure 1(a)). The average SUVmax of MET in the tumors of the malignant group was significantly higher than that of the benign group  $p < 0.005$ ; however, there was a wide overlap in MET uptake between the benign and malignant groups, resulting in many false positive cases with MET-PET (Figure 1(b)).

For the analysis using the  $T/N$  ratio, there was a significant difference between the benign and malignant groups with MeAIB-PET with  $p < 0.001$ , while no significant difference was observed with MET-PET (Figure 2).

Figures 3 and 4 show typical cases in the benign group, which were diagnosed as astrocytoma grade II and low-grade glioma after surgery or stereotactic biopsy. High uptake of MET was in the tumor, while no significant uptake of MeAIB was noted in both cases. In addition, other typical cases in the malignant group are shown in Figures 5 and 8, which were diagnosed as GBM and recurrent GBM; a clear margined tumor was depicted as a high uptake of MeAIB lesion. MET-PET also demonstrated the lesion with the physiological uptake. Higher  $T/N$  ratio was noted in MeAIB-PET image, respectively.

**3.3. Diagnostic Accuracies of MeAIB- and MET-PET.** As for the differential diagnosis of brain tumors between the benign and malignant groups, receiver operating characteristic curve (ROC) analyses for the diagnostic accuracy of MeAIB-PET and MET-PET using a semiquantitative analysis were assessed (Figure 6). For ROC analysis using SUVmax, the area under curve (AUC) value for MeAIB-PET was 0.83 with

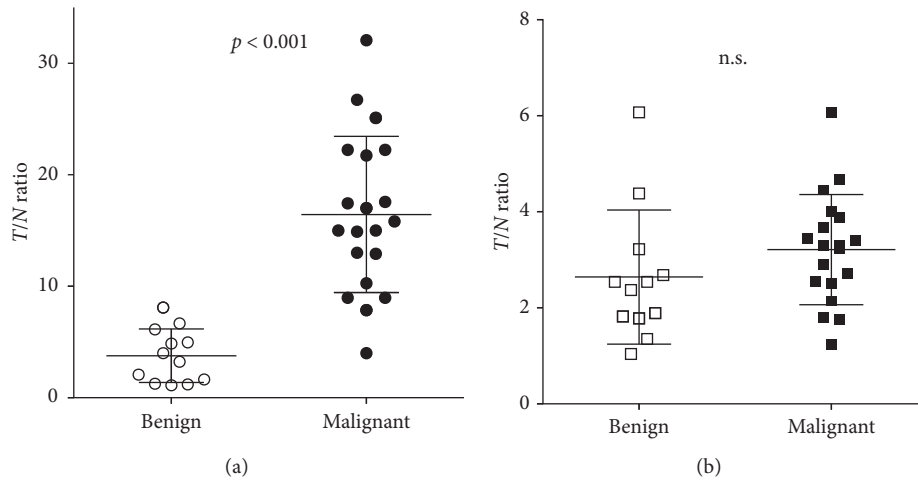


FIGURE 2: Comparison between benign and malignant groups by  $T/N$  ratio in MeAIB-PET (a) and MET-PET (b).

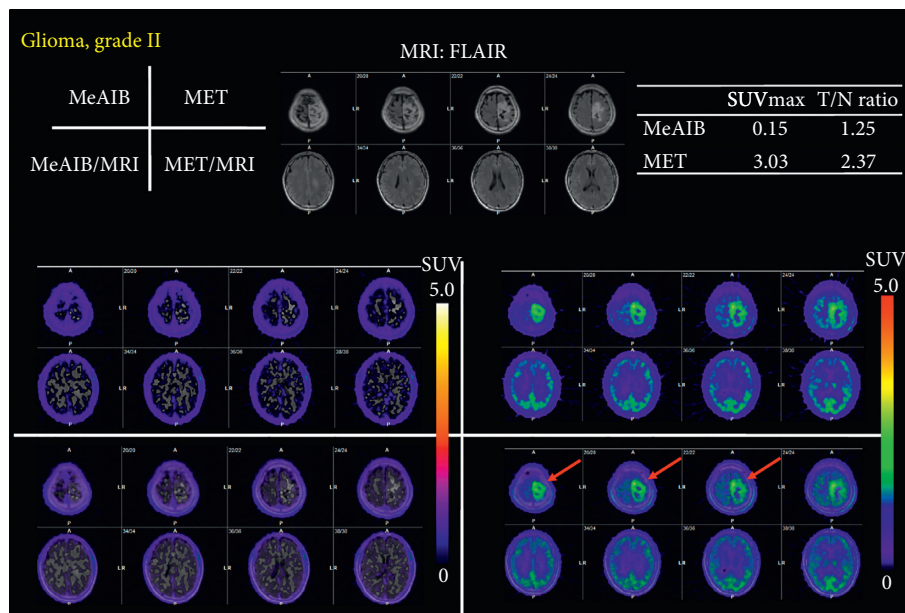


FIGURE 3: A case of a forty-year-old male who had a diffusely irregular-shaped mass in the left frontal lobe, which was diagnosed as astrocytoma, grade II after surgery (benign group) (case #4). High uptake of MET was in the tumor, while no significant uptake of MeAIB was noted.

standard error 0.090, 95% CI 0.65–1.00, and  $p < 0.005$ . The AUC for MET-PET was 0.82 with standard error 0.076, 95% CI 0.67–0.97, and  $p < 0.005$ . There was no significant difference in diagnosis accuracy between them (Figure 6(a)). For ROC analysis using the  $T/N$  ratio, the AUC value for MeAIB-PET was 0.97 with standard error 0.027, 95% CI 0.92–1.02, and  $p < 0.0001$ . The AUC for MET-PET was 0.69 with standard error 0.10, 95% CI 0.48–0.89, and  $p < 0.1$ . These analyses indicated a better diagnosis accuracy for MeAIB-PET for brain tumors than MET-PET ( $p < 0.01$ ) (Figure 6(b)).

When the cutoff value was set as  $SUV_{max} = 2.0$  for MeAIB-PET, the sensitivity, specificity, and accuracy were 73.7%, 91.7%, and 80.6%, respectively, while if the cutoff value was set as  $SUV_{max} = 3.5$  for MET-PET, the sensitivity,

specificity, and accuracy were 73.7%, 75.0%, and 74.2%, respectively. When the cutoff value was set as  $T/N$  ratio = 7.0 for MeAIB-PET, the sensitivity, specificity, and accuracy were 94.7%, 91.7%, and 93.5%, respectively, while if the cutoff value was set as  $T/N$  ratio = 3.0 for MET-PET, the sensitivity, specificity, and accuracy were 57.9%, 75.0%, and 64.5%, respectively.

**3.4. Relationship of  $SUV_{max}$  in the Lesion with MeAIB and MET.** Relationships between  $SUV_{max}$  of MeAIB and that of MET of each lesion in both PET studies using logistic regression are shown in Figure 7. In the benign group, the  $SUV_{max}$  of MeAIB showed a nonsignificant linear relationship with that of MET (Figure 7(a)). On the contrary,

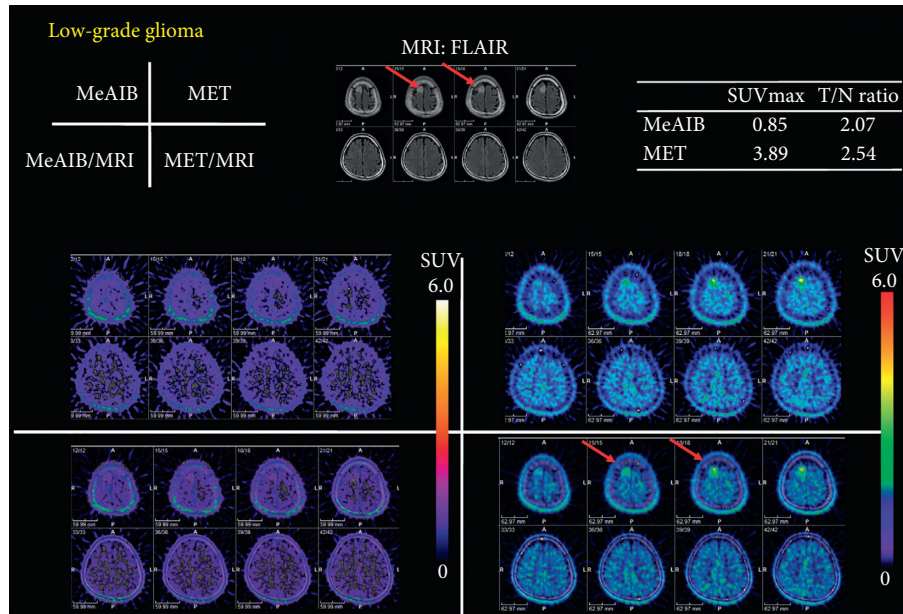


FIGURE 4: A case of a thirty-three-year-old male having newly diagnosed low-grade glioma in the right frontal lobe by stereotactic biopsy (benign group) (case #6). High uptake of MET was in the tumor, while no significant uptake of MeAIB was noted.

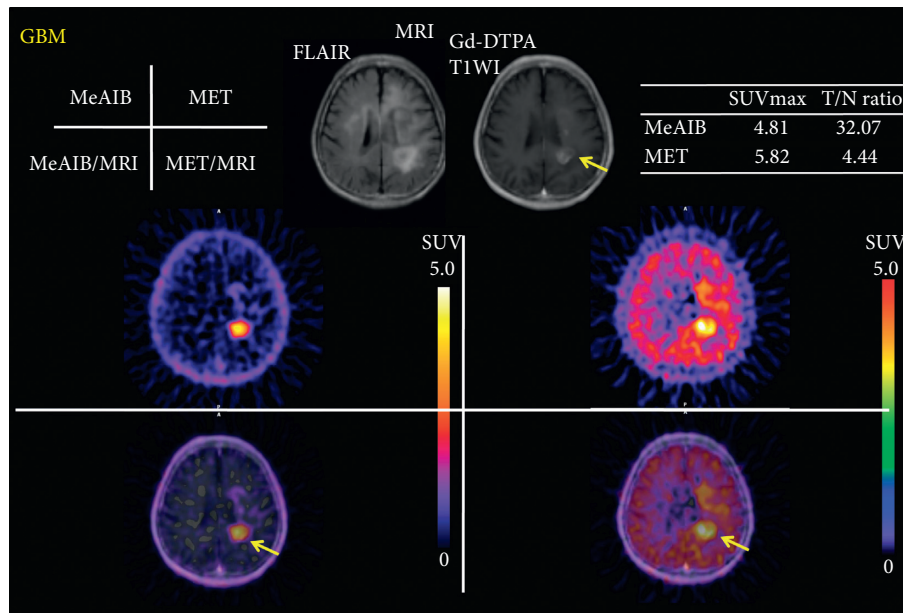


FIGURE 5: A case of a seventy-one-year-old male who had newly diagnosed GBM in the left corpus callosum by stereotactic biopsy (malignant group) (case #13). A clear margined tumor was depicted as a high uptake of MeAIB lesion. MET-PET also demonstrated the lesion with the physiological uptake. Higher  $T/N$  ratio was noted in MeAIB-PET image.

in the malignant group, the SUVmax of MeAIB showed a weak positive correlation with that of MET ( $p = 0.06$ ,  $R^2 = 0.20$ ) (Figure 7(b)).

#### 4. Discussion

System A amino acid transport is  $\text{Na}^+$ - and energy-dependent, highly concentrative, and a putative regulator of cell growth. Malignant transformation is associated with enhanced system A activity [22]. System A is specifically

capable of transporting  $N$ -methylated amino acids [23]. The amino acid analog MeAIB was developed as an ideal tracer for in vivo transport measurements, as the compound is non-metabolizable and concentrated in cells only via system A transport [15, 20]. There are several reports regarding clinical MeAIB-PET in patients with lymphoma [14], head and neck cancer [16], in addition to our previous study on pulmonary and mediastinal mass lesions [18], and prostate cancer [19]. However, there have been no reports evaluating the usefulness of MeAIB-PET for the diagnosis of brain tumors.

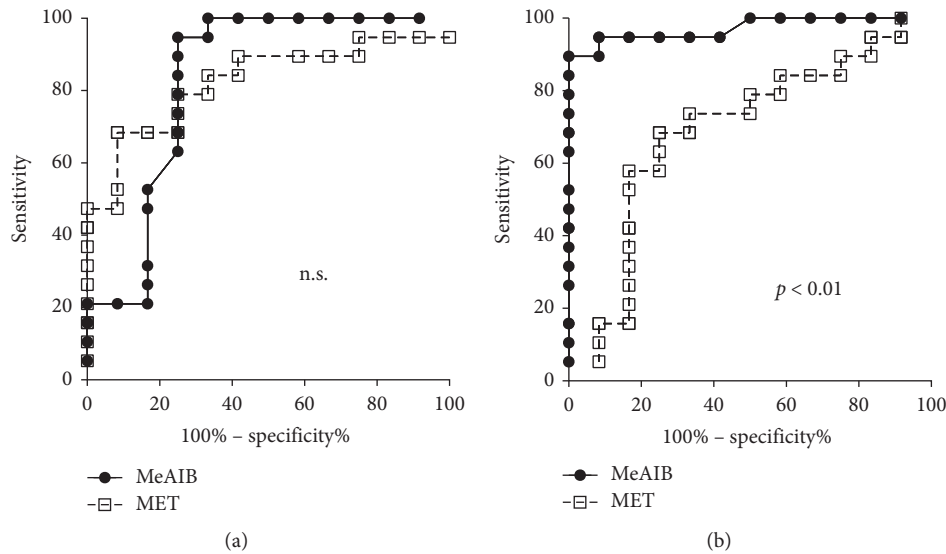


FIGURE 6: Receiver-operating characteristic curve (ROC) analyses for the diagnostic accuracy of MeAIB-PET and MET-PET using semiquantitative analysis. (a) For ROC analysis using SUVmax, the area under the curve (AUC) value for MeAIB PET was 0.83 with standard error 0.090, 95% CI 0.65–1.00, and  $p < 0.005$ . The AUC for MET-PET was 0.82 with standard error 0.076, 95% CI 0.67–0.97, and  $p < 0.005$ . There was no significance of diagnosis accuracy between them. (b) For ROC analysis using  $T/N$  ratio, the AUC value for MeAIB PET was 0.97 with standard error 0.027, 95% CI 0.92–1.02, and  $p < 0.0001$ . The AUC for MET-PET was 0.69 with standard error 0.10, 95% CI 0.48–0.89, and  $p < 0.1$ . These analyses indicated better diagnosis accuracy of MeAIB-PET for brain tumors than MET-PET ( $p < 0.01$ ).

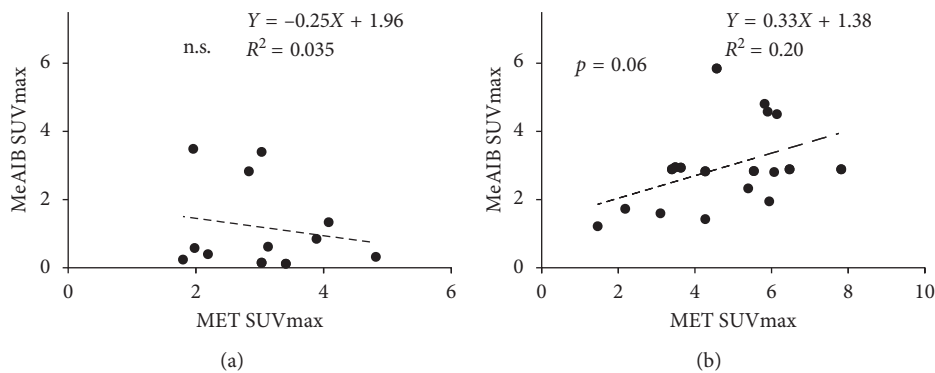


FIGURE 7: Relationship between SUVmax of MeAIB and that of MET of each lesion in both PET study using logistic regression. In the benign group, SUVmax of MeAIB showed nonsignificant linear relationship with that of MET (a). On the contrary, in the malignant group, SUVmax of MeAIB showed a weak positive correlation with that of MET ( $p = 0.06$ ,  $R^2 = 0.20$ ) (b).

Our principal finding is that the diagnostic accuracy of MeAIB using  $T/N$  ratio was better than those of MET-PET when differentiating benign and malignant brain lesions. The  $T/N$  ratio with MeAIB-PET was higher than that with MET because of the faint uptake of MeAIB by normal brains (Figures 3–5 and 8). The reason for this is that MeAIB has difficulty permeating the blood-brain barrier (BBB) [24]. Using the  $T/N$  ratio, MeAIB-PET displayed higher diagnostic accuracy in distinguishing between the benign and malignant groups (Figure 6), which resulted in showing relatively low false negative findings than MET-PET. Therefore, MeAIB-PET may be useful for the diagnosis of malignant brain tumors with broken BBB and high expressions of system A transport. This high  $T/N$  ratio may result in the clear contrast between surrounding brain tissues and the marginal edge of malignant brain tumor. Moreover,

MeAIB-PET may contribute to more accurate depictions of the tumor margin when stereotactic surgery/biopsy or stereotactic radiotherapy is considered for the treatment of malignant brain tumors. The uptake of MeAIB in brain tumors was lower than that of MET. This may represent a difference in expression between system A and L amino acid transport in tumors. Considering the results of the relationships between SUVmax of MeAIB and that of MET for each tumor in the malignant group, SUVmax of MeAIB showed a weak linear relationship, and not significant, with that of MET.

MET is mainly transported by system L amino acid transporters. MET-PET has been widely used for brain tumor imaging [25–28]. However, for tumor grading using MET-PET, Hatakeyama et al. reported that the differences of MET SUVmax and  $T/N$  ratios between grades II and III

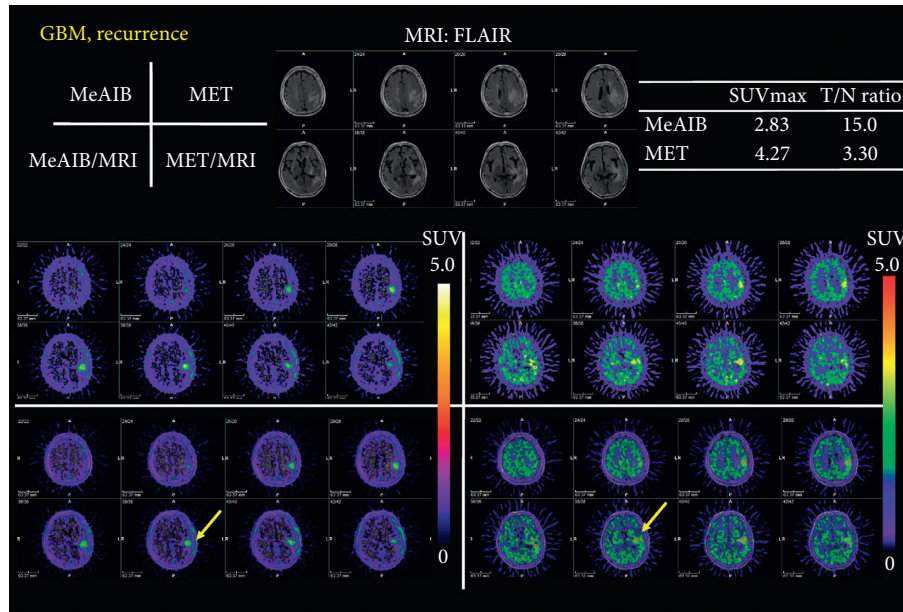


FIGURE 8: A case of a sixty-eight-year-old female who had received chemoradiotherapy before for GBM in the left temporal lobe (malignant group) (case #18). A clear margined tumor was depicted as a high uptake of MeAIB lesion. MET-PET also demonstrated the lesion; however, the margin of the lesion was unclear due to the physiological uptake of MET in the brain. Recurrent GBM was confirmed after stereotactic biopsy.

gliomas were not statistically significant and that low-grade gliomas with oligodendroglial components had relatively high MET uptake [25]. Sasaki et al. noted that MET was highly useful both for detecting astrocytoma and for differentiating between benign and malignant astrocytomas. However, it was not sufficiently useful to evaluate the histological grade of the astrocytomas [27]. In the present study, although MET-PET showed the possibility of distinguishing between low-grade and high-grade astrocytoma using SUVmax, the  $T/N$  ratio was not useful for tumor grading (Figure 2), as suggested in previous reports. Physiological uptake of MET by the brain via system L amino acid transporters is considered to be one of the reasons for this result because MET is known to be utilized for the physiological metabolism of normal brain tissues as a substrate for protein synthesis, neurotransmitters, and energy production [2, 10, 11, 29]. In this study, indeed, MET-PET had a tendency to show false positive findings more than MeAIB-PET. The physiological uptake of MET by the normal brain tissue is considered as one of the reasons. In considering other amino acid PET imaging, Inoue et al. investigated an amino acid PET imaging using L-3-[F-18]-fluoro-alpha-methyl tyrosine (FAMT) and reported the mean value of SUV of the brain tumor as  $2.83 \pm 1.57$  in FAMT-PET [30]. This is similar to the result of MET-PET because FAMT is transported into cancer cells via system L amino acid transporter [31].

In terms of the study limitations, there were a relatively small number in the study population that participated in this study. Most of them are astrocytoma grade II or less and GBM. And there were ten recurrent GBM in addition to newly diagnosed GBM included in this study. Recurrent tumors analyzed in this study were lesions 6 months or more

after successful treatment, so there might be little effect of the treatment for analysis of this PET imaging study. However, detailed examination with large number of subjects was considered to be needed in terms of influences after surgery or chemotherapy on PET image. Moreover, further study is also needed, including that of brain tumors other than astrocytic tumors such as metastatic brain tumors or CNS lymphoma.

## 5. Conclusions

We investigated system A amino acid transport PET imaging, MeAIB-PET, in patients with astrocytoma and GBM and compared the diagnostic results to those obtained by MET-PET. MeAIB-PET could provide better assessments for detecting malignant-type brain tumors. In a differential diagnosis between low-grade and high-grade astrocytoma, MeAIB-PET is a useful diagnostic imaging tool, especially in evaluations using the  $T/N$  ratio.

## Additional Points

**Highlights.** The uptake of MeAIB in brain tumors was lower but showed higher image contrast than those of MET. Using the  $T/N$  ratio, MeAIB-PET showed higher diagnostic accuracy compared to MET-PET. MeAIB-PET contributes to more accurate depictions of the tumor margin. MeAIB-PET provides better assessments for detecting malignant brain tumors.

## Conflicts of Interest

The authors declare that there are no conflicts of interest regarding the publication of this study.

## References

- [1] G. Antoni and B. Langstrom, "Radiopharmaceuticals: molecular imaging using positron emission tomography," *Handbook of Experimental Pharmacology*, vol. 185, no. 1, pp. 177–201, 2008.
- [2] P. L. Jager, W. Vaalburg, J. Pruijm et al., "Radiolabeled amino acids: basic aspects and clinical applications in oncology," *Journal of Nuclear Medicine*, vol. 42, no. 3, pp. 432–445, 2001.
- [3] B. Gulyas and C. Halldin, "New PET radiopharmaceuticals beyond FDG for brain tumor imaging," *Quarterly Journal of Nuclear Medicine and Molecular Imaging*, vol. 56, no. 2, pp. 173–190, 2012.
- [4] W. Wadsak and M. Mitterhauser, "Basics and principles of radiopharmaceuticals for PET/CT," *European Journal of Radiology*, vol. 73, no. 3, pp. 461–469, 2010.
- [5] U. Metser and E. Even-Sapir, "Increased (18)F-fluorodeoxyglucose uptake in benign, nonphysiologic lesions found on whole-body positron emission tomography/computed tomography (PET/CT): accumulated data from four years of experience with PET/CT," *Seminars in Nuclear Medicine*, vol. 37, no. 3, pp. 206–222, 2007.
- [6] P. D. Shreve, Y. Anzai, and R. L. Wahl, "Pitfalls in oncologic diagnosis with FDG PET imaging: physiologic and benign variants," *Radiographics*, vol. 19, no. 1, pp. 61–77, quiz 150–151, 1999.
- [7] Y. Kuang, F. Wang, D. J. Corn, H. Tian, and Z. Lee, "In vitro characterization of uptake mechanism of L-[methyl-(3)H]-methionine in hepatocellular carcinoma," *Molecular Imaging and Biology*, vol. 16, no. 4, pp. 459–468, 2014.
- [8] M. Yoshimoto, H. Kurihara, N. Honda et al., "Predominant contribution of L-type amino acid transporter to 4-borono-2-(18)F-fluoro-phenylalanine uptake in human glioblastoma cells," *Nuclear Medicine and Biology*, vol. 40, no. 5, pp. 625–629, 2013.
- [9] S. Leskinen-Kallio, U. Ruotsalainen, K. Nagren, M. Teras, and H. Joensuu, "Uptake of carbon-11-methionine and fluorodeoxyglucose in non-Hodgkin's lymphoma: a PET study," *Journal of Nuclear Medicine*, vol. 32, no. 6, pp. 1211–1218, 1991.
- [10] Y. Fujibayashi, K. Kawai, Y. Yonekura et al., "Problems of [S-methyl-11C]-L-methionine as a protein synthesis marker in the pancreas," *Annals of Nuclear Medicine*, vol. 4, no. 1, pp. 29–33, 1990.
- [11] H. N. Christensen, "Role of amino acid transport and countertransport in nutrition and metabolism," *Physiological Reviews*, vol. 70, no. 1, pp. 43–77, 1990.
- [12] A. van Waarde, P. L. Jager, K. Ishiwata, R. A. Dierckx, and P. H. Elsinga, "Comparison of sigma-ligands and metabolic PET tracers for differentiating tumor from inflammation," *Journal of Nuclear Medicine*, vol. 47, no. 1, pp. 150–154, 2006.
- [13] Y. Yamada, Y. Uchida, K. Tatsumi et al., "Fluorine-18-fluorodeoxyglucose and carbon-11-methionine evaluation of lymphadenopathy in sarcoidosis," *Journal of Nuclear Medicine*, vol. 39, no. 7, pp. 1160–1166, 1998.
- [14] E. Sutinen, S. Jyrkkio, T. Gronroos et al., "Biodistribution of [11C] methylaminoisobutyric acid, a tracer for PET studies on system A amino acid transport in vivo," *European Journal of Nuclear Medicine*, vol. 28, no. 7, pp. 847–854, 2001.
- [15] S. Kagawa, R. Nishii, T. Higashi et al., "Relationship between [14C]MeAIB uptake and amino acid transporter family gene expression levels or proliferative activity in a pilot study in human carcinoma cells: Comparison with [3H]methionine uptake," *Nuclear Medicine and Biology*, vol. 49, pp. 8–15, 2017.
- [16] E. Sutinen, S. Jyrkkio, K. Alanen, K. Nägren, and H. Minn, "Uptake of [N-methyl-11C]alpha-methylaminoisobutyric acid in untreated head and neck cancer studied by PET," *European Journal of Nuclear Medicine and Molecular Imaging*, vol. 30, no. 1, pp. 72–77, 2003.
- [17] M. R. Asola, K. A. Virtanen, P. Peltoniemi et al., "Amino acid uptake in the skeletal muscle measured using [11C]methylaminoisobutyrate (MEAIB) and PET," *European Journal of Nuclear Medicine and Molecular Imaging*, vol. 29, no. 11, pp. 1485–1491, 2002.
- [18] R. Nishii, T. Higashi, S. Kagawa et al., "Diagnostic usefulness of an amino acid tracer, alpha-[N-methyl-(11)C]-methylaminoisobutyric acid ((11)C-MeAIB), in the PET diagnosis of chest malignancies," *Annals of Nuclear Medicine*, vol. 27, no. 9, pp. 808–821, 2013.
- [19] M. K. Arimoto, T. Higashi, R. Nishii et al., "(11)C-methylaminoisobutyric acid (MeAIB) PET for evaluation of prostate cancer: compared with (18)F-fluorodeoxyglucose PET," *Annals of Nuclear Medicine*, vol. 30, no. 8, pp. 553–562, 2016.
- [20] K. Nägren, E. Sutinen, and S. Jyrkkio, "[N-methyl-11C] MeAIB, a tracer for system A amino acid transport: preparation from [11C]methyl triflate and HPLC metabolite analysis of plasma samples after intravenous administration in man," *Journal of Labelled Compounds and Radiopharmaceuticals*, vol. 43, no. 10, pp. 1013–1021, 2000.
- [21] M. Morooka, K. Kubota, H. Kadowaki et al., "11C-methionine PET of acute myocardial infarction," *Journal of Nuclear Medicine*, vol. 50, no. 8, pp. 1283–1287, 2009.
- [22] J. McConathy and M. M. Goodman, "Non-natural amino acids for tumor imaging using positron emission tomography and single photon emission computed tomography," *Cancer and Metastasis Reviews*, vol. 27, no. 4, pp. 555–573, 2008.
- [23] H. N. Christensen, D. L. Oxender, M. Liang, and K. A. Vatz, "The use of N-methylation to direct route of mediated transport of amino acids," *Journal of Biological Chemistry*, vol. 240, no. 9, pp. 3609–3616, 1965.
- [24] R. G. Blasberg, J. D. Fenstermacher, and C. S. Patlak, "Transport of alpha-aminoisobutyric acid across brain capillary and cellular membranes," *Journal of Cerebral Blood Flow and Metabolism*, vol. 3, no. 1, pp. 8–32, 1983.
- [25] T. Hatakeyama, N. Kawai, Y. Nishiyama et al., "11C-methionine (MET) and 18F-fluorothymidine (FLT) PET in patients with newly diagnosed glioma," *European Journal of Nuclear Medicine and Molecular Imaging*, vol. 35, no. 11, pp. 2009–2017, 2008.
- [26] A. H. Jacobs, A. Thomas, L. W. Kracht et al., "18F-fluoro-L-thymidine and 11C-methylmethionine as markers of increased transport and proliferation in brain tumors," *Journal of Nuclear Medicine*, vol. 46, no. 12, pp. 1948–1958, 2005.
- [27] M. Sasaki, Y. Kuwabara, T. Yoshida et al., "A comparative study of thallium-201 SPET, carbon-11 methionine PET and fluorine-18 fluorodeoxyglucose PET for the differentiation of astrocytic tumours," *European Journal of Nuclear Medicine*, vol. 25, no. 9, pp. 1261–1269, 1998.
- [28] J. Hatazawa, K. Ishiwata, M. Itoh et al., "Quantitative evaluation of L-[methyl-C-11] methionine uptake in tumor using positron emission tomography," *Journal of Nuclear Medicine*, vol. 30, no. 11, pp. 1809–1813, 1989.
- [29] T. K. Narayanan, S. Said, J. Mukherjee et al., "A comparative study on the uptake and incorporation of radiolabeled methionine, choline and fluorodeoxyglucose in human astrocytoma," *Molecular Imaging and Biology*, vol. 4, no. 2, pp. 147–156, 2002.
- [30] T. Inoue, T. Shibasaki, N. Oriuchi et al., "18F alpha-methyl tyrosine PET studies in patients with brain tumors," *Journal of Nuclear Medicine*, vol. 40, no. 3, pp. 399–405, 1999.
- [31] G. Miyashita, T. Higuchi, N. Oriuchi et al., "(1)(8)F-FAMT uptake correlates with tumor proliferative activity in oral squamous cell carcinoma: comparative study with (1)(8)F-FDG PET and immunohistochemistry," *Annals of Nuclear Medicine*, vol. 24, no. 8, pp. 579–584, 2010.

## Review Article

# The Place of PET to Assess New Therapeutic Effectiveness in Neurodegenerative Diseases

Anne-Claire Dupont <sup>1,2</sup>, Bérenger Largeau <sup>2</sup>, Denis Guilloteau,<sup>1,3,4</sup>  
Maria Joao Santiago Ribeiro,<sup>1,4,5</sup> and Nicolas Arlicot<sup>1,2,4</sup>

<sup>1</sup>UMR 1253, iBrain, Université de Tours, Inserm, Tours, France

<sup>2</sup>CHRU de Tours, Unité de Radiopharmacie, Tours, France

<sup>3</sup>CHRU de Tours, Service de Médecine Nucléaire in vitro, Tours, France

<sup>4</sup>INSERM CIC 1415, University Hospital, Tours, France

<sup>5</sup>CHRU de Tours, Service de Médecine Nucléaire in vivo, Tours, France

Correspondence should be addressed to Anne-Claire Dupont; [ac.dupont@chu-tours.fr](mailto:ac.dupont@chu-tours.fr)

Received 29 December 2017; Accepted 1 April 2018; Published 17 May 2018

Academic Editor: Shuang Liu

Copyright © 2018 Anne-Claire Dupont et al. This is an open access article distributed under the Creative Commons Attribution License, which permits unrestricted use, distribution, and reproduction in any medium, provided the original work is properly cited.

In vivo exploration of neurodegenerative diseases by positron emission tomography (PET) imaging has matured over the last 20 years, using dedicated radiopharmaceuticals targeting cellular metabolism, neurotransmission, neuroinflammation, or abnormal protein aggregates (beta-amyloid and intracellular microtubule inclusions containing hyperphosphorylated tau). The ability of PET to characterize biological processes at the cellular and molecular levels enables early detection and identification of molecular mechanisms associated with disease progression, by providing accurate, reliable, and longitudinally reproducible quantitative biomarkers. Thus, PET imaging has become a relevant imaging method for monitoring response to therapy, approved as an outcome measure in bioclinical trials. The aim of this paper is to review and discuss the current inputs of PET in the assessment of therapeutic effectiveness in neurodegenerative diseases connected by common pathophysiological mechanisms, including Parkinson's disease, Huntington's disease, dementia, amyotrophic lateral sclerosis, multiple sclerosis, and also in psychiatric disorders. We also discuss opportunities for PET imaging to drive more personalized neuroprotective and therapeutic strategies, taking into account individual variability, within the growing framework of precision medicine.

## 1. Background

Neurodegenerative diseases (NDDs) are highly morbid hereditary and sporadic conditions characterized by progressive nervous system dysfunction and, ultimately, the loss of neurons. This heterogeneous group of disorders, including Alzheimer's disease (AD) and other dementias, Parkinson's disease (PD), multiple sclerosis (MS), amyotrophic lateral sclerosis (ALS), Huntington's disease (HD), is increasingly affecting the elderly worldwide, with a number of patients expected to double every 20 years [1]. Since these are progressive and irreversible disorders, early detection and differentiation of the disease are primordial for possible therapeutic intervention. Despite different initial clinical manifestations, many studies suggest that overlapping pathophysiological processes may be

involved in various forms of NDD, such as deposition of proteins with altered physicochemical properties in the human brain. Indeed, NDDs are thought to share a common pathogenesis mechanism, the aggregation and deposition of misfolded proteins not only in neurons but also in glial cells, which leads to progressive central nervous system impairments [2]. Thus, NDDs are classified according to current concepts of NDD based on clinical presentation, anatomical regions and cell types affected, and altered proteins involved in the pathogenetic process [3]. Basically, concerning correlation between anatomical involvement and NDD, it is well admitted that hippocampus, entorhinal cortex, or also limbic system are mainly involved in cognitive decline symptoms, whereas basal ganglia, thalamus, motor cortical areas, or cerebellar cortex are more involved in movement disorders. Amyloid- $\beta$  ( $A\beta$ ) and

$\tau$ -protein aggregates in Alzheimer disease, as well as other forms of aggregates such as the  $\alpha$ -synuclein aggregates (or Lewy bodies) found in Parkinson disease and dementia with Lewy bodies are among most proteins associated with the majority of NDDs. Concomitantly, microglial activation has also been linked with degenerative brain diseases by releasing proinflammatory cytokines including interleukin-(IL-)  $1\beta$ , IL-6, and tumor necrosis factor- (TNF-)  $\alpha$ , leading to neuronal damage and loss [4]. These common physiopathological processes suggest that these pathologies contribute to the development of other features of neurodegeneration such as neuronal and synaptic dysfunction in the central nervous system.

## 2. Current PET Imaging of Neurodegenerative Diseases

An early detection of the onset of NDD is pivotal as it can provide a chance for an early treatment that may prevent further progression of the disease. Over the past two decades, the traditional view of NDD, such as AD or PD, as purely clinical entity has been changed to one as a clinicobiological entity. A definite diagnosis has thus far been possible only by histopathologic postmortem assessment of brain tissue. Nevertheless, an important gap between the onset of symptoms and neuropathology in NDD is widely recognized. Hence, it has become increasingly possible to identify in vivo evidence of the specific neuropathology of NDD by use of validated biomarkers. Principal requirements for a good biomarker are preciseness, reliability, and capacity to distinguish healthy and pathological tissues. Among these, numerous neuroimaging biomarkers, being correlated with the NDD physiopathological process, have been introduced into the core diagnosis pathway. Positron emission tomography (PET) is a nuclear medicine imaging technique used to noninvasively assess various biological functions at the molecular level, by tracking a chemical compound of biological significance, called radiopharmaceutical, labeled with short-lived positron emitter radionuclide. In NDD, PET allows noninvasive evaluation of not only regional cerebral metabolism or perfusion but also the change of neurotransmission and presence of abnormal protein such as amyloid- $\beta$ .  $^{18}\text{F}$ -FDG PET is a well-established radiopharmaceutical to measure regional glucose metabolism indicating neuronal function. In different forms of neurodegenerative dementias, specific patterns of neuronal dysfunction have been described [5]. Besides, dopamine transporter and vesicular monoamine transporter imaging are useful in the diagnosis and evaluation of Parkinson disease progression, providing information about the integrity of presynaptic striatal dopaminergic neurons. More recently, PET tracers for molecular imaging of  $A\beta$  have improved early diagnosis by targeting the amyloid deposition. Cholinergic and microglial imaging can be also useful in the early diagnosis of dementia and improve understanding of insights into pathophysiology of neurodegenerative diseases.

Therefore, the ability of molecular imaging to identify and quantify cerebral pathology has significant implications for early detection and differential diagnosis in NDD.

## 3. PET Neuroimaging Interest for Therapeutic Effectiveness Assessment

Molecular PET neuroimaging is a sensitive technique able to identify subtle molecular changes in the brain even before structural changes are present. Thus, one of the most important short-term roles of PET neuroimaging could be in the clinical evaluation and validation of new treatments of NDD, such as anti-amyloid therapies in AD, which have entered in human trials (e.g., passive immunization,  $\gamma$ -secretase, and  $\beta$ -secretase inhibitors). Without a surrogate biomarker to assess the efficacy of these therapeutic agents on their intended central nervous system target, one cannot properly interpret the outcome of a therapeutic trial. All the more so as the assessment of clinical symptoms may therefore not represent an ideal tool for follow-up and therapy monitoring in NDD, it could have an important symptomatic overlap between NDD themselves. The ability of PET to not only provide spatial localization of metabolic changes but also to accurately and consistently quantify their distribution proved valuable for applications in assessment of drug effectiveness. Indeed, the great strength provided by functional and molecular PET approach allows visualizing numerous of the physiopathological pathways involved in NDD. The development of PET radioligands for the in vivo neuroimaging has been the focus of intense research efforts in recent years and most of the pathophysiologic processes involved in NDD mentioned above such as neuroinflammation, neurotransmission or misfolded protein aggregation, could to date be explored. Furthermore, the capacity to obtain quantitative information with PET tracer uptake in the brain could be relevant for the follow-up evaluation in therapy monitoring. The availability of plenty of PET tracers validated in humans (both on pharmacokinetic or dosimetry fields) provides exciting opportunities for the discovery, validation, and development of novel therapeutics in NDD. The new drug candidates may be radiolabeled in order to reflect, for instance, the biodistribution or the blood-brain barrier passage. But PET can especially be used to study the synthesis and release of neurotransmitters and the availability of neurotransmitter receptors. The growing epidemics of NDD such as AD, PD, or ALS have increased the need for new treatments, and their development is conditioned by first, the choice and the knowledge about the target and second, by the optimization of their validation in vivo. Known to be an important tool in both research and clinical care, PET neuroimaging approach in the therapeutic evaluation and optimization in NDD is discussed in this manuscript.

## 4. PET Imaging to Assess Therapeutic Effectiveness

*4.1. Glucose Metabolism Imaging.* Since its first application in humans in 1979 (Table 1) [13],  $^{18}\text{F}$ -FDG PET improves our understanding of many brain disorders. Indeed, its ability to measure local glucose consumption in various structures of the brain allows to detect alterations in local cerebral metabolism.  $^{18}\text{F}$ -FDG uptake by the cortical and subcortical structures in the brain has the advantage to provide valuable

TABLE 1: Glucose metabolism imaging approach to assess therapeutic effectiveness.

Disorder	Physiopathological approach	Radioligand	Population	Therapeutical class	Main findings	References
HD	Glucose metabolism	<sup>18</sup> F-FDG	11 riluzole-treated HD patients versus 12 untreated HD patients	Riluzole (benzothiazole)	Placebo-treated patients showed significantly greater proportional volume loss of grey matter and decrease in metabolic FDG uptake than patients treated with riluzole in all cortical areas ( $p < 0.05$ ).	Squitieri et al. [6]
			6 months treatment pramipexole 20 mild-to-moderate AD, 15 completed all visits	Pramipexole (D2-family dopamine receptor agonist)	Broad regions where glucose uptake decreased suggesting a relative decrease in metabolism (consistent with regions of reduced metabolism in individuals with AD). Nonapparent effect of r-pramipexole on brain regional glucose uptake. Rosiglitazone is associated with an early increase in whole brain glucose metabolism but not with any biological or clinical evidence for slowing progression over a 1 year follow up in the symptomatic stages of AD.	Benett et al. [7]
AD	Glucose metabolism	<sup>18</sup> F-FDG	12 months treatment rosiglitazone versus placebo in 80 mild-to-moderate AD patients	Rosiglitazone (PPAR agonist)		Tzimopoulou et al. [8]
PD	Glucose metabolism	<sup>18</sup> F-FDG	12 patients with advanced PD were assessed before and after 6 months of add-on apomorphine	Apomorphine	Significant metabolic changes were observed, with overall increases in the right fusiform gyrus and hippocampus, alongside a decrease in the left middle frontal gyrus. Consistent correlations between significant changes in clinical scores and metabolism were established.	Auffret et al. [9]
SCZ	Glucose metabolism	<sup>18</sup> F-FDG	18 neuroleptic-naïve first-episode schizophrenic patients	Olanzapine	Glucose metabolism in responders was significantly increased after treatment in the left precentral gyrus, left postcentral gyrus, and left paracentral lobule and significantly decreased in the left hypothalamus. Individuals treated with olanzapine showed increased relative metabolic rates in the frontal lobe more than the occipital lobe while patients treated with haloperidol failed to show increase in frontal metabolic rates and did not show an anteroposterior gradient in medication response.	Yoshimuta et al. [10]
			30 never-previously medicated psychotic adolescents (ages 13–20)	Olanzapine or haloperidol	No significant regional metabolic changes were related to previous treatment with classical neuroleptics.	Buchsbaum et al. [11]
	Glucose metabolism	<sup>18</sup> F-FDG	17 schizophrenic patients previously treated with antipsychotics	Olanzapine		Molina et al. [12]

AD, Alzheimer disease; FDG, fluorodeoxyglucose; HD, Huntington disease; PD, Parkinson disease; PPAR, peroxisome proliferator-activated receptor; SCZ, schizophrenia.

information before any morphological changes become discernible. Thus,  $^{18}\text{F}$ -FDG PET is a well-established tool to identify disease-specific cerebral metabolic brain patterns in several neurodegenerative brain diseases at an early disease stage. In AD, the most prevalent neurodegenerative cause of dementia [14],  $^{18}\text{F}$ -FDG is an effective modality for detecting functional brain changes since AD patients exhibit characteristic temporoparietal glucose hypometabolism. Furthermore, a correlation between the degree of hypometabolism and the severity of dementia has been reported during disease progression [15], in relation with neuronal cell loss and decreased synaptic activity. By assessing indirect functional effects of neurodegeneration,  $^{18}\text{F}$ -FDG can be useful for early diagnosis and the differential diagnosis between AD and other various types of dementia like dementia with Lewy bodies, frontotemporal lobe dementia, and vascular dementia. Thus, it is widely recognized that  $^{18}\text{F}$ -FDG holds a special place for the staging and assessment of AD. Unlike oncology field, where  $^{18}\text{F}$ -FDG is routinely used for treatment evaluation and follow-up,  $^{18}\text{F}$ -FDG has only been used sporadically in the past as a biomarker for predicting therapeutic response in AD. The first multicenter clinical trial in AD using  $^{18}\text{F}$ -FDG measuring brain glucose metabolism as the primary outcome has been described by Tzimopoulou et al. in 2010 [8]. Brain glucose metabolism was studied at baseline and at three later time points (1, 6, and 12 months) after 12 months treatment with the peroxisome proliferator-activated receptor (PPAR) gamma agonist rosiglitazone versus placebo in 80 mild-to-moderate AD patients. Rosiglitazone has been shown to ameliorate insulin resistance in patients with type II diabetes mellitus [16] and seems to improve cognition in AD in preliminary studies [17] but that effect could be limited to APOE4 subjects [18]. No statistically significant difference indicated that active treatment decreased the progression of decline in brain glucose metabolism over a one-year follow-up in the symptomatic stages of AD. Nevertheless, while failing to demonstrate an effect of rosiglitazone on neurodegeneration, these results are consistent with Phase III clinical trials using rosiglitazone in AD [19, 20], which conclude that PET imaging biomarker like  $^{18}\text{F}$ -FDG could provide good mechanistic tests for the evaluation of future therapeutic hypotheses. In 2016, in a safety and tolerability study of 6 months of pramipexole in 15 mild-to-moderate AD patients, Bennett et al. has used PET imaging to complete the study by examination of cognitive performance with  $^{18}\text{F}$ -FDG tracer. In this small single-arm, open-label study, there was no apparent effect of pramipexole because a 3–6% brain glucose uptake decrease has been observed during the 6-month follow-up, consistent with regions of reduced metabolism in AD patients without treatment [7]. Contrary to the minor interest of  $^{18}\text{F}$ -FDG in AD therapeutic assessment, a recent study has shown that apomorphine pump seems to be an interesting option for treating advanced PD patients in therapeutic impasse, thanks to a brain glucose metabolism study [9]. In 12 advanced PD patients, significant metabolic changes were observed, with overall increases in the right fusiform gyrus and hippocampus, alongside a decrease in the left middle frontal gyrus before and after 6 months of add-on apomorphine. Besides, consistent correlations between

significant changes in clinical scores, mainly assessed according to UPDRS (Unified Parkinson's Disease Rating Scale) and MDRS (Mattis Dementia Rating Scale), and metabolism were established. In the same way, metabolic (by  $^{18}\text{F}$ -FDG-PET) and volumetric (by Magnetic Resonance Imaging-MRI) differences in the brain have been investigated to evaluate neuroprotective effects of riluzole in HD [21]. Riluzole interferes with glutamatergic neurotransmission, thereby reducing excitotoxicity and enhancing neurite formation in damaged motoneurons [22]. It also has been reported to inhibit voltage-gated sodium channels and to be neuroprotective by suppressing astrocytosis [23]. The 12 placebo-treated HD patients showed significantly greater proportional volume loss of grey matter and decrease in metabolic  $^{18}\text{F}$ -FDG uptake than the 11 HD patients treated with riluzole in all cortical areas ( $p < 0.05$ ). Not only brain glucose metabolism was preserved in patients receiving riluzole, but also a correlation between the progressive metabolic consumption with worsening clinical scores (UHDRS-I, Unified Huntington Disease Rating Scale) in placebo group was reported. These findings corroborate that antiglutamatergic drugs like riluzole could represent a neuroprotective strategy in HD and that  $^{18}\text{F}$ -FDG-PET may be a valuable tool to assess brain markers of HD. Considered as a neurodegenerative or neurodevelopmental disorder, recent studies have shown the importance of treating schizophrenia, a chronic and severe mental disorder characterized by abnormal social behaviour and failure in assessing reality. Mostly, we distinguish positive (i.e. hallucinations, paranoid delusions, beliefs), negative (i.e. apathy, lack of emotion, and poor or nonexistent social functioning), and cognitive (disorganized thoughts, difficulty concentrating and/or following instructions, difficulty completing tasks, and memory problems) psychotic symptoms; and that is why many structural brain studies have correlated schizophrenia symptoms with reproducible structural brain abnormalities. For instance, progressive prefrontal grey matter atrophy is known to be more related to pronounced negative symptoms [24]. Cerebral metabolic studies with  $^{18}\text{F}$ -FDG have an interest to define brain regions associated with treatment-related improvement of symptoms in schizophrenic patients. Thus, increased relative metabolic rate has been observed in the frontal lobe in 30 psychotic patients treated with olanzapine versus no medication subjects [11]. Such a difference has not been observed in 17 patients previously exposed to antipsychotics [12]. Linking to the interest to treat schizophrenia as soon as possible, Yoshimuta et al. have examined the effects of olanzapine and identified brain regions associated with a positive response in neuroleptic-naive first-episode schizophrenic (FES) patients [10]. Glucose metabolism in responders was significantly increased after treatment in the left precentral gyrus, left postcentral gyrus, and left paracentral lobule and significantly decreased in the left hypothalamus. These observations added to the positive correlation between the changes in "Positive and Negative Syndrome Scale" (PANSS) scores and metabolic changes before and after treatment reinforce the beneficial action of olanzapine in FES patients.

**4.2. Amyloid and Tau Imaging.** Currently, the only FDA-approved AD drugs such as donepezil, galantamine, or memantine act partially on the symptoms of AD, without treating the underlying causes of the disease (Table 2). A worldwide quest is under way to find new treatments to stop, slow, or even prevent AD. Many of the new drugs in development aim at modifying the disease process itself, by impacting one or more of its hallmarks, like extracellular plaque deposits of the  $\beta$ -amyloid peptide ( $A\beta$ ). For this purpose, interest of immunotherapy has grown during the last decade: antibodies are attractive drugs as they can be made highly specific for their target and often confer a lower risk of side effects in a vulnerable patient population during long-term treatment as compared with small-molecule anti- $A\beta$  therapy. Thus, monoclonal antibodies have emerged to lower the beta-amyloid load in the brain, preventing the formation of plaques or even carrying excess beta-amyloid out of the brain. One of the earliest compounds evaluated for the treatment of AD was the bapineuzumab, a humanized N-terminal-specific anti- $A\beta$  monoclonal antibody. Several PET studies measuring  $A\beta$  load have been performed for the clinical evaluation of this antibody, using radiopharmaceuticals developed from the chemical structure of histologic dyes. This noninvasive approach made it possible to track amyloid pathology longitudinally, following the disease progression.

In a study conducted by Rinne et al. in 2010 in 28 AD patients, the amyloid load was found to be reduced in the brains of patients treated with bapineuzumab as compared with placebo, as measured by binding of  $^{11}\text{C}$ -PIB to brain amyloid with PET [25]. In contrast, in a second Phase II study, bapineuzumab subcutaneous once monthly did not demonstrate a significant treatment difference over placebo on cerebral amyloid signal, assessed with  $^{18}\text{F}$ -florbetapir at one year [26]. Then, two Phase III trials of bapineuzumab in mild-to-moderate AD, supported by Janssen Alzheimer Immunotherapy Research & Development and Pfizer Inc. confirmed this result since bapineuzumab failed to reach the clinical endpoint in Phase III, namely, the overall negative clinical findings [27, 28]. The other humanized anti- $A\beta$  monoclonal antibody that has been involved to large Phase III clinical trials is solanezumab, recognizing the central  $A\beta_{13-28}$  region [29]. Two large randomized double-blind controlled Phase III trials tested solanezumab as a potential treatment to slow the progression of mild-to-moderate AD, EXPEDITION 1 and EXPEDITION 2, with, respectively, 1012 and 1040 patients randomized to 400 mg of solanezumab or placebo every 4 weeks for 80 weeks [30]. Solanezumab failed to improve cognition or functional ability assessed with cognitive subscale of the Alzheimer's Disease Assessment Scale (ADAS-cog14) [31]. In both studies, a total of 169 patients and 97 in EXPEDITION 1 and 2, respectively, underwent baseline and follow-up  $^{18}\text{F}$ -florbetapir-PET scanning. The composite SUVR for the anterior and posterior right and left cingulate, plus right and left frontal, lateral temporal, and parietal regions, combined and normalized to the whole cerebellum, did not change significantly in the solanezumab group or the placebo group in either study. Many other anti- $A\beta$  monoclonal antibodies are under development, and among them is the first fully

human antibody, the gantenerumab that also binds specifically to  $A\beta$  plaques. The effect of up to 7 infusions of IV gantenerumab or placebo every 4 weeks on the  $A\beta$  amyloid load as measured by  $^{11}\text{C}$ -PiB has been studied in patients with mild-to-moderate AD in a preliminary PET study [32]. In 16 AD patients, the PET study has shown a dose-dependent reduction in brain  $A\beta$  plaques, but again no consistent treatment effects on cognitive measures were noted. Ongoing Phase III trials on gantenerumab on prodromal or mild stage of AD may clarify whether any reduction in brain  $A\beta$  deposits will successfully translate into clinical practice benefit at well-tolerated doses of gantenerumab [33]. Overall, to date, most of clinical trials trying to stop AD progression has led to reduce amyloid deposition but has little beneficial effect on cognitive improvement. Therefore, new approaches are being investigated, and a preliminary PET study has shown that benfotiamine significantly improved the cognitive abilities of 3 mild-to-moderate AD patients despite the progression of brain amyloid assessed by  $^{11}\text{C}$ -PIB [30]. Benfotiamine is a synthetic thiamine derivative preventing abnormal glucose metabolism via multiple pathways [34]. It is so demonstrated in this study that the alteration of cognitive capability is independent of brain amyloid accumulation, which is consistent with previous results showing that the reduction of brain amyloid accumulation by antibodies has little effect on the cognitive ability and disease progression of AD patients. It will be necessary to validate these results by randomized, double-blinded, placebo-controlled clinical trials.

As  $\beta$ -amyloid peptide, aggregates of hyperphosphorylated tau protein known as neurofibrillary tangles (NFTs) are one of the hallmarks of AD and related disorders, called tauopathies. Aggregates of tau are prominent targets for novel therapeutics as well as for biomarkers for diagnostic in vivo imaging. While immunotherapy targeting  $A\beta$  peptide gave poor results, tau-based immunotherapy clinical trials have recently emerged [35]. Promising results are expected from a new active vaccine, namely, AADvac1, targeting pathological tau protein in Alzheimer's disease [36]. In addition, the recent development of tau-specific PET tracers has allowed in vivo quantification of regional tau deposition and offers the opportunity to monitor the progression of tau pathology along with cognitive impairment. To our knowledge, any study with a tau PET tracer as a reliable outcome measure of drug efficacy assessment has been published yet. As explained by Okamura and Yanai [37], the methods to image analysis with tau PET tracer need to be optimized. Indeed, the variety of the different types of tau deposits is a crucial issue for the development in tau PET tracers. Recent data evidence the existence of off-target binding in areas of tau accumulation. Thus, a longitudinal observation of patients at baseline and post-selegiline (MAO-B inhibitor)  $^{18}\text{F}$ -THK5351 PET scans has tested the hypothesis that a reduction of MAO-B availability also reduces  $^{18}\text{F}$ -THK5351 uptake. In this study, Ng et al. reported that MAO-B was an  $^{18}\text{F}$ -THK5351 off-target binding site; hence, the interpretation of PET images is confounded by the high MAO-B availability [38].

With the increasing interest in antitau therapies, tau PET tracers will certainly be a tool to assess the therapeutic effects

TABLE 2: Amyloid imaging approach to assess therapeutic effectiveness.

Disorder	Physiopathological approach	Radioligand	Population	Therapeutical class	Main findings	References
	Amyloid	<sup>18</sup> F-florbetapir	12 month study to determine long-term effects of monthly SC injections on 146 amyloid positive patients with mild to moderate AD (36 placebo versus 110 bapineuzumab 2 mg, 7 mg, 20 mg)	Bapineuzumab immunotherapy	Bapineuzumab did not demonstrate significant difference over placebo on GCA of 5 SUVR ROI: anterior cingulate, frontal cortex, lateral temporal cortex, parietal cortex, posterior cingulate/precuneus). Subgroup analysis based on disease severity: change in SUVR significant only in 7 mg/month group in patient with mild AD.	Brody et al. [26]
	Amyloid	<sup>11</sup> C-PiB	78 weeks study on 28 patients with mild to moderate AD (8 placebo versus 20 Bapineuzumab IV 0.5 mg/kg, 10 mg/kg, 2.0 mg/kg)	Bapineuzumab immunotherapy	Estimated difference on cerebral retention ratio is significant between Bapineuzumab and placebo group.	Rinne et al. [25]
AD	Amyloid	<sup>11</sup> C-PiB	(7 placebo and 19 bapineuzumab included in PiB PET analysis) Patients with mild to moderate AD 2 substudies: ApoE4 carriers (24 placebo versus 32 bapineuzumab IV 0.5 mg/kg) ApoE4 non carriers (13 placebo versus 17 bapineuzumab IV 0,5 mg/kg) Patients with mild to moderate AD	Bapineuzumab immunotherapy	<sup>11</sup> C-PiB PET seems to be useful in assessing the effects of potential AD treatments on cortical fibrillar amyloid-β load in vivo. Change from baseline to week 78 for GCA SUVR was not statistically significant versus placebo in either study. No significant treatment differences were seen in amyloid burden on PiB-PET.	Vandenbergh et al. [27]
	Amyloid	<sup>11</sup> C-PiB	PiB PET substudy: ApoE ε4 carriers: 75 Bapineuzumab IV versus 40 placebo; ApoE ε4 non-carriers: 22 Bapineuzumab IV versus 15 placebo Patients with mild-to-moderate AD receiving placebo or solanezumab IV 4 weeks for 18 months	Bapineuzumab immunotherapy	Significant differences in mean SUVR were only observed between bapineuzumab and placebo in the ApoE ε4 carrier study.	Salloway et al. [28]
	Amyloid	<sup>18</sup> F-florbetapir	Combining the 2 substudies, a total of 266 patients underwent PET examination at baseline and week 80 or early termination	Solanezumab immunotherapy	The composite SUVR for the anterior and posterior right and left cingulate, plus right and left frontal, lateral temporal, and parietal regions, combined and normalized to the whole cerebellum, did not change significantly in the solanezumab group or the placebo group in either study.	Doody et al. [29]

of these new drugs acting on tau load in the brain. For that purpose, new tau PET tracers (i.e.,  $^{18}\text{F}$ -MK-6240 and  $^{18}\text{F}$ -AM-PBB3) have recently been reported to have less off-target binding than their predecessors [39].

**4.3. Neuroinflammation Imaging.** Initially discovered in Alzheimer's disease (AD), where activated microglia cells were found in postmortem nearby senile plaques (Table 3) [40], it is now clearly established that microglial activation and abnormal protein deposition take part in the process of neurodegenerative disorders such as AD, PD, ALS, and MS [4]. Thus, glial inflammation has heightened interest in the rapid discovery of neuroinflammation-targeted drugs [41]. Given the fact that anti-inflammatory drugs are able to suppress peripheral inflammation, many authors investigated their potential use for central nervous system (CNS) inflammation [42–44]. Nevertheless, only few clinical studies have evaluated, thanks to molecular imaging, and apart from clinical parameters, the ability of these drugs to reduce glial cell-propagated inflammation. In parallel, over the last 20 years, microglia PET imaging has successfully widened through the development of radiopharmaceuticals and the identification of several molecular targets of neuroinflammation. Among these targets, receptors including the translocator protein-18 kDa (TSPO) [45], cannabinoid receptor 2A [46], and adenosine receptor 2A [47, 48] and enzymes such as  $\beta$ -glucuronidase [49] have been targeted to evaluate the scope of microglia PET imaging in neurodegenerative disorders. To our knowledge, only TSPO PET imaging has been used to assess therapeutic efficacy in neurodegenerative disorders. Drugs evaluated in these studies include specific therapeutics which have already granted FDA licensure like interferon beta, [50] glatiramer acetate, [51] and fingolimod [52, 53] in MS, nonspecific drugs which exert anti-inflammatory effects, [54, 55] and new therapeutical class-targeting biochemical pathways involved in neurodegenerative disorder such as the hydrolysis of neuroprotective endocannabinoid [56] and oxidative stress [57]. Microglial activation plays a central role in maintaining the central chronic inflammation in MS [58]. MS is a chronic autoimmune disease of the CNS where the migration of myelin-reactive T-cells into the CNS is followed by microglial activation, recruitment of peripheral macrophages, and oligodendrocytes destruction [59]. Fingolimod blocks the egress of lymphocytes from secondary lymphoid tissues and thereby prevents their entry into the CNS [60]. In line with its mechanism of action, PET imaging showed that fingolimod reduced microglial activation [52, 53], especially in T2 lesion area [53]. Glatiramer acetate, a synthetic polypeptide resembling myelin basic protein, acts further downstream deceiving immune system and inducing immunomodulatory Th2 cells [61]. Ratchford et al. [51] provided proof of concept that microglia PET imaging with  $^{11}\text{C}$ -PK11195 could also be a tool to assess disease-modifying drugs for relapsing-remitting multiple sclerosis (RRMS) efficacy. Indeed, radiopharmaceutical binding potential per unit volume was statistically decreased in the whole brain after one year of glatiramer acetate. This result supported the

in vitro evidence of its mechanism of action in which an inhibition of transformation to an activated microglia form could be responsible for therapeutic effects [61]. In other neurodegenerative disorders, TSPO PET studies have not achieved convincing results. Indeed, authors reported no significant difference [57] in microglial activation or a slight decrease [56] in TSPO density and sometimes an increase in TSPO tracer binding after therapeutic challenge [55].

**4.4. Neurotransmission Imaging.** During the past decades, numerous neurotransmitter systems have been identified and have been demonstrated to be directly involved in NDD. In vivo neuroimaging with PET using labeled ligands can visualize the various receptor and transporter systems and measure in quantitative terms their densities and binding and occupancy status (Table 4). The importance of PET in receptor-system-related drug research has increased tremendously in recent years.

One of the key monoamine neurotransmitters, the dopaminergic transmission plays a major role in neurological and psychiatric disorders such as PD, HD, and SCZ. Although mainly known to be involved in motor feature, dopamine is also involved in cognition and emotion. To investigate pre- and postsynaptic functions, PET tracers have been developed to measure dopamine synthesis and transport and postsynaptic receptors. For measuring dopamine synthesis, the most commonly used tracer is  $^{18}\text{F}$ -DOPA, whereas for dopamine transport, several radiolabeled tropane analogs have been developed. For postsynaptic dopamine receptors, divided on five subtypes of receptors,  $^{11}\text{C}$ -raclopride is the common tracer for D2/D3, whereas  $^{18}\text{F}$ -fallypride is mainly used for the exploration of D2 [62]. In clinical practice, it is well admitted that the extent of dopaminergic neuronal loss in the substantia nigra in PD patients is measured in vivo using  $^{18}\text{F}$ -DOPA considered as the gold-standard for monitoring the course of PD [63]. Unlike for other physiopathological pathways cited above as neuroinflammation or amyloid aggregation, dopamine molecular imaging has already widely been used for a long while to assess drug therapeutic effectiveness in PD essentially. Actually, it could be explained first by the fact that a treatment allowing restoration of dopamine neurotransmission is available for years for PD patients and second by direct dopaminergic transmission radiotracers availability. In 1990s, PET studies with  $^{11}\text{C}$ -raclopride have demonstrated the downregulation of the striatal D<sub>2</sub> receptor binding in PD related to long-term treatment. Indeed, compared to the baseline,  $^{11}\text{C}$ -raclopride binding was significantly decreased in the putamen and caudate nucleus in PD patients treated for 3–5 years with L-DOPA or lisuride, whereas no change was observed in D2 density 3–4 months posttreatment [64, 65]. More recently,  $^{11}\text{C}$ -raclopride PET studies have evaluated the relationship between clinical improvement following a single oral dose of levodopa and drug-induced synaptic dopamine increases. A significant increase of striatal DA in both caudate and putamen after levodopa administration was correlated with the improvement of rigidity and bradykinesia, whereas

TABLE 3: Neuroinflammation imaging approach to assess therapeutic effectiveness.

Disorder	Physiopathological approach	Radioligand	Population	Therapeutical class	Main findings	References
AD	Neuroinflammation TSPO	<sup>18</sup> F-GE180	Preclinical: transgenic APdE9 mice were treated with JZL184 ( <i>n</i> = 7) or with vehicle ( <i>n</i> = 5)  Preclinical: chronic focal EAE-like lesions were induced in rats via stereotactic intrastriatal injection of BCG and subsequent activation using an intradermal injection of BCG Animals were then treated for 28 days with either fingolimod ( <i>n</i> = 5) or vehicle ( <i>n</i> = 3)	Monoacylglycerol lipase inhibitor: JZL184 40 mg/kg/d  Selective immunosuppressant (SIP receptor antagonist): fingolimod 0.3 mg/kg/d	In JZL184-treated mice, there was a very slight decreasing trend in tracer uptake in multiple brains areas compared to vehicle-treated APdE9 mice.  Treatment with fingolimod for 28 days resulted in a clear reduction in the binding of trace when compared with vehicle-treated animals.  Quantification of the binding of the radiotracer revealed a significant reduction in the BP <sub>ND</sub> of <sup>18</sup> F-GE180 after treatment with fingolimod.  Significantly decreased tracer BP <sub>ND</sub> per unit volume 3.17% in whole brain between baseline and 1 year and especially in supratentorial brain, infratentorial brain, cerebral white matter, cortical grey matter, thalamus and putamen.	Pihlaja et al. [56]  Airas et al. [52]
	Neuroinflammation TSPO	<sup>18</sup> F-GE180	Clinical: 9 drug-naïve RRMS patients were scanned at baseline before initiating GA and again after 1 year of GA treatment	Immunomodulatory: GA 20 mg/d		Ratchord et al. [51]
MS	Neuroinflammation TSPO	<sup>11</sup> C-PK11195	Clinical: RRMS patients in acute relapse: 6 drug-naïve patients and 3 patients on interferon beta therapy versus 5 HC  Clinical: 10 RRMS patients were scanned at baseline before initiating fingolimod and again after 6 months of treatment	Immunomodulatory: interferon beta	No significant difference of tracer BP <sub>ND</sub> or V <sub>T</sub> between the three groups: MS without treatment, MS with interferon beta therapy, and normal control.  Tracer binding was reduced (-12.3%) in the T2 lesion area after 6 months of fingolimod treatment, but not in the areas of NAWM or grey matter.	Takano et al. [50]
	Neuroinflammation TSPO	<sup>11</sup> C-PK11195	7 patients were scanned 2 months following the treatment initiation	Selective immunosuppressant (SIP receptor antagonist): fingolimod	5/7 patients showed a slight increase tracer DVR in NAWM during the first 2 months of fingolimod treatment.  6/7 patients showed a slight increase in cortical gray matter after 2 months.	Sucksdorff et al. [53]
MSA	Neuroinflammation TSPO	<sup>11</sup> C-PK11195	Clinical: 8 MSA-P patients: 3 with minocycline versus 5 in placebo arm  Two groups were followed up for 6 months	Tetracycline with anti-inflammatory effects: minocycline 200 mg/d	Compared to baseline, tracer BP <sub>ND</sub> decreased in caudate nucleus, thalamus, midbrain and cerebellum for 2/3 treated patients after 24 weeks of minocycline.  In placebo group, tracer BP <sub>ND</sub> is increased in most regions after 6 months.	Dodel et al. [54]
	Neuroinflammation TSPO	<sup>11</sup> C-PK11195	Clinical: 5 PD patients were scanned before and after one month of celecoxib  Clinical: 24 PD patients: 18 with AZD3241 versus 6 in placebo arm  16 PD patients in AZD3241 arm were followed-up for 8 weeks	COX-2 inhibitor: celecoxib 100 mg/d  Myeloperoxidase inhibitor: AZD3241 600 mg/12 h	Tracer binding potential and distribution volume after celecoxib treatment were slightly higher.  There was no significant difference in changes of V <sub>T</sub> between the treatment groups.  AZD3241 significantly reduced V <sub>T</sub> in regions of the nigrostriatal pathway compared to baseline V <sub>T</sub> -values at 4 weeks and at 8 weeks.	Bartels et al. [55]  Jucaite et al. [57]

AD, Alzheimer's disease; BCG, bacillus Calmette-Guérin; BP<sub>ND</sub>, binding potential; DVR, distribution volume ratio; EAE, experimental autoimmune encephalitis; GA, glatiramer acetate; MS, multiple sclerosis; MSA, multiple system atrophy; NAWM, normal appearing white matter; PD, Parkinson's disease; RRMS, relapsing-remitting multiple sclerosis; SIP, sphingosine 1-phosphate; V<sub>T</sub>, total distribution volume.

TABLE 4: Neurotransmission imaging approach to assess therapeutic effectiveness.

Disorder	Physiopathological approach	Radioligand	Population	Therapeutical class	Main findings	References
PD	Dopamine neurotransmission	<sup>11</sup> C-raclopride	18 previously untreated PD patients and 14 healthy volunteer subjects	Levodopa/lisuride	3 to 4 months' oral therapy with LD or lisuride does not change striatal dopamine D2-receptor density in PD patients. After 3-5 years, binding was significantly reduced in the putamen ( $p < 0.03$ ) and caudate nucleus ( $p < 0.03$ ) compared with baseline. These results indicate long-term downregulation of striatal dopamine D2 receptor binding in PD.	Antonini et al. [64]
	Dopamine neurotransmission	<sup>11</sup> C-raclopride	9 patients with PD at an early drug-naive stage and 3-5 years later and 10 healthy controls in the same age range	Levodopa/lisuride	Following LD, mean caudate and putamen <sup>11</sup> C-raclopride BPs were significantly lower versus baseline, consistent with increased synaptic DA.	Antonini et al. [65]
	Dopamine neurotransmission	<sup>11</sup> C-raclopride	16 advanced PD patients	Levodopa	A two-scan RAC PET study has reported, in advanced PD cases that, improvement in bradykinesia and rigidity scores following oral DA medication administration were significantly correlated with reductions in RAC binding suggesting an effect of increased DA on the striatal D2 receptors.	Pavese et al. [66]
	Dopamine neurotransmission	<sup>18</sup> F-6-fluorodopa	67 patients with IP, 52 with fluctuations and 15 with a stable response to LD	Levodopa	A 28% decrease in presynaptic terminal function in the putamen of PD patients with a fluctuating response to LD compared to the stable responders.	de la Fuente-Fernández et al. [68]
	Dopamine neurotransmission	<sup>18</sup> F-6-fluorodopa	9 patients with PD followed for 10 to 72 months after human embryonic mesencephalic tissue	Human embryonic mesencephalic tissue	<sup>18</sup> F-6-DOPA uptake increases in the striatum following the transplantation.	Wenning et al. [67]
	Dopamine neurotransmission	<sup>18</sup> F-6-fluorodopa	40 patients with PD	Transplantation of human embryonic dopamine neurons	Among younger patients (60 years old or younger), standardized tests of PD revealed significant improvement in the transplantation group as compared with the sham-surgery group when patients were tested in the morning before receiving medication.	Freed et al. [70]
	Dopamine neurotransmission	<sup>18</sup> F-6-fluorodopa	34 patients with advanced PD	Fetal nigral transplantation	Striatal <sup>18</sup> F-6-DOPA uptake was significantly increased after transplantation in both groups and robust survival of dopamine neurons was observed at postmortem examination.	Olanow et al. [71]

TABLE 4: Continued.

Disorder	Physiopathological approach	Radioligand	Population	Therapeutical class	Main findings	References
AD	MAO-B inhibition dopamine neurotransmission	<sup>11</sup> C-L-deprenyl-D2	10 AD patients versus 6 elderly control subjects	Sembragiline MAO-B inhibitor	This PET study confirmed that daily treatment of at least 1 mg sembragiline resulted in near-maximal inhibition of brain MAO-B enzyme in patients with AD. In the galantamine group, there was significant inhibition of AChE activity in all four cortical regions (frontal, parietal, parietotemporal, temporal). The placebo group did not show any significant inhibition compared with baseline.	Sturm et al. [74]
	Acetylcholine neurotransmission	<sup>11</sup> C-PMP	18 subjects (12 galantamine versus 6 placebo) with mild to moderate AD (14 completed 12 months study)	Galantamine	A positive correlation was observed between changes in the average cortical <sup>11</sup> C nicotine binding and plasma galantamine concentrations.	Kadir et al. [75]
		<sup>11</sup> C-nicotine				
PD	Serotonin neurotransmission	<sup>11</sup> C-DASB	2 PD patients who had shown recovery of motor function after intraatrial fetal ventral mesencephalic tissue transplantation but experienced off-phase GIDs	Neural transplantation Buspirone 5-HT <sub>1A</sub> receptor agonist	It was found excessive serotonergic innervation in the grafted putamen in one patient and putamen and caudate nucleus in second patient. Buspirone in low repeated dose markedly attenuated dyskinesia severity in both transplanted patients.	Politis et al. [73]
	GABA neurotransmission	<sup>11</sup> C-flumazenil	17 off-medication SCZ patients versus 22 HC	Tiagabine IGATI	<sup>11</sup> C-flumazenil V <sub>T</sub> was significantly increased across all cortical brain regions in the healthy comparison group but not in the schizophrenia group.	Frankle et al. [72]
SCZ	GABA neurotransmission	<sup>11</sup> C-Ro15-4513	12 healthy male completed the Tiagabine challenge study	Tiagabine IGATI	Tiagabine administration produced significant reductions in hippocampal, parahippocampal, amygdala, and anterior cingulate synaptic α <sup>1</sup> <sup>11</sup> C-Ro15-4513 binding, and a trend significance reduction in the nucleus accumbens.	Stokes et al. [76]

AChE, acetylcholinesterase; AD, Alzheimer disease; BP, binding potential; DA, dopamine; EC, elderly control; GIDs, graft-induced dyskinesia; HC, healthy comparison; MAO-B, monoamine oxidase type B; IP, idiopathic parkinsonism; LD, levodopa; PET, positron emission tomography; RAC, <sup>11</sup>C-raclopride; SCZ, schizophrenia; V<sub>T</sub>, tissue distribution volume.

tremor and axial symptoms are not found to be related to this striatal synaptic dopamine level [66]. This last study indicates that pathways other than nigrostriatal pathway may be implicated in the pathogenesis of parkinsonian tremor and axial features and so other treatments are expected. In parallel, dopaminergic system molecular imaging has broadly been investigated in levodopa-induced dyskinesias (LID) field [67]. LIDs are associated with increased and fluctuating synaptic dopamine levels following levodopa administration [68]. Finally, dopamine in vivo imaging has extensively been used to assess safety after neural transplantation [69–73].

Finally, PET imaging in clinical transplantation trials can provide additional valuable information alongside clinical observations. Although being used in almost every case in PD study, dopamine transmission in vivo imaging has measured brain MAO-B inhibition in patients with AD and elderly controls after oral administration of selegiline [74]. In order to assist in dose selection of the Phase 2 selegiline study in patients with moderate AD, Sturm et al. had to determine the relationship between exposure to selegiline and the inhibition of MAO-B enzyme activity in the brain, thanks to  $^{11}\text{C}$ -L-Deprenyl-D2.

In addition to the dopamine neurotransmission, radioligands have been developed to target cholinergic, serotonergic, or gabaergic transmissions. Thanks to two cholinergic system tracers ( $^{11}\text{C}$ -PMP and  $^{11}\text{C}$ -nicotine), we can see the acetylcholinesterase inhibition by the galantamine up to 12 months in 18 mild AD patients [75]. The inhibitory  $\gamma$ -aminobutyric acid (GABA) is known to be involved in a number of neuropsychiatric disorders including schizophrenia, and that is why, the tiagabine effect, which increases synaptic GABA, has been investigated with  $^{11}\text{C}$ -Ro15-4513 in 12 male participants to show its potential involvement in schizophrenia. Tiagabine produced significant reductions in hippocampal, parahippocampal, amygdala, and anterior cingulate synaptic tracer binding, suggesting that acute increases in endogenous synaptic GABA are detectable in the living human brain using  $^{11}\text{C}$ -Ro15-4513 PET [76]. Then, an in vivo impairment in GABA transmission in schizophrenia has been recently demonstrated with  $^{11}\text{C}$ -flumazenil after administration of tiagabine, in 17 off-medication patients with schizophrenia and 22 healthy comparison subjects [77]. Finally, anecdotal evidence suggests that serotonin PET imaging could also be interesting to assess buspirone efficacy in PD [73].

## 5. Discussion

As PET has become increasingly available and as the range of available brain radioligands continues to expand, the use of PET neuroimaging has increased in drug development assessment in recent years. To date, the neurotransmitter system which has been most widely studied in humans is the dopaminergic system, mainly explored in movement disorders notably, thanks to  $^{18}\text{F}$ -DOPA or even  $^{11}\text{C}$ -raclopride. These dopaminergic relevant biomarkers allowed to improve our knowledge about why PD patients develop daily fluctuations in mobility and troublesome involuntary movements after several years of dopamine

replacement therapy. In vivo dopamine imaging could also help to improve PD patient selection in future clinical trials by selecting those with better predicted outcomes. Another physiopathological approach has surged recently with the development of PET amyloid radioligands. Developed and approved for clinical use as important diagnosis and prognostic biomarkers for AD or mild cognitive impairment (MCI) patients, amyloid tracers are also being used to evaluate therapeutic interventions. Thus far, clinical trials of promising treatment for AD have failed to significantly stop the disease progression [78]. Surprisingly, while almost all research effort has been focused on anti-amyloid therapy for AD, a recent PET study shows that the alteration of cognitive capability is independent of brain amyloid accumulation, and thus, also other physiopathological ways have to be explored to try to reduce AD progression [30].

Thus, it may be of interest to provide perspectives on new targets for which PET tracers are currently under development and which are also considered relevant for therapeutic management of NDD:

- (i) Purinergic ion channel receptors, and especially P2X7 receptor (P2X7R), are known to be overexpressed in activated microglia in animal models of neurodegenerative diseases, such as AD [79], ALS [80], or HD [81], and might be a promising target to assess therapeutics, especially since the GSK1482160, a strong P2X7R antagonist, has been evaluated in Phase 1 clinical study by GSK company [82]. Labeled with carbon-11,  $^{11}\text{C}$ -GSK1482160 is a promising radioligand for neuroinflammation PET imaging, and one would think that this P2X7R antagonist could be an excellent candidate for a theranostic approach.
- (ii) Regarding the protein accumulation, three major types of aggregated hyperphosphorylated proteins (amyloid-beta, tau, and alpha-synuclein ( $\alpha$ -syn)) are involved in the pathogenesis of a variety of neurodegenerative diseases, referred to as proteinopathies. Indeed, PD, Lewy body dementia, and multisystem atrophy are part of a family called synucleinopathies. We have described the importance of amyloid-beta and tau tracers and the criticality of developing selective PET tracers for each type of aggregate above, in order to assess their relative contribution in pathogenesis.  $\alpha$ -Syn appears undoubtedly to be an excellent target for PET radiotracer development for PD and other synucleinopathies.  $\alpha$ -Synuclein inclusions (Lewy bodies) appear before dopaminergic changes, (i.e., premotor PD) so imaging  $\alpha$ -syn could better predict premotor PD [83]. While success in the development of selective  $\alpha$ -syn PET imaging agents has not been realized yet,  $\alpha$ -syn radiotracer could be a potentially useful surrogate marker in clinical trials. Work is ongoing in multiple laboratories throughout the world, and AC Immune and Biogen companies have identified two lead compounds designed to selectively bind to  $\alpha$ -syn aggregates.
- (iii) As mentioned earlier, numerous neurotransmitter systems have been identified and allowed to assess

therapeutics. Among them, the cholinergic system could be of interest for the follow-up of NDD and their treatment. Degeneration of cholinergic neurons is well described in pathophysiology of AD and is associated in several reports with a significant loss of  $\alpha 7$  nicotinic acetylcholine receptor ( $\alpha 7$ -nAChRs) in the cortex and hippocampus of patients.  $\alpha 7$ -nAChR mediates various brain functions and represents an important target for drug discovery. In clinical trials with selective  $\alpha 7$  agonists, activation of the receptor improved cognitive performance in patients with schizophrenia [84]. The recently developed  $^{18}\text{F}$ -ASEM, a highly  $\alpha 7$ -nAChR specific and selective radiotracer for brain PET, opens new horizons for studying  $\alpha 7$ -nAChRs in the living human brain.

Finally, PET imaging in NDD therapeutic development assessment can lead to (i) the study of the role and density of receptor involved, (ii) the study of the mechanism of action of therapeutic drug, and (iii) the optimization of new treatment development by reducing costs and the time required for new drug development.

Nevertheless, the expansion of PET imaging as a reliable biomarker for in vivo treatment evaluation faces the critical lack of effective treatment for NDD patients, especially for AD. Concurrently, new potential applications of these radiotracers initially developed for central application have shown their interest in the field of personalized medicine in numerous peripheral diseases, including cancer.  $^{18}\text{F}$ -DOPA illustrates this concept since it is a well-known excellent tracer for imaging neuroendocrine tumors (NETs), including pheochromocytoma, extraadrenal paraganglioma, medullary thyroid carcinoma, gastro-entero-pancreatic (GEP), or NE tumors (reviewed in [85]). In NET,  $^{18}\text{F}$ -DOPA may be particularly useful in patients with negative  $^{68}\text{Ga}$ -somatostatin analogs. More recently, TSPO PET imaging has been shown to assume a promising involvement in the development of diagnostic strategies in cancer. More recently, TSPO has been introduced as a possible molecular target for peripheral sterile inflammatory diseases PET imaging, making this protein a potential biomarker with the aim of addressing disease heterogeneity, assisting in patient stratification, and contributing to predicting treatment response [86–88]. Finally, amyloid tracers such as  $^{18}\text{F}$ -florbetapir or  $^{11}\text{C}$ -PIB may be promising PET radiotracers for imaging amyloid deposit in cardiac amyloidosis [89, 90], considering that they also exhibit specific affinity for myocardial amyloid fibers.

It would be consider that this field of investigation will grow up in the context of personalized and/or stratified medicine.

## 6. Conclusion

This paper has reviewed findings from PET neuroimaging studies which have contributed to assess efficacy of drugs in NDD. In the last decades, molecular imaging with PET led to the progress in the development of new drugs, thanks to multiple molecular probes imaging biological, functional, and pathological conditions of NDD. Brain PET imaging allows a multiple approach of the disease by assessing several

physiopathological pathways like neuroinflammation, neurotransmission, or protein aggregation in the disease. This multiple approach allows to assess drug efficacy from different perspectives and forms the link between clinical and physiopathological conditions. Complementary to the recent concept called “theranostics” referring to the use of molecular targeting vectors labeled either with diagnostic or therapeutic radionuclides for diagnosis and therapy, respectively, brain PET imaging seems to be a relevant and attractive tool in SNC drug development that could help in therapeutic decision-making within the growing framework of precision medicine.

## Conflicts of Interest

The authors declare no conflicts of interest.

## Acknowledgments

This study was supported by the French National Agency for Research (“Investissements d’Avenir” no. ANR-11-LABX-0018-01), IRON and the European Union’s Seventh Framework Programme (FP7/2004–2013) under grant agreement no. 278850 (INMiND).

## References

- [1] C. Reitz and R. Mayeux, “Alzheimer disease: epidemiology, diagnostic criteria, risk factors and biomarkers,” *Biochemical Pharmacology*, vol. 88, no. 4, pp. 640–651, 2014.
- [2] A. Drzezga, H. Barthel, S. Minoshima, and O. Sabri, “Potential clinical applications of PET/MR imaging in neurodegenerative diseases,” *Journal of Nuclear Medicine*, vol. 55, no. 2, pp. 47S–55S, 2014.
- [3] G. Kovacs and H. Budka, “Current concepts of neuropathological diagnostics in practice: neurodegenerative diseases,” *Clinical Neuropathology*, vol. 29, no. 9, pp. 271–288, 2010.
- [4] W. W. Che, X. Zhang, and W. J. Huang, “Role of neuroinflammation in neurodegenerative diseases (review),” *Molecular Medicine Reports*, vol. 13, no. 4, pp. 3391–3396, 2016.
- [5] K. Herholz, “FDG PET and differential diagnosis of dementia,” *Alzheimer Disease and Associated Disorders*, vol. 9, no. 1, pp. 6–16, 1995.
- [6] F. Squitieri, S. Orobello, M. Cannella et al., “Riluzole protects Huntington disease patients from brain glucose hypometabolism and grey matter volume loss and increases production of neurotrophins,” *European Journal of Nuclear Medicine and Molecular Imaging*, vol. 36, no. 7, pp. 1113–1120, 2009.
- [7] J. Bennett, J. Burns, P. Welch, and R. Bothwell, “Safety and tolerability of R(+) pramipexole in mild-to-moderate Alzheimer’s disease,” *Journal of Alzheimer’s Disease*, vol. 49, no. 4, pp. 1179–1187, 2016.
- [8] S. Tzimopoulou, V. J. Cunningham, T. E. Nichols et al., “A multi-center randomized proof-of-concept clinical trial applying [18F] FDG-PET for evaluation of metabolic therapy with rosiglitazone XR in mild to moderate Alzheimer’s disease,” *Journal of Alzheimer’s Disease*, vol. 22, no. 4, pp. 1241–1256, 2010.
- [9] M. Auffret, F. Le Jeune, A. Maurus et al., “Apomorphine pump in advanced Parkinson’s disease: effects on motor and nonmotor symptoms with brain metabolism correlations,” *Journal of the Neurological Sciences*, vol. 372, pp. 279–287, 2017.

- [10] H. Yoshimuta, M. Nakamura, E. Kanda et al., "The effects of olanzapine treatment on brain regional glucose metabolism in neuroleptic-naive first-episode schizophrenic patients," *Human Psychopharmacology: Clinical and Experimental*, vol. 31, no. 6, pp. 419–426, 2016.
- [11] M. S. Buchsbaum, M. M. Haznedar, J. Aronowitz et al., "FDG-PET in never-previously medicated psychotic adolescents treated with olanzapine or haloperidol," *Schizophrenia Research*, vol. 94, no. 1–3, pp. 293–305, 2007.
- [12] V. Molina, J. D. Gispert, S. Reig et al., "Olanzapine-induced cerebral metabolic changes related to symptom improvement in schizophrenia," *International Clinical Psychopharmacology*, vol. 20, no. 1, pp. 13–18, 2005.
- [13] M. Reivich, D. Kuhl, A. Wolf et al., "The [18F]fluorodeoxyglucose method for the measurement of local cerebral glucose utilization in man," *Circulation Research*, vol. 44, no. 1, pp. 127–137, 1979.
- [14] L. Picanço, P. Ozela, M. F. Brito Brito et al., "Alzheimer's disease: A review from the pathophysiology to diagnosis, new perspectives for pharmacological treatment," *Current Medicinal Chemistry*, vol. 23, no. 999, p. 1, 2016.
- [15] Y. F. Tai, "Applications of positron emission tomography (PET) in neurology," *Journal of Neurology, Neurosurgery & Psychiatry*, vol. 75, pp. 669–676, 2004.
- [16] J. M. Lehmann, L. B. Moore, T. A. Smith-Oliver, W. O. Wilkison, T. M. Willson, and S. A. Kliewer, "An antidiabetic thiazolidinedione is a high affinity ligand for peroxisome proliferator-activated receptor gamma (PPAR gamma)," *Journal of Biological Chemistry*, vol. 270, no. 22, pp. 12953–12956, 1995.
- [17] G. S. Watson, B. A. Cholerton, M. A. Reger et al., "Preserved cognition in patients with early Alzheimer disease and amnesic mild cognitive impairment during treatment with rosiglitazone: a preliminary study," *American Journal of Geriatric Psychiatry*, vol. 13, no. 11, pp. 950–958, 2005.
- [18] M. E. Risner, A. M. Saunders, J. F. B. Altman et al., "Rosiglitazone in Alzheimer's Disease Study Group Efficacy of rosiglitazone in a genetically defined population with mild-to-moderate Alzheimer's disease," *Pharmacogenomics Journal*, vol. 6, no. 4, pp. 246–254, 2006.
- [19] M. Gold, C. Alderton, M. Zvartau-Hind et al., "Rosiglitazone monotherapy in mild-to-moderate Alzheimer's disease: results from a randomized, double-blind, placebo-controlled phase III study," *Dementia and Geriatric Cognitive Disorders*, vol. 30, no. 2, pp. 131–146, 2010.
- [20] C. Harrington, S. Sawchak, C. Chiang et al., "Rosiglitazone does not improve cognition or global function when used as adjunctive therapy to AChE inhibitors in mild-to-moderate Alzheimer's disease: two phase 3 studies," *Current Alzheimer Research*, vol. 8, no. 5, pp. 592–606, 2011.
- [21] F. Squitieri, A. Ciammola, C. Colonnese, and A. Ciarmiello, "Neuroprotective effects of riluzole in Huntington's disease," *European Journal of Nuclear Medicine and Molecular Imaging*, vol. 35, no. 1, pp. 221–222, 2008.
- [22] A. Bergerot, P. J. Shortland, P. Anand, S. P. Hunt, and T. Carlstedt, "Co-treatment with riluzole and GDNF is necessary for functional recovery after ventral root avulsion injury," *Experimental Neurology*, vol. 187, no. 2, pp. 359–366, 2004.
- [23] M. Carbone, S. Duty, and M. Rattray, "Riluzole elevates GLT-1 activity and levels in striatal astrocytes," *Neurochemistry International*, vol. 60, no. 1, pp. 31–38, 2012.
- [24] D. H. Mathalon, E. V. Sullivan, K. O. Lim, and A. Pfefferbaum, "Progressive brain volume changes and the clinical course of schizophrenia in men: a longitudinal magnetic resonance imaging study," *Archives of General Psychiatry*, vol. 58, no. 2, pp. 148–157, 2001.
- [25] J. O. Rinne, D. J. Brooks, M. N. Rossor et al., "11C-PiB PET assessment of change in fibrillar amyloid-beta load in patients with Alzheimer's disease treated with bapineuzumab: a phase 2, double-blind, placebo-controlled, ascending-dose study," *The Lancet Neurology*, vol. 9, pp. 363–372, 2010.
- [26] M. Brody, E. Liu, J. Di et al., "A phase II, randomized, double-blind, placebo-controlled study of safety, pharmacokinetics, and biomarker results of subcutaneous bapineuzumab in patients with mild to moderate Alzheimer's disease," *Journal of Alzheimer's Disease*, vol. 54, no. 4, pp. 1509–1519, 2016.
- [27] R. Vandenberghe, J. O. Rinne, M. Boada et al., "Bapineuzumab 3000 and 3001 clinical study investigators bapineuzumab for mild to moderate Alzheimer's disease in two global, randomized, phase 3 trials," *Alzheimer's Research and Therapy*, vol. 8, no. 1, p. 18, 2016.
- [28] S. Salloway, R. Sperling, N. C. Fox et al., "Bapineuzumab 301 and 302 clinical trial investigators two phase 3 trials of bapineuzumab in mild-to-moderate Alzheimer's disease," *New England Journal of Medicine*, vol. 370, no. 4, pp. 322–333, 2014.
- [29] B. P. Imbimbo, S. Ottonello, V. Frisardi et al., "Solanezumab for the treatment of mild-to-moderate Alzheimer's disease," *Expert Review of Clinical Immunology*, vol. 8, no. 2, pp. 135–149, 2012.
- [30] X. Pan, Z. Chen, G. Fei et al., "Long-term cognitive improvement after benfotiamine administration in patients with Alzheimer's disease," *Neuroscience Bulletin*, vol. 32, no. 6, pp. 591–596, 2016.
- [31] R. S. Doody, M. Farlow, and P. S. Aisen, "Alzheimer's disease cooperative study data analysis and publication committee phase 3 trials of solanezumab and bapineuzumab for Alzheimer's disease," *New England Journal of Medicine*, vol. 370, no. 15, p. 1460, 2014.
- [32] S. Ostrowitzki, D. Deptula, L. Thurfjell et al., "Mechanism of amyloid removal in patients with Alzheimer disease treated with gantenerumab," *Archives of Neurology*, vol. 69, pp. 198–207, 2012.
- [33] F. Panza, V. Solfrizzi, B. P. Imbimbo et al., "Efficacy and safety studies of gantenerumab in patients with Alzheimer's disease," *Expert Review of Neurotherapeutics*, vol. 14, no. 9, pp. 973–986, 2014.
- [34] H. P. Hammes, X. Du, D. Edelstein et al., "Benfotiamine blocks three major pathways of hyperglycemic damage and prevents experimental diabetic retinopathy," *Nature Medicine*, vol. 9, no. 3, pp. 294–299, 2003.
- [35] E. Giacobini and G. Gold, "Alzheimer disease therapy—moving from amyloid- $\beta$  to tau," *Nature Reviews Neurology*, vol. 9, no. 12, pp. 677–686, 2013.
- [36] P. Novak, R. Schmidt, E. Kontsekova et al., "Safety and immunogenicity of the tau vaccine AADvac1 in patients with Alzheimer's disease: a randomised, double-blind, placebo-controlled, phase 1 trial," *The Lancet Neurology*, vol. 16, no. 2, pp. 123–134, 2017.
- [37] N. Okamura and K. Yanai, "Brain imaging: applications of tau PET imaging," *Nature Reviews Neurology*, vol. 13, no. 4, pp. 197–198, 2017.
- [38] K. P. Ng, T. A. Pascoal, S. Mathotaarachchi et al., "Monoamine oxidase B inhibitor, selegiline, reduces (18)F-THK5351 uptake in the human brain," *Alzheimer's Research and Therapy*, vol. 9, p. 25, 2017.
- [39] B. Hall, E. Mak, S. Cervenka, F. I. Aigbirhio, J. B. Rowe, and J. T. O'Brien, "In vivo tau PET imaging in dementia:

- pathophysiology, radiotracer quantification, and a systematic review of clinical findings,” *Ageing Research Reviews*, vol. 36, pp. 50–63, 2017.
- [40] S. Haga, K. Akai, and T. Ishii, “Demonstration of microglial cells in and around senile (neuritic) plaques in the Alzheimer brain. An immunohistochemical study using a novel monoclonal antibody,” *Acta Neuropathologica*, vol. 77, no. 6, pp. 569–575, 1989.
- [41] J. M. Craft, D. M. Watterson, and L. J. Van Eldik, “Neuroinflammation: a potential therapeutic target,” *Expert Opinion on Therapeutic Targets*, vol. 9, no. 5, pp. 887–900, 2005.
- [42] J. Butchart, L. Brook, V. Hopkins et al., “Etanercept in Alzheimer disease: a randomized, placebo-controlled, double-blind, phase 2 trial,” *Neurology*, vol. 84, no. 23, pp. 2161–2168, 2015.
- [43] R. S. Turner, R. G. Thomas, S. Craft et al., “Alzheimer’s disease cooperative study a randomized, double-blind, placebo-controlled trial of resveratrol for Alzheimer disease,” *Neurology*, vol. 85, no. 16, pp. 1383–1391, 2015.
- [44] M. E. Cudkowicz, J. M. Shefner, D. A. Schoenfeld et al., “Trial of celecoxib in amyotrophic lateral sclerosis,” *Annals of Neurology*, vol. 60, no. 1, pp. 22–31, 2006.
- [45] A. C. Dupont, B. Largeau, M. J. Santiago Ribeiro, D. Guilloteau, C. Tronel, and N. Arlicot, “Translocator protein-18 kDa (TSPO) Positron Emission Tomography (PET) imaging and its clinical impact in neurodegenerative diseases,” *International Journal of Molecular Sciences*, vol. 18, no. 4, p. 785, 2017.
- [46] R. Slavik, U. Grether, A. Müller Herde et al., “Discovery of a high affinity and selective pyridine analog as a potential positron emission tomography imaging agent for cannabinoid type 2 receptor,” *Journal of Medicinal Chemistry*, vol. 58, no. 10, pp. 4266–4277, 2015.
- [47] M. Mishina, K. Ishiwata, M. Naganawa et al., “Adenosine A(2A) receptors measured with [<sup>11</sup>C]TMSX PET in the striata of Parkinson’s disease patients,” *PLoS One*, vol. 6, no. 2, article e17338, 2011.
- [48] E. Rissanen, J. R. Virta, T. Paavilainen et al., “Adenosine A2A receptors in secondary progressive multiple sclerosis: a [<sup>11</sup>C]TMSX brain PET study,” *Journal of Cerebral Blood Flow and Metabolism*, vol. 33, no. 9, pp. 1394–1401, 2013.
- [49] I. F. Antunes, J. Doorduyn, H. J. Haisma et al., “<sup>18</sup>F-FEAnGA for PET of  $\beta$ -glucuronidase activity in neuroinflammation,” *Journal of Nuclear Medicine*, vol. 53, no. 3, pp. 451–458, 2012.
- [50] A. Takano, F. Piehl, J. Hillert et al., “In vivo TSPO imaging in patients with multiple sclerosis: a brain PET study with [<sup>18</sup>F]FEDAA1106,” *EJNMMI Research*, vol. 3, no. 1, p. 30, 2013.
- [51] J. N. Ratchford, C. J. Endres, D. A. Hammoud et al., “Decreased microglial activation in MS patients treated with glatiramer acetate,” *Journal of Neurology*, vol. 259, no. 6, pp. 1199–1205, 2012.
- [52] L. Airas, A. M. Dickens, P. Elo et al., “In vivo PET imaging demonstrates diminished microglial activation after fingolimod treatment in an animal model of multiple sclerosis,” *Journal of Nuclear Medicine*, vol. 56, no. 2, pp. 305–310, 2015.
- [53] M. Sucksdorf, E. Rissanen, J. Tuisku et al., “Evaluation of the effect of fingolimod treatment on microglial activation using serial PET imaging in multiple sclerosis,” *Journal of Nuclear Medicine*, vol. 58, no. 10, pp. 1646–1651, 2017.
- [54] R. Dodel, A. Spottke, A. Gerhard et al., “Minocycline 1-year therapy in multiple-system-atrophy: effect on clinical symptoms and [(11)C] (R)-PK11195 PET (MEMSA-trial),” *Movement Disorders*, vol. 25, no. 1, pp. 97–107, 2010.
- [55] A. L. Bartels, A. T. M. Willemsen, J. Doorduyn, E. F. J. de Vries, R. A. Dierckx, and K. L. Leenders, “[<sup>11</sup>C]-PK11195 PET: quantification of neuroinflammation and a monitor of anti-inflammatory treatment in Parkinson’s disease?,” *Parkinsonism and Related Disorders*, vol. 16, no. 1, pp. 57–59, 2010.
- [56] R. Pihlaja, J. Takkinen, O. Eskola et al., “Monoacylglycerol lipase inhibitor JZL184 reduces neuroinflammatory response in APdE9 mice and in adult mouse glial cells,” *Journal of Neuroinflammation*, vol. 12, no. 1, p. 81, 2015.
- [57] A. Jucaite, P. Svenningsson, J. O. Rinne et al., “Effect of the myeloperoxidase inhibitor AZD3241 on microglia: a PET study in Parkinson’s disease,” *Brain*, vol. 138, no. 9, pp. 2687–2700, 2015.
- [58] Z. Gao and S. E. Tsirka, “Animal models of MS reveal multiple roles of microglia in disease pathogenesis,” *Neurology Research International*, vol. 2011, Article ID 383087, 9 pages, 2011.
- [59] A. O. Dulamea, “Role of oligodendrocyte dysfunction in demyelination, remyelination and neurodegeneration in multiple sclerosis,” *Advances in Experimental Medicine and Biology*, vol. 958, pp. 91–127, 2017.
- [60] M. Matloubian, C. G. Lo, G. Cinamon et al., “Lymphocyte egress from thymus and peripheral lymphoid organs is dependent on S1P receptor 1,” *Nature*, vol. 427, no. 6972, pp. 355–360, 2004.
- [61] T. Ziemssen and W. Schrempf, “Glatiramer acetate: mechanisms of action in multiple sclerosis,” *International Review of Neurobiology*, vol. 79, pp. 537–570, 2007.
- [62] P. H. Elsinga, K. Hatano, and K. Ishiwata, “PET tracers for imaging of the dopaminergic system,” *Current Medicinal Chemistry*, vol. 13, no. 18, pp. 2139–2153, 2006.
- [63] A. Antonini and R. DeNotaris, “PET and SPECT functional imaging in Parkinson’s disease,” *Sleep Medicine*, vol. 5, no. 2, pp. 201–206, 2004.
- [64] A. Antonini, J. Schwarz, W. H. Oertel, H. F. Beer, U. D. Madeja, and K. L. Leenders, “[<sup>11</sup>C]raclopride and positron emission tomography in previously untreated patients with Parkinson’s disease: influence of L-dopa and lisuride therapy on striatal dopamine D2-receptors,” *Neurology*, vol. 44, no. 7, pp. 1325–1329, 1994.
- [65] A. Antonini, J. Schwarz, W. H. Oertel, O. Pogarell, and K. L. Leenders, “Long-term changes of striatal dopamine D2 receptors in patients with Parkinson’s disease: a study with positron emission tomography and [<sup>11</sup>C]raclopride,” *Movement Disorders*, vol. 12, no. 1, pp. 33–38, 1997.
- [66] N. Pavese, A. H. Evans, Y. F. Tai et al., “Clinical correlates of levodopa-induced dopamine release in Parkinson disease: a PET study,” *Neurology*, vol. 67, no. 9, pp. 1612–1617, 2006.
- [67] F. Niccolini, L. Rocchi, and M. Politis, “Molecular imaging of levodopa-induced dyskinesias,” *Cellular and Molecular Life Sciences*, vol. 72, no. 11, pp. 2107–2117, 2015.
- [68] R. de la Fuente-Fernández, P. K. Pal, F. J. Vingerhoets et al., “Evidence for impaired presynaptic dopamine function in parkinsonian patients with motor fluctuations,” *Journal of Neural Transmission*, vol. 107, no. 1, pp. 49–57, 2000.
- [69] G. K. Wenning, P. Odin, P. Morrish et al., “Short- and long-term survival and function of unilateral intrastriatal dopaminergic grafts in Parkinson’s disease,” *Annals of Neurology*, vol. 42, no. 1, pp. 95–107, 1997.
- [70] C. R. Freed, P. E. Greene, R. E. Breeze et al., “Transplantation of embryonic dopamine neurons for severe Parkinson’s disease,” *New England Journal of Medicine*, vol. 344, no. 10, pp. 710–719, 2001.
- [71] C. W. Olanow, C. G. Goetz, J. H. Kordower et al., “A double-blind controlled trial of bilateral fetal nigral transplantation in Parkinson’s disease,” *Annals of Neurology*, vol. 54, no. 3, pp. 403–414, 2003.

- [72] M. Politis and P. Piccini, "In vivo imaging of the integration and function of nigral grafts in clinical trials," *Progress in Brain Research*, vol. 200, pp. 199–220, 2012.
- [73] M. Politis and P. Piccini, "Brain imaging after neural transplantation," *Progress in Brain Research*, vol. 184, pp. 193–203, 2010.
- [74] S. Sturm, A. Forsberg, S. Nave et al., "Positron emission tomography measurement of brain MAO-B inhibition in patients with Alzheimer's disease and elderly controls after oral administration of sebragiline," *European Journal of Nuclear Medicine and Molecular Imaging*, vol. 44, no. 3, pp. 382–391, 2017.
- [75] A. Kadir, T. Darreh-Shori, O. Almkvist et al., "PET imaging of the in vivo brain acetylcholinesterase activity and nicotine binding in galantamine-treated patients with AD," *Neurobiology of Aging*, vol. 29, no. 8, pp. 1204–1217, 2008.
- [76] P. R. A. Stokes, J. F. Myers, N. J. Kalk et al., "Acute increases in synaptic GABA detectable in the living human brain: a [11C] Ro15-4513 PET study," *Neuroimage*, vol. 99, pp. 158–165, 2014.
- [77] W. G. Frankle, R. Y. Cho, K. M. Prasad et al., "In vivo measurement of GABA transmission in healthy subjects and schizophrenia patients," *American Journal of Psychiatry*, vol. 172, no. 11, pp. 1148–1159, 2015.
- [78] A. Mallik, A. Drzezga, and S. Minoshima, "Clinical amyloid imaging," *Seminars in Nuclear Medicine*, vol. 47, no. 1, pp. 31–43, 2017.
- [79] L. K. Parvathenani, S. Tertysnikova, and C. R. Greco, "P2X7 mediates superoxide production in primary microglia and is up-regulated in a transgenic mouse model of Alzheimer's disease," *Journal of Biological Chemistry*, vol. 278, no. 15, pp. 13309–13317, 2003.
- [80] Y. Yiangou, P. Facer, and P. Durrenberger, "COX-2, CB2 and P2X7-immunoreactivities are increased in activated microglial cells/macrophages of multiple sclerosis and amyotrophic lateral sclerosis spinal cord," *BMC Neurology*, vol. 6, no. 1, p. 12, 2006.
- [81] M. Díaz-Hernández, M. Díez-Zaera, and J. Sánchez-Nogueiro, "Altered P2X7-receptor level and function in mouse models of Huntington's disease and therapeutic efficacy of antagonist administration," *FASEB Journal*, vol. 23, no. 6, pp. 1893–1906, 2009.
- [82] Z. Ali, B. Laurijssens, and T. Ostefeld, "Pharmacokinetic and pharmacodynamic profiling of a P2X7 receptor allosteric modulator GSK1482160 in healthy human subjects," *British Journal of Clinical Pharmacology*, vol. 75, no. 1, pp. 197–207, 2013.
- [83] D. W. Dickson, H. Braak, and J. E. Duda, "Neuropathological assessment of Parkinson's disease: refining the diagnostic criteria," *The Lancet Neurology*, vol. 8, no. 12, pp. 1150–1157, 2009.
- [84] D. F. Wong, H. Kuwabara, and A. G. Horti, "PET Brain imaging of  $\alpha 7$ -nAChR with [ $^{18}$ F]ASEM: reproducibility, occupancy, receptor density, and changes in schizophrenia," *International Journal of Neuropsychopharmacology*, 2018, In press.
- [85] S. Balogova, J. N. Talbot, and V. Nataf, "18F-fluorodihydroxyphenylalanine vs other radiopharmaceuticals for imaging neuroendocrine tumours according to their type," *European Journal of Nuclear Medicine and Molecular Imaging*, vol. 40, no. 6, pp. 943–966, 2013.
- [86] M. N. Tantawy, H. Charles Manning, and T. E. Peterson, "Translocator protein PET imaging in a preclinical prostate cancer model," *Molecular Imaging and Biology*, vol. 20, no. 2, pp. 200–204, 2017.
- [87] B. Zinnhardt, H. Pigeon, and B. Thézé, "Combined PET imaging of the inflammatory tumor microenvironment identifies margins of unique radiotracer uptake," *Cancer Research*, vol. 77, no. 8, pp. 1831–1841, 2017.
- [88] A. R. Awde, R. Boisgard, and B. Thézé, "The translocator protein radioligand 18F-DPA-714 monitors antitumor effect of erufosine in a rat 9L intracranial glioma model," *Journal of Nuclear Medicine*, vol. 54, no. 12, pp. 2125–2131, 2013.
- [89] S. Dorbala, D. Vangala, and J. Semer, "Imaging cardiac amyloidosis: a pilot study using 18F-florbetapir positron emission tomography," *Imaging Cardiac Amyloidosis*, vol. 41, no. 9, pp. 1652–1662, 2014.
- [90] B. Pilebro, S. Arvidsson, and P. Lindqvist, "Positron emission tomography (PET) utilizing Pittsburgh compound B (PIB) for detection of amyloid heart deposits in hereditary transthyretin amyloidosis (ATTR)," *Journal of Nuclear Cardiology*, vol. 25, no. 1, pp. 240–248, 2016.

## Research Article

# Multimodality Molecular Imaging-Guided Tumor Border Delineation and Photothermal Therapy Analysis Based on Graphene Oxide-Conjugated Gold Nanoparticles Chelated with Gd

Xibo Ma,<sup>1</sup> Yushen Jin,<sup>1</sup> Yi Wang,<sup>1,2</sup> Shuai Zhang,<sup>1,3</sup> Dong Peng,<sup>1</sup>  
Xin Yang,<sup>1</sup> Shoushui Wei,<sup>3</sup> Wei Chai,<sup>2</sup> Xuejun Li ,<sup>4</sup> and Jie Tian <sup>1</sup>

<sup>1</sup>CAS Key Laboratory of Molecular Imaging, Institute of Automation, Chinese Academy of Sciences, Beijing 100190, China

<sup>2</sup>Department of Orthopedics, Chinese PLA General Hospital, Beijing 100853, China

<sup>3</sup>Institute of Biomedical Engineering, School of Control Science and Engineering, Shandong University, Jinan, Shandong 250061, China

<sup>4</sup>Department of Neurosurgery, Xiangya Hospital, Central South University, Changsha 410008, China

Correspondence should be addressed to Xuejun Li; lxjneuro@csu.edu.cn and Jie Tian; tian@ieee.org

Received 20 December 2017; Accepted 28 March 2018; Published 7 May 2018

Academic Editor: Yuebing Wang

Copyright © 2018 Xibo Ma et al. This is an open access article distributed under the Creative Commons Attribution License, which permits unrestricted use, distribution, and reproduction in any medium, provided the original work is properly cited.

Tumor cell complete extinction is a crucial measure to evaluate antitumor efficacy. The difficulties in defining tumor margins and finding satellite metastases are the reason for tumor recurrence. A synergistic method based on multimodality molecular imaging needs to be developed so as to achieve the complete extinction of the tumor cells. In this study, graphene oxide conjugated with gold nanostars and chelated with Gd through 1,4,7,10-tetraazacyclododecane-N,N',N,N'-tetraacetic acid (DOTA) (GO-AuNS-DOTA-Gd) were prepared to target HCC-LM3-fluc cells and used for therapy. For subcutaneous tumor, multimodality molecular imaging including photoacoustic imaging (PAI) and magnetic resonance imaging (MRI) and the related processing techniques were used to monitor the pharmacokinetics process of GO-AuNS-DOTA-Gd in order to determine the optimal time for treatment. For orthotopic tumor, MRI was used to delineate the tumor location and margin *in vivo* before treatment. Then handheld photoacoustic imaging system was used to determine the tumor location during the surgery and guided the photothermal therapy. The experiment result based on orthotopic tumor demonstrated that this synergistic method could effectively reduce tumor residual and satellite metastases by 85.71% compared with the routine photothermal method without handheld PAI guidance. These results indicate that this multimodality molecular imaging-guided photothermal therapy method is promising with a good prospect in clinical application.

## 1. Introduction

Hepatocellular carcinoma (HCC) is the second most common cancer for death rate in the world and claims more than 700000 lives per year worldwide [1]. With advances in surgical techniques (resection, transplantation, and thermal ablation) and imaging techniques, 30% of patients are diagnosed and cured at early stage [2]. However, the management of 70% of patients with more-advanced stages remains challenging [3]. Besides surgical method, photothermal therapy

has garnered the attention because of its tumor destruction ability [4]. Photothermal therapy utilizes photosensitizers to convert light to heat, which could destroy the tumor tissues. Cancer cells take up the photosensitizers, resulting in cell death because of photoablation. To avoid nonspecific heating of healthy cells, photosensitizers must be selectively taken up by cancer cells.

Therefore, designing a high absorption photosensitizer is essential to generate as much heat as possible from optical energy for photothermal therapy. In recent years, graphene

oxide (GO) garnered the attention as a promising material for biomedical applications as a photoabsorber for photothermal therapy and photoacoustic imaging (PAI) due to its superior optical absorption in the NIR and high photothermal conversion efficiency and nanocarrier feature through the  $\pi$ - $\pi$  stacking between drugs and GO nanosheets [5–7]. Functionalized GO is widely used as an efficient theranostic agent due to the existence of sp<sup>2</sup> domain with hydroxyl, epoxy, and carboxyl groups [8]. We previously reported the ability of PLA microcapsules containing GO and Au nanoparticles as a theranostic system for multimodal imaging-guided cancer therapy [9, 10]. However, the micron scale agent cannot easily accumulate at the tumor site through the blood circulation system.

Additionally, the tumor margin must be delineated more accurately so that the treatment can be carried out more precisely to avoid damaging normal tissues. Simultaneously, the photothermal materials should accumulate to its peak value at the tumor site so that the irradiation could be initiated. Therefore, developing an effective imaging technique and analysis method is imperative to detect the tumor margin and monitor the pharmacokinetics process. Molecular imaging, especially optical molecular imaging, has been recently used to monitor the antitumor efficacy and calculate the location of orthotopic tumors [11–13]. However, single-modality imaging technique has its limitations in tumor margin delineation and precise photothermal therapy. Multimodality molecular imaging including MRI, PAI, and optical imaging combined with image processing technologies could solve the above problems.

In this study, GO-AuNS-DOTA nanoparticles chelated with Gd (GO-AuNS-DOTA-Gd) were prepared and used in photothermal therapy against HCC. MRI was used to delineate the tumor margin *in vivo* before treatment; PAI was used to monitor the pharmacokinetics process of GO-AuNS-DOTA-Gd and real-time detect the tumor location during treatment, and bioluminescent imaging was used to evaluate the antitumor therapy. Compared with the current photothermal methods, this synergistic method based on this synergistic method could improve treatment efficacy by 36.36% evaluated by BLI for subcutaneous tumor. For orthotopic tumor, this method could effectively reduce tumor residual and satellite metastases by 85.71% compared with the routine photothermal method without handheld PAI guidance.

## 2. Materials and Methods

**2.1. Materials.** Hydrogen tetrachloroaurate (III) hydrate ( $\text{HAuCl}_4 \cdot 4\text{H}_2\text{O}$ ), sodium citrate, and sodium borohydride ( $\text{NaBH}_4$ ) were obtained from Sinopharm Chemical Reagent Co., Ltd (Shanghai, China). Deionized water (DI water,  $18.2 \text{ M}\Omega/\text{cm}^2$ ) from the Milli-Q gradient system was used in all experiments. CellTiter96® AQUEOUS One Solution Cell Proliferation Assay (MTS, batch No. G358A) was purchased from Promega Company (Madison, WI, USA).

**2.2. Preparation of GO-AuNS-DOTA Nanoparticles Chelated with Gd.** The preparation of GO-AuNS-DOTA nanoparticles

chelated with Gd was carried out using the method reported in [14, 15]. Briefly,  $5 \mu\text{g}/\text{mL}$  graphene oxide was mixed with  $1200 \mu\text{L}$  of  $0.1 \text{ M}$  HEPES and then  $2.4 \mu\text{L}$  of  $\text{HAuCl}_4$  ( $0.1 \text{ M}$ ) was added to the mixture. Subsequently, GO-AuNS hybrids were centrifuged at  $5000 \text{ rpm}$  for  $10 \text{ min}$  to remove HEPES and any free gold nanostars in the supernatant. The precipitate was then resuspended in water.

To prepare the GO-AuNS-DOTA nanoparticles, GSH ( $5.0 \text{ mg}$ ) was added to the above solution with stirring overnight to form the nanoconstruct (GO-AuNS-GSH). After  $12 \text{ h}$ , the solution was centrifuged at  $5000 \text{ rpm}$  for  $10 \text{ min}$ . The precipitate was retained and DI water ( $1.0 \text{ mL}$ ) was added to redissolve the precipitate. Meanwhile, DOTA-NHS was dissolved into DI water under stirring at  $55^\circ\text{C}$ , followed by addition of  $\text{GdCl}_3 \cdot 6\text{H}_2\text{O}$  in  $5 \text{ mL}$  water. The molar ratio of Gd to DOTA-NHS was  $3:1$ ; after chelating for  $30 \text{ min}$ , the GO-AuNS-GSH was added to this solution and stirred for  $24 \text{ h}$  at room temperature to form the GO-AuNS-DOTA nanoparticles chelated with Gd (GO-AuNS-DOTA-Gd).

**2.3. Characterization of GO-AuNS-DOTA Nanoparticles.** The size distribution and zeta potential of GO-AuNS-DOTA nanoparticles were measured using a ZetaPlus dynamic light scattering instrument (Brookhaven Instruments) after dispersion of the nanoparticles at an appropriate concentration ( $200 \mu\text{g}/\text{mL}$ ). Six replicate samples of each type of vesicles were analyzed at a scatter angle of  $\theta = 90^\circ$  and a wavelength of  $660 \text{ nm}$  at room temperature.

The morphology of GO-AuNS-DOTA nanoparticles was observed by transmission electron microscopy (TEM, Tecnai™ G2 at  $200 \text{ kV}$ ). Copper grids with carbon coating were used for sample preparation. First, nanoparticles were dispersed in deionized (DI) water at  $0.2 \text{ mg}/\text{mL}$  concentration. Then,  $10 \mu\text{L}$  of nanoparticle suspension was placed on the grid and absorbed for  $30 \text{ seconds}$ . Finally, the grid was washed with DI water and dried at room temperature in a draught cupboard.

The UV-Vis-NIR absorption spectra of the GO-AuNS-DOTA nanoparticles were acquired with a UV-Vis spectrometer (Varian 4000, USA). The amount of Gd and Au in the nanoparticles was quantified by the inductively coupled plasma (ICP) analysis.

**2.4. In Vitro Photothermal Heating Experiments.** To examine the temperature elevation efficiency, different concentrations of GO-AuNS-DOTA nanoparticles dispersed in DI water were under the irradiation of an  $808 \text{ nm}$  laser with an output power of  $2 \text{ W}$ . The temperature of all samples was monitored and periodically confirmed by a digital thermometer with a thermocouple probe every  $10 \text{ seconds}$ . DI water was irradiated as a control. The heating curve was determined by plotting the measured temperatures.

To confirm the photothermal stability of GO-AuNS-DOTA nanoparticles, solutions of  $50 \mu\text{g}/\text{mL}$  GO-AuNS-DOTA nanoparticles were irradiated with an  $808 \text{ nm}$  NIR laser for  $10 \text{ min}$  (LASER ON), followed by natural cooling to room temperature without NIR laser irradiation for  $30 \text{ min}$  (LASER OFF). This cycle was repeated five times and the

heating curve of the five repeated cycles was plotted to characterize the photothermal stability of nanoparticles.

## 2.5. In Vitro Photothermal Effect against Cancer Cells

**2.5.1. Cell Culture.** Firefly luciferase- (fLuc-) labeled human HCC (HCC-LM3-fLuc) cells were cultured in Dulbecco's Modified Eagle's Medium (DMEM) supplemented with 10% fetal bovine serum (FBS), 100  $\mu\text{g}/\text{mL}$  penicillin, and 100  $\mu\text{g}/\text{mL}$  streptomycin in a humidified incubator at 37°C in a 5%  $\text{CO}_2$  atmosphere. The cells were passaged every 3-4 days.

**2.5.2. Photothermal Effect of the Nanoparticles against HCC-LM3-fLuc Cells.** Photothermal cytotoxicity of GO-AuNS-DOTA was evaluated on HCC-LM3-fLuc cells. For qualitative analysis, HCC-LM3-fLuc cells were seeded onto 6-well plate at a density of  $2 \times 10^5$  cells per well and incubated at 37°C in a humidified atmosphere containing 5%  $\text{CO}_2$  overnight. After incubation with different concentrations of GO-AuNS-DOTA nanoparticles for 4 h, the medium containing nanoparticles was replaced with fresh medium, and the cells were exposed to an 808 nm NIR laser with an output power of 2 W for 5 min. After incubation for 2 h, the cells were stained with propidium iodide (PI) to evaluate the phototherapeutic effect of the nanoparticles on cancer cells and the fluorescence images were collected with an inverted fluorescence microscope (Leica, Germany) equipped with a cooled CCD camera.

For quantitative evaluation of the phototoxicity, HCC-LM3-fLuc ( $1 \times 10^4$  cells per well) were incubated in 96-well plate and incubated overnight to allow the cells to attach to the surface of the wells. After incubation with GO-AuNS-DOTA for 4 h, the medium containing nanoparticles was replaced with fresh medium and the cells were irradiated with a diode NIR laser centered at 808 nm at an output power of 6  $\text{W}/\text{cm}^2$  for different times. After incubation for 4 h, cell viability was determined by Trypan Blue assay in quadruplicate.

**2.5.3. Tumor Models.** Balb/c mice were obtained from the Department of Experimental Animals, Peking University Health Science Center, and experiments were performed under protocols approved by the Institutional Animal Care and Use Committee at Peking University. The HCC-LM3-fLuc subcutaneous tumor-bearing mice were established by injecting  $6 \times 10^6$  cells into the right flanks and used for photothermal therapy when the tumor volume reached about 160  $\text{mm}^3$ .

## 2.6. In Vivo Target Study of GO-AuNS-DOTA-Gd and Photothermal Therapy Based on Subcutaneous Tumor Model and Multimodality Molecular Imaging

**2.6.1. In Vivo Photoacoustic Imaging.** HCC tumor-bearing mice were injected with GO-AuNS-DOTA-Gd via the tail vein (80  $\mu\text{L}$  per mouse). The probe concentration in the blood circulation and tumor was monitored by PAI. The PAI was acquired by a multispectral photoacoustic tomography

system (inVision 128, iTheraMedical GmbH, Munich, Germany). Five excitation wavelengths, 715 nm, 730 nm, 760 nm, 800 nm, and 850 nm, were applied for *in vivo* PAI in order to resolve the equation of drug distribution. The tumors were imaged at preinjection, 1, 2, 3, 5, 7, 12, and 24 h after injection of the probe. For tumor imaging, the mice were scanned from the neck to stomach with a step distance of 0.3 mm. Multispectral processing was used to unmix the signal of the target probe.

**2.6.2. In Vivo MRI and Tumor Margin Delineation and Three-Dimensional Image Processing.** *In vivo* MRI was acquired at preinjection, 2, 5, 7, and 12 h after the tail injection of the probe by an M3™ Compact High-Performance MRI System (Aspect Imaging, Industrial Area Hevel Modi'in, Israel) using 23 inner diameter solenoid coil (named Mouse Head L25 D23). The scanning parameters were set as follows: modality  $T_1$ , slice thickness: 0.8, slice gap: 0.1, TR: 6000. Simultaneously, we determined the longitudinal relaxivity of GO-AuNS-DOTA-Gd NPs under a 3.0-T MRI scanner.

After image acquisition, tumors and outline in mice were segmented according to the gray value difference and the segmented regions of interest (ROI) were visualized using 3D slicer [16]. The maximal radius was deemed to half of maximum value of the distance between two random voxels at the tumor surface, as shown in the following formula:

$$R_{\max} = \frac{1}{2} \max_{2, i, j=1:N} \sqrt{(x_i - x_j)^2 + (y_i - y_j)^2 + (z_i - z_j)^2}, \quad (1)$$

where  $(x_i, y_i, z_i)$ ,  $(x_j, y_j, z_j)$  are two random points on the surface of the segmented tumor.

The average MRI gray value of the tumor in 18 slices was calculated using Philips DICOM Viewer R3.0 SP3 [17]. The tumor volume was calculated according to the following formula:

$$V = \sum_{i=1}^N v_0 n_i, \quad (2)$$

where  $n_i$  is the number of voxels of the tumor ROI in  $i$ th slice,  $v_0$  is the volume of every voxel, and  $N = 18$  is the number of slices.

Meanwhile, the average gray value contrast ratio was used to demonstrate the discrimination ability of the probe for tumor and normal tissue, which was calculated using the following formula:

$$\text{CR} = \frac{\sum_{i=1}^N (\text{AG}_i / \text{AR}_i)}{N}, \quad (3)$$

where  $\text{AG}_i$  is the average gray value of the tumor ROI in the  $i$ th slice and  $\text{AR}_i$  is the average gray value of region around the tumor in the  $i$ th slice. Here, the region around the tumor was acquired through the following two steps.  $N = 18$  is the number of slices. First, the tumor ROI was carried out morphological dilation until the area was twice the tumor ROI, except the background. Then, the total area minus the area of tumor ROI was considered the region around tumor.

**2.6.3. In Vivo Positron Emission Computer Tomography (PET) Using  $^{18}\text{F}$ -FDG.** PET scans were acquired with a micro-PET GENISYS 4 scanner system (Sofie Biosciences, USA) after the mice received a tail-vein injection of  $^{18}\text{F}$ -FDG (100  $\mu\text{Ci}$ ). The mouse was scanned 30 minutes after injection with a 10 min static PET scan. During the scan, the mouse was anesthetized using 2% isoflurane. The image was reconstructed using a 3-dimensional maximum a priori algorithm and into 9696208 matrices with an isometric voxel size of 0.46  $\text{mm}^3$ .

**2.7. Photothermal Therapy.** Female Balb/c mice bearing HCC-LM3-fLuc tumors were divided into 8 groups (7 mice per group) when the tumor volume reached about 150  $\text{mm}^3$ . Three groups were treated with 80  $\mu\text{L}$  of GO-AuNS (GO: 2 mg/mL, Au: 1.31 mg/mL) via tail vein injection and laser treatment was carried out at 2, 5, and 12 h after injection (named (D2) group, (D5) group, and (D12) group), respectively. One group was only treated with 80  $\mu\text{L}$  of GO-AuNS via tail vein but did not receive laser treatment. Two groups were treated with 80  $\mu\text{L}$  of GO-AuNS via intratumor injection and one received laser treatment, while the other group did not. Two groups were treated with 80  $\mu\text{L}$  of 0.9% saline via tail-vein injection and one received laser treatment, while the other group did not. For the laser treatment groups, the tumors were irradiated by an optical fiber coupled with an 808 nm NIR laser (Hi-Tech Optoelectronics Co., Ltd. Beijing, China) at the power density of 0.2  $\text{W}/\text{cm}^2$  for 5 min. The temperature around the tumor after irradiation was collected by using an infrared camera.

**2.8. Orthotopic Tumor Models and Multimodality Molecular Imaging-Guided Cancer Treatment.** The 21 orthotopic tumor models were established by injecting  $2 \times 10^6$  HCC-LM3-fLuc tumor cells into the liver of each BALB/c nude mouse. The mice were randomly separated into 3 groups each consisting of 7 mice. One group (control) was injected i.v. with PBS. The other two groups (treatment) were injected i.v. with GO-AuNS-Gd on the 10th day. *In vivo* MRI was acquired at preinjection, 1, 2, 3 and 12 h after the tail injection. Photothermal therapy was conducted on all mice of the three groups. The process included the following two steps. First, the abdomen of mice was opened and the liver was exposed to the air. Then handheld photoacoustic imaging scanning was conducted on mice of one treatment group and, according to the PAI which indicated the tumor location, photothermal therapy was conducted using an optical fiber coupled 808 nm NIR laser at the power density of 0.2  $\text{W}/\text{cm}^2$  for 6 min.

**2.9. Evaluation of the Antitumor Efficacy.** After treatment, *in vivo* BLI obtained through an IVIS Spectrum imaging system (PerkinElmer, USA) was used to evaluate the antitumor efficacy. For subcutaneous tumor models, the image was acquired at the 8th minute after the injection of 100  $\mu\text{L}$  D-Luciferin (15 mg/mL) into the abdomen of the experimental mice on days 0, 2, 5, 8, 11, 15, and 20 after treatment. For orthotopic tumor models, the image was acquired on 5th

day. The antitumor efficacy was calculated according to the following:

$$\text{Antitumor efficacy} = \left(1 - \frac{\text{BI}_{\text{ex}}}{\text{BI}_{\text{control}}}\right) \times 100\%, \quad (4)$$

where  $\text{BI}_{\text{ex}}$  is the average bioluminescent intensity of mice tumors in experiment group.  $\text{BI}_{\text{control}}$  is the average bioluminescent intensity of mice tumors in control group.

**2.10. Drug Toxicity Assessment and Biodistribution Study.** For subcutaneous tumor experiments, to assess the toxicity of GO-AuNS-DOTA-Gd and photothermal efficacy, six organs including the heart, liver, spleen, lung, kidney, and tumor were harvested after euthanasia on the 21st day after tail injection and stained with hematoxylin and eosin (H&E). Mouse weight was also acquired on days 0, 2, 5, 8, 11, 15, and 20 after treatment and plotted as a weight graph in OriginPro for each group. For orthotopic tumor experiments, tumors from PBS group and probe group after treatment were harvested and stained with H&E.

For biodistribution assay, HCC-LM3-fLuc subcutaneous tumor-bearing mice were sacrificed at 2 h, 5 h, and 12 h after *i.v.* injection of GO-AuNS-DOTA-Gd (200  $\mu\text{L}$  per mice,  $n = 3$ ). Major organs including heart, liver, spleen, lung, kidney, intestines, brain, and tumor were collected, weighed, and then solubilized by aqua regia. The concentrations of Au and Gd in those tissue lysate samples were measured by inductively coupled plasma mass spectrometry (ICP). The levels of GO-AuNS-DOTA-Gd in various organs are presented as the percentage of injected dose per gram of tissue (ID  $\mu\text{g}/\text{g}$ ). In addition, the concentrations of Au and Gd in liver tumor and normal liver including above tissues based on the orthotopic tumor model were measured by ICP. The mice were sacrificed at 1 h and 12 h after *i.v.* injection of GO-AuNS-DOTA-Gd (200  $\mu\text{L}$  per mice,  $n = 3$ ).

**2.11. Statistical Analysis.** Quantitative data are expressed as mean  $\pm$  SD. Results of two sets were compared using one-way analysis of variance (ANOVA) and a Student *t*-test, and *p* values  $< 0.05$  were considered statistically significant difference.

### 3. Results

**3.1. Preparation and Characterization of the GO-AuNS-DOTA Nanoparticles.** The synthesis of GO-AuNS-DOTA-Gd nanoparticles was carried out according to Figure 1. The mean diameter of GO-AuNS-DOTA-Gd nanoparticles was 41.6 nm as determined by dynamic laser scattering (DLS) and TEM (Figures 2(a) and 2(b)) and zeta potentials of the nanoparticles in DI water and PBS (pH 7.4) were  $-17.2$  mV and  $-2.3$  mV, respectively. The amount of Gd and Au in the nanoparticles was 0.77 mg Gd and 1.31 mg Au per 2 mg GO according to (ICP) experiments, respectively.

GO-AuNS-DOTA showed a distinct absorption peak at 810 nm due to the existence of Au nanostars. UV-Vis-NIR spectra of GO-AuNS-DOTA in RPMI-1640 culture medium demonstrated (Figure 2(c)) no obvious difference in the

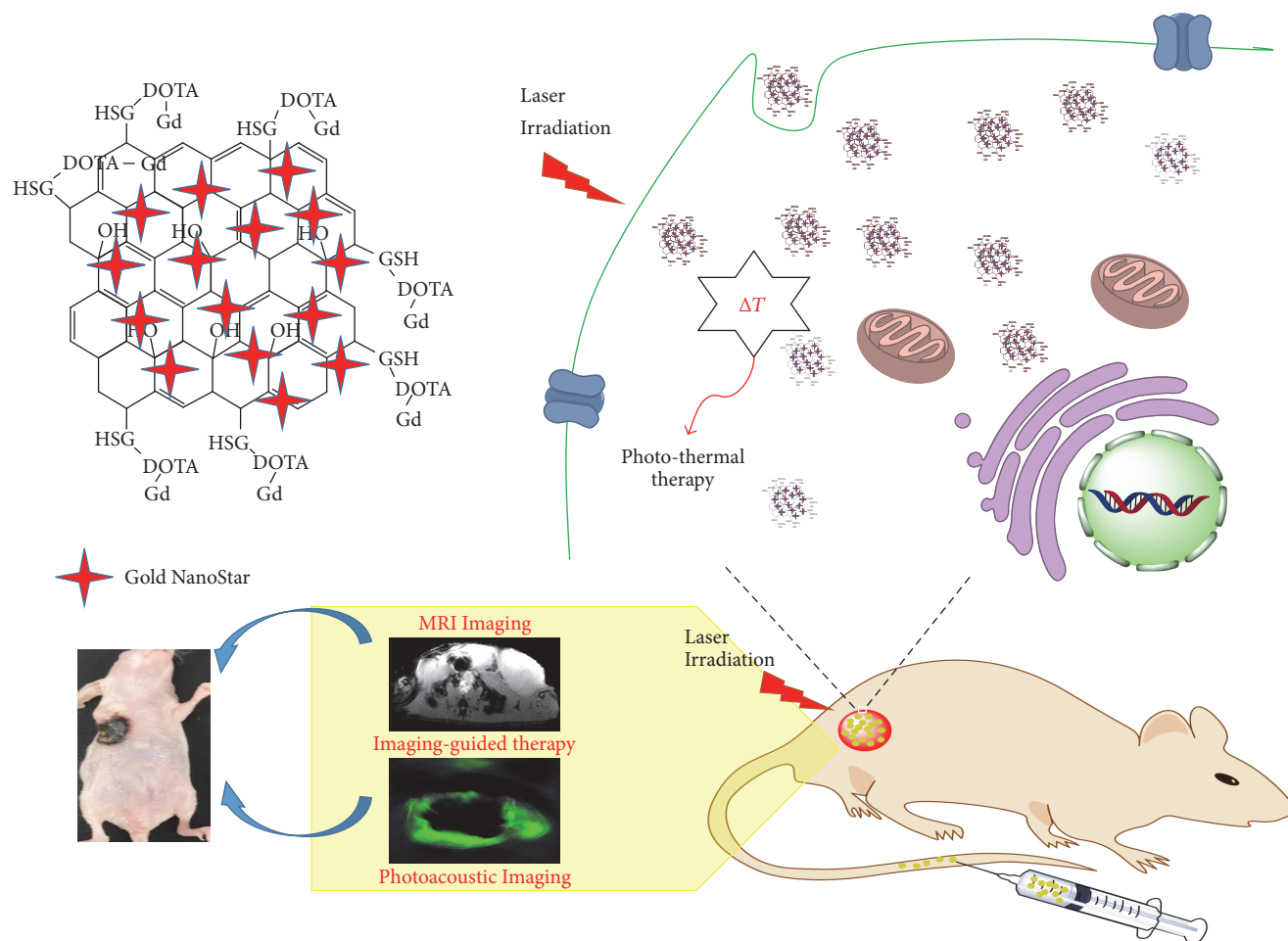


FIGURE 1: Synthesis of GO-AuNS-DOTA-Gd, imaging-guided tumor margin detection, and photothermal therapy analysis.

absorption spectra and suggested good colloidal stability of GO-AuNS-DOTA nanoparticles. Moreover, absorption increased linearly as the nanoparticle concentration increased (Figure 2(d)), indicating the excellent dispersity of GO-AuNS-DOTA nanoparticles in culture medium.

**3.2. In Vitro Photothermal Effects of GO-AuNS-DOTA Nanoparticles.** The temperature of nanoparticle solutions showed a rapid increase within 4 min of laser irradiation, and the temperature elevation rose as the nanoparticle concentration increased (Figure 3(a)). In contrast, no apparent temperature change was detected for PBS. As shown in Figure 2(b), the temperature increased 27°C after the first LASER ON and, in the next four cycles, no significant variation of temperature elevation was observed.

The result of *in vitro* photothermal experiment indicated that cancer cells in three control groups, including GO-AuNS-DOTA group, laser irradiation group, and group without any treatments, maintained their healthy state (Figure 3(c)). In contrast, cells from experimental groups with both GO-AuNS-DOTA and laser irradiation treatment showed a bright red fluorescence in the laser irradiation region, indicating that GO-AuNS-DOTA could mediate the photothermal destruction of HCC-LM3-fFluc cells.

Cell viability using MTT method (Figure 3(d)) demonstrated GO-AuNS-DOTA nanoparticles without laser irradiation exhibited little cytotoxicity on HCC-LM3-fFluc cells. In contrast, GO-AuNS-DOTA nanoparticles followed by laser irradiation (808 nm and 2 W/cm<sup>2</sup>) induced cell cytotoxicity in a dose- and time-dependent fashion.

**3.3. In Vivo Target Study of GO-AuNS-DOTA-Gd Based on Subcutaneous Tumor Model and Multimodality Molecular Imaging.** PAI and MRI were performed to investigate targeting ability of GO-AuNS-DOTA-Gd in tumor-bearing mice. Figures 4(a) and 4(c) depict drug concentration within tumor as a function of time before and after tail-vein injection of probe and quantitative analysis of the corresponding imaging using PAI. The signals in cross-sectional images of tumor region of interest (tumor ROI) started to accumulate from 2 h and reached a peak at 5 h with a nearly 2.4-fold enhancement compared with that of preinjection until 24 h in close proximity to that of preinjection.

Figures 4(b) and 4(d) depict MRI imaging and quantitative analysis of average gray of tumor ROI using MRI, respectively. The gray value in the coronal plane images of tumor ROI on 5th h obviously exceeded the value on the other three time points. The relaxivity of  $T_1$  was measured to be

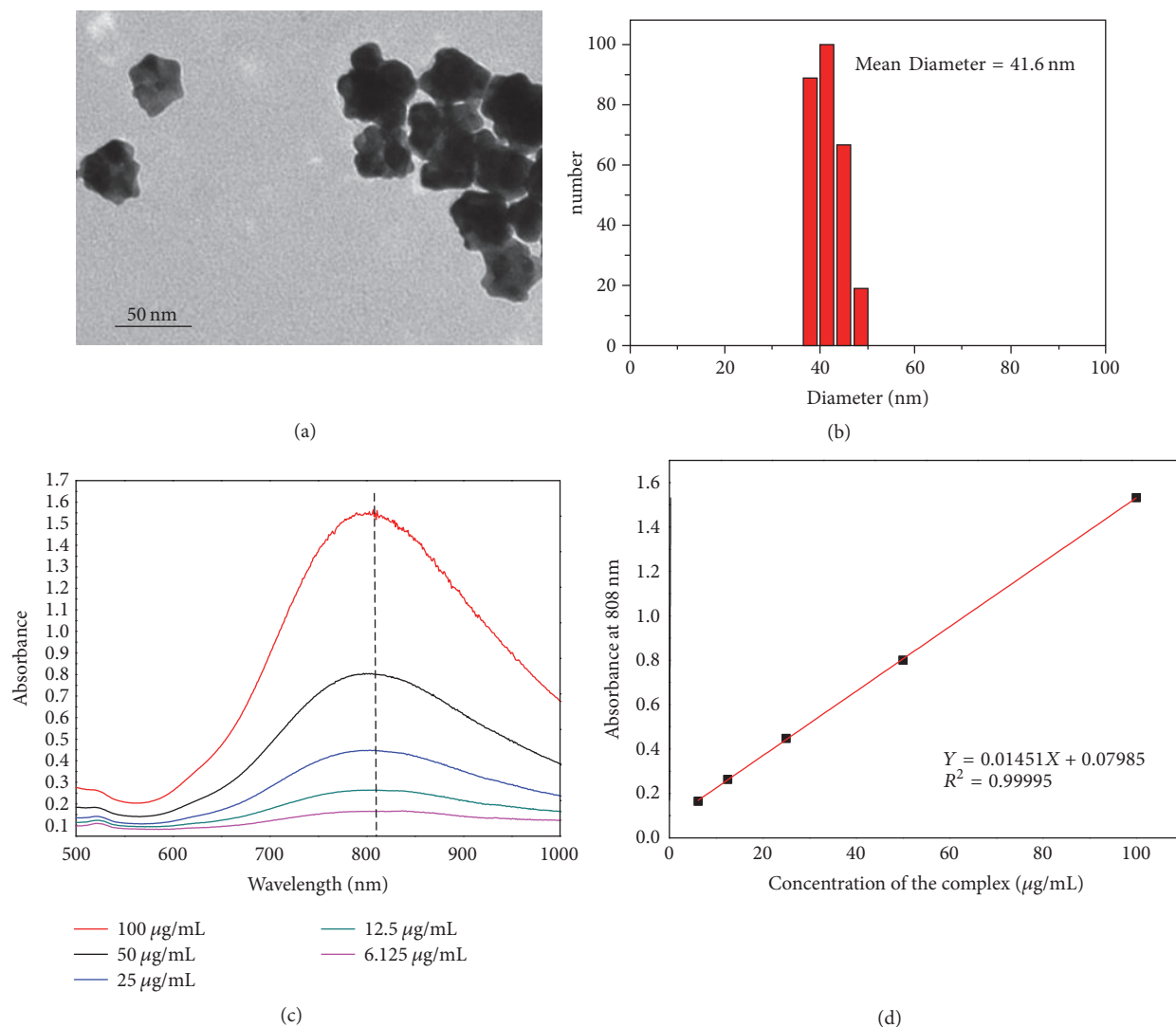


FIGURE 2: (a) TEM image of GO-AuNS-DOTA-Gd nanoparticles; (b) distribution of the nanoparticles analyzed by DLS; (c) increased UV-Vis-NIR absorption spectra of various concentrations of GO-AuNS-DOTA nanoparticles in RPMI-1640 culture medium; (d) the absorbance of GO-AuNS-DOTA-Gd nanoparticles dispersed in RPMI-1640 culture medium at 808 nm increased as the concentration increased.

TABLE 1: Maximal radius of tumor, tumor volume, and gray contrast ratio of tumor versus other tissue around the tumor based on MRI.

	Pre	2 h	5 h	12 h
Tumor volume ( $\text{mm}^3$ )	249.32	249.53	289.39	271.70
Maximal diameter (mm)	6.824	7.086	7.345	7.331
Gray contrast ratio	1.3520	1.3573	1.8533	1.5343

Note. One voxel is  $0.1 \times 0.065625 \times 1 \text{ mm}^3$  according to the MRI image.

$1.044e - 5 \mu\text{M}^{-1} \cdot \text{ms}^{-1}$  (Figures 4(f) and 4(g)). In contrast with  $^{18}\text{F}$ -FDG PET image (Figure 4(h)), the MRI image after probe injection allowed us to distinguish tumor margin from the normal tissue. To quantitatively analyze the probe's ability of tumors targeting and enhancement, the tumor was segmented and visualized using 3D slicer (Figure 4(e)). The calculated tumor volume and maximal radius on 5 h exceeded that of preinjection and on 2 h and then the value declined slowly over 5 h (Table 1). Gray contrast ratio of tumor versus

peripheral tissue on 5 h was higher than that on the other three time points. The results indicated that probe concentration in the tumor on 5 h reached a peak and presented the best ability to distinguish the tumor from normal tissues.

**3.4. In Vivo Antitumor Efficacy Evaluation Based on Image Data Analysis.** The temperature of tumor on GO-AuNS-DOTA-Gd treated mice ((D2), (D5), (D12), and (F)) reached more than  $140^\circ\text{F}$  after irradiation ((D2):  $140^\circ\text{F}$ , (D5):  $148^\circ\text{F}$ , (D12):  $145^\circ\text{F}$ , and (F):  $149^\circ\text{F}$ ), while GO-AuNS-DOTA-Gd tail-injected and intratumor injected without irradiation and all saline treated mice with and without irradiation showed no temperature increment (Figure 5(a) only shows saline control group and (D5) group). As shown in Figure 5(c), the bioluminescence intensity of the mice of (D5) and (F) groups was zero on day 5 after treatment, leaving the original tumor sites as black scars. The quantitative analysis of the eight groups demonstrated that treatment with laser irradiation on

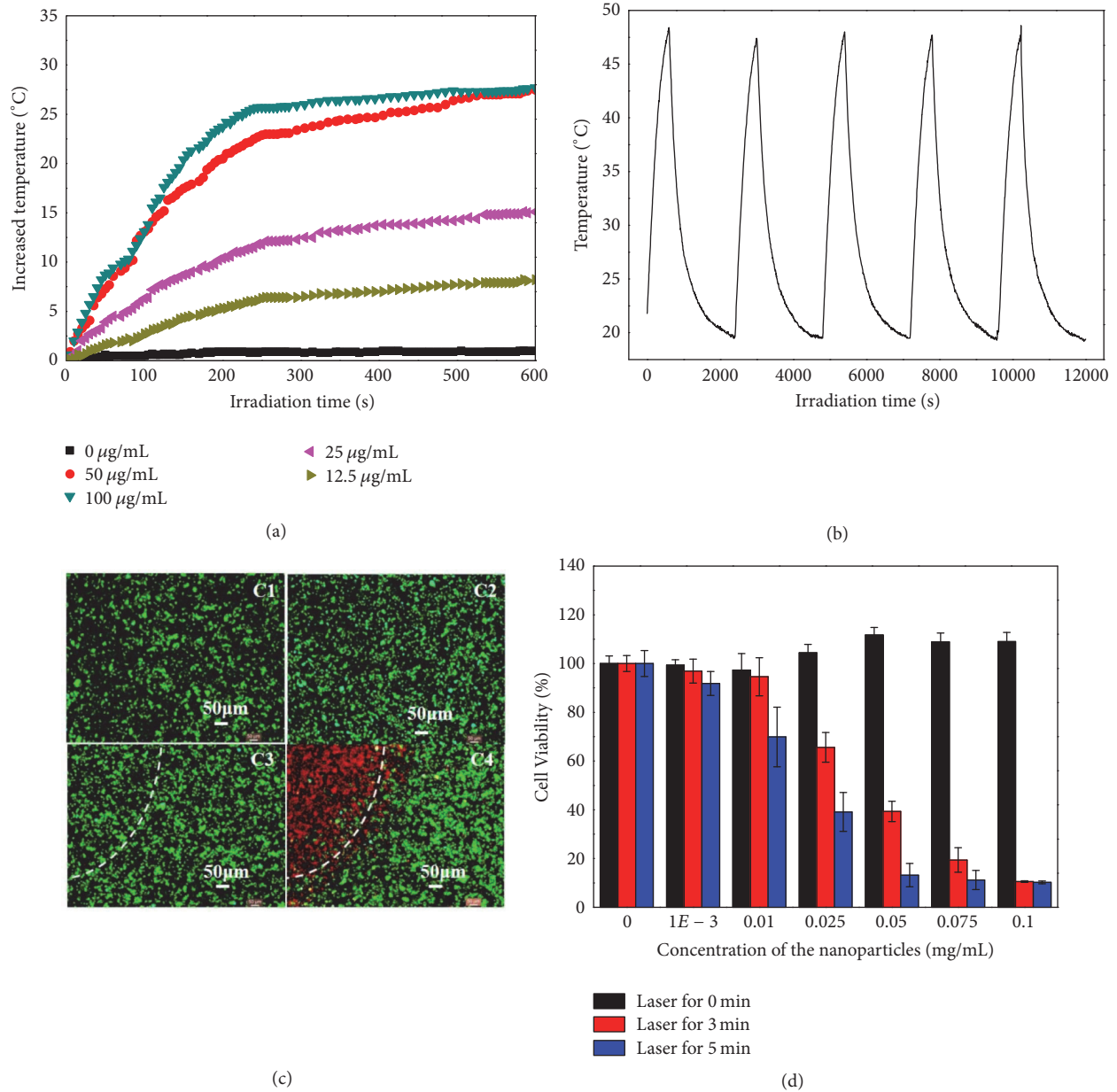
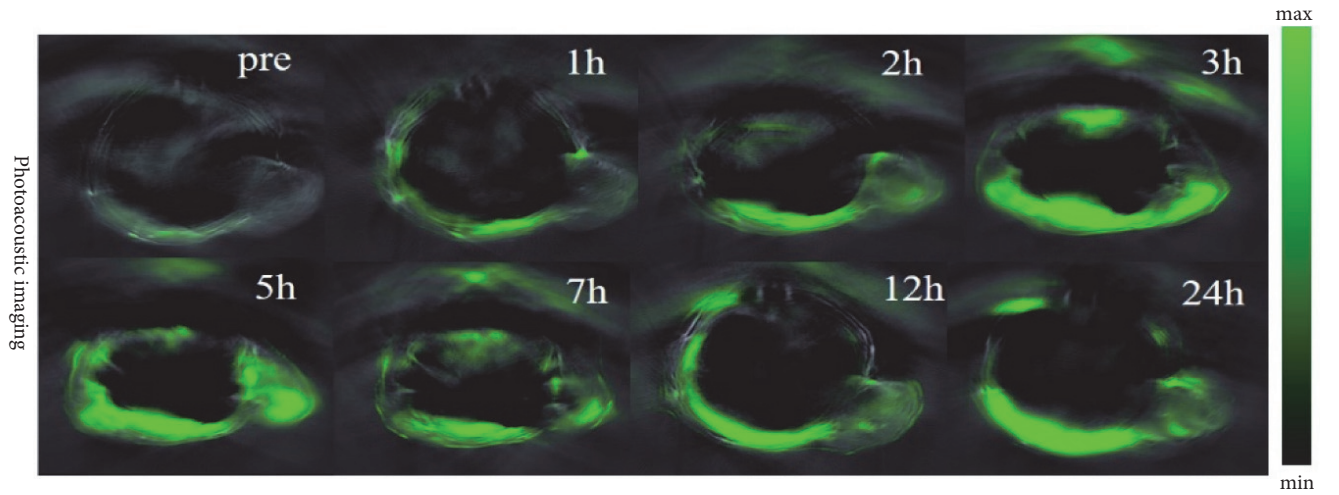


FIGURE 3: (a) Temperature elevation of aqueous solution of GO-AuNS-DOTA-Gd nanoparticles at different concentrations over 10 min under NIR laser irradiation (808 nm, 2 W) recorded every 10 seconds with a digital thermometer; (b) temperature elevation of aqueous solution of GO-AuNS-DOTA-Gd nanoparticles over five LASER ON/OFF cycles of NIR laser irradiation (808 nm, 2 W) (LASER ON time: 10 min; LASER OFF time: 30 min); (c) photothermal destruction of HCC-LM3-fLuc cells with different treatments. C1: no irradiation and no agent; C2: agent of 25 µg/mL only; C3: 5 min irradiation, no agent; C4: 5 min irradiation, agent of 25 µg/mL. White dashes indicate the laser boundary; dead cells are labeled in red, while viable cells are labeled in green; (d) cell viability after treatment with different concentrations of GO-AuNS-DOTA-Gd nanoparticles and different NIR laser irradiation time. \*\* $p < 0.01$  and \* $p < 0.05$ .

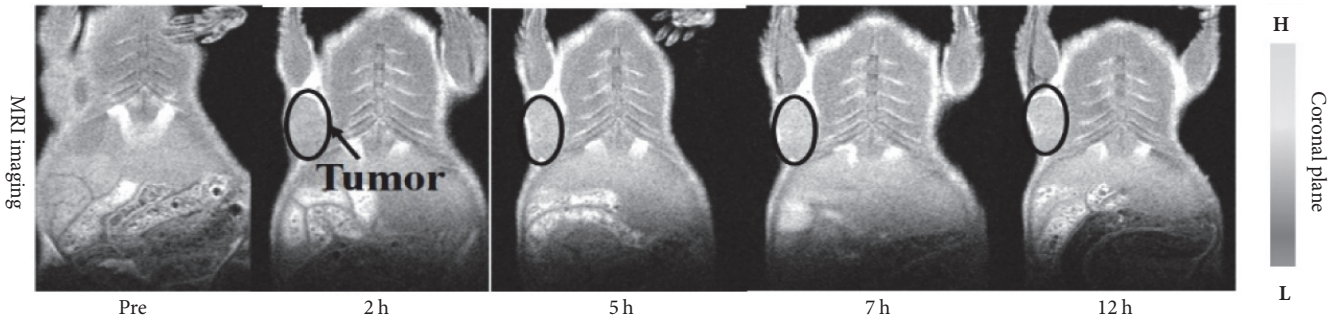
tumor at 5th h after probe injection via tail vein achieved the same antitumor effect as laser irradiation treatment on tumor after intratumor injection (Figure 5(d)). Compared with the current photothermal methods (for (D12) group, if the therapy was initiated on 12th h postinjection (7-8)), this synergistic method based on multimodality molecular imaging (for (D5) group) could improve treatment efficacy by 36.36% on 2nd day evaluated by BLI for subcutaneous tumor. Tumor growth for groups (D2) and (D12) was inhibited after

treatment until day 4 and then tumor grew slowly close to that of the other groups.

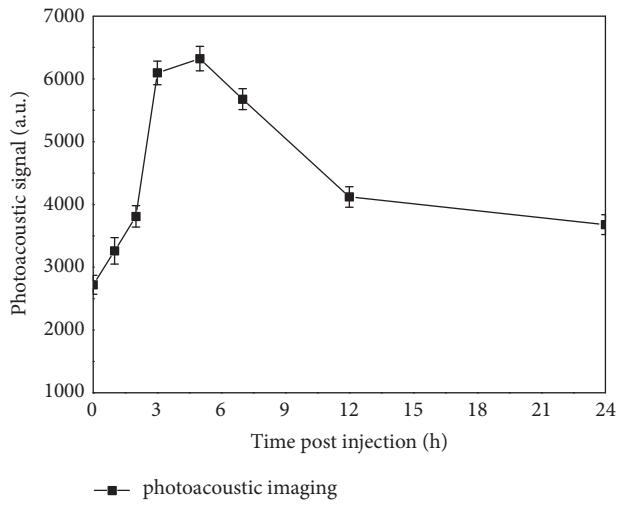
To evaluate the toxicity of the probe, body weight of mice was monitored throughout the antitumor study. None of mouse weight in the eight groups declined more than 20% of its original weight (Figure 5(e)). H&E staining of the heart, liver, spleen, lung, and kidney of the mice showed no distinct damage for all drug treatment groups (Figure 5(b), only showing (D5) group and saline control group). ICP results



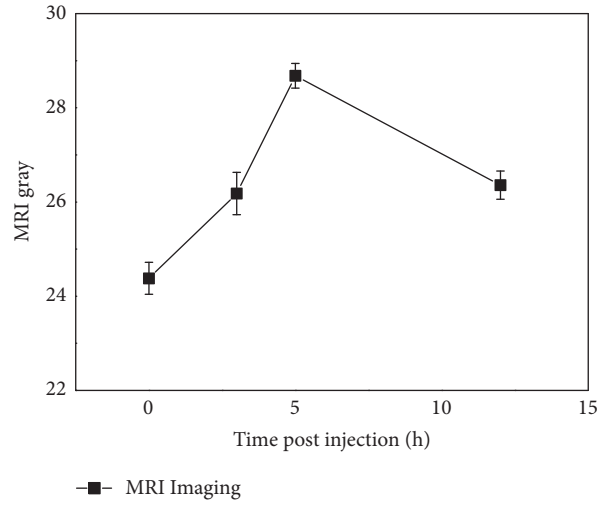
(a)



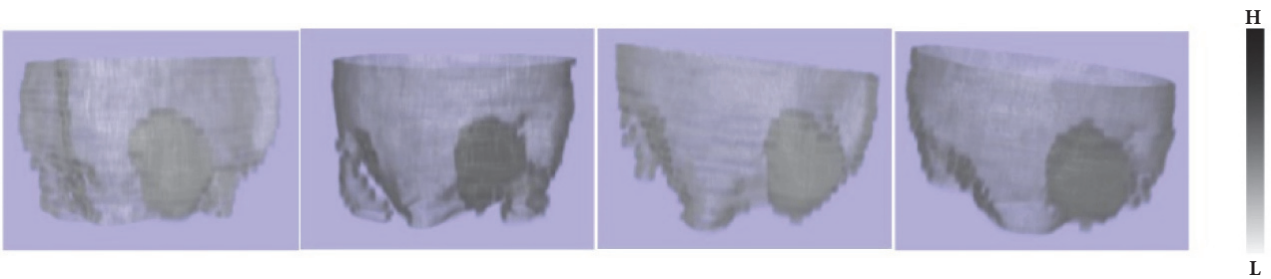
(b)



(c)



(d)



(e)

FIGURE 4: Continued.

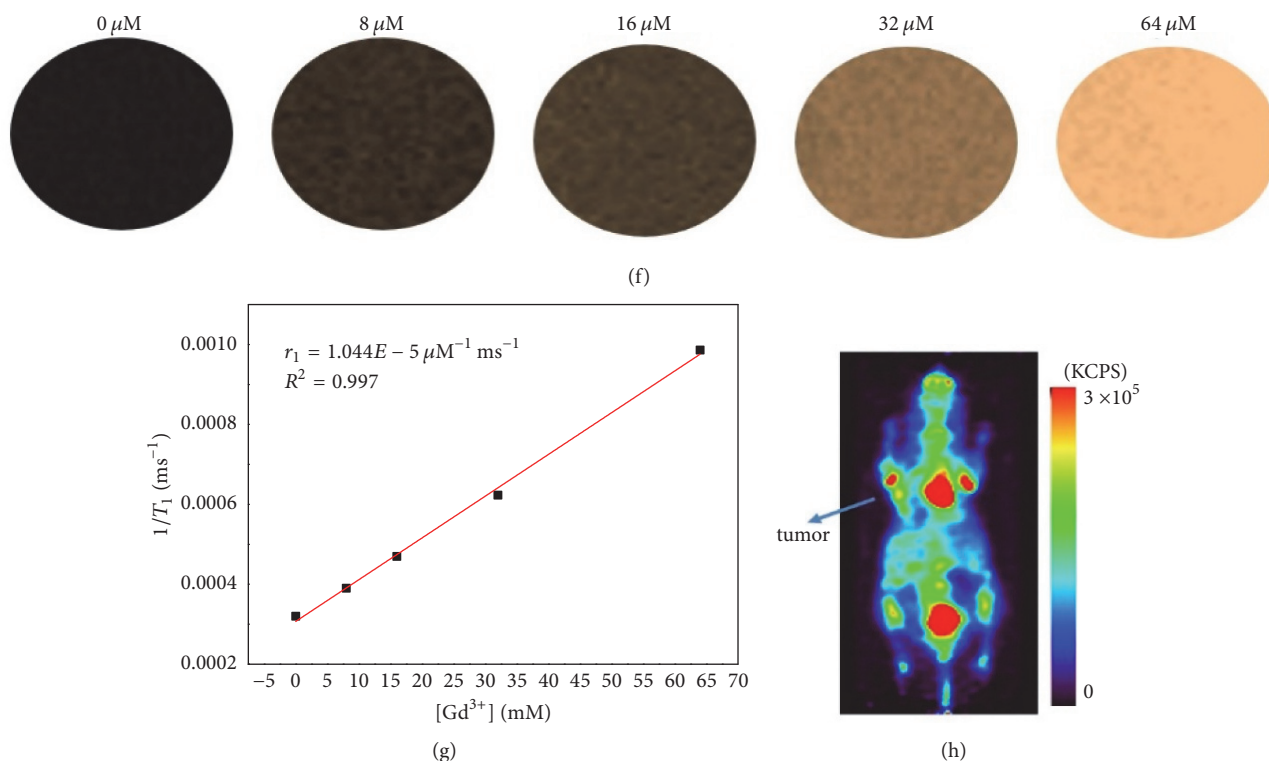


FIGURE 4: (a) Photoacoustic signal distribution of GO-AuNS-DOTA-Gd in tumor regions at different time points before and after injection; (b) MRI image of GO-AuNS-DOTA-Gd on the coronal plane in tumor regions at different time points before and after injection; (c) quantitative analysis of the PAI signal in the tumor regions; (d) quantitative analysis of MRI gray intensity in the tumor regions; (e) reconstructed 3D image and 3D visualization of tumor and its surrounding tissue based on the MRI slice images; (f) MRI image of GO-AuNS-DOTA-Gd at different concentrations; (g) linear relationship between  $T_1$  relaxation rate ( $1/T_1$ ) and  $Gd^{3+}$  concentrations in GO-AuNS-DOTA-Gd aqueous solutions; (h) representative vertical PET images of a mouse with tumor after  $^{18}F$ -FDG injection.

demonstrated that the probe concentration in the tumor reaches to the summit on 5th h and probe concentration in liver and spleen gradually declined postinjection (shown in Figures 6(a), 6(b), and 6(c)). The concentration of Au NPs is linearly dependent on the concentration of Gd with 0.99 correlation coefficient and 1.65 slope which is nearly consistent with mass ratio of Au NPs and Gd determined by ICP (in Result1, Au/Gd = 1.31 : 0.77).

**3.5. Multimodality Molecular Imaging-Guided Orthotopic Tumor Treatment.** Figures 7(a) and 7(b) demonstrated that GO-AuNS-DOTA-Gd can target liver orthotopic tumor and reach to the top concentration on 1st h postinjection via tail vein. Figure 7(c) depicted the treatment process using handheld photoacoustic imaging. During treatment, the temperature of the liver tumor on GO-AuNS-DOTA-Gd treated mice and reached more than  $150^{\circ}F$  after irradiation, while the temperature of liver tumor on PBS treated mice did not show obvious temperature increment (Figures 7(d) and 7(e)). Compared with PBS group, tumor of mice for probe group was inhibited completely on day 5th after treatment under handheld PAI guidance (antitumor efficacy is 100%). Without handheld PAI guidance, residual tumors were found on six of seven mice after probe injection and photothermal therapy (antitumor efficacy is 14.29%) (Figure 7(f)). ICP results based on the orthotopic mouse demonstrated that the

probe can be concentrated in the tumor site at 1st h (shown in Figures 6(e) and 6(f)). All experiment results demonstrated that this synergistic method could effectively reduce tumor residual and satellite metastases by 85.71% compared with the photothermal method without handheld PAI guidance ( $100\% - 14.29\% = 85.71\%$ ). On the other hand,  $^{18}F$ -FDG PET image cannot distinguish the tumor from the liver so it cannot be used for guidance in the treatment (Figure 7(g)). The H&E staining result demonstrated that the tumor cells were damaged by the photothermal therapy after probe injection, while the tumor cells were kept in good condition for PBS group.

## 4. Discussion

Graphene has been used for photothermal therapy and has shown promise in many *in vitro* and *in vivo* studies [18, 19]. However, photothermal therapy based on graphene and its related detailed imaging analysis, including tumor volume and gray contrast ratio, have been rarely reported [20]. In this study, GO-AuNS-DOTA-Gd was prepared and its physicochemical properties indicated that the GO-AuNS-DOTA-Gd could act as an efficient material for photothermal therapy and be used for precisely delineating the tumor margin from normal tissues. GO is believed to have a role in promoting

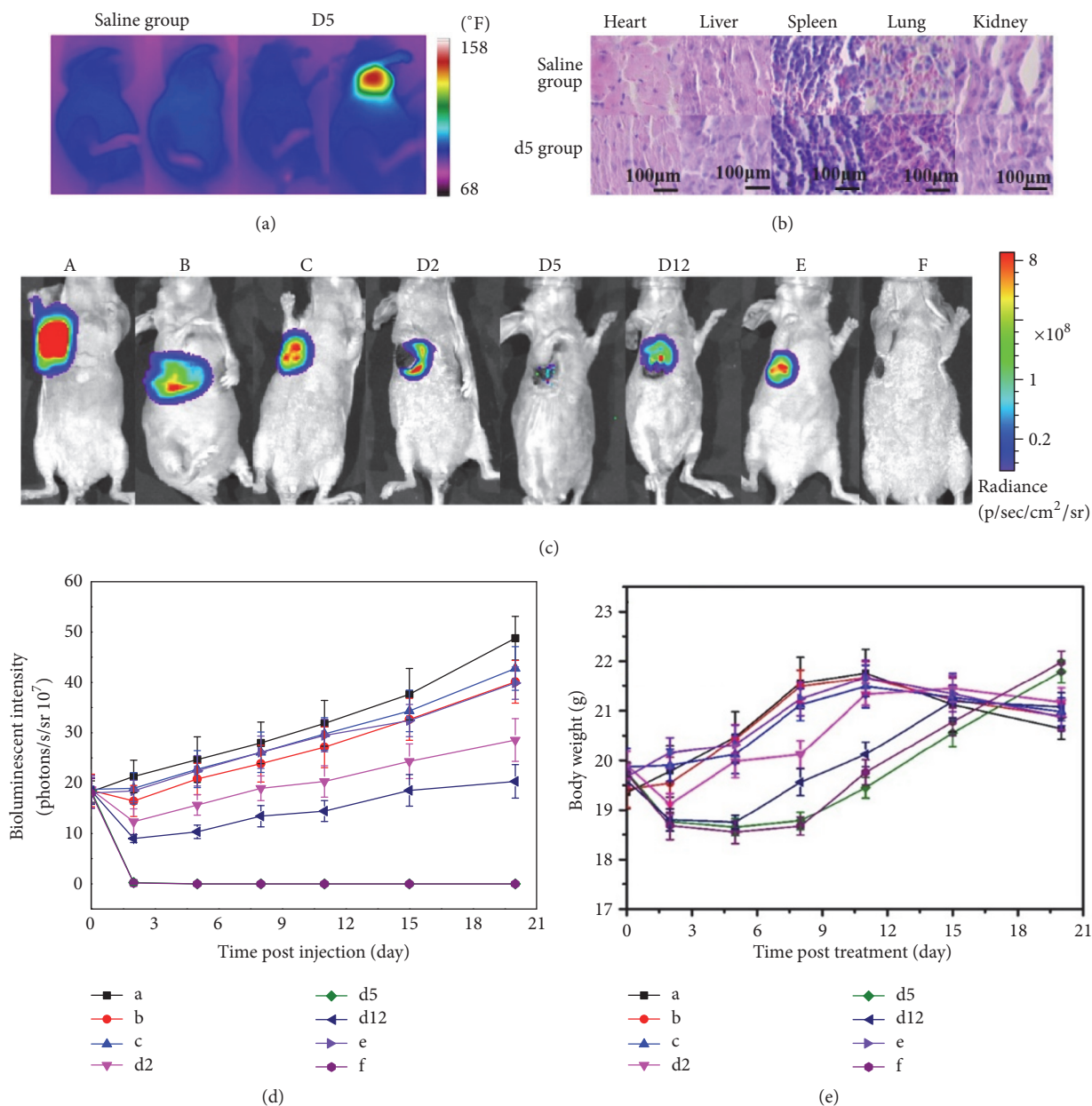


FIGURE 5: (a) Thermal image of mice before and after irradiation for the saline group and (D5) group; (b) sections of the heart, liver, spleen, lung, and kidney of mice stained with H&E after saline and GO-AuNS treatment; (c) bioluminescence images of the HCC-LM3-fluc tumor-bearing nude mice that received (A) saline through tail vein without laser irradiation, (B) saline through tail vein with laser irradiation, (C) GO-AuNS through tail vein without laser irradiation, (D2) laser irradiation on 2nd h postinjection of GO-AuNS through tail vein, (D5) laser irradiation on 5th h postinjection of GO-AuNS through tail vein, (D12) laser irradiation on 12th h postinjection of GO-AuNS through tail vein, (E) GO-AuNS via intratumor injection without laser irradiation, and (F) laser irradiation on 2nd h postinjection of GO-AuNS via intratumor injection; (d) the quantified bioluminescence intensity of tumors from the eight groups on day 5 posttreatment; (e) the average body weight of mice from the eight groups over time ( $n = 5$  per group).

Au nanostar photothermal transduction efficacy in certain studies which deserved further study [21].

Determining tumor boundary is important and can influence the tumor surgery and treatment [22]. In contrast with  $^{18}\text{F}$ -FDG PET imaging, MRI imaging based on GO-AuNS-DOTA-Gd can accurately distinguish the tumor from normal tissues. Furthermore, MRI and PAI analysis demonstrated

that the concentration of GO-AuNS-DOTA-Gd reached its peak in tumor regions at 5th h for subcutaneous tumor and 1st h for orthotopic tumor after tail-vein injection, which was determined as the optimal implementing time of photothermal therapy. For orthotopic tumor, handheld PAI guided photothermal therapy can effectively reduce the tumor residual and ensured the killing of tumor cells.

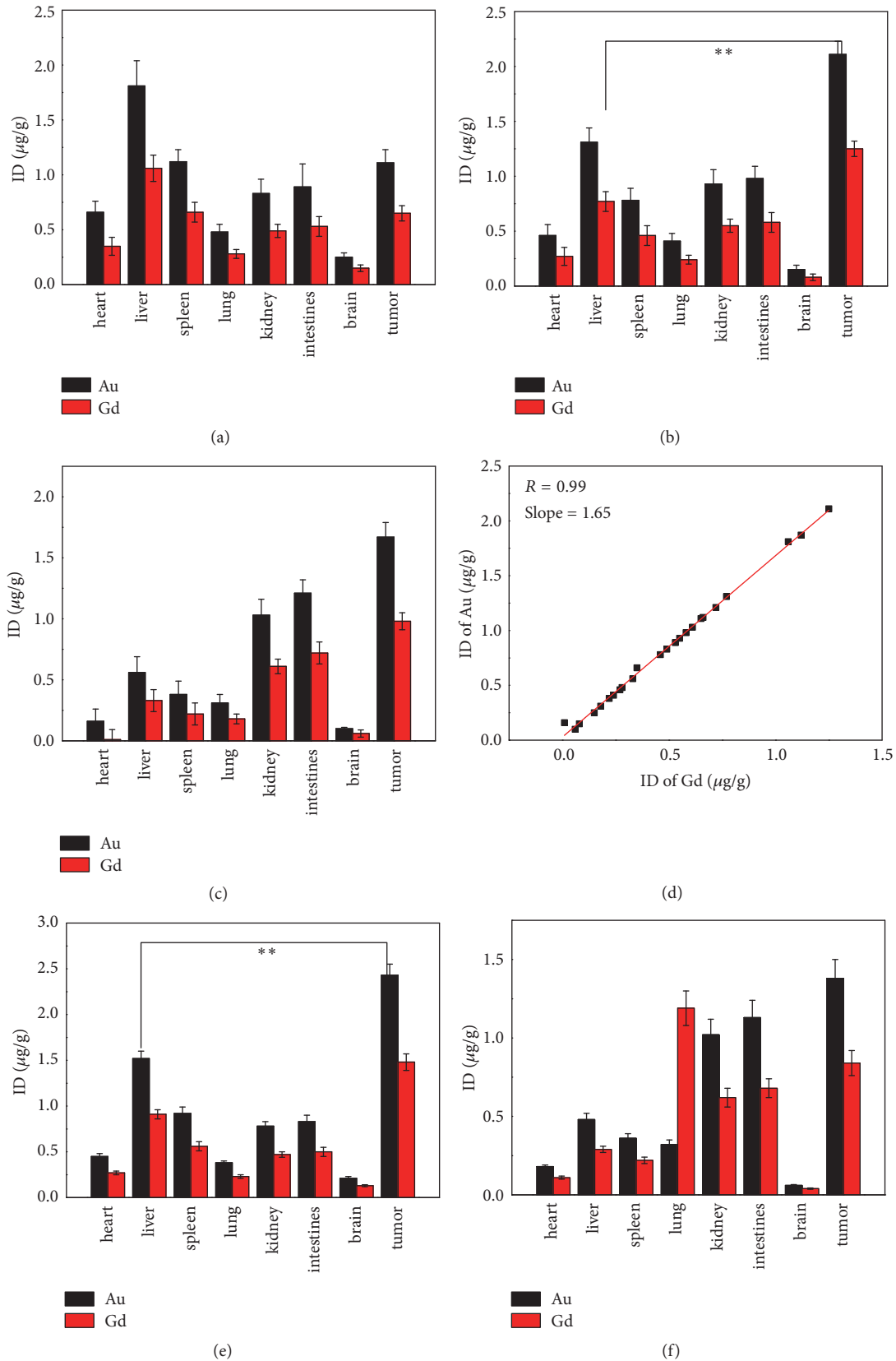


FIGURE 6: Quantitative tissue biodistribution of Au and Gd in HCC-LM3-fLuc subcutaneous tumor-bearing mice after intravenous injection: 2 h (a), 5 h (b), and 12 h (c). Data was presented as mean  $\pm$  SD ( $n = 5$ ),  $**p < 0.01$ , significant difference compared with the other tissue distribution of Au and Gd; (d) the correlation between concentrations of Au and Gd. (e) and (f) Quantitative tissue biodistribution of Au and Gd in HCC-LM3-fLuc orthotopic tumor-bearing mice after intravenous injection: 1 h (e) and 12 h (f).

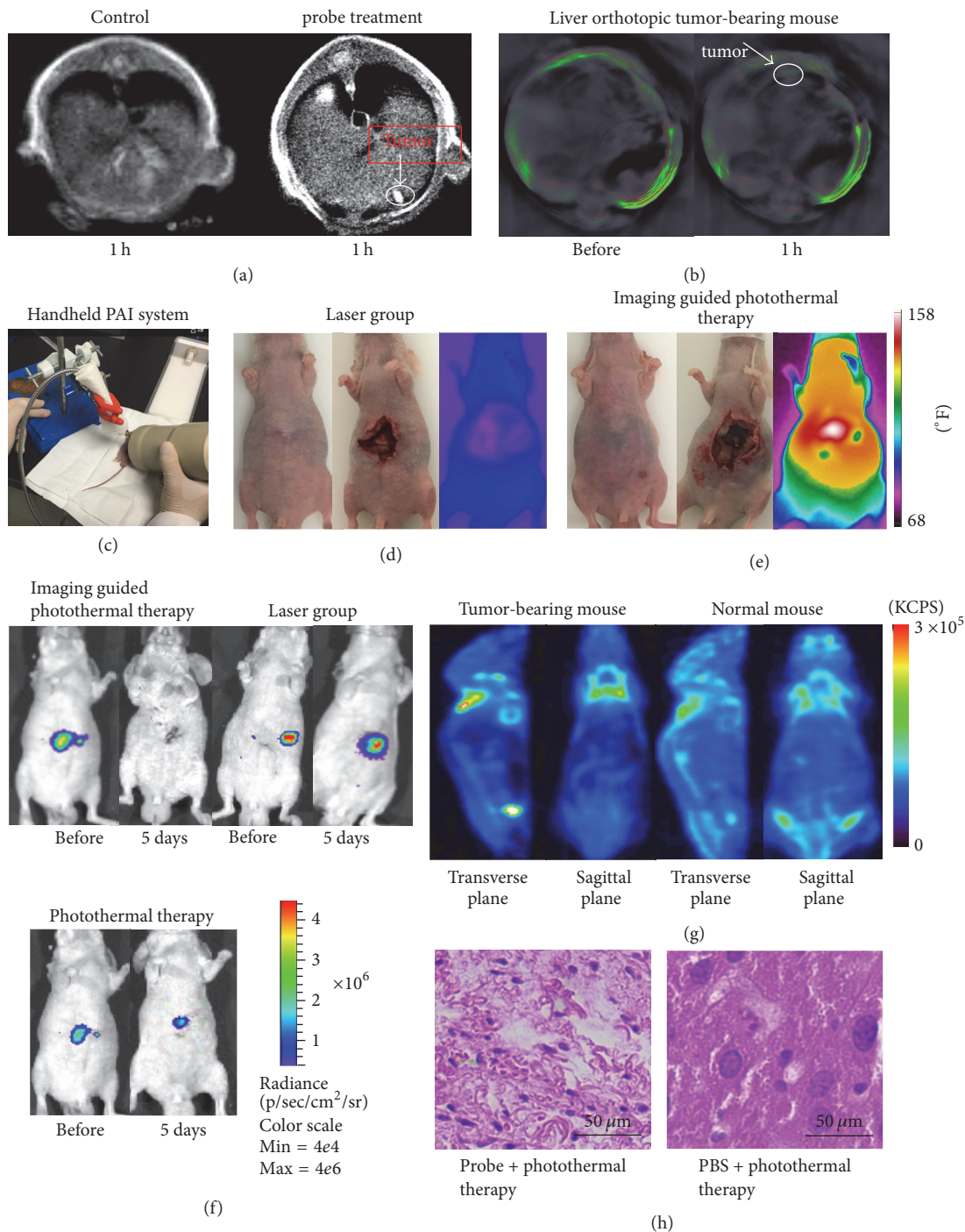


FIGURE 7: (a) MRI image of GO-AuNS-DOTA-Gd on the coronal plane in the tumor regions on 1st h postinjection; (b) photoacoustic signal distribution of GO-AuNS-DOTA-Gd in the tumor regions on 1st h postinjection; (c) handheld photoacoustic imaging-guided photothermal therapy; (d) and (e) are mice image before treatment, treatment, and after irradiation of PBS group and probe group with handheld PAI guidance; (f) bioluminescence image of mice from probe with PAI guidance, PBS group, and probe without PAI guidance; (g)  $^{18}\text{F}$ -FDG PET image of liver orthotopic tumor-bearing mouse and normal mouse; (h) H&E staining of tumors posttreatment from control group and probe group.

Molecular imaging has been widely used in tumor research [23–25]. However, reports on multimodality molecular imaging-guided tumor margin delineation and tumor treatment with deep tumor feature analysis are scarce. Imaging analysis has gradually showed its importance not only for

subcutaneous tumor but also for orthotopic tumor and some groups developed image processing methods to resolve problems encountered in tumor surgery and cancer research. However, there are still some technological difficulties to be resolve, including quick acquisition of massive data and

image segmentation accuracy [24, 25]. In the future, with the development of multidiscipline research, better solutions will be developed to solve biomedical problems using more mature imaging technologies.

## 5. Conclusions

In this study, GO-AuNS-DOTA-Gd was prepared and its physicochemical properties indicated that the probe could act as an efficient photosensitizer for photothermal therapy and be used for precisely delineating the tumor margin from normal tissues based on multimodality molecular imaging. This multimodality imaging strategy is a promising technology for clinical use, especially for the orthotopic tumor, which deserves further development for application in other tumor surgery and treatment.

## Conflicts of Interest

The authors declare no conflicts of interest.

## Authors' Contributions

Xibo Ma, Yushen Jin, and Yi Wang contributed equally to this paper.

## Acknowledgments

This work was supported by the National Key Research Program of China under Grants 2016YFA0100900 and 2016YFA0100902, the National Natural Science Foundation of China under Grants 81227901, 815270805, 61231004, 81471739, 81472594, and 81770781, the Key Research Program of the Chinese Academy of Sciences under Grant KGZD-EW-T03, the Scientific Research and Equipment Development Project of Chinese Academy of Sciences under Grant YZ201457, and the Beijing Natural Science Foundation (no. 7174314). The authors thank Jing Li (Cnkingbio Company, Ltd., Beijing, China) for biotechnical support (HCC-LM3-*fluc* cells were constructed by them).

## References

- [1] S. Vilarinho and T. H. Taddei, "New frontier in liver cancer treatment: Oncolytic viral therapy," *Hepatology*, vol. 59, no. 1, pp. 343–346, 2014.
- [2] J. M. Llovet, "Liver cancer: time to evolve trial design after everolimus failure," *Nature Reviews Clinical Oncology*, vol. 11, no. 9, pp. 506–507, 2014.
- [3] S. Lin, K. Hoffmann, and P. Schemmer, "Treatment of hepatocellular carcinoma: a systematic review," *Liver Cancer*, vol. 1, no. 3–4, pp. 144–158, 2012.
- [4] J. T. Robinson, S. M. Tabakman, Y. Liang et al., "Ultrasmall reduced graphene oxide with high near-infrared absorbance for photothermal therapy," *Journal of the American Chemical Society*, vol. 133, no. 17, pp. 6825–6831, 2011.
- [5] J. Song, X. Yang, O. Jacobson et al., "Sequential drug release and enhanced photothermal and photoacoustic effect of hybrid reduced graphene oxide-loaded ultrasmall gold nanorod vesicles for cancer therapy," *ACS Nano*, vol. 9, no. 9, pp. 9199–9209, 2015.
- [6] M. A. Patel, H. Yang, P. L. Chiu et al., "Direct production of graphene nanosheets for near infrared photoacoustic imaging," *ACS Nano*, vol. 7, no. 9, pp. 8147–8157, 2013.
- [7] B. Tian, C. Wang, S. Zhang, L. Feng, and Z. Liu, "Photothermally enhanced photodynamic therapy delivered by nanographene oxide," *ACS Nano*, vol. 5, no. 9, pp. 7000–7009, 2011.
- [8] A. Bagri, C. Mattevi, M. Acik, Y. J. Chabal, M. Chhowalla, and V. B. Shenoy, "Structural evolution during the reduction of chemically derived graphene oxide," *Nature Chemistry*, vol. 2, no. 7, pp. 581–587, 2010.
- [9] Y. Jin, J. Wang, H. Ke, S. Wang, and Z. Dai, "Graphene oxide modified PLA microcapsules containing gold nanoparticles for ultrasonic/CT bimodal imaging guided photothermal tumor therapy," *Biomaterials*, vol. 34, no. 20, pp. 4794–4802, 2013.
- [10] C. Bao, J. Conde, E. Polo et al., "A promising road with challenges: Where are gold nanoparticles in translational research?" *Nanomedicine*, vol. 9, no. 15, pp. 2353–2370, 2014.
- [11] X. Ma, H. Hui, Y. Jin et al., "Enhanced immunotherapy of SM5-1 in hepatocellular carcinoma by conjugating with gold nanoparticles and its in vivo bioluminescence tomographic evaluation," *Biomaterials*, vol. 87, pp. 46–56, 2016.
- [12] X. Ma, Z. Cheng, Y. Jin et al., "SM5-1-Conjugated PLA nanoparticles loaded with 5-fluorouracil for targeted hepatocellular carcinoma imaging and therapy," *Biomaterials*, vol. 35, no. 9, pp. 2878–2889, 2014.
- [13] C. Qin, J. Feng, S. Zhu, X. Ma, J. Zhong, P. Wu et al., "Recent advances in bioluminescence tomography: methodology and system as well as application," *Laser & Photonics Reviews*, vol. 8, pp. 94–114, 2014.
- [14] M.-K. Chuang, S.-W. Lin, F.-C. Chen, C.-W. Chu, and C.-S. Hsu, "Gold nanoparticle-decorated graphene oxides for plasmonic-enhanced polymer photovoltaic devices," *Nanoscale*, vol. 6, no. 3, pp. 1573–1579, 2014.
- [15] N. Venkatesha, P. Poojar, S. Geethanath, and C. Srivastava, "Graphene oxide-gadolinium (III) oxide nanoparticle composite: A novel MR contrast agent with high longitudinal and transverse relaxivity," *Materials Research Express*, vol. 1, no. 4, Article ID 045008, 2015.
- [16] Z. Ma, X. Chen, Y. Huang et al., "MR diffusion-weighted imaging-based subcutaneous tumour volumetry in a xenografted nude mouse model using 3D Slicer: An accurate and repeatable method," *Scientific Reports*, vol. 5, Article ID 15653, 2015.
- [17] S. C. Wriessnegger, D. Steyrl, K. Koschutnig, and G. R. Müller-Putz, "Cooperation in mind: Motor imagery of joint and single actions is represented in different brain areas," *Brain and Cognition*, vol. 109, pp. 19–25, 2016.
- [18] K. Yang, S. Zhang, G. Zhang, X. Sun, S.-T. Lee, and Z. Liu, "Graphene in mice: ultrahigh in vivo tumor uptake and efficient photothermal therapy," *Nano Letters*, vol. 10, no. 9, pp. 3318–3323, 2010.
- [19] C. Xu, S. Shi, L. Feng et al., "Long circulating reduced graphene oxide-iron oxide nanoparticles for efficient tumor targeting and multimodality imaging," *Nanoscale*, vol. 8, no. 25, pp. 12683–12692, 2016.
- [20] E. Karamitopoulou, I. Zlobec, V. H. Koelzer, R. Langer, H. Dawson, and A. Lugli, "Tumour border configuration in colorectal cancer: Proposal for an alternative scoring system based on the

- percentage of infiltrating margin,” *Histopathology*, vol. 67, no. 4, pp. 464–473, 2015.
- [21] F. Wang, Q. Sun, B. Feng et al., “Polydopamine-Functionalized Graphene Oxide Loaded with Gold Nanostars and Doxorubicin for Combined Photothermal and Chemotherapy of Metastatic Breast Cancer,” *Advanced Healthcare Materials*, vol. 5, no. 17, pp. 2227–2236, 2016.
- [22] S. C. Davis, K. S. Samkoe, K. M. Tichauer et al., “Dynamic dual-tracer MRI-guided fluorescence tomography to quantify receptor density in vivo,” *Proceedings of the National Academy of Sciences of the United States of America*, vol. 110, no. 22, pp. 9025–9030, 2013.
- [23] K. M. Tichauer, K. S. Samkoe, J. R. Gunn et al., “Microscopic lymph node tumor burden quantified by macroscopic dual-tracer molecular imaging,” *Nature Medicine*, vol. 20, no. 11, pp. 1348–1353, 2014.
- [24] C. Kut, K. L. Chaichana, J. Xi et al., “Detection of human brain cancer infiltration ex vivo and in vivo using quantitative optical coherence tomography,” *Science Translational Medicine*, vol. 7, no. 292, Article ID 292ra100, 2015.
- [25] Y. Gu, C. Wang, T. Peterka, R. Jacob, and S. H. Kim, “Mining Graphs for Understanding Time-Varying Volumetric Data,” *IEEE Transactions on Visualization and Computer Graphics*, vol. 22, no. 1, pp. 965–974, 2016.

## Research Article

# Investigation of Newly Prepared Biodegradable $^{32}\text{P}$ -chromic Phosphate-poly lactide-co-glycolide Seeds and Their Therapeutic Response Evaluation for Glioma Brachytherapy

Guoqiang Shao,<sup>1</sup> Yuebing Wang ,<sup>2</sup> Xianzhong Liu,<sup>3</sup> Meili Zhao,<sup>1</sup> Jinhua Song,<sup>4</sup> Peiling Huang,<sup>5</sup> Feng Wang ,<sup>1</sup> and Zizheng Wang <sup>1</sup>

<sup>1</sup>Department of Nuclear Medicine, Nanjing First Hospital, Nanjing Medical University, Nanjing 210006, China

<sup>2</sup>Department of Biochemistry, School of Medicine, Nankai University, Tianjin 300071, China

<sup>3</sup>Department of Surgical Oncology, Bayi Hospital Affiliated to Nanjing University of Chinese Medicine, Nanjing 210006, China

<sup>4</sup>Department of Invasive Technology, Nanjing First Hospital, Nanjing Medical University, Nanjing 210006, China

<sup>5</sup>Department of Pathology, Medical College of Southeast University, Nanjing 210000, China

Correspondence should be addressed to Zizheng Wang; 13770920210@163.com

Received 27 September 2017; Accepted 14 March 2018; Published 29 April 2018

Academic Editor: Ralf Schirmacher

Copyright © 2018 Guoqiang Shao et al. This is an open access article distributed under the Creative Commons Attribution License, which permits unrestricted use, distribution, and reproduction in any medium, provided the original work is properly cited.

$^{32}\text{P}$  high-dose rate brachytherapy allows high-dose radiation delivery to target lesions with less damage to adjacent tissues. The early evaluation of its therapeutic effect on tumours is vital for the optimization of treatment regimes. The most commonly used  $^{32}\text{P}$ -CP colloid tends to leak with blind therapeutic area after intratumour injection. We prepared  $^{32}\text{P}$ -chromic phosphate-poly lactide-co-glycolide ( $^{32}\text{P}$ -CP-PLGA) seeds with biodegradable PLGA as a framework and investigated their characteristics *in vitro* and *in vivo*. We also evaluated the therapeutic effect of  $^{32}\text{P}$ -CP-PLGA brachytherapy for glioma with the integrin  $\alpha\text{v}\beta 3$ -targeted radiotracer  $^{68}\text{Ga}$ -3PRGD<sub>2</sub>.  $^{32}\text{P}$ -CP-PLGA seeds (seed group, SG, 185 MBq) and  $^{32}\text{P}$ -CP colloid (colloid group, CG, 18.5 MBq) were implanted or injected into human glioma xenografts in nude mice. Scanning electron microscopy (SEM) of the seeds, micro-SPECT imaging, and biodistribution studies were performed at different time points. The tumour volume was measured using a caliper, and  $^{68}\text{Ga}$ -3PRGD<sub>2</sub> micro-PET-CT imaging was performed to evaluate the therapeutic effect after  $^{32}\text{P}$  intratumour administration. The delayed release of  $^{32}\text{P}$ -CP was observed with biodegradation of vehicle PLGA. Intratumoural effective half-life of  $^{32}\text{P}$ -CP in the SG ( $13.3 \pm 0.3$ ) d was longer than that in the CG ( $10.4 \pm 0.3$ ) d ( $P < 0.05$ ), with liver appearance in the CG on SPECT. A radioactivity gradient developed inside the tumour in the SG, as confirmed by micro-SPECT and SEM. Tumour uptake of  $^{68}\text{Ga}$ -3PRGD<sub>2</sub> displayed a significant increase on day 0.5 in the SG and decreased earlier (on day 2) than the volume reduction (on day 8). Thus,  $^{32}\text{P}$ -CP-PLGA seeds, controlling the release of entrapped  $^{32}\text{P}$ -CP particles, are promising for glioma brachytherapy, and  $^{68}\text{Ga}$ -3PRGD<sub>2</sub> imaging shows potential for early response evaluation of  $^{32}\text{P}$ -CP-PLGA seeds brachytherapy.

## 1. Introduction

Glioblastoma multiforme (GBM) accounts for approximately 60% to 70% of malignant gliomas. The prognosis of patients with GBM remains dismal, with a median survival time of less than one year. This poor prognosis primarily reflects the high proliferative, infiltrative, and invasive properties of GBM [1]. Systemic administration of most potentially active drugs is not effective because of failing to cross the blood-brain

barrier. Residual cells at the margins of the resection or GBM stem cells, a subpopulation of stem-like cells, frequently lead to tumour recurrence or metastasis.

Compared with external-beam radiation, brachytherapy has the advantage of delivering high doses of radiation to target sites without subjecting normal tissues to undue radiation and damage [2].  $^{32}\text{P}$  is ideal because of its relatively long half-life of 14.28 day(s), maximum energy of 1.711 MeV, mean range of 3–4 mm in soft tissues, and high relative biological effect.

Recent studies have focused on better vehicles or carriers, and many of these studies have used  $^{32}\text{P}$  bandages or films for the brachytherapy of superficial cancers and intracranial and spinal tumours [3–9]. However, the main hurdles to these vehicles were poor target ratios in the tumour, complex preparation, and serious side effects resulting from migration and permanent stagnation, such as lung migration and gastric fistula *in vivo* [7–9].

Polymers, such as poly(lactic acid) (PLA), poly(glycolic acid) (PGA), and their copolymer poly(lactide-co-glycolide) (PLGA), have extensively been used in drug delivery systems because of their biodegradability, tissue compatibility, and versatile degradation kinetics [10–13]. Compared with poly(L-lactide) (PLLA), PLGA has attracted more attention, reflecting its degradation rate and relative ease in manipulating its release of encapsulating drugs by changing the degradation-determining factors, such as its molecular weight, lactide/glycolide ratio, and degree of crystallinity [14, 15]. In a previous study, we completed the formulation and determined the fabricating parameters of  $^{32}\text{P}$ -CP-PLGA seeds (unpublished observations). As one potential biodegradable seed for brachytherapy,  $^{32}\text{P}$ -CP-PLGA is meaningful for further preclinical studies, and the therapeutic effect evaluation of  $^{32}\text{P}$  brachytherapy has rarely been reported.

Integrin  $\alpha\text{v}\beta_3$ , specifically targeted by the arginine-glycine-aspartic acid (RGD) tripeptide sequence, is highly expressed in both glioma cells and neovasculature but not in quiescent blood vessels. Integrin  $\alpha\text{v}\beta_3$  targeted imaging had higher sensitivity in GBM than  $^{18}\text{F}$ -FDG, reflecting a clear lack of RGD affinity, particularly in brain areas where gliomas are prone to occur [16]. In an orthotopic U87MG human glioma mouse model, the tumour-to-brain ratio of radiolabelled RGD is approximately 20 times that of  $^{18}\text{F}$ -FDG [17].  $^{68}\text{Ga}$ , easily accessible via elution from the  $^{68}\text{Ge}$ - $^{68}\text{Ga}$  generator, can produce Cerenkov radiation and allow the combination of PET-Cerenkov luminescence imaging (CLI) for both tumour diagnosis and visual guidance for further surgery [17].  $^{68}\text{Ga}$ -labelled DOTA-3PRGD<sub>2</sub> ( $^{68}\text{Ga}$ -3PRGD<sub>2</sub>) was reported to reflect the tumour response to antiangiogenic therapy much earlier and more accurately than  $^{18}\text{F}$ -FDG PET imaging [18]. Integrin-targeted imaging detects early responses preceding clinical regression as early as day 3 after the initiation of abraxane treatment, while  $^{18}\text{F}$ -FDG imaging demonstrated increased tumour uptake on days 3 and 7 [19]. For  $^{32}\text{P}$  brachytherapy, early response is also important for treatment direction; however, few studies have been reported.

In our previous study, we found that radiolabelling RGD is excellent for monitoring  $\alpha\text{v}\beta_3$  expression and glioma necrosis during tumour growth [20]. The present study reports (a) the preparation, biodegradation, and ultrastructural changes of  $^{32}\text{P}$ -CP-PLGA seeds and the biodistribution of  $^{32}\text{P}$ -CP particles both systemically and inside the tumour and (b) the anticancer effect on glioma in an animal model after intratumour seeds implantation and therapeutic effect evaluation with integrin  $\alpha\text{v}\beta_3$  receptor targeting radiotracer  $^{68}\text{Ga}$ -3PRGD<sub>2</sub>.

## 2. Materials and Methods

**2.1. Materials.**  $^{32}\text{P}$ -CP colloid, supplied by Beijing Atom High-Tech Co., Ltd., China, is a green colloid solution with radioactive chemical purity > 98%, particle size 20–50 nm, and specific radioactivity ~ 1850 MBq/ml. PLGA (50 : 50; MW-85,000 Da) was obtained from Hefei University of Technology, China.  $^{68}\text{Ge}$ - $^{68}\text{Ga}$  generator (ITG, Germany), 3PRGD<sub>2</sub>, was donated by Dr. Shuang Liu (Purdue University). Nude mice (male, 14–16 g, 5–6 weeks) bearing human glioma (U87MG) xenografts in the flank were obtained from the Chinese Academy of Medical Sciences, China. All animal procedures were performed in accordance with the standards of the Institutional Animal Care and Utilization Committee. The following were used: hamster anti-integrin  $\beta_3$  antibody (1 : 100, BD Biosciences, San Jose, CA), rat anti-CD31 antibody (1 : 100, BD Biosciences), Cy3-conjugated goat anti-hamster secondary antibody (1 : 100, Jackson Immuno Research Inc., West Grove, PA), fluorescein- (FITC-) conjugated goat anti-rat secondary antibody (1 : 100, Jackson Immuno Research Inc., West Grove, PA), CRC-Enhanced  $\beta$  calculator (Capintec Corporation, USA), Gamma counter (TY6017, Wizard, PerkinElmer, USA), Electronic Balance (BS-110S, Sartorius Corporation, Germany), Scanning electron microscope (S-3000N, Hitachi High-Technologies Corporation, Japan), Olympic BX51 fluorescence microscope (Olympus America Inc., Center Valley, PA), micro-SPECT (Milabs, Utrecht, The Netherlands), and micro-PET/CT (Inveon, Siemens, Germany).

**2.2. Preparation of  $^{32}\text{P}$ -CP-PLGA Seeds and In Vitro Study.** A total of 100 mg of PLGA (0.1–1.0  $\mu\text{m}$ ) and 2 ml of colloidal  $^{32}\text{P}$ -CP (1850 MBq/ml) were mixed with 2–3 ml of dehydrated alcohol as a dispersing agent. These components were blended and dried at 60°C in a vacuum drying oven for 9–12 h. Magnesium stearate (1.0–1.5 mg) served as a surface lubricant, and the  $^{32}\text{P}$ -CP-PLGA seeds were home-prepared using an automatic precise piercer. The physical characteristics of the  $^{32}\text{P}$ -CP-PLGA seeds were investigated. *In vitro* releasing experiments were performed by incubating the  $^{32}\text{P}$ -CP-PLGA seeds in 6 ml of PBS at 37°C for 90 day(s), and 0.2 ml of the sample was withdrawn every other day from the releasing solution after stirring to generate a homogenous mixture.

**2.3. Radiopharmaceutical Administration and Biodistribution Study.** Nude mice bearing U87MG human gliomas (tumour long diameter of 0.6–0.8 cm) were randomized into the  $^{32}\text{P}$ -CP-PLGA seed group (SG,  $n = 36$ ) and the  $^{32}\text{P}$ -CP colloid group (CG,  $n = 36$ ). One  $^{32}\text{P}$ -CP-PLGA seed (18.5 MBq) or 0.02 ml of colloidal  $^{32}\text{P}$ -CP (18.5 MBq) was implanted or slowly injected into the tumour core. The injection sites were gently compressed for 60 s. The mice were sacrificed at 0.5, 1, 2, 4, 8, 16, 32, 49, and 64 days (5 mice each time point each group) for biodistribution study and pathology examination.

Important organs were harvested, weighed, and counted for radioactivity using a  $\beta$  calculator or Gamma counter. Tumour xenografts harvested at 0.5, 1, 2, 4, 8, and 16 days

were further divided into 3 parts according to their distances from the core of the tumour. The 3 parts of the tumour and adjacent tissues were weighed and counted for radioactivity.  $^{32}\text{P}$  distribution was expressed as the percent injected dose per gram (%ID/g). The remaining seeds and tumour tissues were prepared for SEM examination. For the mice sacrificed on day 64, micro-SPECT imaging was selectively performed, and faeces and urine were collected.

**2.4. Micro-SPECT and Micro-SPECT/CT Imaging.** Anesthesia of mice (SG and CG) was induced using isoflurane. Micro-SPECT images were obtained on days 1, 4, 16, and 64 using a micro-SPECT scanner equipped with a 0.6 mm multipinhole collimator. The specified  $^{32}\text{P}$ -CP-PLGA seeds and  $^{32}\text{P}$ -CP colloids, same as those used in the SG and CG, were served as markers and imaged, respectively. Regions of interest (ROIs) of the targeted tumour (T) and the marker ( $T_{\text{mk}}$ ) were drawn to estimate the  $T/T_{\text{mk}}$  ratio and intratumoural effective half-life of  $^{32}\text{P}$ -CP. After SPECT acquisition (75 projections over 30 min per frame, 2 frames), SPECT reconstruction was performed using a POSEM (pixelated ordered subsets by expectation maximization) algorithm with 6 iterations and 16 subsets. Micro-CT imaging was added on day 1 using the “normal” acquisition settings at 45 kV and 500 A. CT data were reconstructed using a cone-beam filtered back-projection algorithm (NRecon v1.6.3, Skyscan). After reconstruction, the SPECT and CT data were automatically coregistered according to the movement of the robotic stage and then resampled to equivalent voxel sizes. Coregistered images were further rendered and visualized using PMOD software (PMOD Technologies, Zurich, Switzerland).

**2.5. Therapeutic Effect of  $^{32}\text{P}$ -CP-PLGA Seeds for Gliomas.** 39 nude mice bearing U87MG gliomas (long diameter of 0.6–0.8 cm) were randomly divided into  $^{32}\text{P}$ -CP-PLGA seed group (18.5 MBq,  $n = 17$ ),  $^{32}\text{P}$ -CP colloid group (18.5 MBq, 0.02 ml,  $n = 5$ ), and P-CP-PLGA seed group (no radioactivity,  $n = 17$ ). Tumour diameter was measured with digital caliper every other day and tumour volume was estimated by the formula  $(\text{length} \times \text{width}^2)/2$  (5 mice each group for three group).  $^{68}\text{Ga}$ -3PRGD<sub>2</sub> micro-PET-CT imaging was performed on days 0.5, 2, 8, and 16 after seeds administration ( $n = 5$  of each group). Four mice were sacrificed on days 0.5, 2, and 4 in SG and P-CP-PLGA seed group and tumour xenografts were harvested for immunohistochemistry (IHC) examination.

**2.6.  $^{68}\text{Ga}$ -3PRGD<sub>2</sub> Micro-PET-CT Imaging.** We prepared  $^{68}\text{Ga}$ -3PRGD<sub>2</sub> as previously described [18]. In brief,  $^{68}\text{GaCl}_3$  was eluted from  $^{68}\text{Ge}/^{68}\text{Ga}$ -generator with 0.05 M HCl. The conjugation of 3PRGD<sub>2</sub> with DOTA-OSu was performed for the synthesis of DOTA-3PRGD<sub>2</sub>. The DOTA-3PRGD<sub>2</sub> and  $^{68}\text{GaCl}_3$  were mixed and heated in a water bath at 90°C for 15 min. The radiochemical purity was then determined with radio-HPLC.

0.1 mL of  $^{68}\text{Ga}$ -3PRGD<sub>2</sub> (74 MBq/mL) was injected via tail vein under isoflurane anesthesia. Ten-minute static PET scans were acquired and images were reconstructed by an

OSEM 3D (Three-Dimensional Ordered Subsets Expectation Maximum) algorithm followed by MAP (Maximization/Maximum A Posteriori). The 3D ROIs were drawn over the tumour guided by CT images and tracer uptake was measured using the software of Inveon Research Workplace (IRW) 3.0. Mean standardized uptake values (SUV) were determined by dividing the relevant ROI concentration by the ratio of the injected activity to the body weight.

**2.7. Seeds Ultrastructure Changes and Glioma Integrin  $\alpha\beta_3$  Expression.** SEM examination was performed to investigate the ultrastructure changes of  $^{32}\text{P}$ -CP-PLGA seeds. Frozen glioma tissues were cut into 5  $\mu\text{m}$  slices and blocked with 10% goat serum for 30 min and then incubated with the hamster anti-integrin  $\beta_3$  antibody and rat anti-CD31 antibody for 1 h at room temperature. After incubating with the Cy3-conjugated goat anti-hamster and fluorescein- (FITC-) conjugated goat anti-rat secondary antibodies and washing with PBS, the fluorescence was visualized using a fluorescence microscope.

**2.8. Statistical Analysis.** Data are shown as mean  $\pm$  SD. Differences in tissues uptake between SG and CG were statistically analyzed at each time point with SPSS 11.5 software. Student's *t*-test was used for statistical analysis. *P* values less than 0.05 were considered statistically significant.

### 3. Results

**3.1. Basic Characteristics and Biodegradation of  $^{32}\text{P}$ -CP-PLGA Seeds.**  $^{32}\text{P}$ -CP-PLGA seeds are cylindrical with a diameter of  $(0.9 \pm 0.02)$  mm, length of  $(1.9 \pm 0.2)$  mm, weight of  $(1.2 \pm 0.15)$  mg each, hardness of  $(5.7 \pm 1.4)$  N, and apparent radioactivity of  $(18.5 \pm 3.7)$  MBq. The release of  $^{32}\text{P}$ -CP-PLGA seeds can be divided into the rapid release phase (0~8 d, phase I), the stable release phase (8~60 d, phase II), and the disintegration release phase (60 d ~, phase III) according to time-release curve slope (Figure 1(a)).

Figure 1(b) displays the SEM results of  $^{32}\text{P}$ -CP-PLGA seeds before and 8, 16, 32, and 64 days after intratumour implantation. The seed was uniform and dense in texture, showing a mosaic of  $^{32}\text{P}$ -CP particles prior to implantation. An increasing number of micropores, tunnels, cellular structures, cavities, and fragments were observed with increasing seed brittleness and inability to maintain shape during release. Figure 1(c) displays the ultrastructure of  $^{32}\text{P}$ -CP particles before the preparation of  $^{32}\text{P}$ -CP-PLGA seeds and those released from the  $^{32}\text{P}$ -CP-PLGA seeds.

**3.2. Biodistribution of  $^{32}\text{P}$ -CP Particles.** The biodistribution of  $^{32}\text{P}$ -CP in SG and CG is shown in Tables 1 and 2. The released radioactivity reached up to  $(7.3 \pm 1.4)\%$  on day 8 and increased to approximately  $(21 \pm 3.8)\%$  on day 64, among which approximately  $(14.6 \pm 2.7)\%$  remained in the tumour,  $(5.2 \pm 1.3)\%$  was primarily aggregated in the liver, spleen, and bone, and approximately  $(3.1 \pm 0.86)\%$  was eliminated in faeces and urine. Leakage of  $^{32}\text{P}$ -CP colloid was detected around the tumour xenograft in the CG. Compared with the CG, the peak uptake of  $^{32}\text{P}$ -CP in the liver  $(3.1 \pm 0.3)\%$ ,

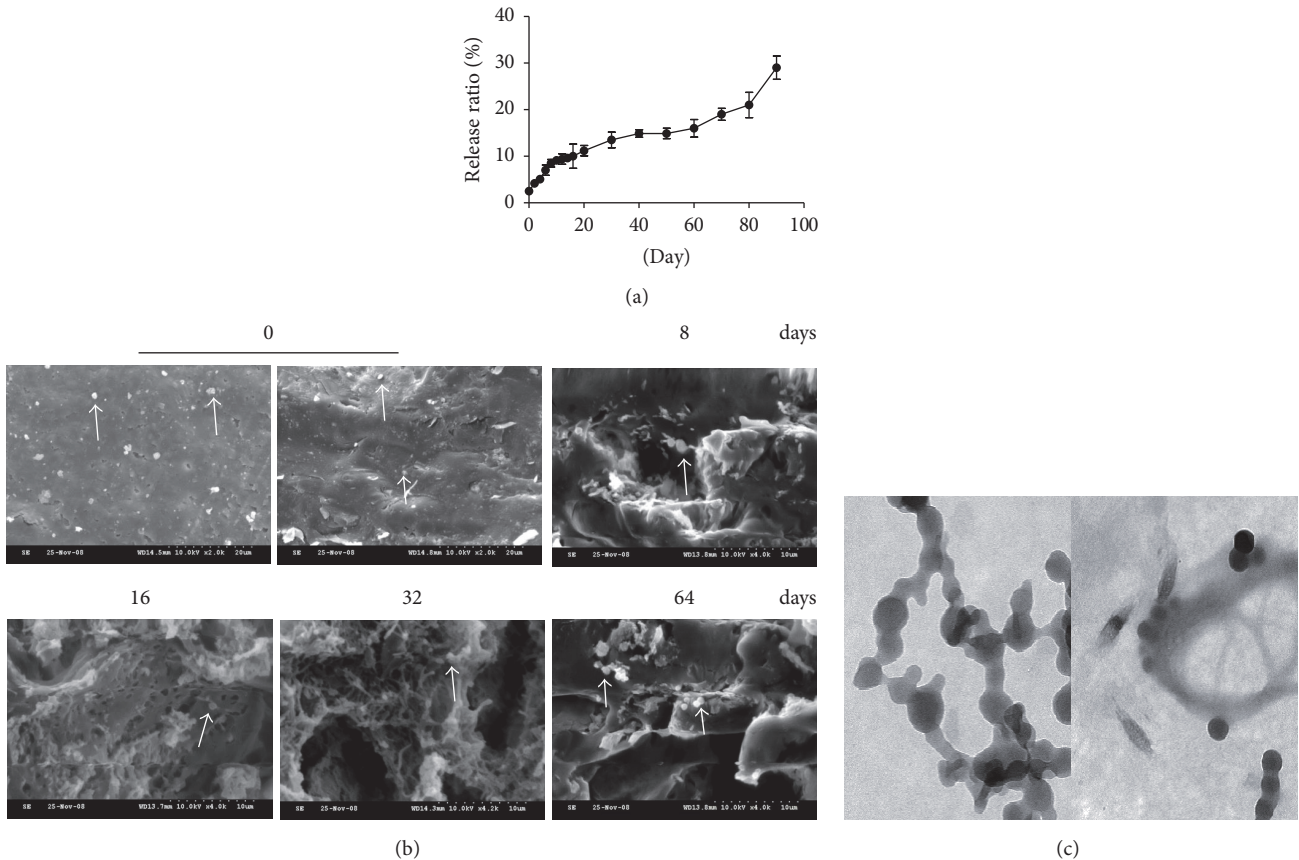


FIGURE 1: Time-release curve of  $^{32}\text{P}$ -CP particles from  $^{32}\text{P}$ -CP-PLGA seeds and ultrastructure changes of  $^{32}\text{P}$ -CP-PLGA seeds by SEM *in vitro*. (a) *In vitro* releasing experiment was performed by incubating the  $^{32}\text{P}$ -CP-PLGA seeds in 6.0 ml of PBS at  $37^\circ\text{C}$  for 90 day(s). (b) SEM was performed before day 0 (left: surface; right: cross-section) and 8, 16, 32, and 64 day(s) after intratumoural implantation.  $^{32}\text{P}$ -CP particles, indicated with white arrow, encapsulated in the seeds and released with the structure erosion of carrier PLGA polymer. (c) The ultrastructure of  $^{32}\text{P}$ -CP particles released from the PLGA *in vitro* (50 nm).

spleen ( $1.3 \pm 0.1\%$ ), and bone ( $4.3 \pm 1.8\%$ ) was significantly less in the SG [ $(1.2 \pm 0.1\%)$  in liver, ( $0.8 \pm 0.2\%$ ) in spleen, and ( $1.5 \pm 0.1\%$ ) in the bone, all of  $P < 0.05$ ] (Figure 2). Intratumoural radioactive effective half-life of  $^{32}\text{P}$ -CP in the SG ( $13.3 \pm 0.3$  d) was longer than that in the CG [ $(11.4 \pm 0.7)$  d,  $P < 0.05$ ]. Pathological examination of the liver, spleen, lung, and bone demonstrated no abnormality in the SG.

**3.3. Radioactivity Gradient Developed in Tumour and Surrounding Tissues.** Figure 3 demonstrated the distribution of the released  $^{32}\text{P}$ -CP particles in tumour and adjacent normal tissues in the CG or SG after eradication and radioactivity counting of the remaining  $^{32}\text{P}$ -CP-PLGA seeds. Most of released  $^{32}\text{P}$ -CP particles in the SG were stagnant in the tumour core with a decreasing gradient towards the periphery in the SG (Figure 3(b)). This finding was confirmed by using SEM (Figure 3(c)). The gradient existed for approximately 2 weeks and became insignificant on day 14. The %ID/g tumour uptake of  $^{32}\text{P}$ -CP significantly increased on day 16, primarily reflecting tumour shrinkage. Conversely, the intratumoural distribution of  $^{32}\text{P}$ -CP in the CG was irregular and a slight increase of %ID/g tumour uptake was observed

with tumour shrinkage. The regional peak uptake in tumour tissues (t2) on day 16 was higher than day 8 (t1) (Figure 3(a)).

**Micro-SPECT/CT Imaging.**  $^{32}\text{P}$  bremsstrahlung facilitates SPECT-CT imaging to monitor the intratumour administration of  $^{32}\text{P}$ -CP colloid (Figure 4(a)) and  $^{32}\text{P}$ -CP-PLGA seeds (Figure 4(b)). As shown in Figure 4(b),  $^{32}\text{P}$ -CP-PLGA seeds showed dot-like focal radioactivity accumulation on days 1 and 4. The released  $^{32}\text{P}$ -CP showed a vague appearance of tumour on days 16 and 64 in the SG.  $^{32}\text{P}$ -CP colloids displayed irregular shapes in and/or close to the tumour location, with abnormal distribution in the liver in the CG on day 16, and this effect was even more apparent on day 64. The  $T/T_{\text{mk}}$  decreased to  $89.3\% \pm 2.4\%$  (SG) and  $65.8\% \pm 3.1\%$  (CG) on day 64 based on micro-SPECT/CT images.

**3.4.  $^{68}\text{Ga}$ -3PRGD<sub>2</sub> Micro-PET/CT Imaging and Tumour Growth Monitoring.** As shown in Figure 5, the tumour uptake heterogeneity of  $^{68}\text{Ga}$ -3PRGD<sub>2</sub> was observed on days 2 and 4 with internal absence on day 8. Scar formation was observed on day 16 in the SG. In the P-CP-PLGA seed group, the distribution of  $^{68}\text{Ga}$ -3PRGD<sub>2</sub> was uniform for 8 day(s), and

TABLE 1: Biodistribution of <sup>32</sup>P-CP particle in nude mice bearing U87MG glioma after intratumor implantation of <sup>32</sup>P-CP-PLGA seed (*n* = 5).

Tissue		Radioactivity distribution (%ID/g)								
		0.5 d	1 d	2 d	4 d	8 d	16 d	32 d	48 d	64 d
Tumor	Mean	556.686	547.778	626.172	666.063	724.118	903.226	---	---	---
	1 SD	24.016	61.301	76.528	59.454	132.290	128.155	---	---	---
Blood	Mean	0.007	0.008	0.016	0.020	0.017	0.018	0.010	0.019	0.010
	1 SD	0.004	0.008	0.008	0.017	0.013	0.011	0.000	0.005	0.004
Heart	Mean	0.028	0.046	0.079	0.167	0.213	0.128	0.062	0.018	0.027
	1 SD	0.012	0.013	0.011	0.015	0.006	0.024	0.015	0.011	0.012
Liver	Mean	0.020	0.035	0.179	0.656	1.125	0.738	0.430	0.369	0.165
	1 SD	0.010	0.082	0.115	0.136	0.038	0.100	0.037	0.041	0.016
Spleen	Mean	0.031	0.069	0.369	0.556	0.913	0.538	0.321	0.469	0.253
	1 SD	0.030	0.028	0.121	0.078	0.221	0.061	0.087	0.011	0.112
Lung	Mean	0.013	0.017	0.206	0.115	0.093	0.068	0.094	0.071	0.062
	1 SD	0.000	0.018	0.020	0.027	0.012	0.015	0.013	0.021	0.010
Kidney	Mean	0.033	0.057	0.137	0.074	0.109	0.065	0.039	0.039	0.021
	1 SD	0.030	0.028	0.021	0.027	0.017	0.013	0.007	0.034	0.010
Stomach	Mean	0.009	0.017	0.404	0.030	0.039	0.038	0.026	0.049	0.036
	1 SD	0.004	0.003	0.011	0.008	0.017	0.011	0.015	0.021	0.019
Intestine	Mean	0.023	0.099	0.154	0.159	0.292	0.225	0.113	0.176	0.148
	1 SD	0.010	0.038	0.035	0.063	0.127	0.051	0.031	0.063	0.030
Pancreas	Mean	0.008	0.024	0.125	0.312	0.057	0.051	0.043	0.035	0.055
	1 SD	0.000	0.002	0.011	0.015	0.024	0.01	0.021	0.012	0.022
Brain	Mean	0.017	0.006	0.028	0.099	0.065	0.033	0.037	0.041	0.024
	1 SD	0.009	0.011	0.01	0.023	0.024	0.011	0.012	0.021	0.014
Thyroid	Mean	0.016	0.034	0.026	0.044	0.032	0.042	0.032	0.041	0.035
	1 SD	0.000	0.007	0.011	0.013	0.015	0.021	0.011	0.022	0.013
Testis	Mean	0.022	0.021	0.038	0.021	0.042	0.058	0.029	0.033	0.036
	1 SD	0.010	0.013	0.022	0.008	0.010	0.031	0.008	0.016	0.011
Bone	Mean	0.233	0.377	0.369	1.049	1.518	1.081	0.930	0.569	0.656
	1 SD	0.021	0.035	0.121	0.236	0.049	0.211	0.084	0.308	0.182
Muscle	Mean	0.011	0.035	0.034	0.043	0.052	0.041	0.034	0.029	0.025
	1 SD	0.000	0.010	0.015	0.017	0.023	0.026	0.017	0.021	0.020

ID: injected dose. 0.5, 1, 2, 4, 8, 16, 32, 48, and 64 d were time at which animals were anesthetized and sacrificed, blood was collected, tissues were weighed, and radioactivity was quantified. *n* = 5 mice at each time point.

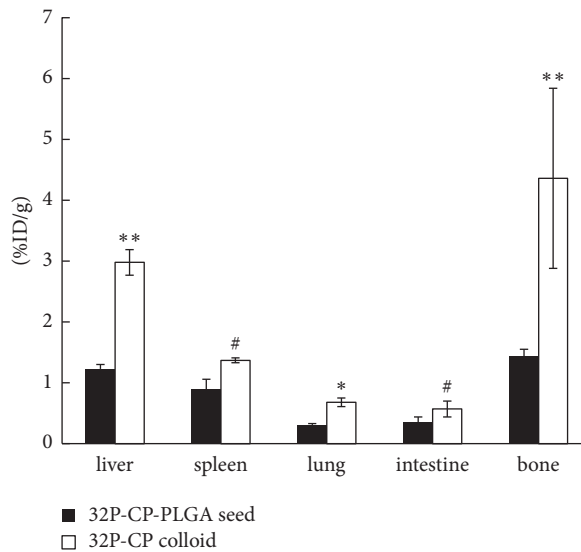


FIGURE 2: Bar graphs of the peak uptake of <sup>32</sup>P-CP in important organs after intratumour administration of <sup>32</sup>P-CP-PLGA seeds and <sup>32</sup>P-CP colloids (\*\* indicates *P* < 0.01, \* indicates *P* < 0.05, and # indicates *P* > 0.05).

TABLE 2: Biodistribution of  $^{32}\text{P}$ -CP particle in nude mice bearing U87MG glioma after intratumor injection of  $^{32}\text{P}$ -CP colloids ( $n = 5$ ).

Tissue		Radioactivity distribution (%ID/g)								
		0.5 d	1 d	2 d	4 d	8 d	16 d	32 d	48 d	64 d
Tumor	Mean	429.1	455.60	570.5	470.76	525.57	676.25	---	---	---
	1 SD	110.2	265.72	159.4	218.05	52.21	61.15	---	---	---
Blood	Mean	0.057	0.073	0.079	0.046	0.022	0.048	0.02	0.079	0.070
	1 SD	0.021	0.035	0.010	0.011	0.047	0.014	0.011	0.014	0.012
Heart	Mean	0.171	0.124	0.232	0.207	0.148	0.097	0.009	0.246	0.183
	1 SD	0.052	0.013	0.151	0.105	0.049	0.054	0.035	0.113	0.071
Liver	Mean	0.253	0.146	1.690	1.656	2.918	1.219	1.122	2.629	2.465
	1 SD	0.110	1.077	0.745	1.076	0.076	0.171	2.037	0.041	0.016
Spleen	Mean	0.324	0.249	0.559	1.241	0.913	0.769	0.334	0.469	0.356
	1 SD	0.197	0.128	0.121	0.052	0.021	0.061	0.087	0.011	0.019
Lung	Mean	0.233	0.163	0.239	0.256	0.433	0.512	0.222	0.041	0.052
	1 SD	0.103	0.018	0.078	0.127	0.212	0.015	0.013	0.021	0.010
Kidney	Mean	0.192	0.153	0.269	0.256	0.019	0.071	0.210	0.269	0.056
	1 SD	0.074	0.028	0.121	0.127	0.017	0.092	0.007	0.034	0.019
Stomach	Mean	0.056	0.097	0.016	0.033	0.019	0.113	0.241	0.049	0.036
	1 SD	0.034	0.003	0.011	0.008	0.017	0.011	0.015	0.021	0.019
Intestine	Mean	0.203	0.038	0.154	0.159	0.156	0.136	0.408	0.176	0.248
	1 SD	0.109	0.012	0.035	0.063	0.127	0.051	0.031	0.063	0.030
Pancreas	Mean	0.030	0.101	0.049	0.074	0.077	0.182	0.020	0.035	0.055
	1 SD	0.024	0.002	0.011	0.015	0.024	0.01	0.021	0.012	0.022
Brain	Mean	0.017	0.026	0.011	0.036	0.024	0.013	0.008	0.013	0.024
	1 SD	0.019	0.021	0.010	0.023	0.014	0.011	0.012	0.021	0.014
Thyroid	Mean	0.016	0.077	0.026	0.044	0.026	0.022	0.012	0.021	0.035
	1 SD	0.021	0.007	0.011	0.013	0.015	0.021	0.011	0.022	0.013
Testis	Mean	0.022	0.041	0.038	0.021	0.042	0.018	0.029	0.033	0.036
	1 SD	0.012	0.013	0.022	0.008	0.010	0.031	0.008	0.016	0.011
Bone	Mean	0.762	2.343	2.369	3.856	4.004	3.541	2.605	2.869	2.656
	1 SD	0.421	0.035	0.121	0.236	1.093	0.211	0.084	0.308	0.182
Muscle	Mean	0.007	0.083	0.034	0.043	0.046	0.092	0.053	0.049	0.045
	1 SD	0.003	0.010	0.015	0.017	0.023	0.026	0.017	0.021	0.020

ID: injected dose. 0.5, 1, 2, 4, 8, 16, 32, 48, and 64 d were time at which animals were anesthetized and sacrificed, blood was collected, tissues were weighed, and radioactivity was quantified.  $n = 5$  mice at each time point.

internal heterogeneity was observed on day 8, reflecting natural necrosis. The tumour uptake (%ID/cm<sup>3</sup>) of  $^{68}\text{Ga}$ -3PRGD<sub>2</sub> in the SG ( $8.50 \pm 1.32$ ) was higher than that in the P-CP-PLGA group ( $7.15 \pm 1.49$ ,  $p < 0.05$ ) on day 0.5, while the tumour uptake in the SG ( $5.13 \pm 1.06$ ) was lower than that in the P-CP-PLGA group ( $8.16 \pm 1.26$ ,  $p < 0.01$ ) on day 2. The tumour time-growth curve displayed no significant changes during 10 days in the SG or CG after  $^{32}\text{P}$  administration, and 40% (2/5) of the mice demonstrated tumour growth near the scar on day 20.

**3.5. Immunohistochemistry Examination.** Immunofluorescence staining was performed to examine the  $\alpha_v\beta_3$  and CD31 expression levels in tumour tissues from the xenografted gliomas in the SG and P-CP-PLGA group on days 0.5, 2, and 4; as shown in Figure 6, compared with the P-CP-PLGA seed group, the quantitation of the glioma anti- $\alpha_v\beta_3$  immunofluorescence levels in the SG revealed a 1.37-fold ( $\pm 0.15$ ) mean increase ( $\pm$ SD) on day 0.5 and 0.74-fold ( $\pm 0.22$ )

and 0.15-fold ( $\pm 0.05$ ) decreases on days 2 and 4, respectively. IHC examination was not performed on days 8 and 16 due to increased areas of necrosis and scar formation.

#### 4. Discussion

$^{32}\text{P}$ -CP-PLGA seed is a biodegradable dosage form of  $^{32}\text{P}$ , utilizing PLGA as the controlled release carrier for drug delivery. In addition to its easy preparation in large amounts, the main advantage of  $^{32}\text{P}$ -CP-PLGA seeds is their delivery of high-dose radiation to the tumour and long intratumoural radioactive effective half-life with minimal distribution and damage to systemic tissues. A radioactivity gradient formed inside the tumour with potential effect to enhance the intratumour fire effect, reduce damage to adjacent tissues, and avoid the implantation of low radioactivity seeds in the peripheral part of the tumours.

No significant difference was observed in tumour uptake of  $^{32}\text{P}$ -CP particles in the SG and CG immediately after

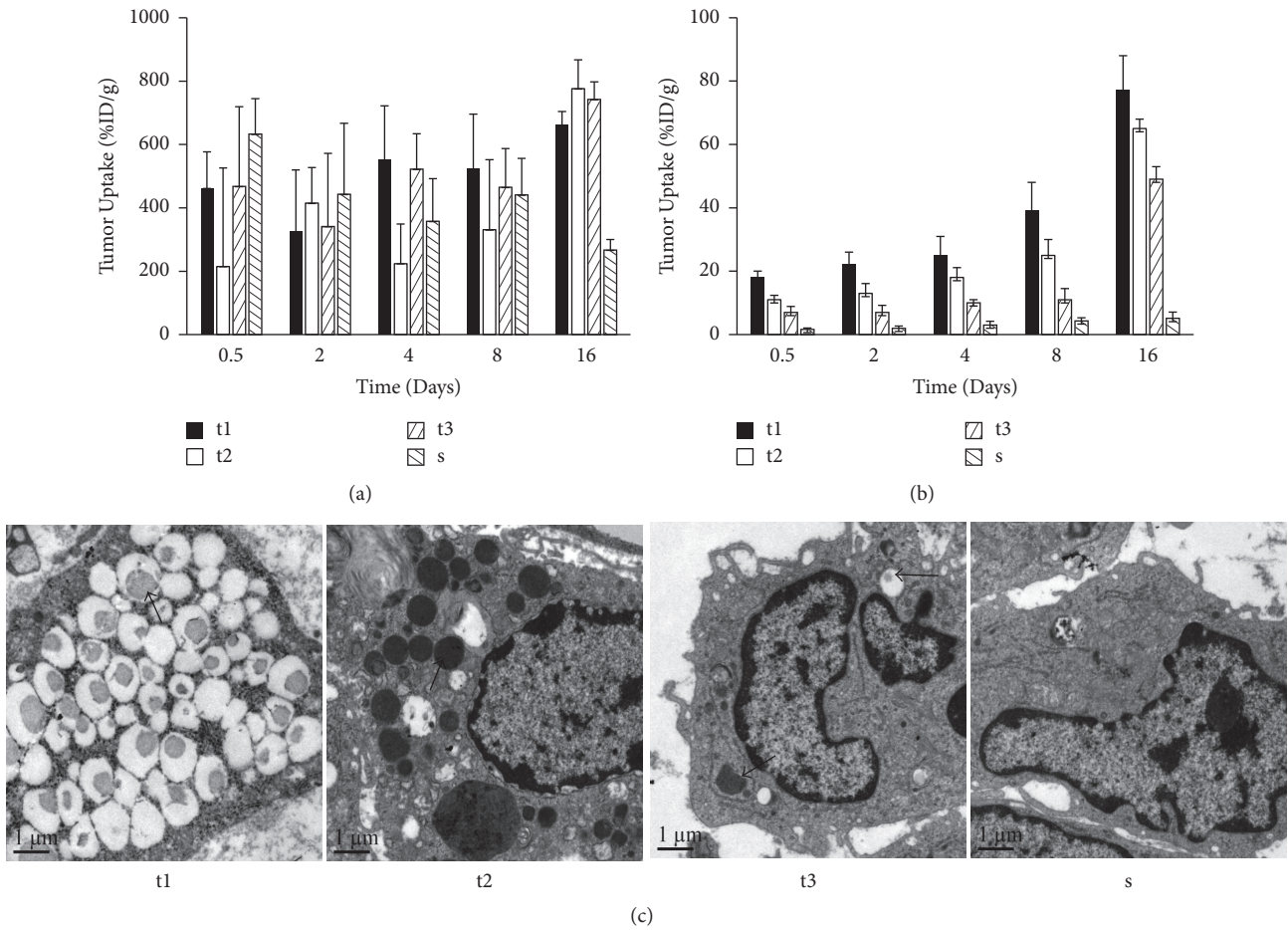


FIGURE 3: Bar graphs and SEM results of <sup>32</sup>P-CP distribution in tumour and adjacent normal tissues at different time points after the intratumoural administration of SG and CG. (a) <sup>32</sup>P-CP distribution in tumour and adjacent normal tissues at different time points in CG. The regional peak uptake in tumour tissues (t2) on day 16 was higher than day 8 (t1) (# means  $P < 0.05$ ) [t1, t2, and t3 indicate tumour tissues at different distance from the seed (SG) or the core of the tumour (CG), near to far, and “s” indicates tissues surrounding the tumour]. (b) <sup>32</sup>P-CP distribution in tumour and adjacent normal tissues in the SG (significant difference between t1 and t2, t2 and t3, and t3 and s,  $P < 0.05$ ) (c). SEM results of tumour and adjacent normal tissues (t1, t2, t3, and s). The <sup>32</sup>P-CP particles are indicated with a black arrow. Irregularity of radioactivity distribution can be observed in the tumour and adjacent tissues in the CG, while a radioactivity gradient formed in the SG. The results were confirmed by SEM.

administration, except for the occurrence of leakage of colloidal <sup>32</sup>P-CP in the CG. However, the dynamic radioactivity distribution indicated more retention and longer effective half-life of <sup>32</sup>P-CP in the tumour and less or even undetectable distribution in other tissues in the SG compared with that in the CG. The principal mechanism likely involved the arrest of <sup>32</sup>P-CP particles inside the seeds using the framework of PLGA, and their release and slow drainage was determined by the biodegradation of PLGA. A radioactivity concentration gradient, formed by the <sup>32</sup>P-CP particles released from the <sup>32</sup>P-CP-PLGA seeds, was observed inside the tumour. The tumour uptake (%ID/g) was extremely high, primarily because more than 95% (%ID) of the implanted <sup>32</sup>P remained in the small tumour tissues (approximately 0.2 cm<sup>3</sup>) during the first few days. The increased uptake primarily reflected tumour shrinkage on day 16 and scar formation. The released <sup>32</sup>P-CP particles increase the killing

range and enhance the therapeutic effect without noticeable damage to adjacent tissues. The gradient gap was predominant in the first few days and narrowed with increasing release of <sup>32</sup>P-CP particles and tumour shrinkage. However, the irregular and uneven intratumour distribution of <sup>32</sup>P-CP colloids in the CG led to a therapeutic blind area, tumour relapse, and leakage from the injection site, resulting in damage to the adjacent tissues.

The <sup>32</sup>P-CP particles drained from the tumour were primarily distributed throughout reticuloendothelial systems, such as the liver in the CG, and were less than reported [9]. This effect potentially reflects the use of gelatine sponge to prevent or reduce the leakage of <sup>32</sup>P-CP colloids. The uptake of <sup>32</sup>P-CP particles in normal tissues peaked at 16 days and likely involved the following three mechanisms. First, <sup>32</sup>P-CP particles at the surface or inlaying the outer 1/3 of the seeds tended to be released, while those inlaid

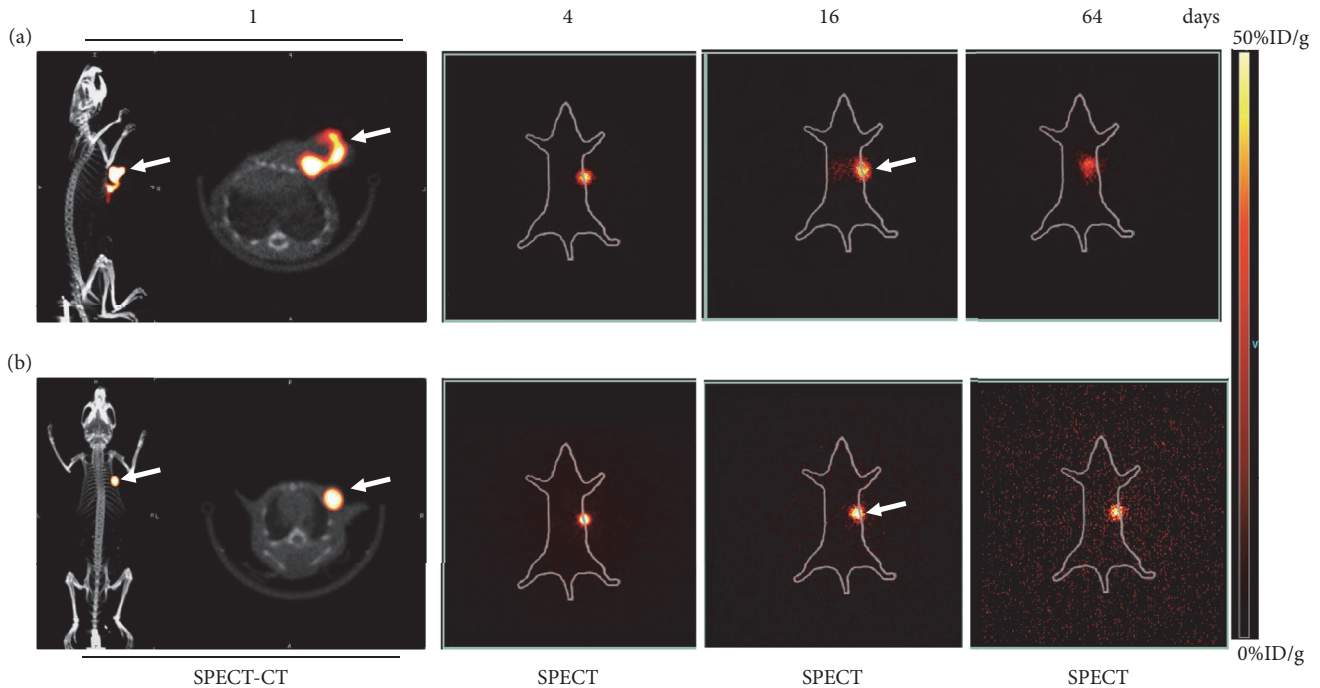


FIGURE 4: Representative micro-SPECT/CT or micro-SPECT images in the SG and CG. Micro-SPECT/CT images on day 1 and micro-SPECT images on days 4, 16, and 64 were obtained after intratumoural injection of colloidal  $^{32}\text{P}$ -CP ((a)  $^{32}\text{P}$ -CP colloids were in irregular shapes with leak from injection site and much notable abnormal distribution and liver appearance) and intratumoural implantation of  $^{32}\text{P}$ -CP-PLGA seeds ((b)  $^{32}\text{P}$ -CP-PLGA seeds demonstrated the shape of a dot. No significant difference or appearance of other organs was observed until 64 days). The white arrows refer to tumors.

near the core stagnated inside, although there was gradual formation of tunnels and cavities. Second, the decrease or lack of regional circulation around the seeds resulting from tumour tissue necrosis and scar formation may inhibit the drainage of released  $^{32}\text{P}$ -CP particles. Third, the experimental period used in the present study may not be long enough. Pathological changes of important organs were absent in the SG.

$^{32}\text{P}$  bremsstrahlung SPECT imaging facilitates the positioning, effective for half-life evaluation under physical conditions [21]. Any immigration or abnormal uptake can easily be detected, and SPECT-CT fusion techniques with a certain postprocessing attenuation correction algorithm may contribute to precise localization, dosimetry studies, and future establishment of brachytherapy in clinical settings [6].

$^{18}\text{F}$ -FDG PET-CT imaging was widely used to monitor therapeutic effect of tumour treatment. However, two potential disadvantages limit its use in gliomas. One disadvantage is the high distribution of glioma in normal brain tissues, particularly in the cerebral cortex, basal ganglia, and thalamus, where glioma is prone to occur. The other disadvantage is the increased accumulation of tumour tissue when inflammatory cells, such as macrophages, are present, particularly at the early stages of treatment [19].  $^{18}\text{F}$ -FPPRGD<sub>2</sub> is superior to  $^{18}\text{F}$ -FDG because the uptake of  $^{18}\text{F}$ -FPPRGD<sub>2</sub> is not influenced by tumour-associated macrophages after chemotherapy, and the remarkable distribution of  $^{68}\text{Ga}$ -3PRGD<sub>2</sub> in the

U87MG xenografts is observed with low background in the normal brain tissues compared with  $^{18}\text{F}$ -FDG [17, 19].  $^{68}\text{Ga}$  is easily accessible from a  $^{68}\text{Ge}$ - $^{68}\text{Ga}$  generator and showed similar labelling characteristics with therapeutic isotopes, such as  $^{177}\text{Lu}$ , with DOTA and NOTA as linkers. In the present study, the initial increased uptake of  $^{68}\text{Ga}$ -3PRGD<sub>2</sub> in glioma was observed on day 0.5 after  $^{32}\text{P}$ -CP-PLGA seed implantation. The possible mechanism involves the rapid upregulation of integrin expression induced by a low-to-intermediate dose of radiation, as previously reported [22]. Thus, the increased glioma uptake of  $^{68}\text{Ga}$ -3PRGD<sub>2</sub> on day 0.5 in the SG is possibly due to radiation, while the decrease on day 2 is due to cell damage resulting from accumulated  $^{32}\text{P}$  radiation and therapeutic effects [23]. This effect occurred much earlier than the tumour volume reduction and was confirmed using IHC.  $^{68}\text{Ga}$ -3PRGD<sub>2</sub> imaging has potential to serve as an important tool for the therapeutic evaluation of  $^{32}\text{P}$  brachytherapy of glioma as early as day 2. Thus, the precise relationship between the  $\beta^-$  radiation dose and integrin expression upregulation needs further study.

## 5. Conclusions

$^{32}\text{P}$ -CP-PLGA seeds, controlling the release of entrapped  $^{32}\text{P}$ -CP particles, are promising for glioma brachytherapy.  $^{68}\text{Ga}$ -3PRGD<sub>2</sub> imaging shows potential for early response evaluation of  $^{32}\text{P}$ -CP-PLGA seeds brachytherapy.

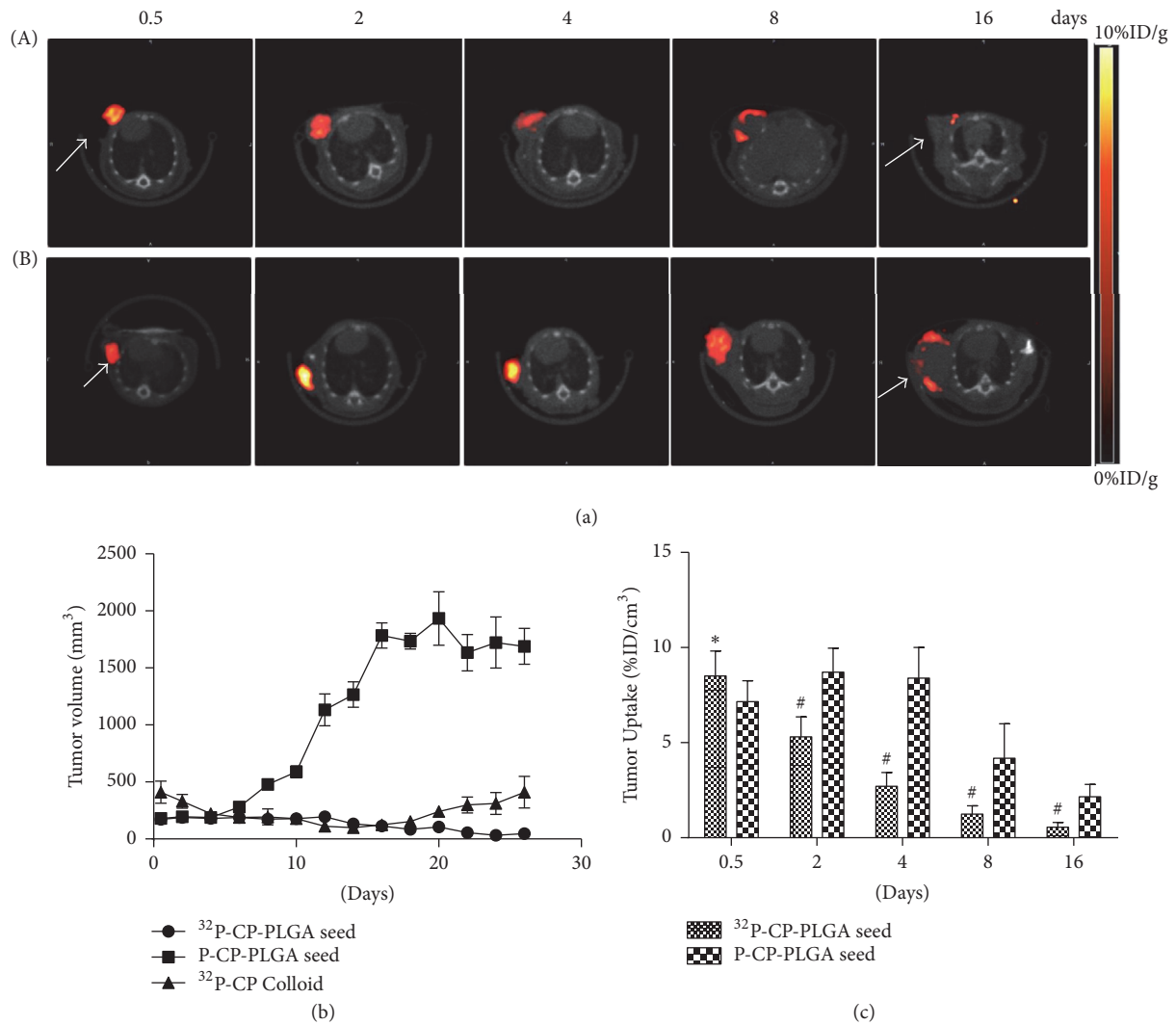


FIGURE 5: <sup>68</sup>Ga-3PRGD<sub>2</sub> micro-PET-CT imaging during <sup>32</sup>P brachytherapy and tumour volume measurement using a caliper. (a) The <sup>68</sup>Ga-3PRGD<sub>2</sub> micro-PET/CT transverse images of nude mice bearing glioma on days 0.5, 2, 4, 8, and 16 after intratumoural implantation of radioactive <sup>32</sup>P-CP-PLGA seeds (A) and nonradioactive P-CP-PLGA seeds (B). (b) Tumour volume was measured using a caliper every other day after intratumoural administration of <sup>32</sup>P-CP-PLGA seeds, <sup>32</sup>P-CP colloid, and nonradioactive P-CP-PLGA seed. (c) Tumour uptake of <sup>68</sup>Ga-3PRGD<sub>2</sub> was quantified based on micro-PET/CT imaging and compared between radioactive and nonradioactive seeds group. Tumour uptake (%ID/g) of <sup>68</sup>Ga-3PRGD<sub>2</sub> was significantly different at the same points. In <sup>32</sup>P-CP-PLGA seeds group, distribution heterogeneity of <sup>68</sup>Ga-3PRGD<sub>2</sub> was observed on day 2 and was even significant and toroidal on day 4, with slight accumulation of radiotracer on day 8 and being almost negative on day 16. The distribution of <sup>68</sup>Ga-3PRGD<sub>2</sub> was uniform at 8 days after nonradioactive seed implantation. Internal absence was observed on day 16, reflecting ulcer formation. # means tumour uptake of <sup>68</sup>Ga-3PRGD<sub>2</sub> in P-CP-PLGA seeds group was significantly lower than <sup>32</sup>P-CP-PLGA seeds group (*P* < 0.05) while \* means tumour uptake of <sup>68</sup>Ga-3PRGD<sub>2</sub> in P-CP-PLGA seeds group was significantly higher than <sup>32</sup>P-CP-PLGA seeds group (*P* < 0.05). The white arrows refer to tumors.

**Abbreviations**

- <sup>32</sup>P: Phosphorus-32
- <sup>68</sup>Ga: Gallium-68
- <sup>18</sup>F: Fluorine-18
- CT: Computed tomography
- PET: Positron emission tomography
- SPECT: Single photon emission computed tomography
- <sup>32</sup>P-CP: <sup>32</sup>P-chromic phosphate

- <sup>32</sup>P-CP-PLGA: <sup>32</sup>P-chromic phosphate-poly(lactide-co-glycolide)
- %ID/g: Percent injected dose per gram
- FDG: Fludeoxyglucose.

**Disclosure**

Guoqiang Shao, Yuebing Wang, and Xianzhong Liu are co-first authors. An earlier version of this work was presented as an abstract at MTAI: Educational Exhibits Posters 2017.

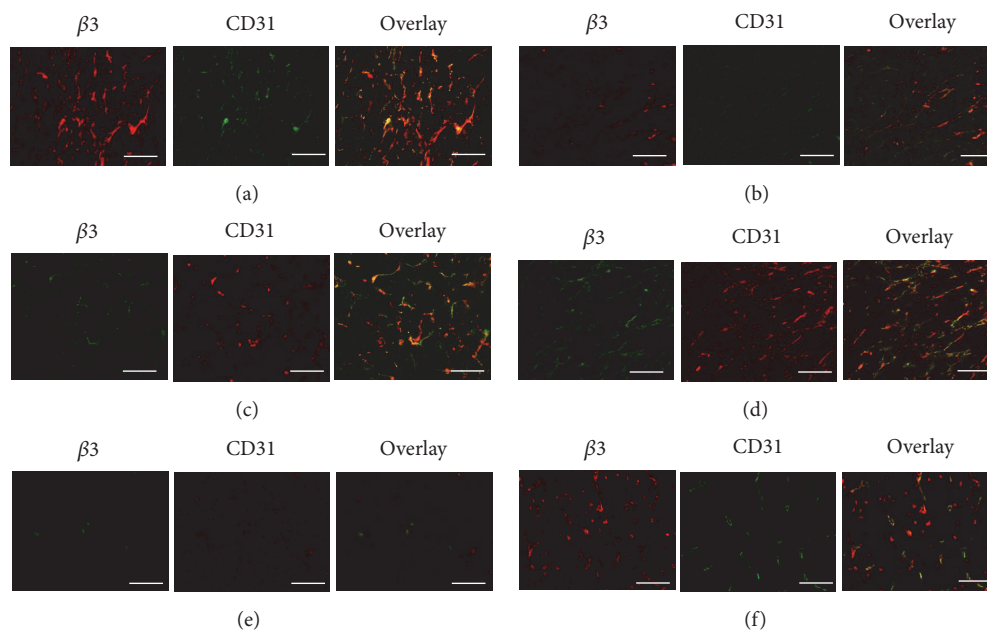


FIGURE 6: Representative immunohistochemical images for frozen glioma slices from xenografted glioma tumours at different time points (day 0.5: (a, b); day 2: (c, d); day 4: (e, f)) after intratumoural implantation of radioactive  $^{32}\text{P}$ -CP-PLGA seeds (a, c, e) and nonradioactive P-CP-PLGA seeds (b, d, f). The CD31 was used to label the tumour endothelial cells on blood vessels. The integrin  $\beta 3$  was visualized with Cy3 (red), and CD31 was visualized with fluorescein isothiocyanate (green) under an Olympus fluorescence system, scale bar: 50  $\mu\text{m}$ .

## Conflicts of Interest

The authors declare that they have no conflicts of interest.

## Authors' Contributions

Guoqiang Shao, Yuebing Wang, Xianzhong Liu, Meili Zhao, Jinhua Song, Peiling Huang, Feng Wang, and Zizheng Wang participated in the study design, execution, and analysis, manuscript drafting, and critical discussions. Guoqiang Shao, Yuebing Wang, and Xianzhong Liu have contributed equally to this work.

## Acknowledgments

This study was partly supported by grants from the National High Technology Research and Development Program of China (2007AA02Z471), the National Key Research and Development Program of China (2017YFA0103201), the National Natural Science Foundation of China (81301247, 81501528), the Natural Science Foundation of Jiangsu Province (BK20130082), Jiangsu Provincial Medical Youth Talent (QNRC2016075), and the Tianjin Natural Science Foundation (15JCQNJC10600).

## References

- [1] K. H. Plate, A. Scholz, and D. J. Dumont, "Tumor angiogenesis and anti-angiogenic therapy in malignant gliomas revisited," *Acta Neuropathologica*, vol. 124, no. 6, pp. 763–775, 2012.
- [2] M. I. Ruge, P. Kickingereder, S. Grau et al., "Stereotactic iodine-125 brachytherapy for the treatment of WHO grades II and III gliomas located in the central sulcus region," *Neuro-Oncology*, vol. 15, no. 12, pp. 1721–1731, 2013.
- [3] M. J. Salgueiro, H. Duran, M. Palmieri et al., "Bioevaluation of  $^{32}\text{P}$  patch designed for the treatment of skin diseases," *Nuclear Medicine and Biology*, vol. 35, no. 2, pp. 233–237, 2008.
- [4] B. P. Marr, D. H. Abramson, G. N. Cohen, M. J. Williamson, B. McCormick, and C. A. Barker, "Intraoperative high-dose rate of radioactive phosphorus 32 brachytherapy for diffuse recalcitrant conjunctival neoplasms: A retrospective case series and report of toxicity," *JAMA Ophthalmology*, vol. 133, no. 3, pp. 283–289, 2015.
- [5] M. R. Folkert, M. H. Bilsky, G. N. Cohen et al., "Intraoperative  $^{32}\text{P}$  high-dose rate brachytherapy of the dura for recurrent primary and metastatic intracranial and spinal tumors," *Neurosurgery*, vol. 71, no. 5, pp. 1003–1010, 2012.
- [6] A. M. Denis-Bacelar, M. Romanchikova, S. Chittenden et al., "Patient-specific dosimetry for intracavitary  $^{32}\text{P}$ -chromic phosphate colloid therapy of cystic brain tumours," *European Journal of Nuclear Medicine and Molecular Imaging*, vol. 40, no. 10, pp. 1532–1541, 2013.
- [7] K. A. Alimi, N. Firusian, and W. Dempke, "Effects of intralésional  $^{32}\text{P}$  chromic phosphate in refractory patients with head and neck tumours," *Anticancer Research*, vol. 27, no. 4 C, pp. 2997–3000, 2007.
- [8] I. J. Jaca Montijo, V. Khurana, W. M. Alazmi, S. E. Order, and J. S. Barkin, "Vascular pancreatic gastric fistula: A complication of colloidal  $^{32}\text{P}$  injection for nonresectable pancreatic cancer," *Digestive Diseases and Sciences*, vol. 48, no. 9, pp. 1758–1759, 2003.
- [9] J. H. Tian, B. X. Xu, J. M. Zhang, B. W. Dong, P. Liang, and X. D. Wang, "Ultrasound-guided internal radiotherapy using yttrium-90-glass microspheres for liver malignancies, Journal

- of nuclear medicine : official publication," *Society of Nuclear Medicine*, vol. 37, pp. 958–963, 1996.
- [10] G. Gu, Q. Hu, X. Feng et al., "PEG-PLA nanoparticles modified with APTEDB peptide for enhanced anti-angiogenic and anti-glioma therapy," *Biomaterials*, vol. 35, no. 28, pp. 8215–8226, 2014.
- [11] D. Jain, A. Bajaj, R. Athawale et al., "Surface-coated PLA nanoparticles loaded with temozolomide for improved brain deposition and potential treatment of gliomas: Development, characterization and in vivo studies," *Drug Delivery*, vol. 23, no. 3, pp. 999–1016, 2016.
- [12] R. Tong, N. P. Gabrielson, T. M. Fan, and J. Cheng, "Polymeric nanomedicines based on poly(lactide) and poly(lactide-co-glycolide)," *Current Opinion in Solid State & Materials Science*, vol. 16, no. 6, pp. 323–332, 2012.
- [13] X. He, R. Jia, L. Xu et al., "<sup>32</sup>P-chromic phosphate-poly(L-lactide) seeds of sustained release and their brachytherapy for prostate cancer with lymphatic metastasis," *Cancer Biotherapy and Radiopharmaceuticals*, vol. 27, no. 7, pp. 446–451, 2012.
- [14] I. Bala, S. Hariharan, and M. N. V. R. Kumar, "PLGA nanoparticles in drug delivery: the state of the art," *Critical Reviews in Therapeutic Drug Carrier Systems*, vol. 21, no. 5, pp. 387–422, 2004.
- [15] J. S. C. Loo, C. P. Ooi, and F. Y. C. Boey, "Degradation of poly(lactide-co-glycolide) (PLGA) and poly(L-lactide) (PLLA) by electron beam radiation," *Biomaterials*, vol. 26, no. 12, pp. 1359–1367, 2005.
- [16] D. Li, X. Zhao, L. Zhang et al., "<sup>68</sup>Ga-PRGD2 PET/CT in the evaluation of glioma: A prospective study," *Molecular Pharmaceutics*, vol. 11, no. 11, pp. 3923–3929, 2014.
- [17] D. Fan, X. Zhang, L. Zhong et al., "<sup>68</sup>Ga-Labeled 3PRGD<sub>2</sub> for Dual PET and Cerenkov Luminescence Imaging of Orthotopic Human Glioblastoma," *Bioconjugate Chemistry*, vol. 26, no. 6, pp. 1054–1060, 2015.
- [18] J. Shi, Z. Jin, X. Liu et al., "PET imaging of neovascularization with <sup>68</sup>Ga-3PRGD2 for assessing tumor early response to endostar antiangiogenic therapy," *Molecular Pharmaceutics*, vol. 11, no. 11, pp. 3915–3922, 2014.
- [19] X. Sun, Y. Yan, S. Liu et al., "<sup>18</sup>F-FPPRGD2 and <sup>18</sup>F-FDG PET of response to Abraxane therapy," *Journal of Nuclear Medicine*, vol. 52, no. 1, pp. 140–146, 2011.
- [20] G. Shao, Y. Zhou, F. Wang, and S. Liu, "Monitoring glioma growth and tumor necrosis with the U-SPECT-II/CT scanner by targeting integrin  $\alpha v \beta 3$ , Molecular imaging," 12, pp. 39–48, 2013.
- [21] S. Balachandran, L. McGuire, S. Flanigan, H. Shah, and C. M. Boyd, "Bremsstrahlung imaging after <sup>32</sup>P treatment for residual suprasellar cyst," *International Journal of Nuclear Medicine and Biology*, vol. 12, no. 3, pp. 215–221, 1985.
- [22] H. Yao, Z.-Z. Zeng, K. S. Fay et al., "Role of  $\alpha 5 \beta 1$  integrin up-regulation in radiation-induced invasion by human pancreatic cancer cells," *Translational Oncology*, vol. 4, no. 5, pp. 282–292, 2011.
- [23] S. Ning, J. Tian, D. J. Marshall, and S. J. Knox, "Anti- $\alpha v$  integrin monoclonal antibody intetumumab enhances the efficacy of radiation therapy and reduces metastasis of human cancer xenografts in nude rats," *Cancer Research*, vol. 70, no. 19, pp. 7591–7599, 2010.

## Research Article

# Preparation of $^{68}\text{Ga}$ -PSMA-11 with a Synthesis Module for Micro PET-CT Imaging of PSMA Expression during Prostate Cancer Progression

Yuebing Wang <sup>1</sup>, Guoqiang Shao,<sup>2</sup> Jianping Wu,<sup>3</sup> Can Cui,<sup>2</sup> Shimin Zang,<sup>2</sup>  
Fan Qiu,<sup>2</sup> Ruipeng Jia <sup>3</sup>, Zizheng Wang <sup>2</sup>, and Feng Wang <sup>2</sup>

<sup>1</sup>Department of Biochemistry, School of Medicine, Nankai University, Tianjin 300071, China

<sup>2</sup>Department of Nuclear Medicine, Nanjing First Hospital, Nanjing Medical University, Nanjing 210006, China

<sup>3</sup>Department of Urology Surgery, Nanjing First Hospital, Nanjing Medical University, Nanjing 210006, China

Correspondence should be addressed to Zizheng Wang; 13770920210@163.com and Feng Wang; fengwangcn@hotmail.com

Received 29 September 2017; Accepted 4 March 2018; Published 26 April 2018

Academic Editor: Barbara Palumbo

Copyright © 2018 Yuebing Wang et al. This is an open access article distributed under the Creative Commons Attribution License, which permits unrestricted use, distribution, and reproduction in any medium, provided the original work is properly cited.

**Objective.** To synthesize  $^{68}\text{Ga}$ -Glu-urea-Lys(Ahx)-HBED-CC ( $^{68}\text{Ga}$ -PSMA-11) with a synthesis module and investigate PET-CT imaging to monitor PSMA expression during prostate cancer (PCa) progression and tumor growth in mice bearing subcutaneous PCa xenografts. **Method.** The radiochemical purity and stability of  $^{68}\text{Ga}$ -PSMA-11 were determined via radio-HPLC. The PCa cell lines of different PSMA expression levels (PC3, VCAP±, CWR22RV1+, and LNCaP++) were selected to mimic the PCa progression.  $^{68}\text{Ga}$ -PSMA-11 biodistribution was studied by dissection method and *in vivo* imaging with micro PET-CT. The expression levels of PSMA in tumor cells and tissues were analyzed by immunofluorescence, flow cytometry, and western blot. The correlation between PSMA expression and radio-uptake was also evaluated. 2-PMPA preadministration served as a block group. **Results.** The radiochemical purity of  $^{68}\text{Ga}$ -PSMA-11 was  $99.6 \pm 0.1\%$  and stable *in vitro* for 2 h. The equilibrium binding constant (Kd) of  $^{68}\text{Ga}$ -PSMA-11 to LNCaP, CWR22Rv1, PC-3, and VCAP cells was  $4.3 \pm 0.8$  nM,  $16.4 \pm 1.3$  nM,  $225.3 \pm 20.8$  nM, and  $125.6 \pm 13.1$  nM, respectively. Results of tumor uptake (% ID and % ID/g or % ID/cm<sup>3</sup>) of  $^{68}\text{Ga}$ -PSMA-11 in biodistribution and micro PET imaging were LNCaP > CWR22RV1 > PC-3 and VCAP due to different PSMA expression levels. It was confirmed by flow cytometry, western blot, and immunofluorescence. Tumor uptake (% ID/cm<sup>3</sup>) of  $^{68}\text{Ga}$ -PSMA-11 increased with the tumor anatomical volume in quadratic polynomial fashion and reached the peak (when tumor volume was 0.5 cm<sup>3</sup>) earlier than tumor uptake (% ID). Tumor uptake (% ID/cm<sup>3</sup>) of  $^{68}\text{Ga}$ -PSMA-11 based on functional volume correlated well with the PSMA expression in a linear manner ( $y = 9.35x + 2.59$ ,  $R^2 = 0.8924$ , and  $p < 0.0001$ ); however, low dose 2-PMPA causes rapid renal clearance of increased tumor/kidney uptake of  $^{68}\text{Ga}$ -PSMA-11. **Conclusions.** The  $^{68}\text{Ga}$ -PSMA-11 PET-CT imaging could invasively evaluate PSMA expression during PCa progression and tumor growth with % ID/cm<sup>3</sup> (based on functional volume) as an important index. Low dose 2-PMPA preadministration might be a choice to decrease kidney uptake of  $^{68}\text{Ga}$ -PSMA-11.

## 1. Introduction

In spite of great efforts and recent advances in early diagnosis and surgical intervention, prostate cancer (PCa) remains the most commonly diagnosed cancer and second leading cause of cancer-related death in men over 40 years [1]. Therapeutic effects for localized PCa in patients of stages I, II, and III are relatively fine by standard employed treatments. PCa patients with relapse, distant metastasis (stage IV), and high risk of

PCa progression and/or death are all considered as advanced PCa [2, 3]. Most of them become resistant to hormonal approach and developed a metastatic castration-resistant prostate cancer (mCRPC) shortly after androgen deprivation therapy. Docetaxel therapy, most widely used for mCRPC, is of decreasing therapeutic efficacy due to lack of specificity and associated side effects. It becomes a main challenge to effectively diagnose and select appropriate treatment options for advanced PCa and mCRPC.

Prostate-specific membrane antigen (PSMA), a type II extracellular glycoprotein, is highly expressed in most prostate cancer cells and low or negative in most normal organ systems [4–6]. As a consequence, PSMA represents an ideal target for specific prostate cancer imaging and endoradiotherapy; moreover, PSMA-targeting antibodies, inhibitors, and peptides have been rapidly developed for prostate cancer targeting endoradiotherapy and chemotherapy. Importantly, PSMA is presented on the cell surface or in the cell plasma, and it is not shed into the circulation [7], so it is not a convenient biomarker to be examined in blood as serum PSA. Pathology diagnosis served as the gold standard and decisions for PSMA-targeting therapies are mainly made on the basis of PSMA expression in primary tumors. However, PSMA expression levels vary in different prostate cancers. The PSMA expression is highly upregulated in advanced, poorly differentiated PCas and increases with tumor aggressiveness [6, 8]. The expression levels of PSMA are reported to be associated with tumor grade and clinical outcome [9, 10]. Biopsies of recurrent or metastasis lesions are infrequently performed. Pretreatment imaging or biomarkers for patient selection and response predicting to PSMA-directed therapy are urgently needed.

Glu-urea-Lys(Ahx)-HBED-CC(Glu-urea-lys-(*N,N'*-bis-[2-hydroxy-5-(carboxyethyl)benzyl]ethylenediamine-*N,N'*-diacetic acid)) containing a HBED-CC chelator is used for the preparation of  $^{68}\text{Ga}$ -PSMA-II.  $^{68}\text{Ga}$ -PSMA-II prepared in standard protocol at 95°C can bind to PSMA with high affinity and specificity [11–13]. In this study, we prepared  $^{68}\text{Ga}$ -PSMA-II with semiautomatic module. PCa cell lines with different PSMA expression levels were selected to mimic PCa progression.  $^{68}\text{Ga}$ -PSMA-II imaging was performed to monitor PSMA expression changes during tumor growth. The aim of this study was to evaluate the feasibility of  $^{68}\text{Ga}$ -PSMA-II PET-CT imaging to reflect tumor progression and growth for further PSMA-targeted therapy in the clinic.

## 2. Materials and Methods

**2.1. Materials.** LNCaP, CWR22Rv1, PC-3, and VCAP prostate cancer cell lines were obtained from the American Type Culture Collection (ATCC, Manassas, VA). Nude mice (male, 14–16 g, 5–6 wk) were supplied by the Chinese Academy of Medical Sciences, Shanghai, China. Primary antibody is anti-PSMA antibody (YPSMA-1, Abcam, USA). Secondary antibody is goat anti-rabbit IgG-HRP (Santa Cruz biotechnology, USA). DAPI (4',6-Diamidino-2-Phenylindole, Dihydrochloride) was purchased from Life Technologies (USA). All other chemicals and cell-culture reagents were purchased from Sigma-Aldrich or Gibco Corporation. The radio-high performance liquid chromatography (radio-HPLC) was performed using a LabAlliance system (Scientific Systems, Inc., State College, PA) equipped with a  $\beta$ -ram IN-US detector and Zorbax C18 column (4.6 mm  $\times$  250 mm, 300 Å pore size).  $^{68}\text{Ge}$ - $^{68}\text{Ga}$  generator and automated module for  $^{68}\text{Ga}$  labeling were offered by ITG Corporation (Germany). We also used Micro PET/CT (Inveon, Siemens, Germany);  $\gamma$ -counter (TY6017, Wizard, PerkinElmer, USA); flow cytometry (Cytomics FC 500, Beckman, USA); Olympic BX51 fluorescence microscope (Olympus America Inc., Center Valley, PA).

**2.2. Cell Culture and Animal Model Establishment.** The LNCaP and CWR22Rv1 cells were cultured in RPMI medium (ATCC, Manassas, VA). PC-3 and VCAP cells were grown in the F-12K medium (ATCC, Manassas, VA). All medium was supplemented with 10% fetal bovine serum (FBS, ATCC) and 1% antibiotic solution (Sigma-Aldrich, St. Louis, MO). Cells were cultured at 37°C in a humidified atmosphere of 5%  $\text{CO}_2$  in air. Cells were grown as monolayers and were harvested or split when they reached 80% confluence to maintain exponential growth. One day before the cell binding experiment, PCa cells were seeded in 24-well plates.

All animal experiments were conducted in accordance with standards of the Institutional Animal Care and Utilization Committee of Nanjing Medical University.  $5 \times 10^6$  PC-3, LNCaP, CWR22Rv1, or PCa cells in 50% Matrigel (Becton Dickinson, Heidelberg, Germany) were injected subcutaneously into the mice left armpit to establish animal models.

**2.3. Synthesis of  $^{68}\text{Ga}$ -PSMA-II with the Synthesis Module and In Vitro Stability Study.**  $^{68}\text{Ga}$ -PSMA-II was semiautomatically synthesized using the labeling module (iTG) as shown in Supplemental Figure 1. The system was lead shielded and the synthesis was performed in Grade IV lab. In brief, the C18 cartridge was preconditioned by passing first 5 ml 70% ethanol through followed by 10 ml PBS via “A” indicated on Supplemental Figure 1. 5  $\mu\text{g}$  (5.3 nmol) of HBED-CC-Lys-CO-Glu in 1 ml of sodium acetate buffer (0.25 M) was injected manually into the reaction vial.  $^{68}\text{GaCl}_3$ , eluted from  $^{68}\text{Ge}$ - $^{68}\text{Ga}$  generator by slow injection of 4 ml of 0.05 M HCl via “C,” was sent to the reactor and kept at 95°C for 5 min. The reaction mixture was pushed through the C18 cartridge and the effluent was collected in the waste vial. The product that remained on the C18 cartridge will pass through a 0.22  $\mu\text{m}$  pore size filter by ethanol (60%) injection via “B” and will be collected in the product vial. Ethanol concentration in product was no more than 10% before use [14].

Radiochemical yield of  $^{68}\text{Ga}$ -PSMA-II prepared using synthesis module is calculated by comparing the activity of  $^{68}\text{Ga}$ -PSMA-II with the total activity. The *in vitro* stability of  $^{68}\text{Ga}$ -PSMA-II was studied by incubating in NaOAC/HAC buffer solutions with PH value of 4, 5.5, and 7.4. Radiochemical stability of  $^{68}\text{Ga}$ -PSMA-II was analyzed using radio-HPLC 2 h after incubation at 37°C. Radio-HPLC was conducted on an LC-20AT system (Shimadzu, Japan) equipped with Zorbax-Rx C18 HPLC column (4.6  $\times$  250 mm). The mobile phase was isocratic with solvent A (water containing 0.05% trifluoroacetic acid, TFA) and solvent B (acetonitrile with 0.05% TFA). Gradient mobile phase was from 0% B and 100% A at 0 min to 100% B and 0% A at 30 min. The flow rate was 1 mL/min.

**2.4. Scatchard Analysis of  $^{68}\text{Ga}$ -PSMA-II.** Scatchard analysis was the standard method for analyzing the equilibrium binding parameters and the dissociation constant (Kd) of a radiolabeled drug with its receptor. The experiment was performed as reported [15]. Briefly, LNCaP, CWR22Rv1, PC-3, and VCAP cells were cultured in 24-well plates for 4 h. They were then coincubated with gradient concentrations

of  $^{68}\text{Ga}$ -PSMA-11 (0.02–40 nM) in 1 ml RPMI1640 containing 0.5% w/v bovine serum albumin for another 3 h on ice. Cells were washed three times with ice-cold PBS and the cell-associated radioactivity was calculated using  $\gamma$ -counter. Nonspecific binding was determined by coincubation with overdose (100  $\mu\text{M}$ ) cold PSMA-11. The specific binding  $^{68}\text{Ga}$ -PSMA-11 was plotted against the bound radioligand/free radioligand ratio. Data were analyzed by linear regression to determine PSMA antigen density per cell and the slope of the line is equal to  $-1/\text{Kd}$ .

**2.5. Biodistribution Studies.**  $^{68}\text{Ga}$ -PSMA-11 biodistribution studies were performed when the long diameter of tumors reached 0.7–0.8 cm. Mice bearing subcutaneous PCa (LNCaP, CWR22Rv1, and PC-3) xenografts were anesthetized by isoflurane inhalation and injected 1.0 MBq of  $^{68}\text{Ga}$ -PSMA-11 in 100  $\mu\text{L}$  of saline via tail vein. Mice bearing LNCaP xenografts with 10 min preinjection of 250  $\mu\text{g}$  (high dose) and 2.5  $\mu\text{g}$  (low dose) 2-(phosphonomethyl) pentane-1,5-dioic acid (2-PMPA) served as the PSMA-block group. Mice were sacrificed for biodistribution analysis 1 h ( $n = 5$  for each) after tail vein injection of  $^{68}\text{Ga}$ -PSMA-11. Important organs and tumor xenografts were harvested, weighed, and counted on  $\gamma$ -counter (PerkinElmer Wizard 1480, Shelton, CT). The percentage of injected dose per organ (% ID) and percentage of injected dose per gram of tissue (% ID/g) were calculated.

**2.6.  $^{68}\text{Ga}$ -PSMA-11 Micro PET-CT Imaging in Mice Bearing PCa Xenografts of Different Cell Line and Tumor Size.** When the long diameter of LNCaP, CWR22Rv1, and PC-3 tumor xenografts reached 0.7–0.8 cm, mice bearing PCa xenografts ( $n = 4$ ) were imaged using micro PET-CT (Inveon, Siemens) 1 h after tail vein injection of  $^{68}\text{Ga}$ -PSMA-11 (5.5 MBq in 100  $\mu\text{L}$  of saline). The energy window ranged from 384 keV to 638 keV. PET scans were acquired for 10 min in list mode followed by CT scans for 5 min. PET images were reconstructed with three-dimensional ordered subsets expectation maximum (3D-OSEM/MAP) algorithm and CT images were reconstructed with Filtered backprojection (FBP). Micro PET-CT images were analyzed using the Inveon Research Workplace software. Region of interest (ROI) and volume of interest (VOI) were drawn slice by slice based on micro PET and micro CT images, respectively, according to our previous study and another report [16, 17]. Briefly, tumor boundary was drawn on micro PET images in transversal section slice by slice with the threshold of 40% of the maximum of standard uptake value (SUV max). Tumor uptake (% ID) was obtained from uptake values within VOI while tumor uptake (% ID/ $\text{cm}^3$ ) on micro CT or micro PET was calculated by dividing tumor uptake (% ID) with tumor volume obtained from micro CT (anatomical volume,  $V_{\text{ct}}$ ) or micro PET (functional volume,  $V_{\text{pet}}$ ).

For the blocking study, mice ( $n = 4$ ) were preinjected with 250  $\mu\text{g}$  or 2.5  $\mu\text{g}$  of 2-PMPA in 100  $\mu\text{L}$  saline 10 min prior to the injection of  $^{68}\text{Ga}$ -PSMA-11. To monitor changes of tumor uptake of  $^{68}\text{Ga}$ -PSMA-11 and PSMA expression during tumor growth, nude mice bearing different size of LNCaP xenografts ( $n = 9$ , from 0.07  $\text{cm}^3$  to 1.72  $\text{cm}^3$ ) accepted  $^{68}\text{Ga}$ -PSMA-11 micro PET-CT imaging.

**2.7. Flow Cytometry, Western Blot, and Immunofluorescence Assessment for PSMA Expression in Tumor Cells and Tumor Tissues.** To analyze PSMA expression, cultured PCa cells or cell suspensions from tumor tissues ( $3 \times 10^5$ ) were incubated with the primary antibody (1 : 50) at 4°C for 2 h. After washing with PBS (1x) three times, cells were incubated with secondary antibody at 4°C for 30 min. After washing and resuspension with PBS, the cells were analyzed using flow cytometry.

Western blot analysis of PSMA cells were performed as reported [18]. In brief, total protein lysates were prepared and quantified using the Bio-Rad DC Protein Assay. The samples were prepared for gel electrophoresis and each well of the gel was loaded with 15  $\mu\text{g}$  protein to run for 40 min. The blotting step was carried out with the Bio-Rad Trans-Blot®Turbo™ RTA Transfer kit. The primary antibody against PSMA (Dako M3620, monoclonal mouse) and HRP-labeled anti-mouse secondary antibodies (Dako, dilution 1/1000) were used. Chemiluminescent substrate (ECL system by Amersham Bioscience, Freiburg, Germany) was used to determine relative density.

Frozen tumor tissue slices (LNCaP, CWR22Rv1, thickness of 5  $\mu\text{m}$ ) were fixed with 4% paraformaldehyde for 1 hour and then were blocked with 5% bovine serum albumin for 45 min. After being incubated with the primary antibody overnight at 4°C and three washes with PBS, cells were incubated with the AlexaFluor488 labeled-secondary antibody (Invitrogen) for 45 min and visualized with a fluorescence microscope.

**2.8. Statistical Analysis.** All data were expressed as the means plus standard deviation. *Student's t-test* was used for statistical analysis. Statistical analysis was performed by one-way analysis of variance (ANOVA) followed by the Newman-Keuls test for multiple comparisons. The level of significance was set at  $p < 0.05$ . For linear and quadratic polynomial regression analysis, we used the GraphPad Prism 5 software (GraphPad Software Inc., La Jolla, CA).

### 3. Results

**3.1. In Vitro Characteristics of  $^{68}\text{Ga}$ -PSMA-11.** Radioactivity in the waste vial and cartridge in all the reactions was less than 5%. The radiochemical yield of  $^{68}\text{Ga}$ -PSMA-11 from the synthesis module was more than 95%. Figure 1(a) displays the radio-HPLC result of the  $^{68}\text{Ga}$ -PSMA-11 immediately after preparation at 95°C. There were two peaks with averaged retention time of 11.1 min and 11.5 min (peak 1 and peak 2), which was corresponding to different diastereomers of  $^{68}\text{Ga}$ -PSMA-11. The peak 2 fraction of  $^{68}\text{Ga}$ -PSMA-11 ( $7.1\% \pm 2.4\%$ ) is significantly less than peak 1 ( $p < 0.001$ ). The radiochemical purity of  $^{68}\text{Ga}$ -PSMA-11 (including all diastereomers) was as high as ( $99.6 \pm 0.1\%$ ) and stable *in vitro* for 2 h (PH 7.4). The peak 1 fraction or radiochemical purity in buffer solution (PH 7.4) at 2 h *in vitro* was insignificantly different from that in buffer solution (PH 4.0 or PH 5.5).

**3.2.  $^{68}\text{Ga}$ -PSMA-11 Binding to PSMA-Expressing PCa Cells.** The saturation binding experiments of the binding of  $^{68}\text{Ga}$ -PSMA-11 to LNCaP, CWR22Rv1, PC-3, and VCAP cells *in*

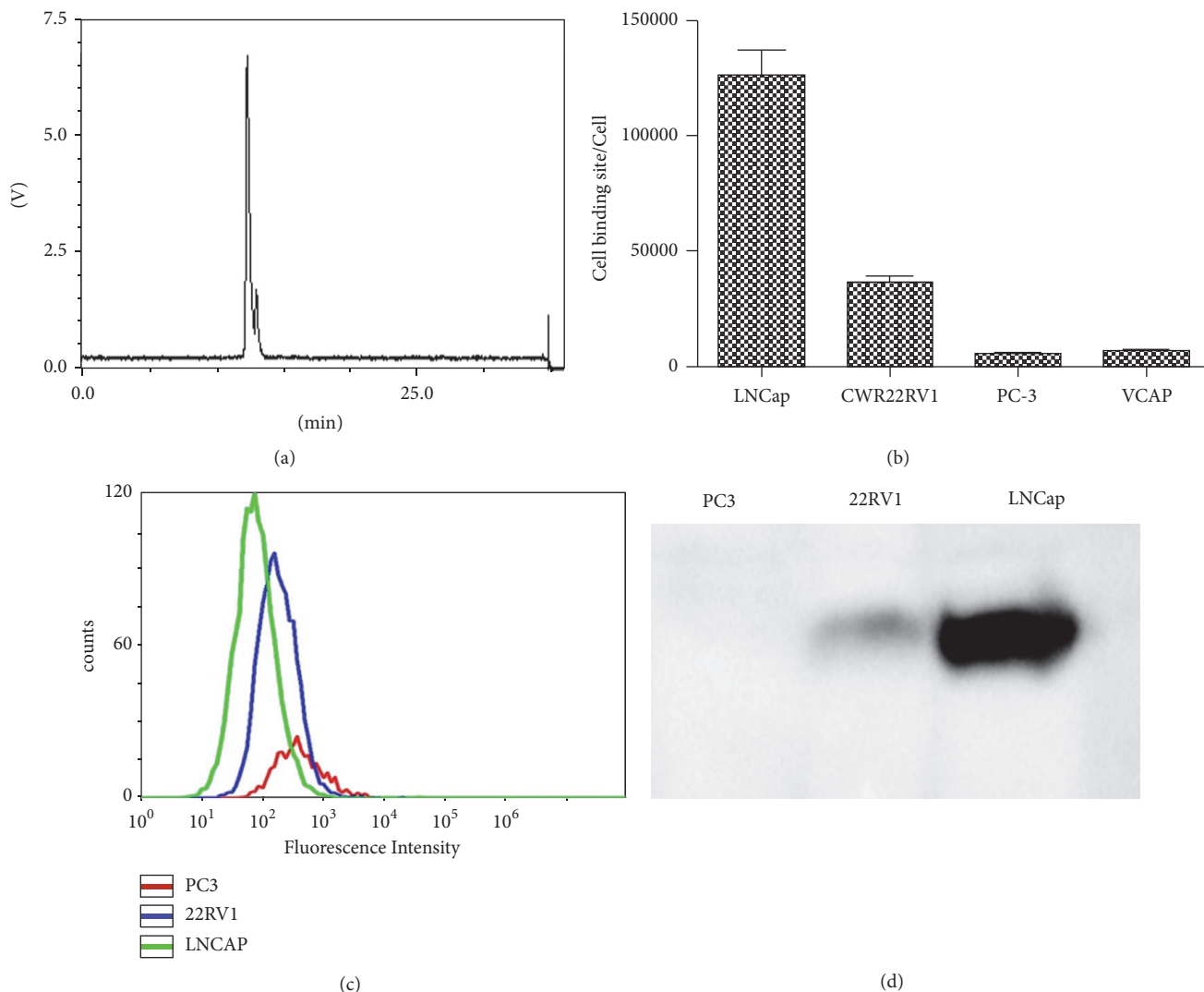


FIGURE 1: (a) The radio-HPLC results of  $^{68}\text{Ga}$ -PSMA-11 prepared using the synthesis module 2 h after its preparation. (b) The cell binding sites of  $^{68}\text{Ga}$ -PSMA-11 in LNCaP, CWR22Rv1, PC-3, and VCAP cells from the saturation binding experiments. (c) Representative flow cytometry image of PSMA expression levels. (d) Representative western blot image of PSMA expression levels.

*in vitro* showed that the equilibrium dissociation constant (Kd) of  $^{68}\text{Ga}$ -PSMA-11 to these cell lines was  $4.3 \pm 0.8$  nM,  $16.4 \pm 1.3$  nM,  $225.3 \pm 20.8$  nM, and  $125.6 \pm 13.1$  nM, respectively. The number of  $^{68}\text{Ga}$ -PSMA-11 binding sites for PCa cell lines was shown in Figure 1(b). The results were confirmed by cell-based flow cytometry (Figure 1(c)) and western blot assays (Figure 1(d)). The binding sites of  $^{68}\text{Ga}$ -PSMA-11 were highest for LNCaP, modest for CWR22RV1, and lowest or even negative for PC-3 and VCAP. The binding specificity of  $^{68}\text{Ga}$ -PSMA-11 to PSMA was confirmed by blocking study with overdose cold PSMA-11.

**3.3.  $^{68}\text{Ga}$ -PSMA-11 Biodistribution and PSMA Expression in Cell Suspension from Tumor Tissues.** Figure 2 showed the biodistribution of  $^{68}\text{Ga}$ -PSMA-11 in LNCaP, CWR22Rv1, and PC-3 tumor-bearing mice at 1 h after tail vein injection. LNCaP tumor uptake (% ID/g) of  $^{68}\text{Ga}$ -PSMA-11 ( $7.28 \pm 0.82$ )

was significantly higher than that of CWR22Rv1 ( $3.12 \pm 0.35$ ,  $p < 0.01$ ) and PC3 ( $1.21 \pm 0.07$ ,  $p < 0.001$ ) and can be blocked by preinjection of 2-PMPA indicating PSMA binding specificity. The PSMA expression levels in LNCaP and CWR22Rv1 tumor tissues were confirmed by immunofluorescence and it was almost negative in PC-3 cells. Preinjection of 2-PMPA in LNCaP group reduced uptake of  $^{68}\text{Ga}$ -PSMA-11 in kidneys ( $p < 0.01$ ). Tumor uptake of  $^{68}\text{Ga}$ -PSMA-11 (% ID/g) was reduced significantly by preinjection of high dose of 2-PMPA while it showed insignificant difference after preinjection of low dose 2-PMPA. The tumor/kidney uptake ratio ( $0.13 \pm 0.02$ ) in the 2-PMPA low dose group was significantly higher than that in LNCaP group ( $0.088 \pm 0.005$ ,  $p < 0.001$ ), while the tumor/liver uptake ratio demonstrates insignificant increase after the preinjection of low dose 2-PMPA (from  $6.32 \pm 1.21$  to  $7.039 \pm 1.37$ ,  $p > 0.05$ ). Preinjection of low dose 2-PMPA in LNCaP group insignificantly reduced tracer distribution of  $^{68}\text{Ga}$ -PSMA-11 in salivary glands.



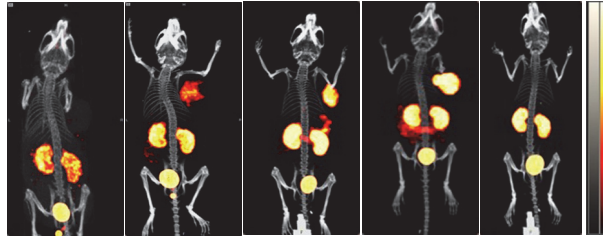


FIGURE 3: The 3D views of representative micro PET-CT images of nude mice bearing PC-3, CWR22Rv1, LNCaP, and LNCaP xenografts with low dose ( $2.5 \mu\text{g}$ ) or high dose ( $250 \mu\text{g}$ ) preinjection of 2-PMPA (from left to right). PET-CT scan was performed 1 h after intravenous injection of  $^{68}\text{Ga}$ -PSMA-11 with preinjection of overdose 2-PMPA to verify its specific binding to PSMA.

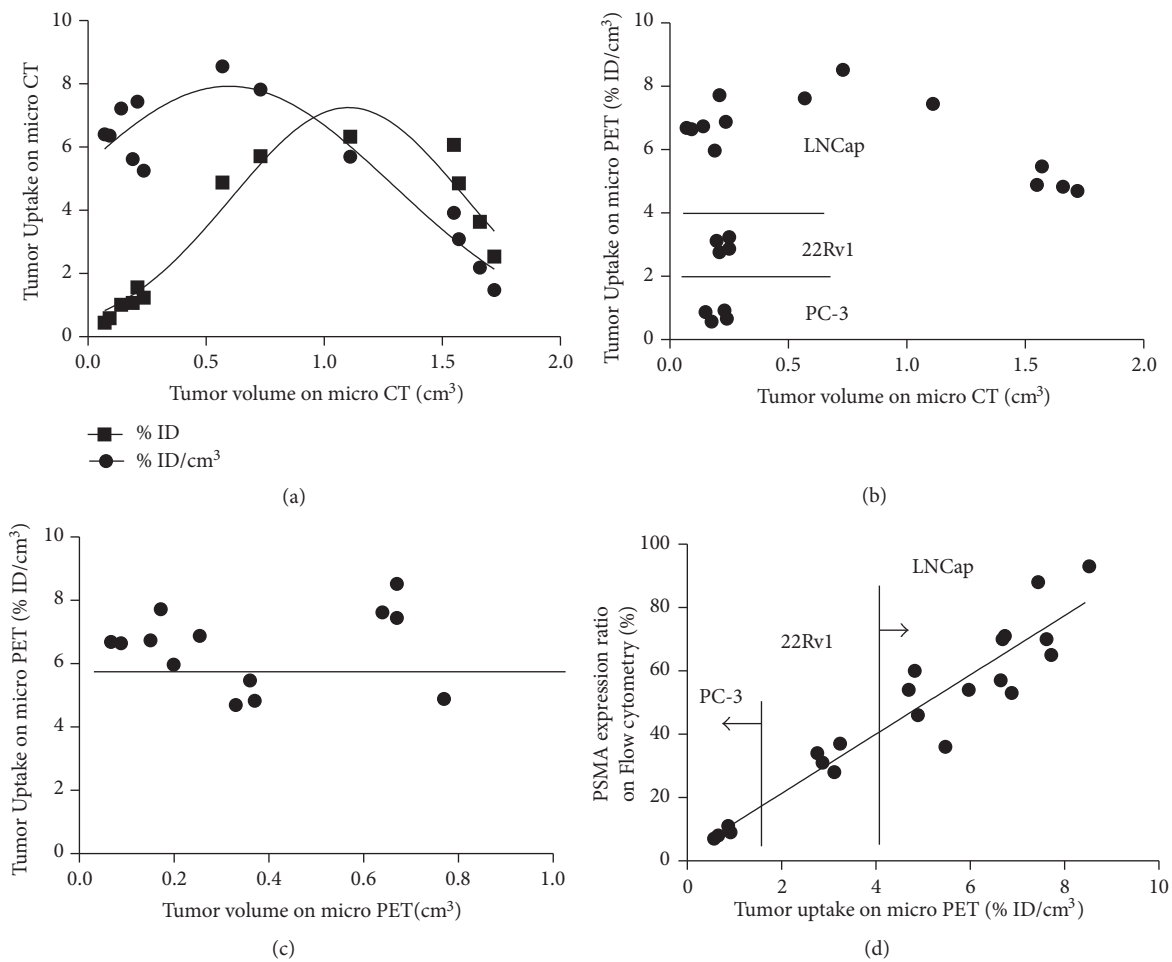


FIGURE 4: LNCaP tumor uptake (% ID and % ID/ $\text{cm}^3$ ) of  $^{68}\text{Ga}$ -PSMA-11 with tumor growth and relationship with PSMA expression. (a) Graph displays the LNCaP tumor uptake (% ID and % ID/ $\text{cm}^3$ ) changes with tumor anatomical volume increase. Tumor uptake (% ID/ $\text{cm}^3$ ) reached peak when anatomical volume was about  $0.5 \text{ cm}^3$ , less than that of % ID tumor uptake ( $1.2 \text{ cm}^3$ ). (b) Tumor uptake (% ID/ $\text{cm}^3$ ) of radiotracer in tumors with different PSMA expression and anatomical volume. When tumor size was less than  $0.5 \text{ cm}^3$ , tumor uptake (% ID/ $\text{cm}^3$ ) of  $^{68}\text{Ga}$ -PSMA-11 was LNCaP > CWR22Rv1 > PC-3 and it decreased when tumor grew more than  $1.0 \text{ cm}^3$ . (c) LNCaP tumor uptake (% ID/ $\text{cm}^3$ ) of radiotracer with functional tumor volume changes. LNCaP tumor uptake (% ID/ $\text{cm}^3$ ) was more than 6.0. In four mice bearing large LNCaP tumor xenografts with anatomical volume >  $1.0 \text{ cm}^3$  and functional volume of about  $0.4 \text{ cm}^3$ , the tumor uptake (% ID/ $\text{cm}^3$ ) is less than 6.0 (below horizontal line). (d) Tumor uptake of  $^{68}\text{Ga}$ -PSMA-11 (% ID/ $\text{cm}^3$ ) based on functional volume correlated well with PSMA expression determined by flow cytometry in a linear manner ( $y = 9.35x + 2.59$ ,  $R^2 = 0.8924$ , and  $p < 0.0001$ ).

of  $^{68}\text{Ga}$ -PSMA-11 (% ID/cm<sup>3</sup>) on micro PET was stable. When different cell lines and different tumor size of PCa xenografts were considered, tumor uptake of  $^{68}\text{Ga}$ -PSMA-11 (% ID/cm<sup>3</sup>) on micro PET correlated well with PSMA expression determined by flow cytometry in linear manner ( $y = 9.35x + 2.59$ ,  $R^2 = 0.8924$ , and  $p < 0.0001$ ).

#### 4. Discussion

$^{68}\text{Ga}$ -PSMA-11 is one urea based PSMA-targeted radiotracer with HBED-CC as a chelator. HBED-CC, representing an efficient complexing agent suitable for radiogallium labeling of antibody, peptide at RT, forms three diastereomers (RR, RS, and SS configurations) and conformed to NMR examinations [11, 12, 18–20]. RR is potentially thermodynamically favored and is the main fraction. These diastereomers were stable in solutions of different PH value as shown in our study and demonstrate similar binding specificity and affinity to PSMA [21].

PSMA expression is rarely reported in other tumor cells such as clear cell renal cell carcinoma and transitional cell carcinomas of the bladder and endothelial cells of tumor-associated neovasculature. No endothelial expression of PSMA is observed under physiologic conditions. PSMA expression in PCa varies tremendously in different stage or clinical course. Its evaluation is reported to be associated with clinical management selection, personalized treatment, and clinical outcome [9, 10, 22–24]. Among increasing number of PSMA-targeted agents,  $^{68}\text{Ga}$ -PSMA-11 can be prepared simply using synthesis module and shows high contrast and favorable targeting specificity. Tumor expression of PSMA was determined by the cell expression density and tumor burden. Cell lines with different PSMA expression level were selected to mimic PCa progression. Cell binding site of  $^{68}\text{Ga}$ -PSMA-11 per PCa cell follows LNCaP > CWR22Rv1 > PC-3. Cell-based tracer uptake of  $^{68}\text{Ga}$ -PSMA-11 was consistent with PSMA expression as revealed by flow cytometry and western blot.

“Liquid biopsy” on circulating tumor cells (CTC) characterization has been studied to address the question of PSMA-targeted therapeutic decision [25]. But PSMA profiling is not only determined by the cell line. Judgement of the PSMA expression level as whole can offer more information for tumor burden evaluation, treatment individualization, and dose determination.  $^{68}\text{Ga}$ -PSMA-11 micro PET-CT imaging has great potential.

The influence of tumor cell line and tumor size for the evaluation of PSMA expression was seen in Figure 4, and tumor uptake (% ID) of  $^{68}\text{Ga}$ -PSMA-11 increased with tumor anatomical volume (less than 1.0 cm<sup>3</sup>) in quadratic polynomial fashion while tumor uptake (% ID/cm<sup>3</sup>) started to decrease when tumor anatomical volume is only 0.5 cm<sup>3</sup>. The reduction or inner absence of radiotracer was mainly due to intratumor irregular tumor natural necrosis, reduced blood perfusion, and interstitial space [26]. Accurate metabolic tumor volume (MTV), reported based on  $^{18}\text{F}$ FDG PET or  $^{18}\text{F}$ -RGD PET imaging, is promising for target tumor volume delineation of lung cancer and breast cancer [17, 27, 28].

Micro PET is better to provide reproducible results for delineation of tumors characterized by heterogeneous activity distributions while micro CT can reduce influence from intense cardiac uptake and high tracer background. We found that the tumor % ID/cm<sup>3</sup> changes little during early period and decreased to great degree when necrosis occurs. The possible mechanism is regional ischemia and reduced uptake of  $^{68}\text{Ga}$ -PSMA-11. The low radioactivity density (% ID/cm<sup>3</sup>) may suggest the existence of large lesion on CT and necrosis in the same patient. So the tumor burden is little even though the tumor size is large. But this type of lesion may respond less to PSMA-targeted radiotherapy.

As further confirmed by biodistribution studies,  $^{68}\text{Ga}$ -PSMA-11 PET-CT imaging is excellent candidate for diagnostics of advanced PCa with high PSMA expression. However, elevated uptake and undesired retention of  $^{68}\text{Ga}$ -PSMA-11 in the kidneys were expected due to the substantial PSMA expression [29]. It was the major concern for therapeutic application. Besides the tumor, we found that uptake of  $^{68}\text{Ga}$ -PSMA-11 in PSMA-expressing kidneys can be significantly blocked by preinjection of 2-PMPA. Increasing tumor/kidney ratio was revealed when the injected dose of 2-PMPA is low. Similar to antifolate pemetrexed which has been used to improve tumor uptake and kidney clearance of radiofolate, 2-PMPA as PSMA inhibitor may have great potential to be used in the PSMA-targeted treatment via coadministration [30].

In summary, the tumor uptake on  $^{68}\text{Ga}$ -PSMA-11 micro PET (% ID/cm<sup>3</sup>) is correlated well with PSMA expression in a linear manner.  $^{68}\text{Ga}$ -PSMA-11 micro PET imaging could evaluate the density of PSMA expression, which will be of great value for the selection of PSMA-targeted radiotherapy. As a PSMA inhibitor, 2-PMPA may have the potential to be used to decrease renal uptake and retention of PSMA-targeted reagent.

#### Abbreviations

$^{68}\text{Ga}$ :	Gallium-68
PSMA:	Prostate-specific membrane antigen
PCa:	Prostate cancer
CT:	Computed tomography
PET:	Positron emission tomography
FDG:	Fludeoxyglucose
$^{18}\text{F}$ :	Fluorine-18.

#### Disclosure

Yuebing Wang and Guoqiang Shao are co-first authors.

#### Conflicts of Interest

The authors declare that they have no conflicts of interest.

#### Authors' Contributions

Yuebing Wang, Guoqiang Shao, Jianping Wu, Can Cui, Shimin Zang, Fan Qiu, Ruipeng Jia, Zizheng Wang, and Feng Wang participated in the study design, execution,

and analysis, manuscript drafting, and critical discussions. Yuebing Wang and Guoqiang Shao have contributed equally to this work.

## Acknowledgments

The authors thank Dr. Rui Chen (Tianjin Institute of Agricultural Quality Standard and Testing Technology) for the analysis of data. This study was partly supported by grants from the National Key Research and Development Program of China (2017YFA0103201), the National High Technology Research and Development Program of China (2007AA02Z471), the National Natural Science Foundation of China (81301247, 81501528), the Natural Science Foundation of Jiangsu Province (BK20130082), the Jiangsu Provincial Medical Youth Talent (QNRC2016075), the Nanjing Municipal Science Fund for Distinguished Young Scholars (JQX14009), and the Tianjin Natural Science Foundation (15JCQNJC10600).

## Supplementary Materials

Supplemental Figure 1: the synthesis module (Supplemental Figure 1(A)) was offered by ITC Company and the synthesis of  $^{68}\text{Ga}$  radiopharmaceuticals was performed in the sterile environment. It is set up lead shielded and consists of the  $^{68}\text{Ge}$ – $^{68}\text{Ga}$  generator, the fluid transfer system (with a  $0.22\ \mu\text{m}$  pore size filter to avoid microbial contamination at each transfer valves) (Supplemental Figure 1(B)) and reaction, and collection system. Supplement Figure 1(C) gives the schematic of the fluidic system in the synthesis module. It consists of a peptide pump, through which the peptide (a) and the generator eluent (c) are passed to reactor vial (heating vial) through V2. The outlet from the reactor is connected to the C18 cartridge via V3 after injection of air via v6. F1, F2, and F3 are three-way valves, introduced to control the direction of liquid and air. So the product and waste can be collected in different vials after the reaction mixture passed through the cartridge. (*Supplementary Materials*)

## References

- [1] R. Siegel, J. Ma, Z. Zou, and A. Jemal, "Cancer statistics, 2014," *CA: A Cancer Journal for Clinicians*, vol. 64, no. 1, pp. 9–29, 2014.
- [2] J. W. Moul, "The evolving definition of advanced prostate cancer," *Reviews in urology*, vol. 6, no. 8, pp. 10–17, 2004.
- [3] J. W. Moul, H. Wu, L. Sun et al., "Early versus delayed hormonal therapy for prostate specific antigen only recurrence of prostate cancer after radical prostatectomy," *The Journal of Urology*, vol. 171, no. 3, pp. 1141–1147, 2004.
- [4] A. J. Chang, K. A. Autio, M. Roach, and H. I. Scher, "High-risk prostate cancer-Classification and therapy," *Nature Reviews Clinical Oncology*, vol. 11, no. 6, pp. 308–323, 2014.
- [5] J. Cuzick, M. A. Thorat, G. Andriole et al., "Prevention and early detection of prostate cancer," *The Lancet Oncology*, vol. 15, no. 11, pp. e484–e492, 2014.
- [6] A. Ghosh and W. D. W. Heston, "Tumor target prostate specific membrane antigen (PSMA) and its regulation in prostate cancer," *Journal of Cellular Biochemistry*, vol. 91, no. 3, pp. 528–539, 2004.
- [7] N. Schülke, O. A. Varlamova, G. P. Donovan et al., "The homodimer of prostate-specific membrane antigen is a functional target for cancer therapy," *Proceedings of the National Academy of Sciences of the United States of America*, vol. 100, no. 22, pp. 12590–12595, 2003.
- [8] D. A. Silver, I. Pellicer, W. R. Fair, W. D. W. Heston, and C. Cordon-Cardo, "Prostate-specific membrane antigen expression in normal and malignant human tissues," *Clinical Cancer Research: an official journal of the American Association for Cancer Research*, vol. 3, no. 1, pp. 81–85, 1997.
- [9] C. Marchal, M. Redondo, M. Padilla et al., "Expression of prostate specific membrane antigen (PSMA) in prostatic adenocarcinoma and prostatic intraepithelial neoplasia," *Histology and Histopathology*, vol. 19, no. 3, pp. 715–718, 2004.
- [10] S. Perner, M. D. Hofer, R. Kim et al., "Prostate-specific membrane antigen expression as a predictor of prostate cancer progression," *Human Pathology*, vol. 38, no. 5, pp. 696–701, 2007.
- [11] M. Eder, A. V. Krivoshein, M. Backer, J. M. Backer, U. Haberkorn, and M. Eisenhut, "ScVEGF-PEG-HBED-CC and scVEGF-PEG-NOTA conjugates: comparison of easy-to-label recombinant proteins for [ $^{68}\text{Ga}$ ]PET imaging of VEGF receptors in angiogenic vasculature," *Nuclear Medicine and Biology*, vol. 37, no. 4, pp. 405–412, 2010.
- [12] M. Eder, B. Wängler, S. Knackmuss et al., "Tetrafluorophenolate of HBED-CC: A versatile conjugation agent for  $^{68}\text{Ga}$ -labeled small recombinant antibodies," *European Journal of Nuclear Medicine and Molecular Imaging*, vol. 35, no. 10, pp. 1878–1886, 2008.
- [13] M. Eder, M. Schäfer, U. Bauder-Wüst et al., " $^{68}\text{Ga}$ -complex lipophilicity and the targeting property of a urea-based PSMA inhibitor for PET imaging," *Bioconjugate Chemistry*, vol. 23, no. 4, pp. 688–697, 2012.
- [14] R. Nanabala, M. K. Anees, A. Sasikumar, A. Joy, and M. R. A. Pillai, "Preparation of [ $^{68}\text{Ga}$ ]PSMA-II for PET-CT imaging using a manual synthesis module and organic matrix based  $^{68}\text{Ge}/^{68}\text{Ga}$  generator," *Nuclear Medicine and Biology*, vol. 43, no. 8, pp. 463–469, 2016.
- [15] K. L. S. Chatalic, S. Heskamp, M. Konijnenberg et al., "Towards personalized treatment of prostate cancer: PSMA I&T, a promising prostate-specific membrane antigen-targeted therapeutic agent," *Theranostics*, vol. 6, no. 6, pp. 849–861, 2016.
- [16] G. Shao, Y. Zhou, F. Wang, and S. Liu, "Monitoring glioma growth and tumor necrosis with the U-SPECT-II/CT scanner by targeting integrin  $\alpha\text{v}\beta\text{3}$ ," *Molecular imaging*, vol. 12, pp. 39–48, 2013.
- [17] U. Nestle, S. Kremp, A. Schaefer-Schuler et al., "Comparison of different methods for delineation of  $^{18}\text{F}$ -FDG PET-positive tissue for target volume definition in radiotherapy of patients with non-small cell lung cancer," *Journal of Nuclear Medicine*, vol. 46, no. 8, pp. 1342–1348, 2005.
- [18] S. Ray Banerjee, Z. Chen, M. Pullambhatla et al., "Preclinical comparative study of  $^{68}\text{Ga}$ -labeled DOTA, NOTA, and HBED-CC chelated radiotracers for targeting PSMA," *Bioconjugate Chemistry*, vol. 27, no. 6, pp. 1447–1455, 2016.
- [19] M. Eder, O. Neels, M. Müller et al., "Novel preclinical and radiopharmaceutical aspects of [ $^{68}\text{Ga}$ ]Ga-PSMA-HBED-CC: A new PET tracer for imaging of prostate cancer," *Pharmaceuticals*, vol. 7, no. 7, pp. 779–796, 2014.
- [20] J. Schuhmacher, G. Klivenyi, W. E. Hull et al., "A bifunctional HBED-derivative for labeling of antibodies with  $^{67}\text{Ga}$ ,  $^{111}\text{In}$  and

- 59Fe. Comparative biodistribution with <sup>111</sup>In-DPTA and <sup>131</sup>I-labeled antibodies in mice bearing antibody internalizing and non-internalizing tumors,” *Nuclear Medicine and Biology*, vol. 19, no. 8, pp. 809–824, 1992.
- [21] J. Schuhmacher, G. Klivényi, and R. Matys, “Multistep tumor targeting in nude mice using bispecific antibodies and a gallium chelate suitable for immunoscintigraphy with positron emission tomography,” *Cancer Research*, vol. 55, no. 1, pp. 115–123, 1995.
- [22] B. Meller, F. Bremmer, C. O. Sahlmann et al., “Alterations in androgen deprivation enhanced prostate-specific membrane antigen (PSMA) expression in prostate cancer cells as a target for diagnostics and therapy,” *EJNMMI Research*, vol. 5, no. 1, article no. 66, pp. 1–11, 2015.
- [23] M. Eiber, T. Maurer, M. Souvatzoglou et al., “Evaluation of hybrid <sup>68</sup>Ga-PSMA ligand PET/CT in 248 patients with biochemical recurrence after radical prostatectomy,” *Journal of Nuclear Medicine*, vol. 56, no. 5, pp. 668–674, 2015.
- [24] F. Sterzing, C. Kratochwil, H. Fiedler et al., “<sup>68</sup>Ga-PSMA-11 PET/CT: a new technique with high potential for the radiotherapeutic management of prostate cancer patients,” *European Journal of Nuclear Medicine and Molecular Imaging*, vol. 43, no. 1, pp. 34–41, 2016.
- [25] T. M. Gorges, S. Riethdorf, O. von Ahsen et al., “Heterogeneous PSMA expression on circulating tumor cells - a potential basis for stratification and monitoring of PSMA-directed therapies in prostate cancer,” *Oncotarget*, vol. 7, no. 23, pp. 34930–34941, 2016.
- [26] R. K. Jain, “Transport of molecules in the tumor interstitium: a review,” *Cancer Research*, vol. 47, no. 12, pp. 3039–3051, 1987.
- [27] J. Bradley, W. L. Thorstad, S. Mutic et al., “Impact of FDG-PET on radiation therapy volume delineation in non-small-cell lung cancer,” *International Journal of Radiation Oncology • Biology • Physics*, vol. 59, no. 1, pp. 78–86, 2004.
- [28] A. C. Paulino and P. A. S. Johnstone, “FDG-PET in radiotherapy treatment planning: Pandora’s box?” *International Journal of Radiation Oncology • Biology • Physics*, vol. 59, no. 1, pp. 4–5, 2004.
- [29] S. Aggarwal, R. M. Ricklis, S. A. Williams, and S. R. Denmeade, “Comparative study of PSMA expression in the prostate of mouse, dog, monkey, and human,” *The Prostate*, vol. 66, no. 9, pp. 903–910, 2006.
- [30] C. Müller, R. Schibli, E. P. Krenning, and M. De Jong, “Pemetrexed improves tumor selectivity of <sup>111</sup>In-DTPA-folate in mice with folate receptor-positive ovarian cancer,” *Journal of Nuclear Medicine*, vol. 49, no. 4, pp. 623–629, 2008.

## Review Article

# Evans Blue Dye: A Revisit of Its Applications in Biomedicine

Linpeng Yao <sup>1</sup>, Xing Xue,<sup>1</sup> Peipei Yu,<sup>1,2</sup> Yicheng Ni <sup>3</sup>, and Feng Chen <sup>1</sup>

<sup>1</sup>Department of Radiology, The First Affiliated Hospital, Zhejiang University School of Medicine, 79 Qingchun Road, Hangzhou, Zhejiang 310003, China

<sup>2</sup>Department of Radiology, Sanmen County People's Hospital, Sanmen, Zhejiang 317100, China

<sup>3</sup>Radiology Section, University Hospitals, University of Leuven, 3000 Leuven, Belgium

Correspondence should be addressed to Feng Chen; [chenfenghz@zju.edu.cn](mailto:chenfenghz@zju.edu.cn)

Received 6 November 2017; Accepted 6 March 2018; Published 22 April 2018

Academic Editor: Yuebing Wang

Copyright © 2018 Linpeng Yao et al. This is an open access article distributed under the Creative Commons Attribution License, which permits unrestricted use, distribution, and reproduction in any medium, provided the original work is properly cited.

Evans blue (EB) dye has owned a long history as a biological dye and diagnostic agent since its first staining application by Herbert McLean Evans in 1914. Due to its high water solubility and slow excretion, as well as its tight binding to serum albumin, EB has been widely used in biomedicine, including its use in estimating blood volume and vascular permeability, detecting lymph nodes, and localizing the tumor lesions. Recently, a series of EB derivatives have been labeled with PET isotopes and can be used as theranostics with a broad potential due to their improved half-life in the blood and reduced release. Some of EB derivatives have even been used in translational applications in clinics. In addition, a novel necrosis-avid feature of EB has recently been reported in some preclinical animal studies. Given all these interesting and important advances in EB study, a comprehensive revisiting of EB has been made in its biomedical applications in the review.

## 1. Introduction

Dating back to the early 20th century, lots of blue dyes were synthesized like Methylene blue, Patent blue, Trypan blue, and so forth, and a comparison of main blue dyes was given in Table 1 [1–4]. Among those, Evans blue (EB) dye is just one that has a long history as a biological dye and clinical diagnostic agent [5]. As a synthetic bis-azo dye, EB dye is also named T-1824 and Direct Blue 53. Differently, with the first staining application initiated by Herbert McLean Evans in 1914, this dye became famous when it was sold by the Eastman Kodak Company under the name of “Evans blue” in recognition of Mr. Evan’s contributions to the development and use of dyes since 1936 [5, 6]. From that moment, the name “Evans blue” was widely accepted.

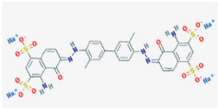
EB dye, with a molecular weight of 961 Da and high water solubility (280 g/l), strongly binds to serum albumin *in vivo* and *in vitro* and, thereby, becomes a high molecular weight protein tracer (69 kDa) [7–10]. When injected intravenously or intraperitoneally, albumin-bound EB remains stable in the blood and distributes throughout the entire body. Once injected in excess, EB dye can stain an entire animal including eyes, ears, nose, and paws with an intense blue color [11, 12].

In addition, Steinwall and Klatzo in 1966 reported that EB dye can emit a bright red fluorescence when activated with green light [7]. Thus, the dye provides a simple and convenient way of identification both macroscopically and microscopically using fluorescence for both morphological investigation and quantification. The fluorescent feature of EB dye has been used in various aspects including the characterization of the lymph nodes that drain the liver [13], confirmation of a satisfactory injection into the heart chambers of a zebrafish embryo [14], and observation of the extravasation of the dye from blood vessels into tissues [15–17].

Due to its high water solubility and slow excretion, as well as its firm binding to serum albumin, EB is also widely used in biomedicine including the estimation of blood volume, the assessment of vascular permeability to macromolecules, the detection of lymph nodes, and the location of the tumor lesions [12, 18–24].

More recently, a series of EB derivatives have been labeled with PET isotopes and can be used as theranostics with broad potential applications [25, 26]. EB also has a necrosis-avid feature as EB-bound albumin preferentially enters damaged cells, but not healthy cells, and persists within the damaged

TABLE 1: Characteristics of different blue dyes.

Dye	Molecular formula	Chemical structure	Number of -SO <sub>3</sub> H groups	Size (Da)	Max spectral absorption (nm)	% bound to plasma proteins [27]	Time of complete clearance from plasma (minutes) [1]	Applications in biomedicine
Methylene blue	C <sub>16</sub> H <sub>18</sub> ClN <sub>3</sub> S		0	320	670	0.0 ± 0.0	<20	Treating methemoglobinemia [4, 27]
Patent blue	C <sub>27</sub> H <sub>31</sub> N <sub>2</sub> O <sub>6</sub> S <sub>2</sub>		2	567	640	4.7 ± 1.2	<25	Detection of lymph nodes [3]
Trypan blue	C <sub>34</sub> H <sub>24</sub> N <sub>6</sub> Na <sub>4</sub> O <sub>14</sub> S <sub>4</sub>		4	961	600	62.2 ± 2.0	<120	Staining biopsies, living cells, and organisms [2]
Evans blue	C <sub>34</sub> H <sub>24</sub> N <sub>6</sub> Na <sub>4</sub> O <sub>14</sub> S <sub>4</sub>		4	961	620	68.1 ± 3.5	>120	Estimation of blood volume, detection of lymph nodes, localization of tumors, and so forth [6, 12, 18]

cells [14]. Thus, EB can be used as an agent for tissue viability assessment. This article reviews the features of EB and its potential applications in biomedicine.

## 2. Applications Derived from Albumin-Binding Characteristic of Evans Blue Dye

The strong binding capacity of EB dye to serum albumin has been demonstrated and this property has become widely accepted [7, 8, 10]. Tsopelas and Sutton investigated a series of 20 sulfonic acid dyes in 2002 and elaborated that protein binding ability was correlated with dye molecular structure. He demonstrated that the EB dye with tetrasulfonic acid group yielded 70% protein binding affinities (Table 1) [27]. Moreover, sulfonation reaction between sulfonic acid group of dye and amino group on protein surface was responsible for the dye-protein binding mechanism.

In various species, the binding capacity of albumin appears to be strongest in humans and dogs as 8–14 moles of Evans blue [28]. When injected intravenously, EB becomes fully albumin-bound and only a small proportion of free EB (0.11%–0.31%) can be found in the blood. The fact that EB dye is confined to the blood makes it unique among other dyes, for example, sodium fluorescein, which evenly distributes between the blood and organs such as the liver [10].

EB is eliminated from the circulating blood by the liver but not kidneys over time, which avoids the coloration of urine [27]. Wolman et al. [8] briefly reported the gradual disappearance of EB from the plasma and found that the EB in the plasma dropped rapidly over 24 h and remained very low in the blood after 3 days and was hardly detectable in their experiments. Importantly, as its unique characteristic, EB-protein complex with a high molecular weight may prevent

its passage into living cells or across the blood-brain barrier. This leads to a variety of clinical applications that will be elaborated later in this article [29–31].

*2.1. Use of Evans Blue Dye for Estimation of Blood Volume.* The evaluation of changes in total blood volume is an interesting topic. The use of EB dye for this purpose was introduced by Keith et al. in 1915 [28, 34]. Earlier researchers in the field used red dyes from this class such as vital red, new vital red, and Congo Red. Until 1920, EB dye was considered superior to all the red dyes based on the investigations of Dawson et al., whose working principle of EB dye is now briefly described [35].

When a known quantity of dye ( $N$ ) is injected into the blood stream, after an interval required for complete mixing, the quantity of dye ( $n$ ) in 1 ml of withdrawn blood sample is analyzed. According to the relationship  $V = N/n$ , the plasma volume ( $V$ ) can be calculated [36]. Then the total blood volume can be correctly calculated from the plasma volume according to the value of the hematocrit. Clearly, the only measurement that can be influenced by vital processes is that of  $n$ .

The dye dilution method using EB dye to measure plasma volume gained wide acceptance in the middle of the 20th century [37]. A wide variety of improvements and extraction methods were studied by researchers from various countries [34, 38–42]. To date, quantitation of EB dye can be optimized in limited tissue samples as much as 30  $\mu$ l [43]. However, since radioisotopic method to measure plasma volume was first introduced by Gibson and his coworkers in 1946, it has gradually replaced the EB dye dilution method [36, 44]. Compared with the dye method (which occasionally overestimates the plasma volume), <sup>131</sup>I-labeled protein has been

confirmed as an accurate measurement of plasma volume in both dogs and human subjects [45]. However, the method has its shortcomings due to the prolonged stay of radiolabeled material in the body; for example, repeated studies are not suggested on the same patient. Therefore, other methods such as trivalent chromium [ $^{51}\text{Cr}(\text{III})$ ], hemoglobin-based oxygen carriers (HBOC), and carbon monoxide have been investigated as potential methods to estimate plasma volume [46, 47].

The carbon monoxide method appeared to be promising, especially in critically ill patients [46]. Yet et al. [47] developed a novel approach using HBOC in rabbits in 2001, which is inexpensive and not time-consuming, while Baby et al. [45] used  $^{51}\text{Cr}(\text{III})$  in rabbits in 2014 and found that it was easy and quick and could be performed repeatedly in the clinical setting as  $^{51}\text{Cr}(\text{III})$  is not bound to albumin or red blood cells (RBCs). To some extent, the Evans blue dye method to measure plasma and blood volumes is limited in animals, but, in humans,  $^{51}\text{Cr}(\text{III})$  and HBOC are more promising for future clinical applications [48].

*2.2. Use of Evans Blue Dye for Determination of Cardiac Output.* The measurement of cardiac output by the dye injection method was established by Stewart [49] and later modified by Hamilton et al. [50]. Evans blue dye, as a vital stain, had been widely used in this aspect and the validity of the EB dye injection method has been shown to correlate well with the Fick procedure under different experimental conditions in dogs and humans [50, 51]. However, because of the slow excretion and undesirable discoloration, the EB dye was limited when repeated injections in patients were required. By contrast, Lacy et al. [20] demonstrated indigo carmine as an alternative to EB due to its firm binding to albumin and rapid removal by the liver and kidneys in 1955. In addition, Davis et al. [1] investigated a series of blue dyes in 1958 and found three rapid bloodstream clearance rates of dyes suitable for frequent serial estimation of the cardiac output. These included Patent blue A, Brilliant blue, and Patent blue V. However, owing to the invasiveness of the Fick technique and the dye injection method, they have been replaced by other more modern and simplified techniques including thermodilution techniques, lithium dilution, bioreactance, and Doppler technique or echocardiography [52, 53]. A few detailed reviews on this topic can be referred [52–54]. Therefore, EB and other blue dyes are no longer suitable for the determination of cardiac output except when used as a reference.

*2.3. Use of Blood Pool Effect of Evans Blue Dye.* EB dye is a permeable dye that can be easily taken up by degenerated or damaged cells but not by cells with an intact membrane [14]. However, interestingly, EB dye and triphenyl tetrazolium chloride (TTC) *ex vivo* double-staining are usually used together to assess the infarct size in acute myocardial infarction in both canine and murine models, where EB is delivered to the coronary arteries and TTC is applied to stain the surface of cardiac sections [47, 55–59]. When perfused into the aorta and coronary arteries in a retrograde manner, EB dye can uniformly distribute to everywhere in the vascular

bed of normal myocardium, while infarcted myocardium or areas at risk cannot be stained due to the occlusion of the affected coronary arterial branch. The rationale behind TTC staining is that infarcted myocardium has lost dehydrogenase so that the colorless dead tissue on TTC cannot be converted to a red formazan [60]. Thus, the nonischemic area is stained blue, while the viable myocardium in the area at risk is stained red, and the infarcted myocardium appears to be pale [47].

EB dye can also be used alone to delineate which region of myocardium is perfused or hypoperfused based on accessibility to the dye [58]. But it seems to be paradoxical that the EB-perfused area, which is not at risk, is totally different from EB-stained cardiomyocytes that experience injury [61]. Indeed, due to the blood pool effect of EB, when perfused *ex vivo*, the EB-perfused area can stain rapidly following the branches of coronary artery. In contrast, the EB-staining of necrotic cardiomyocytes is due to the dye's affinity for dead cells, which will be addressed. Therefore, it is rational to say that EB dye could have a dual function, that is, assessment of the myocardial area at risk and assessment of infarcted myocardium.

*2.4. Use of Evans Blue Dye for Assessment of Vascular Permeability.* Integration of selective permeable barriers is vital for proper organ functioning and the maintenance of homeostasis. Such barriers include the endothelial cell barrier of blood vessels, the blood-brain barrier (BBB), the blood-retinal barrier, the blood-spinal cord barrier, and the blood-placental barrier [62]. The majority of selective permeable barriers are constituted primarily of tight junctions between endothelial cells to maintain barrier integrity. Under physiologic conditions, selective permeable barriers permit a selective transport of micromolecular substances but are impermeable to macromolecules such as albumin [63]. Thus, the EB dye, which strongly binds to albumin, remains restricted within the blood circulation and cannot cross the barrier. When various diseases result in a disruption of the barrier and increased vascular permeability, EB-bound albumin may extravasate from the circulation into neighboring tissues. Leak of dye across the BBB or blood vessel signifies a disintegration of the barrier, and the accumulation of EB dye can be quantified after extraction from the stained tissue. The advantage of using EB dye as a tracer is its ability to be identified macroscopically, which gives a gross indication of its distribution. Furthermore, the extravasated EB dye within tissue can be observed by red fluorescence in tissue sections by fluorescence microscopy and quantified by colorimetry, spectrophotometry, and spectrofluorometry [62, 64, 65]. Thus, EB dye is extensively used to assess vascular permeability and BBB permeability described in various models, such as the classical Miles assay [24, 66, 67], the endothelial damage model caused by trauma [68], the stroke model [69], the cerebral ischemic model [64], and the breast cancer brain metastasis model [30].

In addition, Soubeyrand et al. [70] and Pettersson et al. [71] used EB dye to measure the permeability of the blood-spinal cord barrier and Xu et al. [72] detected the blood-retinal barrier breakdown by quantification using EB. It is worth noting that the stain administration route by

intraperitoneal and intravenous injection had no difference on the amount of EB dye stain accumulated but a strong time-dependent tendency towards increase in stain accumulation [73]. As a rapid and inexpensive method, EB dye is still the most commonly used marker of brain barrier integrity and vascular permeability; however, its associated problems of tissue discoloration and potential toxicity need to be considered.

### 2.5. Use of Evans Blue Dye for Detection of Lymph Nodes.

Visualization of the lymphatic system plays a significant role in assessing various malignancies and immune responses to foreign antigens in humans and in animal models [18]. The use of EB dye has become a major method for mapping lymphatic drainage. Due to the conjugation of the dye to plasma proteins by sulfonation reaction, the complex is sufficiently large to be trapped inside the lymphatic lumen and transported along with lymphatic flow [27]. Upon subcutaneous administration, the dye is quickly taken up by the lymphatic vessels to the draining nodes. Once the lymphatic mapping is shown by the blue color of EB dye, subsequent sentinel node biopsy becomes possible, which is critical for studies of solid tumor metastasis and of regional immune responses following immunization [18, 74].

Due to this mechanism of action, Bobin et al. [75] were able to evaluate the feasibility of sentinel lymph node identification in 100 breast cancer patients and confirmed the sensitivity of this technique (95%) in detecting nodal metastases. Harrell et al. [18] accurately and rapidly identified lymph nodes and lymphatic drainage in the mouse by injecting the dye into the mouse footpad or tail. Zheng et al. [13] successfully characterized the liver-draining lymph nodes by intrahepatic injection. Similarly, Tervalá et al. [76] detected axillary lymph nodes and grafted lymph nodes by injecting EB dye solution intradermally. In addition, they analyzed the lymphatic vessel function by the way of quantifying the leakage of EB dye into the blood.

Except the EB dye, several other dyes are useful for identification of sentinel lymph nodes and include Chicago sky blue, Patent blue, and Trypan blue [27, 77]. It was previously reported that when scintigraphy and EB dye are used in tandem, the false-negative rate for sentinel node localization is decreased compared with using either agent alone [77]. On the whole, EB dye is a promising method for the assessment of malignancy and lymphedema in humans and subsequent sentinel node biopsy, as well as the evaluation of lymphatic vessel function.

### 2.6. Use of Evans Blue Dye for the Diagnosis and Identification of Tumors.

Most tumors are known to exhibit highly enhanced vascular permeability, which is considered to facilitate tumor growth and perhaps metastasis [12, 15]. Visual demarcation of tumor margins during operation will provide greater accuracy in tumor resection. The use of a visible small molecular dye to address this challenge was suggested by Ozawa et al. [78]. EB dye is perfectly in accord with this demand, because EB dye may bind strongly to albumin, extravasates, and remains for a prolonged time in the extravascular space due to the enhanced permeability and retention (EPR) effect of tumors [79].

Lots of articles using EB dye to demarcate tumor margins were published [12, 30, 80, 81]. Prabhu et al. [80] calculated the uptake of the dye within an intracranial tumor to determine the volume of tumor and demonstrated that the method showed good correlation with the volume estimation from histological sections and gadolinium-enhanced magnetic resonance imaging. Likewise, a study by Elsen et al. investigated the biodistribution of Evans blue in a normal rat bladder and a bladder carcinoma and they found a significant difference of EB absorption between malignant tissues and normal bladder tissues after intravesical instillations [81]. Thus, the method of EB instillations combined with white-light cystoscopy could be a useful tool for diagnosing bladder cancer in clinical settings in the future.

Interestingly, by developing a liposomally nanoencapsulated Evans blue dye (nano-EB), Roller [12] demonstrated that clearer tumor margins were demarcated with nano-EB in an invasive tumor model compared with unencapsulated EB. This indicated that nano-EB could be deposited specifically to tumor tissue, which is normally considered as the tumor-specific feature of the EB dye [12, 82].

As we know, liposomal nanocarriers as drug carriers have been extensively investigated in nanomedicine; the special structure of liposomes can facilitate itself, evading the reticuloendothelial system and prolonging the circulation time in the bloodstream [83, 84]. Much effort has been made to design and optimize liposomal nanocarriers. For instance, incorporation of targeting moieties to tumors onto the liposomal may help to reduce the accumulation in nontarget organs [84]. Therefore, nano-EB may be used to provide accurate visual cues for the surgeon to intraoperatively delineate the tumor margins via two mechanisms: either via tumor EPR effect or via tumor-receptor targeting strategy [12].

In general, EB dye, especially liposomal nanocarriers-encapsulated Evans blue, could be a useful agent to localize and demarcate the solid tumors more precisely due to its selective accumulation in the tumor site. This so-called tumor-specific feature may actually be attributed to the EPR effect that may be used to explain the mechanism of EB applications in many clinical settings.

## 3. Use of Evans Blue Dye as a Necrosis-Avid Agent

As we know, life and death are two forms of cellular existence. Cell death is an essential form in cell development. Cell death includes at least two independent modes, that is, apoptosis and necrosis. EB dye was first reported by Gaff and Okong-O'Gola as a vital stain for plant cells in 1971 [85]. In their study, EB dye leaked through damaged membranes and stained the dead cells but was excluded by viable cells.

EB dye has been further investigated and used extensively for specifying cell death in microscopic studies [86]. Although EB dye has been shown to be reliable for the assessment of viability in plant cells, it remains unclear whether EB dye can be also used in mammalian cells. In 1995, Matsuda et al. [87] attempted a new method using EB dye to identify degenerated muscle fibers in the mdx

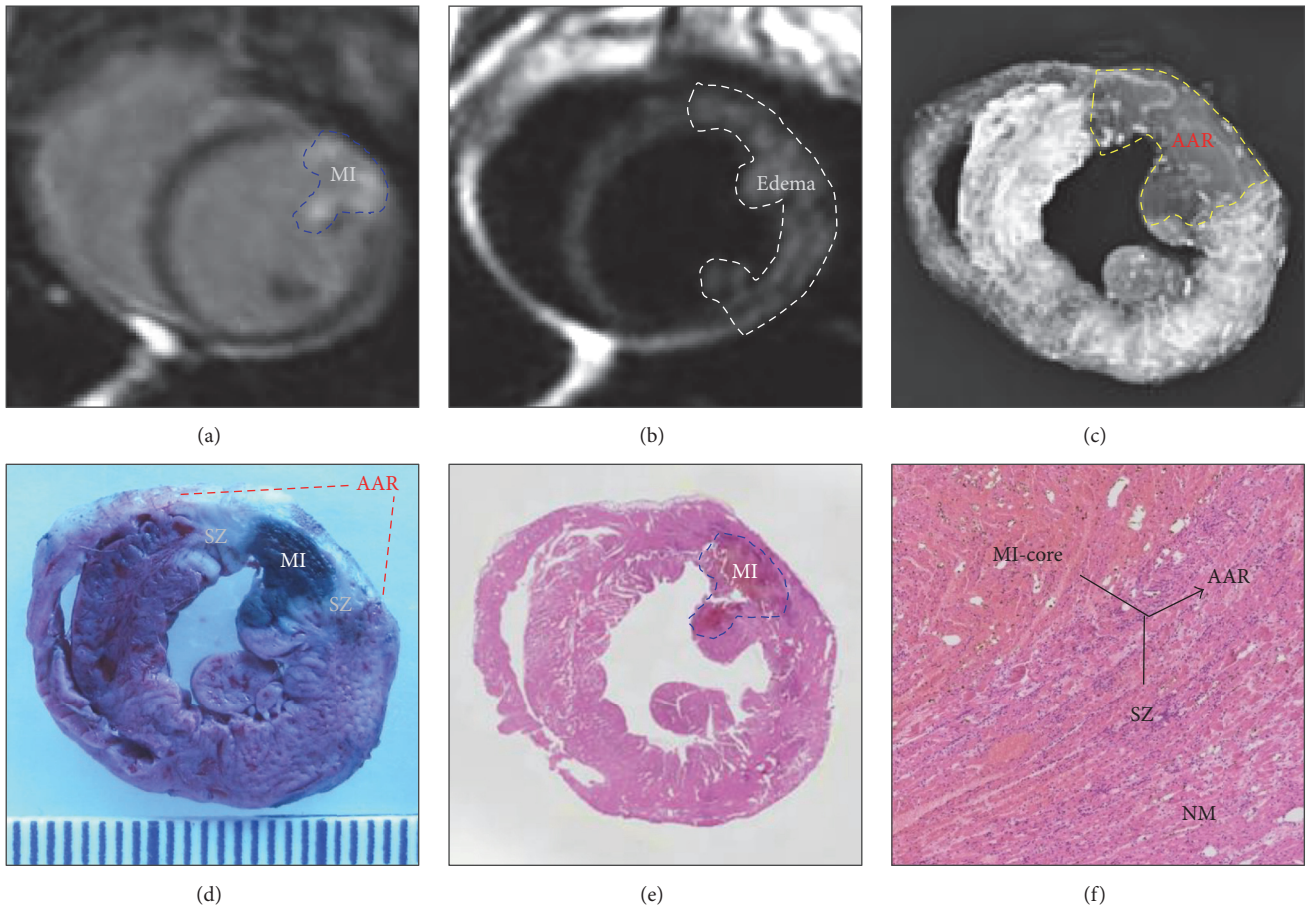


FIGURE 1: Evaluation of myocardial infarction core (MI-core), area at risk (AAR), and salvageable zone (SZ) in a rabbit with reperfused MI by *in vivo* and *ex vivo* imaging techniques and dynamic imaging quantification [32]. (a) Delayed, enhanced cardiac magnetic resonance imaging displays the MI-core as a transmural hyperenhanced area involving anterior papillary muscle; (b) T2-weighted imaging shows an extensive hyperintense region in the anterolateral wall; (c) digital radiograph of the red iodized oil-stained heart section shows a filling defect with few collateral vessels in the anterolateral wall in contrast to the rest of opaque left ventricle; (d) photograph of the heart section stained by multifunctional staining depicts the MI-core as an Evans blue dye-stained blue lesion simulating what is seen in (a) and shows the normal ventricular wall in red leaving the AAR (including the blue MI-core) unstained, which perfectly matches with the AAR in (c) and whitish zones which are suggestive of the SZ; (e) photomacroscopy of HE-stained heart slice views the MI-core as a hemorrhagic infarct similar in size to the blue lesion in (f); (f) photomicroscopy ( $\times 100$ ) of HE-stained heart slice confirms the presence of the AAR (necrotic MI-core plus the viable but inflammatory SZ) and remote normal myocardium (NM) (reprinted and modified with permission from Feng Y, Chen F, Ma Z, Dekeyzer F, Yu J, Xie Y, Cona MM, Oyen R, Ni Y. *Theranostics*. 2013, 4: 24–35).

mouse and showed that EB-stained muscle fibers were either hypercontracted or degrading, which was consistent with the terminal-deoxynucleotidyl transferase mediated nick end labeling- (TUNEL-) positive myonuclei as supportive evidence for apoptosis. In contrast, a study by Straub et al. in 1997 identified that muscular fibers showing EB dye staining under fluorescence microscopy were necrotic fibers [88]. Similarly, Miller et al. [61] used EB dye to stain cardiomyocytes induced by myocardial contrast echocardiography in rats in 2007 and showed that the EB-stained cardiomyocytes had no TUNEL-positive nuclei after 24 h, which is evidence for necrosis instead of apoptosis. Klyen et al. also confirmed that the area of EB dye accumulation was consistent with the necrotic myofibers shown on hematoxylin and eosin staining and optical coherence tomography images [89].

Many researchers used EB dye to discriminate among injured cells in various animal models, such as the zebrafish models of neuromuscular disease [14], mouse models of muscular dystrophy [90] and experimental injury and repair [91], rat models of stroke and cardiomyocyte injury [92], myocardial infarction core in a rabbit model [32] (Figure 1), and reperfused partial liver infarction model in rats [33] (Figure 2).

Furthermore, some studies have shown that EB's derivatives, such as EB-DTPA-Gd, have a specific binding affinity to a vascular lesion with endothelial damage, which is independent of serum proteins or the blood stream. EB-DTPA-Gd was also found to have a high affinity for atherosclerotic plaques *in vivo* in ApoE<sup>-/-</sup> mice [93]. These findings implied the nature of necrosis-avidity for EB dye. Although the EB

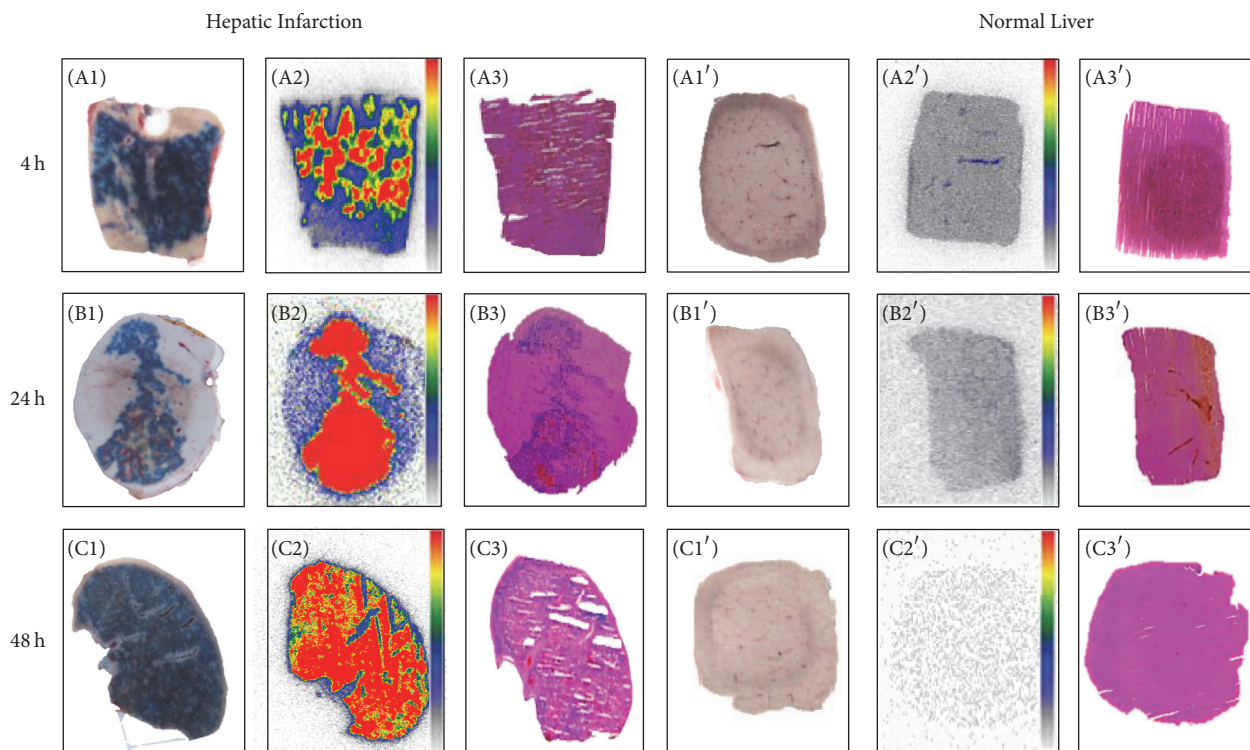


FIGURE 2: Postmortem analysis of necrotic and viable liver from rats with reperused partial liver infarction that received iodine-123-labeled monoiodohypericin followed by the necrosis-avid dye, Evans blue [33]. At 4, 24, and 48 hours (h) after radioactivity injection, liver necrosis is outlined by the Evans blue as a blue region (A1, B1, and C1), with viable liver without staining (A1', B1', and C1'). Autoradiograms of 50  $\mu\text{m}$  thick sections show higher tracer accumulation in the hepatic infarction (A2, B2, and C2) than in viable liver (A2', B2', and C2'). The color code bar represents the coding scheme for the radioactivity. On histologic sections, the presence of scattered liver necrosis (A3, B3, and C3) and the location of the normal liver (A3', B3', and C3') are confirmed (reprinted and modified with permission from Miranda Cona M, Koole M, Feng Y, Liu Y, Verbruggen A, Oyen R, Ni Y. *International Journal of Oncology* 2014, 44: 819–829).

dye was considered as a necrosis-avid agent, the specific mechanism is still not clear [94].

#### 4. Radiolabeled Evans Blue Derivatives as Theranostics

In general, radiolabeling EB, such as in  $^{99\text{m}}\text{Tc}$ -EB, scarcely alters the pharmacodynamic properties of EB itself.  $^{99\text{m}}\text{Tc}$ -EB demonstrated that its affinity for plasma protein was not significantly different from that of unlabeled EB and both agents had similar dynamics regarding the sentinel lymph node [27, 74]. With the advantages of both radioactive and color signals in a single dose, it appears to be superior to the dual-injection technique of radiocolloid/blue dye in mapping the lymphatic system and discriminating sentinel lymph nodes [23, 95]. Therefore,  $^{99\text{m}}\text{Tc}$ -EB could be a promising agent in the clinical setting to guide sentinel node biopsy in various solid tumors in the near future.

Taking full advantage of the albumin-binding feature of EB, Liu et al. developed a number of radiolabeled EB derivatives [25, 26, 96–98]. These EB derivatives may be conjugated onto a therapeutic small molecule, peptide, or an oligonucleotide aptamer. Thus, they may be used as theranostics with

a broad potential due to their improved half-life in the blood and reduced release. For instance, a version of truncated EB conjugated to 1,4,7-triazacyclononane- $\text{N},\text{N}'\text{N}''$ -triacetic acid (NOTA) has been recently synthesized, named NEB. The NEB can be labelled with different PET isotopes including  $^{18}\text{F}$ -AlF,  $^{64}\text{Cu}$ , and  $^{68}\text{Ga}$  [96, 97]. These radiolabeled NEB derivatives were initially used as blood pool agents to evaluate myocardial infarction and vessel leakage in inflammation and tumors [96]. After local injection,  $^{18}\text{F}$ -AlF-NEB can be used to visualize and detect the sentinel lymph nodes with a high signal-to-noise ratio. More interestingly, as a blood pool imaging agent and PET tracer,  $^{68}\text{Ga}$ -NEB has already had translational applications in clinics. A preliminary study showed the potential of  $^{68}\text{Ga}$ -NEB in differentiating hepatic hemangioma from other focal hepatic lesions [97].  $^{68}\text{Ga}$ -NEB also outperformed conventional  $^{99\text{m}}\text{Tc}$ -SC lymphoscintigraphy in the evaluation of patients with different suspected lymphatic drainage abnormalities [98].

When EB-maleimide, one of the truncated EB derivatives, was conjugated to antidiabetic drug exendin-4 (denoted as Abextide), it showed great potential to treat type 2 diabetic mice due to the significantly extended biological half-life of Abextide through complexation with albumin in situ [25, 26].

This strategy provides possibilities for the development of long-acting therapeutic drugs for other small molecules and biologics [26].

## 5. Toxicity of Evans Blue Dye

EB dye has been widely used for different applications in the clinic and research, but few researchers have considered the probable toxicity of the dye. EB dye can cause delayed death in all mice at doses above 200 mg/kg body weight [99], but the usual dosage of 2% EB, 0.5 mL/kg (10 mg/kg), or even lower causes much less toxicity compared to higher doses. In most cases, few reports of adverse reactions were seen. However, it was reported by Gibson and Gregersen in 1935 that pulmonary embolism was observed after intravenous injection of EB in rats. In 1974, Giger et al. demonstrated that EB can cause platelet aggregation when the molar ratio of EB:albumin is >1:1 [100]. Similarly, by the late end of the 20th century, Moos and Mollgard found that free dye (albumin-unbound EB) in plasma caused 60% of neonatal and 20% of the adult animal deaths during their experiments, and the toxicity of free dye led to alteration of the BBB permeability, while it appeared to be safe when EB was used as single intravenous injection at a conventional clinical dose [100, 101]. In addition, Jackiewicz et al. also proved that EB dye caused a significant simplification of the junctional morphology in normal and regenerating endothelium, which should be taken into account when using EB dye to assess various insults to blood vessels, in 1998 [68]. Recently, an ex vivo experiment by Giansanti et al. investigated the safety of EB dye. They found damage of ARPE-19 cells and RGC5 cells with halogen and xenon light exposure should be a concern when the dye is used during vitrectomy [102]. The point that many researchers have easily ignored is that azo dyes, as a class, can potentially induce mutagenicity and carcinogenicity when split off or degraded into component aromatic amines, especially in the fetus. Although there is a lack of reports about the carcinogenicity of EB, it is necessary to consider the possibility when using EB in clinical practice.

## 6. Conclusion

In summary, the once widely used EB dye dilution method has gradually been replaced by newer methods, such as radiolabeled albumin and radiolabeled red cells, for the estimation of blood volume and cardiac output. The blood pool effect of EB dye is limited when evaluating perfused or hypoperfused myocardium, but its utility in assessing vascular permeability and BBB integrity has increased. In addition, the use of radiolabeled EB and its derivatives will play an important role in clinical imaging of tumor lesions, evaluation of lymphatic disorders, and development of long-acting therapeutics. Importantly, the newly discovered necrosis-avid affinity of EB will facilitate the identification of necrotic tissues including myocardial infarction, cerebral stroke, degenerating muscular diseases, and even amyloidosis [103], as well as the assessment of therapeutic efficacy and prognosis of solid tumors. Although the mechanisms are still unclear and further investigation is required, EB dye as a vital stain has greatly contributed to biomedical research

and may continue to benefit the development of medical practice and patient care. Therefore, the main advantage of new applications of Evans blue lies in its great potential use in clinical practice as mentioned above.

## Conflicts of Interest

The authors declare that there are no conflicts of interest regarding the publication of this paper.

## Acknowledgments

This work was partly supported by the National Natural Science Foundation of China (NSFC) (Project 30670603) and the Health and Family Planning Commission of the Zhejiang Province of China (Project 2014PYA009).

## References

- [1] H. A. Davis, W. al-Fadly, and L. H. Gibson, "Use of Dyes with Rapid Bloodstream Clearance for Serial Determination of Cardiac Output," *Proceedings of the Society for Experimental Biology and Medicine*, vol. 98, no. 2, pp. 345–347, 1958.
- [2] C. J. Cooksey, "Quirks of dye nomenclature. 3. Trypan blue," *Biotechnic & Histochemistry*, vol. 89, no. 8, pp. 564–567, 2014.
- [3] C. J. Cooksey, "Quirks of dye nomenclature. 8. Methylene blue, azure and violet," *Biotechnic & Histochemistry*, vol. 92, no. 5, pp. 347–356, 2017.
- [4] R. Gelmini, M. Campanelli, F. Cabry et al., "Role of sentinel node in differentiated thyroid cancer: a prospective study comparing patent blue injection technique, lymphoscintigraphy and the combined technique," *Journal of Endocrinological Investigation*, pp. 1–8, 2017.
- [5] H. M. Evans and W. Schulemann, "The action of vital stains belonging to the benzidine group," *Science*, vol. 39, no. 1004, pp. 443–454, 1914.
- [6] C. J. Cooksey, "Quirks of dye nomenclature. 1. Evans blue," *Biotechnic & Histochemistry*, vol. 89, no. 2, pp. 111–113, 2014.
- [7] O. Steinwall and I. Klatzo, "Selective vulnerability of the blood-brain barrier in chemically induced lesions," *Journal of Neuropathology & Experimental Neurology*, vol. 25, no. 4, pp. 542–559, 1966.
- [8] M. Wolman, I. Klatzo, E. Chui et al., "Evaluation of the dye-protein tracers in pathophysiology of the blood-brain barrier," *Acta Neuropathologica*, vol. 54, no. 1, pp. 55–61, 1981.
- [9] A. Saria and J. M. Lundberg, "Evans blue fluorescence: quantitative and morphological evaluation of vascular permeability in animal tissues," *Journal of Neuroscience Methods*, vol. 8, no. 1, pp. 41–49, 1983.
- [10] L. F. Yen, V. C. Wei, E. Y. Kuo, and T. W. Lai, "Distinct Patterns of Cerebral Extravasation by Evans Blue and Sodium Fluorescein in Rats," *PLoS ONE*, vol. 8, no. 7, Article ID e68595, 2013.
- [11] A. Manaenko, H. Chen, J. Kammer, J. H. Zhang, and J. Tang, "Comparison Evans Blue injection routes: Intravenous versus intraperitoneal, for measurement of blood-brain barrier in a mice hemorrhage model," *Journal of Neuroscience Methods*, vol. 195, no. 2, pp. 206–210, 2011.
- [12] B. T. Roller, J. M. Munson, B. Brahma, P. J. Santangelo, S. B. Pai, and R. V. Bellamkonda, "Evans blue nanocarriers visually demarcate margins of invasive gliomas," *Drug Delivery and Translational Research*, vol. 5, no. 2, pp. 116–124, 2015.

- [13] M. Zheng, J. Yu, and Z. Tian, "Characterization of the liver-draining lymph nodes in mice and their role in mounting regional immunity to HBV," *Cellular & Molecular Immunology*, vol. 10, no. 2, pp. 143–150, 2013.
- [14] S. J. Smith, E. J. Horstick, A. E. Davidson, and J. Dowling, "Analysis of zebrafish larvae skeletal muscle integrity with evans blue dye," *Journal of Visualized Experiments*, vol. 2015, no. 105, Article ID e53183, 2015.
- [15] H. Maeda, J. Fang, T. Inutsuka, and Y. Kitamoto, "Vascular permeability enhancement in solid tumor: Various factors, mechanisms involved and its implications," *International Immunopharmacology*, vol. 3, no. 3, pp. 319–328, 2003.
- [16] A. Mammoto, T. Mammoto, M. Kanapathipillai et al., "Control of lung vascular permeability and endotoxin-induced pulmonary oedema by changes in extracellular matrix mechanics," *Nature Communications*, vol. 4, article no. 1759, 2013.
- [17] J. Bábíčková, B. M. Klinkhammer, E. M. Buhl et al., "Regardless of etiology, progressive renal disease causes ultrastructural and functional alterations of peritubular capillaries," *Kidney International*, vol. 91, no. 1, pp. 70–85, 2017.
- [18] M. I. Harrell, B. M. Iritani, and A. Ruddell, "Lymph node mapping in the mouse," *Journal of Immunological Methods*, vol. 332, no. 1–2, pp. 170–174, 2008.
- [19] W. O. Caster, A. B. Simon, and W. D. Armstrong, "Analytical Problems in Determination of Evans Blue: Caused by Absorption on Glass and Protein Surfaces," *Analytical Chemistry*, vol. 26, no. 4, pp. 713–715, 1954.
- [20] W. W. Lacy, C. Ugaz, and E. V. Newman, "The use of indigo carmine for dye dilution curves," *Circulation Research*, vol. 3, no. 6, pp. 570–574, 1955.
- [21] A. C. Lawrence and G. Walters, "The extraction of Evans blue (T1824) from plasma and the measurement of plasma volume," *Journal of Clinical Pathology*, vol. 12, no. 2, pp. 123–127, 1959.
- [22] S. Szabo, J. S. Trier, A. Brown, and J. Schnoor, "Early Vascular Injury and Increased Vascular Permeability in Gastric Mucosal Injury Caused by Ethanol in the Rat," *Gastroenterology*, vol. 88, no. 1, pp. 228–236, 1985.
- [23] C. Tsopelas, E. Bevington, J. Kollias et al., "99mTc-Evans blue dye for mapping contiguous lymph node sequences and discriminating the sentinel lymph node in an ovine model," *Annals of Surgical Oncology*, vol. 13, no. 5, pp. 692–700, 2006.
- [24] M. Radu and J. Chernoff, "An in vivo assay to test blood vessel permeability," *Journal of visualized experiments : JoVE*, no. 73, p. e50062, 2013.
- [25] Y. Liu, G. Wang, H. Zhang et al., "Stable Evans Blue Derived Exendin-4 Peptide for Type 2 Diabetes Treatment," *Bioconjugate Chemistry*, vol. 27, no. 1, pp. 54–58, 2016.
- [26] H. Chen, G. Wang, L. Lang et al., "Chemical conjugation of evans blue derivative: A strategy to develop long-acting therapeutics through albumin binding," *Theranostics*, vol. 6, no. 2, pp. 243–253, 2016.
- [27] C. Tsopelas and R. Sutton, "Why certain dyes are useful for localizing the sentinel lymph node," *Journal of Nuclear Medicine*, vol. 43, no. 10, pp. 1377–1382, 2002.
- [28] N. R. Saunders, K. M. Dziegielewska, K. Møllgård, and M. D. Habgood, "Markers for blood-brain barrier integrity: How appropriate is Evans blue in the twenty-first century and what are the alternatives?" *Frontiers in Neuroscience*, vol. 9, article no. 385, 2015.
- [29] Y. Shen et al., "Fluorescence imaging of Evans blue extravasation into mouse brain induced by low frequency ultrasound with microbubble," *Bio-Medical Materials and Engineering*, vol. 24, no. 6, p. 2831, 2014.
- [30] J. Do, D. Foster, C. Renier et al., "Ex vivo Evans blue assessment of the blood brain barrier in three breast cancer brain metastasis models," *Breast Cancer Research and Treatment*, vol. 144, no. 1, pp. 93–101, 2014.
- [31] L. L. Muldoon, M. A. Pagel, J. P. Netto, and E. A. Neuwelt, "Intra-arterial administration improves temozolomide delivery and efficacy in a model of intracerebral metastasis, but has unexpected brain toxicity," *Journal of Neuro-Oncology*, vol. 126, no. 3, pp. 447–454, 2016.
- [32] Y. Feng, F. Chen, Z. Ma et al., "Towards stratifying ischemic components by cardiac MRI and multifunctional stainings in a rabbit model of myocardial infarction," *Theranostics*, vol. 4, no. 1, pp. 24–35, 2014.
- [33] M. M. Cona, M. Koole, Y. Feng et al., "Biodistribution and radiation dosimetry of radioiodinated hypericin as a cancer therapeutic," *International Journal of Oncology*, vol. 44, no. 3, pp. 819–829, 2014.
- [34] J. G. Gibson and W. A. Evans, "Clinical studies of the blood volume. I. Clinical application of a method employing the azo dye "evans blue" and the spectrophotometer," *The Journal of Clinical Investigation*, vol. 16, no. 3, pp. 301–316, 1937.
- [35] A. B. Dawson, H. M. Evans, and G. H. Whipple, "Blood volume studies," *American Journal of Physiology-Legacy Content*, vol. 51, no. 2, pp. 232–256, 1920.
- [36] E. B. Reeve, T. H. Allen, and J. E. Roberts, "Blood Volume Regulation," *Annual Review of Physiology*, vol. 22, no. 1, pp. 349–380, 1960.
- [37] J. F. M and J. P. Shillingford, "A comparison of direct and extraction methods for the determination of T-1824 (Evans blue) in plasma and serum," *Journal of Clinical Pathology*, vol. 11, no. 2, pp. 170–172, 1958.
- [38] A. C. Croke and C. J. O. Morris, "The determination of plasma volume by the Evans blue method," *The Journal of Physiology*, vol. 101, no. 2, pp. 217–223, 1942.
- [39] J. Hopper, H. Tabor, and A. W. Winkler, "Simultaneous measurements of the blood volume in man and dog by means of evans blue dye, T1824, and by means of carbon monoxide. I. Normal subjects 1," *The Journal of Clinical Investigation*, vol. 23, no. 5, pp. 628–635, 1944.
- [40] E. W. H. Cruickshank and I. C. Whitfield, "The behaviour of T. 1824 (Evans's blue) in circulating blood and a modified method for the estimation of plasma volume," *The Journal of Physiology*, vol. 104, no. 1, pp. 52–59, 1945.
- [41] M. Hobsley and E. D. Dew, "An extraction technique for the estimation of Evans blue in plasma," *Journal of Clinical Pathology*, vol. 11, no. 5, pp. 451–454, 1958.
- [42] J. Farjanel, C. Denis, J. C. Chatard, and A. Geysant, "An accurate method of plasma volume measurement by direct analysis of Evans blue spectra in plasma without dye extraction: Origins of albumin-space variations during maximal exercise," *European Journal of Applied Physiology*, vol. 75, no. 1, pp. 75–82, 1996.
- [43] H.-L. Wang and T. W. Lai, "Optimization of Evans blue quantitation in limited rat tissue samples," *Scientific Reports*, vol. 4, article no. 6588, 2014.
- [44] D. Margoueff, "Blood volume determination, a nuclear medicine test in evolution," *Clinical Nuclear Medicine*, vol. 38, no. 7, pp. 534–537, 2013.
- [45] P. M. Baby, P. Kumar, R. Kumar et al., "A novel method for blood volume estimation using trivalent chromium in rabbit models," *Indian Journal of Plastic Surgery*, vol. 47, no. 2, pp. 242–248, 2014.

- [46] J. Dingley, B. A. Foëx, M. Swart et al., "Blood volume determination by the carbon monoxide method using a new delivery system: Accuracy in critically ill humans and precision in an animal model," *Critical Care Medicine*, vol. 27, no. 11, pp. 2435–2441, 1999.
- [47] S. Yet, R. Tian, M. D. Layne et al., "Cardiac-specific expression of heme oxygenase-1 protects against ischemia and reperfusion injury in transgenic mice," *Circulation Research*, vol. 89, no. 2, pp. 168–173, 2001.
- [48] E. F. Lucking, K. D. O'Halloran, and J. F. X. Jones, "Increased cardiac output contributes to the development of chronic intermittent hypoxia-induced hypertension," *Experimental Physiology*, vol. 99, no. 10, pp. 1312–1324, 2014.
- [49] G. N. Stewart, "Researches on the Circulation Time and on the Influences which affect it," *The Journal of Physiology*, vol. 22, no. 3, pp. 159–183, 1897.
- [50] W. F. Hamilton, R. L. Riley, A. M. Attyah et al., "Comparison of the fick and dye injection methods of measuring the cardiac output in man," *American Journal of Physiology-Legacy Content*, vol. 153, no. 2, pp. 309–321, 1948.
- [51] A. C. Witham, J. W. Fleming, and W. L. Bloom, "The effect of the intravenous administration of dextran on cardiac output and other circulatory dynamics," *The Journal of Clinical Investigation*, vol. 30, no. 9, pp. 897–902, 1951.
- [52] X. García, L. Mateu, J. Maynar, J. Mercadal, A. Ochagavía, and A. Ferrandiz, "Estimating cardiac output. Utility in the clinical practice. Available invasive and non-invasive monitoring," *Medicina Intensiva (English Edition)*, vol. 35, no. 9, pp. 552–561, 2011.
- [53] R. H. Thiele, K. Bartels, and T. J. Gan, "Cardiac output monitoring: A contemporary assessment and review," *Critical Care Medicine*, vol. 43, no. 1, pp. 177–185, 2015.
- [54] L. S. Nguyen and P. Squara, "Non-Invasive Monitoring of Cardiac Output in Critical Care Medicine," *Frontiers in Medicine*, vol. 4, 2017.
- [55] J. L. Romson, B. G. Hook, S. L. Kunkel, G. D. Abrams, M. A. Schork, and B. R. Lucchesi, "Reduction of the extent of ischemic myocardial injury by neutrophil depletion in the dog," *Circulation*, vol. 67, no. 5, pp. 1016–1023, 1983.
- [56] S. R. Jolly, W. J. Kane, M. B. Bailie, G. D. Abrams, and B. R. Lucchesi, "Canine myocardial reperfusion injury. Its reduction by the combined administration of superoxide dismutase and catalase," *Circulation Research*, vol. 54, no. 3, pp. 277–285, 1984.
- [57] S. Bialik, D. L. Geenen, I. E. Sasson et al., "Myocyte apoptosis during acute myocardial infarction in the mouse localizes to hypoxic regions but occurs independently of p53," *The Journal of Clinical Investigation*, vol. 100, no. 6, pp. 1363–1372, 1997.
- [58] K. M. Kurrelmeyer, L. H. Michael, G. Baumgarten et al., "Endogenous tumor necrosis factor protects the adult cardiac myocyte against ischemic-induced apoptosis in a murine model of acute myocardial infarction," *Proceedings of the National Academy of Sciences of the United States of America*, vol. 97, no. 10, pp. 5456–5461, 2000.
- [59] H. Stanton, F. M. Rogerson, C. J. East et al., "ADAMTS5 is the major aggrecanase in mouse cartilage in vivo and in vitro," *Nature*, vol. 434, no. 7033, pp. 648–652, 2005.
- [60] M. C. Fishbein, S. Meerbaum, J. Rit et al., "Early phase acute myocardial infarct size quantification: Validation of the triphenyl tetrazolium chloride tissue enzyme staining technique," *American Heart Journal*, vol. 101, no. 5, pp. 593–600, 1981.
- [61] D. L. Miller, P. Li, C. Dou, W. F. Armstrong, and D. Gordon, "Evans Blue Staining of Cardiomyocytes Induced by Myocardial Contrast Echocardiography in Rats: Evidence for Necrosis Instead of Apoptosis," *Ultrasound in Medicine & Biology*, vol. 33, no. 12, pp. 1988–1996, 2007.
- [62] M. Kaya and B. Ahishali, "Assessment of permeability in barrier type of endothelium in brain using tracers: Evans blue, sodium fluorescein, and horseradish peroxidase," *Methods in Molecular Biology*, vol. 763, pp. 369–382, 2011.
- [63] P. Kozler and J. Pokorný, "Altered Blood-Brain Barrier Permeability and Its Effect on the Distribution of Evans Blue and Sodium Fluorescein in the Rat Brain Applied by Intracarotid Injection," *Physiological Research*, vol. 52, no. 5, pp. 607–614, 2003.
- [64] O. Uyama, N. Okamura, M. Yanase, M. Narita, K. Kawabata, and M. Sugita, "Quantitative evaluation of vascular permeability in the gerbil brain after transient ischemia using Evans blue fluorescence," *Journal of Cerebral Blood Flow & Metabolism*, vol. 8, no. 2, pp. 282–284, 1988.
- [65] M. Slama, D. Susic, J. Varagic, J. Ahn, and E. D. Frohlich, "Echo cardiographic measurement of cardiac output in rats," *American Journal of Physiology-Heart and Circulatory Physiology*, vol. 284, no. 2, pp. H691–H697, 2003.
- [66] W. G. Roberts and G. E. Palade, "Increased microvascular permeability and endothelial fenestration induced by vascular endothelial growth factor," *Journal of Cell Science*, vol. 108, no. 6, pp. 2369–2379, 1995.
- [67] L. Huang, W. Cao, Y. Deng, G. Zhu, Y. Han, and H. Zeng, "Hypertonic saline alleviates experimentally induced cerebral oedema through suppression of vascular endothelial growth factor and its receptor VEGFR2 expression in astrocytes," *BMC Neuroscience*, vol. 17, no. 1, article no. 64, 2016.
- [68] T. A. Jackiewicz, J. K. McGeachie, R. M. London, and M. Tennant, "Evans blue dye modifies the ultrastructure of normal and regenerating arterial endothelium in rats," *Microsurgery*, vol. 18, no. 1, pp. 47–54, 1998.
- [69] F. Chen, Y. Suzuki, N. Nagai et al., "Visualization of stroke with clinical MR imagers in rats: a feasibility study," *Radiology*, vol. 233, no. 3, pp. 905–911, 2004.
- [70] M. Soubeyrand, A. Badner, R. Vawda, Y. S. Chung, and M. G. Fehlings, "Very high resolution ultrasound imaging for real-time quantitative visualization of vascular disruption after spinal cord injury," *Journal of Neurotrauma*, vol. 31, no. 21, pp. 1767–1775, 2014.
- [71] C. Å. V. Pettersson, H. S. Sharma, and Y. Olsson, "Vascular permeability of spinal nerve roots - A study in the rat with Evans blue and lanthanum as tracers," *Acta Neuropathologica*, vol. 81, no. 2, pp. 148–154, 1990.
- [72] Q. Xu, T. Qaum, and A. P. Adamis, "Sensitive blood-retinal barrier breakdown quantitation using Evans blue," *Investigative Ophthalmology & Visual Science*, vol. 42, no. 3, pp. 789–794, 2001.
- [73] J. A. Alves da Silva, K. C. Oliveira, and M. A. P. Camillo, "Gyroxin increases blood-brain barrier permeability to Evans blue dye in mice," *Toxicol*, vol. 57, no. 1, pp. 162–167, 2011.
- [74] R. Sutton, C. Tsopelas, J. Kollias, B. E. Chatterton, and B. J. Coventry, "Sentinel node biopsy and lymphoscintigraphy with a technetium 99m labeled blue dye in a rabbit model," *Surgery*, vol. 131, no. 1, pp. 44–49, 2002.
- [75] J. Y. Bobin et al., "Tagging sentinel lymph nodes: a study of 100 patients with breast cancer," *European Journal of Cancer*, vol. 35, no. 4, pp. 569–573, 1999.

- [76] T. V. Tervala, P. Hartiala, T. Tammela et al., "Growth factor therapy and lymph node graft for lymphedema," *Journal of Surgical Research*, vol. 196, no. 1, pp. 200–207, 2015.
- [77] S. S. Bass et al., "The role of sentinel lymph node biopsy in breast cancer," *Journal of the American College of Surgeons*, vol. 189, no. 2, pp. 183–194, 1999.
- [78] T. Ozawa, G. W. Britz, D. H. Kinder et al., "Bromophenol blue staining of tumors in a rat glioma model," *Neurosurgery*, vol. 57, no. 5, pp. 1041–1046, 2005.
- [79] H. Maeda, H. Nakamura, and J. Fang, "The EPR effect for macromolecular drug delivery to solid tumors: Improvement of tumor uptake, lowering of systemic toxicity, and distinct tumor imaging in vivo," *Advanced Drug Delivery Reviews*, vol. 65, no. 1, pp. 71–79, 2013.
- [80] S. S. Prabhu, W. C. Broaddus, C. Oveissi, S. S. Berr, and G. T. Gillies, "Determination of intracranial tumor volumes in a rodent brain using magnetic resonance imaging, Evans Blue, and histology: A comparative study," *IEEE Transactions on Biomedical Engineering*, vol. 47, no. 2, pp. 259–265, 2000.
- [81] S. Elsen, E. Lerut, B. Van Cleynenbreugel, F. Van Der Aa, H. Van Poppel, and P. A. De Witte, "Biodistribution of Evans blue in an orthotopic AY-27 rat bladder urothelial cell carcinoma model: Implication for the improved diagnosis of non-muscle-invasive bladder cancer (NMIBC) using dye-guided white-light cystoscopy," *BJU International*, vol. 116, no. 3, pp. 468–477, 2015.
- [82] M. Roelants, A. Huygens, I. Crnolatac et al., "Evans blue as a selective dye marker for white-light diagnosis of non-muscle-invasive bladder cancer: An in vitro study," *BJU International*, vol. 109, no. 2, pp. 300–305, 2012.
- [83] X. Zhang, Y. Xie, Y. Jin, X. Hou, L. Ye, and J. Lou, "The effect of RMP-7 and its derivative on transporting evens blue liposomes into the brain," *Drug Delivery: Journal of Delivery and Targeting of Therapeutic Agents*, vol. 11, no. 5, pp. 301–309, 2004.
- [84] K. M. McNeeley, A. Annapragada, and R. V. Bellamkonda, "Decreased circulation time offsets increased efficacy of PEGylated nanocarriers targeting folate receptors of glioma," *Nanotechnology*, vol. 18, no. 38, Article ID 385101, 2007.
- [85] C. Morera and M. A. Villanueva, "Heat treatment and viability assessment by Evans blue in cultured *Symbiodinium kawagutii* cells," *World Journal of Microbiology and Biotechnology*, vol. 25, no. 6, pp. 1125–1128, 2009.
- [86] C. Jacyn Baker and N. M. Mock, "An improved method for monitoring cell death in cell suspension and leaf disc assays using evans blue," *Plant Cell, Tissue and Organ Culture*, vol. 39, no. 1, pp. 7–12, 1994.
- [87] R. Matsuda, A. Nishikawa, and H. Tanaka, "Visualization of dystrophic muscle fibers in Mdx mouse by vital staining with Evans blue: evidence of apoptosis in dystrophin-deficient muscle," *The Journal of Biochemistry*, vol. 118, no. 5, pp. 959–964, 1995.
- [88] V. Straub, J. A. Rafael, J. S. Chamberlain, and K. P. Campbell, "Animal models for muscular dystrophy show different patterns of sarcolemmal disruption," *The Journal of Cell Biology*, vol. 139, no. 2, pp. 375–385, 1997.
- [89] B. R. Klyen, T. Shavlakadze, H. G. Radley-Crabb, M. D. Grounds, and D. D. Sampson, "Identification of muscle necrosis in the mdx mouse model of Duchenne muscular dystrophy using three-dimensional optical coherence tomography," *Journal of Biomedical Optics*, vol. 16, no. 7, Article ID 076013, 2011.
- [90] C. I. Wooddell, G. Zhang, J. B. Griffin, J. O. Hegge, T. Huss, and J. A. Wolff, "Use of Evans blue dye to compare limb muscles in exercised young and old mdx mice," *Muscle & Nerve*, vol. 41, no. 4, pp. 487–499, 2010.
- [91] P. W. Hamer, J. M. McGeachie, M. J. Davies, and M. D. Grounds, "Evans Blue Dye as an in vivo marker of myofibre damage: optimising parameters for detecting initial myofibre membrane permeability," *Journal of Anatomy*, vol. 200, no. 1, pp. 69–79, 2002.
- [92] D. L. Miller, P. Li, C. Dou, D. Gordon, C. A. Edwards, and W. F. Armstrong, "Influence of contrast agent dose and ultrasound exposure on cardiomyocyte injury induced by myocardial contrast echocardiography in rats," *Radiology*, vol. 237, no. 1, pp. 137–143, 2005.
- [93] S. Yasuda, K. Ikuta, T. Uwatoku et al., "In vivo magnetic resonance imaging of atherosclerotic lesions with a newly developed evans blue-DTPA-gadolinium contrast medium in apolipoprotein-E-deficient mice," *Journal of Vascular Research*, vol. 45, no. 2, pp. 123–128, 2008.
- [94] Y. Ni, G. Bormans, F. Chen, A. Verbruggen, and G. Marchal, "Necrosis avid contrast agents: Functional similarity versus structural diversity," *Investigative Radiology*, vol. 40, no. 8, pp. 526–535, 2005.
- [95] C. Tsopeles, M. Bellon, E. Bevington, J. Kollias, S. Shibli, and B. E. Chatterton, "Lymphatic mapping with <sup>99m</sup>Tc-Evans Blue dye in sheep," *Annals of Nuclear Medicine*, vol. 22, no. 9, pp. 777–785, 2008.
- [96] G. Niu, L. Lang, D. O. Kiesewetter et al., "In vivo labeling of serum albumin for PET," *Journal of Nuclear Medicine*, vol. 55, no. 7, pp. 1150–1156, 2014.
- [97] J. Zhang, L. Lang, Z. Zhu, F. Li, G. Niu, and X. Chen, "Clinical translation of an albumin-binding PET radiotracer <sup>68</sup>Ga-NEB," *Journal of Nuclear Medicine*, vol. 56, no. 10, pp. 1609–1614, 2015.
- [98] W. Zhang, P. Wu, F. Li, G. Tong, X. Chen, and Z. Zhu, "Potential applications of using <sup>68</sup>Ga-evans blue PET/CT in the evaluation of lymphatic disorder preliminary observations," *Clinical Nuclear Medicine*, vol. 41, no. 4, pp. 302–308, 2016.
- [99] S. H. Taylor and J. M. Thorp, "Properties and biological behaviour of coomassie blue," *Heart*, vol. 21, no. 4, pp. 492–496, 1959.
- [100] M. Giger, H. R. Baumgartner, and G. Zbinden, "Toxicological effects of Evans blue and Congo red on blood platelets," *Agents and Actions Supplements*, vol. 4, no. 3, pp. 173–180, 1974.
- [101] T. Moos and K. Mollgard, "Cerebrovascular permeability to azo dyes and plasma proteins in rodents of different ages," *Neuropathology and Applied Neurobiology*, vol. 19, no. 2, pp. 120–127, 1993.
- [102] F. Giansanti, N. Schiavone, L. Papucci et al., "Safety testing of blue vital dyes using cell culture models," *Journal of Ocular Pharmacology and Therapeutics*, vol. 30, no. 5, pp. 406–412, 2014.
- [103] U. Abildgaard, "Rapid Elimination of Evans Blue in Amyloidosis," *Journal of Internal Medicine*, vol. 180, no. 6, pp. 709–714, 1966.

## Research Article

# Thyroid Cancer Detection by Ultrasound Molecular Imaging with SHP2-Targeted Perfluorocarbon Nanoparticles

ZhongQian Hu <sup>1</sup>, Bin Yang,<sup>2</sup> Tiankuan Li,<sup>1</sup> and Jia Li <sup>1</sup>

<sup>1</sup>Department of Ultrasound, Zhongda Hospital, Southeast University, Nanjing, China

<sup>2</sup>Department of Ultrasound, Jinling Clinical Medical College, Nanjing Medical University, Nanjing, China

Correspondence should be addressed to ZhongQian Hu; hzq920@126.com and Jia Li; 13951609892@163.com

Received 7 November 2017; Revised 22 January 2018; Accepted 29 January 2018; Published 8 March 2018

Academic Editor: Yuebing Wang

Copyright © 2018 ZhongQian Hu et al. This is an open access article distributed under the Creative Commons Attribution License, which permits unrestricted use, distribution, and reproduction in any medium, provided the original work is properly cited.

**Background.** Contrast-enhanced ultrasound imaging has been widely used in the ultrasound diagnosis of a variety of tumours with high diagnostic accuracy, especially in patients with hepatic carcinoma, while its application is rarely reported in thyroid cancer. The currently used ultrasound contrast agents, microbubbles, cannot be targeted to molecular markers expressed in tumour cells due to their big size, leading to a big challenge for ultrasound molecular imaging. Phase-changeable perfluorocarbon nanoparticles may resolve the penetrability limitation of microbubbles and serve as a promising probe for ultrasound molecular imaging. **Methods.** 65 thyroid tumour samples and 40 normal samples adjacent to thyroid cancers were determined for SHP2 expression by IHC. SHP2-targeted PLGA nanoparticles (NPs-SHP2) encapsulating perfluoropentane (PFP) were prepared with PLGA-PEG as a shell material, and their specific target-binding ability was assessed in vitro and in vivo, and the effect on the enhancement of ultrasonic imaging induced by LIFU was studied in vivo. **Results.** In the present study, we verified that tumour overexpression of SHP2 and other protein tyrosine phosphatases regulated several cellular processes and contributed to tumorigenesis, which could be introduced to ultrasound molecular imaging for differentiating normal from malignant thyroid diagnostic nodes. The IHC test showed remarkably high expression of SHP2 in human thyroid carcinoma specimens. In thyroid tumour xenografts in mice, the imaging signal was significantly enhanced by SHP2-targeted nanoparticles after LIFU induction. **Conclusion.** This study provides a basis for preclinical exploration of ultrasound molecular imaging with NPs-SHP2 for clinical thyroid nodule detection to enhance diagnostic accuracy.

## 1. Introduction

In recent years, the incidence of thyroid cancer increased significantly [1]. Conventional ultrasonography (US) imaging to distinguish normal from malignant thyroid tissues has better sensitivity, but the specificity is weak (58.5%) [2]. Contrast-enhanced US (CEUS) represents an important advance in US imaging and has been used as a tool in the clinic for many years to locate tumours, such as liver tumours, with good accuracy [3–6]. Nevertheless, the diagnostic validity of current CEUS methods in thyroid tumour detection is unsatisfactory, leading to many needless surgeries and biopsies. In addition, the sensitivity of CEUS, when used alone for detection of early thyroid cancer, is lower in some reports [7, 8]. Therefore, further improvement of ultrasonic diagnosis ability is very necessary for use in thyroid carcinoma scanning.

Targeted CEUS imaging using phase-shift nanoparticles as contrast agents is considered to be with a great promising tool for molecular imaging [9–11]. These nanoparticles can be labeled with specific molecular markers as ultrasound contrast agents to target tissue sites expressing these markers, resulting in a distinct signal enhancement under ultrasound imaging after LIFU exposure. By virtue of their small size (nanometres grade), the contrast nanoparticles can pass through the vessel wall and remain predominantly within the tissue. This feature makes targeted CEUS uniquely attractive as a novel molecular imaging method to detect and monitor the tumour [12–17].

Previous studies have reported that the abnormal expression of Src homology 2 domain-containing phosphotyrosine phosphatase 2 (SHP2) plays important roles in tumour occurrence and metastasis [18–20]. SHP2 is a proven oncogene;

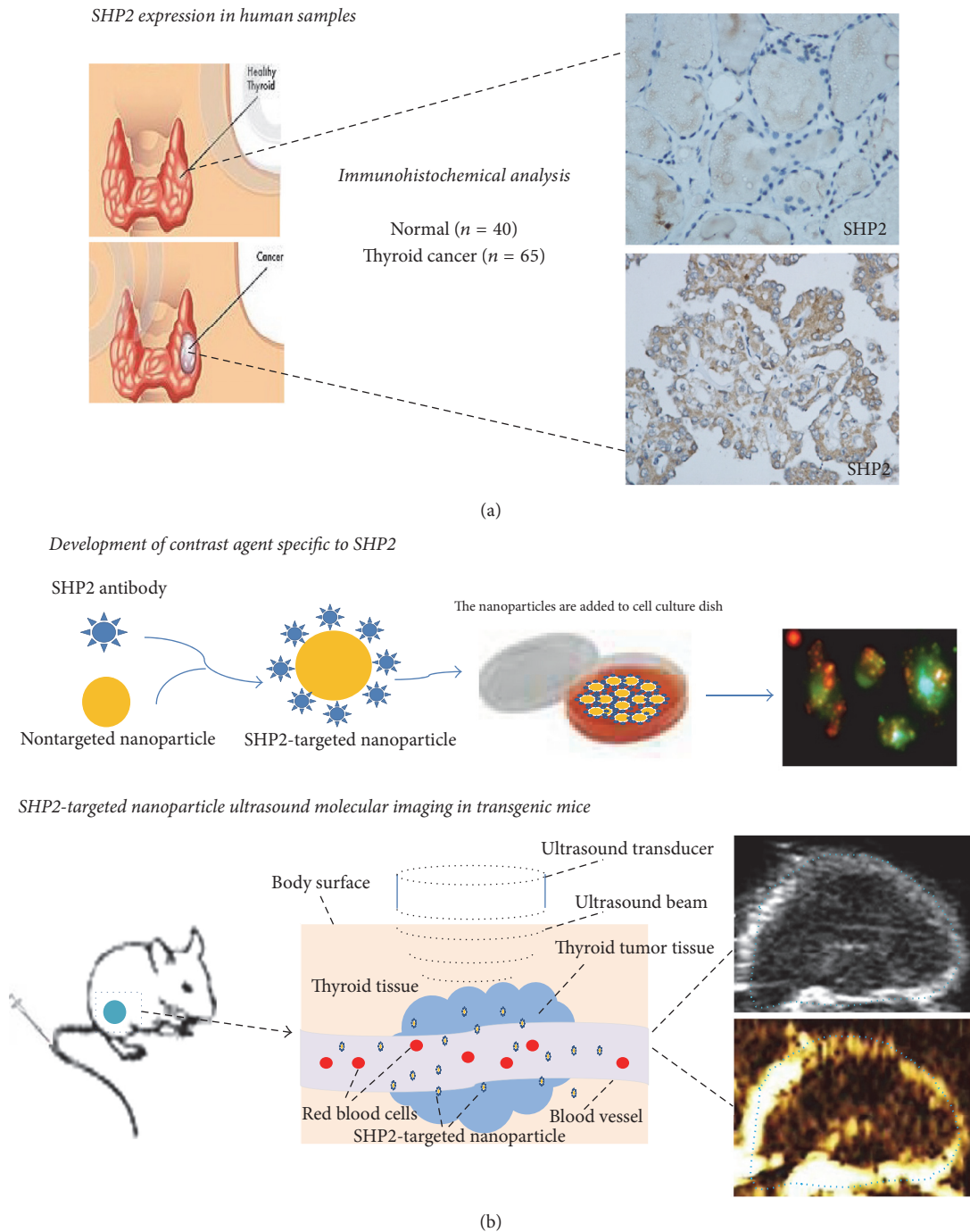


FIGURE 1: The study drawn scheme. (a) Variant expression of SHP2 in thyroid cancer was assessed on normal and malignant thyroid tissues that were collected from patients undergoing biopsy or surgical operation. (b) SHP2-targeted nanoparticles were produced and tested in vitro and in vivo.

SHP2 and other PTPs regulate many diseases' progress and contribute to tumorigenesis. Mutations of PTPN11 (encoding SHP2) were found in myeloid leukaemia patients (especially childhood leukaemia patients) and some solid tumours [21, 22]. Our findings showed that SHP2 was overexpressed in thyroid tumour cell line and in tumour tissues [23].

Although monoclonal antibodies have been applied to targeted CEUS molecular imaging over ten years [24–26], it is not known whether SHP2 can serve as a new molecular

marker for thyroid tumour detection using ultrasound imaging. In this study, we bound SHP2 antibody to the surface of nanoparticles to produce targeted probe for ultrasound molecular imaging on thyroid cancer. The imaging signal in tumour area was significantly enhanced by these phase-changeable nanoparticles after LIFU induction.

The aim of our study includes two aspects (Figure 1): (1) to compare the SHP2 expression in thyroid tumour tissue and that in normal tissue by IHC analysis and (2) to develop

TABLE 1: Summary table of different thyroid cancer pathologies analysed.

Histology	Subtype	Number ( <i>n</i> )
Normal thyroid tissue		40
	Papillary	31
Thyroid cancer	Follicle	22
	Medullary	11
	Undifferentiated	1

SHP2-targeted phase-changeable PLGA nanoparticles as a novel molecular probe for ultrasound imaging, providing a practicable method for thyroid cancer detection.

## 2. Materials and Methods

See (Figure 1) the experiment design scheme.

**2.1. Selection of Human Thyroid Tissue Samples.** In the present study, 65 human thyroid cancer samples and 40 normal thyroid samples were collected at the Department of Pathology for retrospective comparison (Table 1). The thyroid samples were processed into thyroid tissue microarray using standard protocols and the experiment methods of IHC analysis of SHP2 expression in thyroid tissue and cell culture experiments were the same as those in our previous reports [23, 27].

**2.2. Preparation of SHP2-Targeted PLGA Nanoparticles.** PFP/PLGA-PEG nanoparticles were prepared by double emulsion solvent evaporation method. In brief, 100 mg of PLGA was dissolved in 2 mL of trichloromethane and added with 200  $\mu$ L of PFP (Sigma-Aldrich Chemical Co., USA); the primary emulsion was obtained by an ultrasonic probe (VCX-130, Sonics & Materials Inc., USA). The precipitate was collected by centrifugation, washed, and resuspended with PBS (pH = 6.0) to disperse nanoparticles concentration of 10 mg/mL. The coupling activator EDC (0.1 mL, 50 mg/mL) and NHS (0.1 mL, 50 mg/mL) were dissolved in 1 mL of double distilled water and then were mixed with the PLGA nanoparticle solution. After shocking the reaction at room temperature for 2 h, the sample was dispersed again in deionized water after multiple centrifugal separations and purifications in the appropriate amount of PBS (pH = 8.0); 200  $\mu$ L of SHP2 antibody solution was added, followed by the reaction at room temperature for 2 h. After washing, the sample was redispersed in a suitable amount of PBS. Then, 500  $\mu$ L of polyethylenimine dissolved in 2 mL of deionized water was added to this solution, and dilute hydrochloric acid was added as necessary to adjust the pH to 8.0. After shocking the homogeneous reaction at room temperature for 2 h, the solution was purified by centrifugation and redispersed in PBS (pH = 8.0). Then, 30 nmol DOTA-NHS was added to the solution and reacted for 2 h; after washing, the product was dispersed in PBS solution (pH = 8.0).

**2.3. In Vitro Binding Specificity of SHP2-Targeted Nanoparticles.** The cells were seeded in six-well plates for 24 h until

50% confluence was reached. The cell membrane was then stained with DiO (Keygen, China). The cells were treated with either NPs-SHP2 or control nontargeted nanoparticles (NPs-Control) at 37°C for 30 minutes; both groups of nanoparticles were stained with Dil (Keygen, China) in advance. The cells were washed and fixed and then imaged.

**2.4. Mouse Model.** Animal protocols were approved by the Animal Studies Core Facility at the Chongqing Medical University. Subcutaneous human thyroid cancer xenograft tumours were established in the right flank region of 10 female 4-week-old nude mice ( $n = 10$ ) by subcutaneous injection of  $2 \times 10^6$  SW579 cells in 100  $\mu$ L of PBS. Tumours were allowed to grow to a mean maximum diameter of 10 mm (range: 8–10 mm). The mice were examined 3 weeks after tumour inoculation.

**2.5. SHP2-Targeted Contrast-Enhanced Ultrasound Imaging of Mice.** The mice bearing thyroid tumours were imaged. Each mouse was injected with 0.1 mL of NPs-SHP2 into the caudal vein, and the same amount of NPs-Control was used in the control groups. Images of the signal from adherent nanoparticles appeared as green maps on contrast-mode images, which were automatically calculated using Vevo CQ software (VisualSonics). The colour map scale used was the same for all images.

**2.6. Analysis of Mouse Tumour Imaging Data.** Imaging data of all mice were analysed offline using software. All data were analysed in a blinded manner. Regions of representing signal were drawn over as colour maps in thyroid tumour contrast images, and quantification of the imaging signal from attached nanoparticles was assessed by calculating imaging signals [19, 27, 28].

**2.7. Statistical Analysis.** All data are expressed as the means  $\pm$  SD. Means were compared using one-way analysis of variance (ANOVA) and Student's *t*-test, and *P* values < 0.05 were considered statistically significant.

## 3. Results

**3.1. SHP2 Expression in Human Thyroid Cancer Tissues.** To investigate the roles of SHP2 in thyroid cancer, we compared the expression of SHP2 in thyroid cancers and normal thyroid tissues through standard immunohistochemistry (IHC); it was performed on thyroid tissues representing 65 thyroid tumours (Table 1). In the 65 samples that were processed into a thyroid cancer TMA, the positive signal of SHP2 in the cytoplasm and nuclei of the thyroid tumour cells was markedly stronger ( $P < 0.001$ ) compared to that in the surrounding normal tissue (Figure 2). The mean composite IHC score of tumours was also increased.

**3.2. In Vitro Binding Specificity of SHP2-Targeted Nanoparticles.** NPs-SHP2 and NPs-Control were prepared, the particle diameter of the nanoparticles is centralized and distributed as a single peak with a mean diameter of  $531.2 \pm 13.5$  nm,

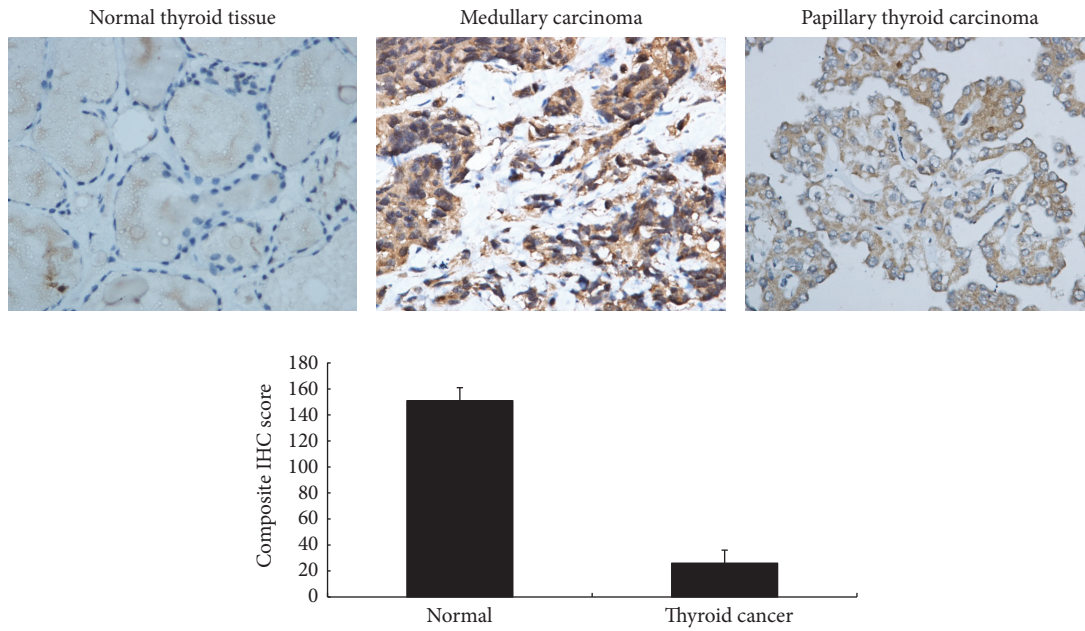


FIGURE 2: SHP2 expression in human thyroid tissues. It shows emblematic dyeing results from normal thyroid and from thyroid cancer tissues of various types. The graph displays composite IHC scores for SHP2-dyed normal and thyroid cancer tissues.  $P < 0.001$ .

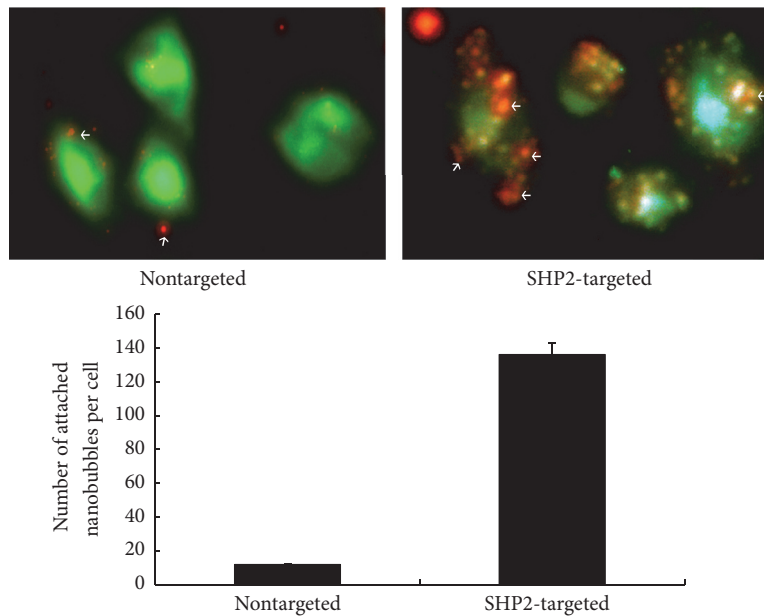


FIGURE 3: The SHP2-targeted nanoparticles binding specificity test. Representative results from in vitro experiments after exposure to SHP2-targeted and nontargeted nanoparticles. Note the specific attachment of SHP2-targeted nanoparticles and the substantial binding inhibition following the administration of nontargeted nanoparticles. Nanoparticles are shown as red dots.  $P < 0.01$ .

an electric potential of  $-14.0$  mV (NPs-Control), with a mean diameter of  $535.7 \pm 14.7$  nm, and an electric potential of  $-13.7$  mV (NPs-SHP2), and the targeting ability to SHP2 was checked by in vitro experiments. Figure 3 shows the NPs-SHP2 and NPs-Control targeting to SW579 cells in six-well plates. The number of NPs-SHP2 attached per cell was notably higher ( $P < 0.001$ ) than that of NPs-Control.

**3.3. NPs-SHP2 Ultrasound Imaging In Vivo Experiment.** The ultrasound molecular imaging with NPs-SHP2 was performed in thyroid tumour bearing mice. After NPs-SHP2 injection followed by LIFU irradiation ( $1.40$  w/cm<sup>2</sup> for 20 min), the ultrasound signal in tumour area was significantly increased, while no enhancement was found after NPs-Control administrated as shown in Figure 4. There was a

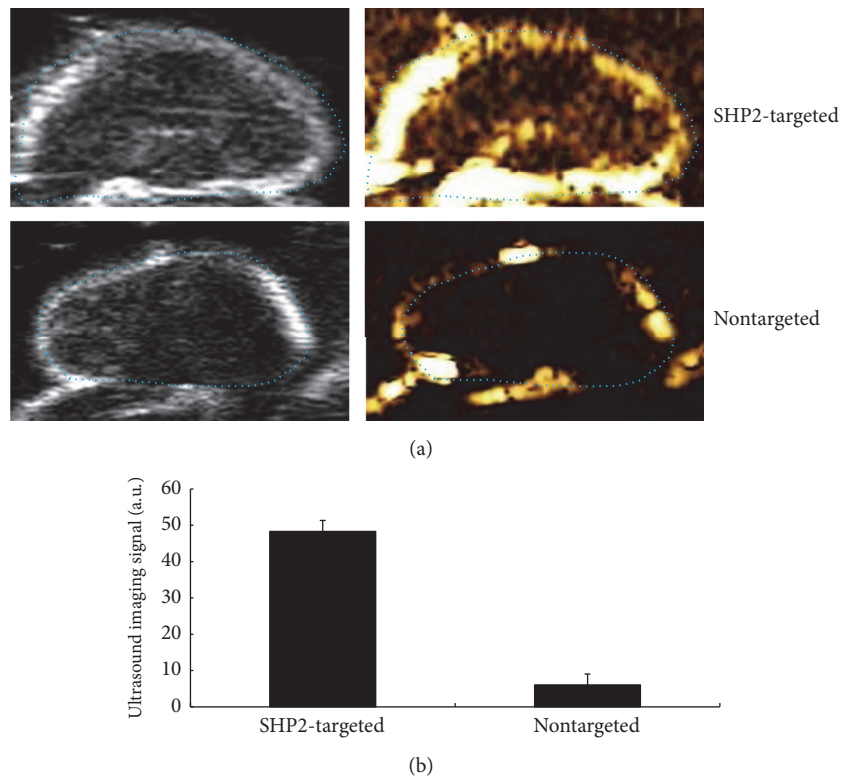


FIGURE 4: Target molecular imaging in vivo experiments after LIFU irradiation  $1.40 \text{ w/cm}^2$  for 20 min. (a) Different ultrasound images mode following the injection of SHP2-signed contrast nanoparticles showing a high signal in thyroid tumour and showing only background signal when using nontargeted contrast nanoparticles. (b) A bar graph summarizing the quantitative signal obtained using ultrasound imaging with SHP2-signed and nontargeted nanoparticles in a thyroid cancer mouse model; a significantly increased imaging signal was observed in the SHP2-targeted nanoparticles compared to the nontargeted nanoparticles in the tumour tissue.  $P < 0.001$ .

significant difference between NPs-SHP2 ( $48.32 \pm 2.9 \text{ a.u.}$ ) and NPs-Control ( $6.03 \pm 1.6 \text{ a.u.}$ ) groups ( $P < 0.001$ ).

#### 4. Discussion

SHP2, which is encoded by the PTPN11 gene in humans, is essential for multiple cellular signaling pathways that modulate cell apoptosis and motility as well as embryonic and haematopoietic cell development [18–23]. Some studies have shown that SHP2 expression of the tumour may increase the risk of metastasis in various types of cancer, including liver [23], colon [27], and breast cancers [29–31]. In thyroid cancer, the tumour expression of SHP2 was positively associated with tumour differentiation and progression. In our previous study, we also found that SHP2 expression was increased markedly in thyroid carcinoma tissue and was associated with thyroid cancer metastasis. From the previous reports, targeted CEUS imaging has been used to improve the diagnostic accuracy of ultrasound for the early detection of pancreatic [10, 28], breast [11, 32], and ovarian cancers [33]. However, whether SHP2 may be used as a novel ultrasound imaging target for thyroid cancer imaging remains unclear.

In this study, SHP2 was confirmed to be discriminatively expressed in human thyroid tumour and normal tissues as shown by IHC, which allowed it to be a potential marker for

the identification of thyroid tumour by molecular ultrasound imaging with higher diagnostic accuracy.

SHP2-targeted (NPs-SHP2) nanoparticles were then designed and their binding specificity was investigated by in vitro and in vivo experiments. The results of cell-based experiments showed high affinity of NPs-SHP2 targeting to thyroid cancer cells. The contrast ultrasound imaging signal in thyroid tumour tissue in nude mice was strikingly higher after caudal vein injection with SHP2-targeted nanoparticles compared to that with NPs-Control injection followed by LIFU irradiation. These results together suggest that SHP2-targeted ultrasound imaging protocol should be further explored as a real-time, noninvasive, and inexpensive method for thyroid tumour detection and characterization in clinic.

In conclusion, the results of this study indicate that SHP2 is upregulated in thyroid cancer tissues compared with normal thyroid tissue obtained from surgical operation or biopsy. NPs-SHP2 had high specificity targeting to thyroid tumour in vitro and vivo and could be activated by LIFU irradiation to enhance ultrasound molecular imaging in thyroid cancer model. Future work should aim at the development of SHP2-targeted contrast agents with clinical grade and much efforts need to be made to promote the clinical translation of ultrasound molecular imaging technique, which could improve the diagnostic accuracy of thyroid lesions by ultrasonography.

## Conflicts of Interest

The authors have no conflicts of interest to declare.

## Authors' Contributions

ZhongQian Hu, Jia Li, and Bin Yang conceived and designed the experiment. ZhongQian Hu and Tiankuan Li collected, observed, designed, and analysed the clinical data and wrote the paper.

## Acknowledgments

This work was supported by a grant from the National Natural Science Foundation of China (81501444). The authors acknowledge the Institute of Ultrasound Imaging of Chongqing Medical University and Animal Studies Core Facility at the Chongqing Medical University.

## References

- [1] C. D. Lansford and T. N. Teknos, "Evaluation of the thyroid nodule," *Cancer Control*, vol. 13, no. 2, pp. 89–98, 2006.
- [2] Z. W. Baloch, S. Fleisher, V. A. LiVolsi, and P. K. Gupta, "Diagnosis of "follicular neoplasm": A gray zone in thyroid fine-needle aspiration cytology," *Diagnostic Cytopathology*, vol. 26, no. 1, pp. 41–44, 2002.
- [3] C. J. Harvey, M. J. K. Blomley, R. J. Eckersley, and D. O. Cosgrove, "Developments in ultrasound contrast media," *European Radiology*, vol. 11, no. 4, pp. 675–689, 2001.
- [4] M. Friedrich-Rust, T. Klopffleisch, J. Nierhoff et al., "Contrast-enhanced ultrasound for the differentiation of benign and malignant focal liver lesions: a meta-analysis," *Liver International*, vol. 33, no. 5, pp. 739–755, 2013.
- [5] S. Kersting, R. Konopke, F. Kersting et al., "Quantitative perfusion analysis of transabdominal contrast-enhanced ultrasonography of pancreatic masses and carcinomas," *Gastroenterology*, vol. 137, no. 6, pp. 1903–1911, 2009.
- [6] Y.-X. Jiang, H. Liu, J.-B. Liu, Q.-L. Zhu, Q. Sun, and X.-Y. Chang, "Breast Tumor Size Assessment: Comparison of Conventional Ultrasound and Contrast-Enhanced Ultrasound," *Ultrasound in Medicine & Biology*, vol. 33, no. 12, pp. 1873–1881, 2007.
- [7] T. V. Bartolotta, M. Midiri, M. Galia et al., "Qualitative and quantitative evaluation of solitary thyroid nodules with contrast-enhanced ultrasound: Initial results," *European Radiology*, vol. 16, no. 10, pp. 2234–2241, 2006.
- [8] V. Cantisani, F. Consorti, A. Guerrisi et al., "Prospective comparative evaluation of quantitative-elastosonography (Q-elastography) and contrast-enhanced ultrasound for the evaluation of thyroid nodules: Preliminary experience," *European Journal of Radiology*, vol. 82, no. 11, pp. 1892–1898, 2013.
- [9] F. Kiessling, S. Fokong, P. Koczera, W. Lederle, and T. Lammers, "Ultrasound microbubbles for molecular diagnosis, therapy, and theranostics," *Journal of Nuclear Medicine*, vol. 53, no. 3, pp. 345–348, 2012.
- [10] K. Foygel, H. Wang, S. MacHteler et al., "Detection of pancreatic ductal adenocarcinoma in mice by ultrasound imaging of thymocyte differentiation antigen 1," *Gastroenterology*, vol. 145, no. 4, pp. 885–e3, 2013.
- [11] S. V. Bachawal, K. C. Jensen, A. M. Lutz et al., "Earlier detection of breast cancer with ultrasound molecular imaging in a transgenic mouse model," *Cancer Research*, vol. 73, no. 6, pp. 1689–1698, 2013.
- [12] Q. Wen, S. Wan, Z. Liu, S. Xu, H. Wang, and B. Yang, "Ultrasound contrast agents and ultrasound molecular imaging," *Journal of Nanoscience and Nanotechnology*, vol. 14, no. 1, pp. 190–209, 2014.
- [13] F. Kiessling, S. Fokong, J. Bzyl, W. Lederle, M. Palmowski, and T. Lammers, "Recent advances in molecular, multimodal and theranostic ultrasound imaging," *Advanced Drug Delivery Reviews*, vol. 72, pp. 15–27, 2014.
- [14] M. A. Pysz and J. K. Willmann, "Targeted contrast-enhanced ultrasound: An emerging technology in abdominal and pelvic imaging," *Gastroenterology*, vol. 140, no. 3, pp. 785–e6, 2011.
- [15] J. Ma, M. Shen, C. S. Xu, Y. Sun, Y. R. Duan, and L. F. Du, "Biodegradable double-targeted PTX-mPEG-PLGA nanoparticles for ultrasound contrast enhanced imaging and antitumor therapy in vitro," *Oncotarget*, vol. 7, no. 48, pp. 80008–80018, 2016.
- [16] C. Brazzale, R. Canaparo, L. Racca et al., "Enhanced selective sonosensitizing efficacy of ultrasound-based anticancer treatment by targeted gold nanoparticles," *Nanomedicine*, vol. 12, no. 23, pp. 3053–3070, 2016.
- [17] H. S. Min, S. Son, D. G. You et al., "Chemical gas-generating nanoparticles for tumor-targeted ultrasound imaging and ultrasound-triggered drug delivery," *Biomaterials*, vol. 108, pp. 57–70, 2016.
- [18] R. Pandey, M. Saxena, and R. Kapur, "Role of SHP2 in hematopoiesis and leukemogenesis," *Current Opinion in Hematology*, vol. 24, no. 4, pp. 307–313, 2017.
- [19] T. Han, D.-M. Xiang, W. Sun et al., "PTPN11/Shp2 overexpression enhances liver cancer progression and predicts poor prognosis of patients," *Journal of Hepatology*, vol. 63, no. 3, article no. 5638, pp. 651–660, 2015.
- [20] C.-K. Qu and G.-S. Feng, "Shp2 has a positive regulatory role in ES cell differentiation and proliferation," *Oncogene*, vol. 17, no. 4, pp. 433–439, 1998.
- [21] S. Mitra, C. Beach, G.-S. Feng, and R. Plattner, "SHP-2 is a novel target of Abl kinases during cell proliferation," *Journal of Cell Science*, vol. 121, no. 20, pp. 3335–3346, 2008.
- [22] F. Zhang, X. Liu, C. Chen et al., "CD244 maintains the proliferation ability of leukemia initiating cells through SHP-2/p27kip1 signaling," *Haematologica*, vol. 102, no. 4, pp. 707–718, 2017.
- [23] Z.-Q. Hu, R. Ma, C.-M. Zhang et al., "Expression and clinical significance of tyrosine phosphatase SHP2 in thyroid carcinoma," *Oncology Letters*, vol. 10, no. 3, pp. 1507–1512, 2015.
- [24] D. B. Ellegala, H. Leong-Poi, J. E. Carpenter et al., "Imaging tumor angiogenesis with contrast ultrasound and microbubbles targeted to  $\alpha v \beta 3$ ," *Circulation*, vol. 108, no. 3, pp. 336–341, 2003.
- [25] M. Palmowski, J. Huppert, G. Ladewig et al., "Molecular profiling of angiogenesis with targeted ultrasound imaging: early assessment of antiangiogenic therapy effects," *Molecular Cancer Therapeutics*, vol. 7, no. 1, pp. 101–109, 2008.
- [26] J. K. Willmann, A. M. Lutz, R. Paulmurugan et al., "Dual-targeted contrast agent for US assessment of tumor angiogenesis in vivo," *Radiology*, vol. 248, no. 3, pp. 936–944, 2008.
- [27] P. Cai, W. Guo, H. Yuan et al., "Expression and clinical significance of tyrosine phosphatase SHP-2 in colon cancer," *Biomedicine & pharmacotherapy = Biomédecine & pharmacothérapie*, vol. 68, no. 3, p. 285, 2014.

- [28] M. A. Pysz, S. B. Machtaler, E. S. Seeley et al., "Vascular endothelial growth factor receptor type 2-targeted contrast-enhanced us of pancreatic cancer neovasculature in a genetically engineered mouse model: Potential for earlier detection," *Radiology*, vol. 274, no. 3, pp. 790–799, 2015.
- [29] Z. Hu, X. Wang, H. Fang et al., "A tyrosine phosphatase SHP2 gain-of-function mutation enhances malignancy of breast carcinoma," *Oncotarget*, vol. 7, no. 5, pp. 5664–5676, 2016.
- [30] Z. Hu, H. Fang, X. Wang, D. Chen, Z. Chen, and S. Wang, "Overexpression of SHP2 tyrosine phosphatase promotes the tumorigenesis of breast carcinoma," *Oncology Reports*, vol. 32, no. 1, pp. 205–212, 2014.
- [31] X.-D. Zhou and Y. M. Agazie, "Inhibition of SHP2 leads to mesenchymal to epithelial transition in breast cancer cells," *Cell Death & Differentiation*, vol. 15, no. 6, pp. 988–996, 2008.
- [32] G. Korpanty, J. G. Carbon, P. A. Grayburn, J. B. Fleming, and R. A. Brekken, "Monitoring response to anticancer therapy by targeting microbubbles to tumor vasculature," *Clinical Cancer Research*, vol. 13, no. 1, pp. 323–330, 2007.
- [33] A. M. Lutz, S. V. Bachawal, C. W. Drescher, M. A. Pysz, J. K. Willmann, and S. S. Gambhir, "Ultrasound molecular imaging in a human CD276 expression-modulated murine ovarian cancer model," *Clinical Cancer Research*, vol. 20, no. 5, pp. 1313–1322, 2014.

## Research Article

# One-Step $^{18}\text{F}$ -Labeling of Estradiol Derivative for PET Imaging of Breast Cancer

Hongbo Huang, Ke Li, Gaochao Lv, Guiqing Liu, Xueyu Zhao, Qingzhu Liu, Shanshan Wang, Xi Li, Ling Qiu , and Jianguo Lin 

Key Laboratory of Nuclear Medicine of Ministry of Health and Jiangsu Key Laboratory of Molecular Nuclear Medicine, Jiangsu Institute of Nuclear Medicine, Wuxi 214063, China

Correspondence should be addressed to Ling Qiu; [qiuling@jsinm.org](mailto:qiuling@jsinm.org) and Jianguo Lin; [linjianguo@jsinm.org](mailto:linjianguo@jsinm.org)

Received 19 September 2017; Accepted 17 January 2018; Published 5 March 2018

Academic Editor: Yuebing Wang

Copyright © 2018 Hongbo Huang et al. This is an open access article distributed under the Creative Commons Attribution License, which permits unrestricted use, distribution, and reproduction in any medium, provided the original work is properly cited.

Positron emission tomography (PET) imaging is a useful method to evaluate in situ estrogen receptor (ER) status for the early diagnosis of breast cancer and optimization of the appropriate treatment strategy. The  $^{18}\text{F}$ -labeled estradiol derivative has been successfully used to clinically assess the ER level of breast cancer. In order to simplify the radiosynthesis process, one-step  $^{18}\text{F}$ - $^{19}\text{F}$  isotope exchange reaction was employed for the  $^{18}\text{F}$ -fluorination of the tracer of [ $^{18}\text{F}$ ]AmBF<sub>3</sub>-TEG-ES. The radiotracer was obtained with the radiochemical yield (RCY) of ~61% and the radiochemical purity (RCP) of >98% within 40 min. Cell uptake and blocking assays indicated that the tracer could selectively accumulate in the ER-positive human breast cancer cell lines MCF-7 and T47D. In vivo PET imaging on the MCF-7 tumor-bearing mice showed relatively high tumor uptake (1.4~2.3 %D/g) and tumor/muscle uptake ratio (4~6). These results indicated that the tracer is a promising PET imaging agent for ER-positive breast cancers.

## 1. Introduction

Breast cancer has become the most common malignancy in women and the incidence of breast cancer is increasing over the world [1]. One of the primary reasons that cause death from breast cancer may be due to the lack of effective early diagnosis method [1]. Therefore, development of novel effective early diagnosis methods is critical for the treatment and survival of patients with breast cancer. It is acknowledged that estrogen plays an important role in the initiation and progression of breast cancer [2, 3]. The stimulatory effect of estrogen is mediated by nuclear estrogen receptors (ERs) [4]. Therefore, the estrogen receptor can serve as an important predictive biomarker of breast cancers [5]. The understanding of ER level is also essential for prognosis and optimization of the treatment strategy. The ER-positive (ER<sup>+</sup>) tumors often respond to the hormonal therapy, whereas the ER-negative (ER<sup>-</sup>) tumors usually require the surgical and chemotherapeutic interventions [2, 6, 7].

Positron emission tomography (PET) as an efficient non-invasive imaging technology has been applied successfully in

clinic to provide the possibility for assessing the entire lesion and highly sensitive images of cancer diseases. Fluorine-18 is the most widely used radioisotope because of its ideal nuclear properties, such as low positron energy (0.64 MeV) and suitable physical half-life (109.8 min). Some fluorine-18-labeled estradiol derivatives, such as 16 $\alpha$ -[ $^{18}\text{F}$ ]fluoroestradiol ([ $^{18}\text{F}$ ]FES) and C3-7 $\alpha$ -[ $^{18}\text{F}$ ]FES, have been studied in preclinical evaluation, and tumor uptakes in PET imaging studies show a good correlation with the ER expression levels [7, 8]. However, the preparation of these radiotracers always require multisteps, including at least one drying step and semi-prep high performance liquid chromatography (HPLC) purification step. This will increase the risk of radiosynthesis failure and reduce the radiochemical yield (RCY) of radiotracer [9]. The multistep procedures are also challenged by the relatively short half-life of the radioisotope fluorine-18 [10]. Therefore, simplification of the radiosynthesis process is essential for the development and application of PET tracers based on the estradiol derivatives.

Recently, Liu and coworkers have developed a one-step  $^{18}\text{F}$ -labeling method with high radiochemical yield and high

specific activity [9]. The  $^{18}\text{F}$ -labeling can be realized by the simple  $^{18}\text{F}$ - $^{19}\text{F}$  isotope exchange reaction on an ammonio-methyl-trifluoroborate ( $\text{AmBF}_3$ ) group without further drying of fluoride-18 ion and HPLC purification. Compared with other multistep radiolabeling methods, the one-step  $^{18}\text{F}$ -labeling approach is much more practical for clinical applications. However, this method is still not used widely to prepare PET imaging agents [11] and even no studies using this method to develop tracers of estradiol derivatives were reported.

Encouraged by the previous studies [11], in the present work we attempt to develop a novel estradiol-based PET tracer for imaging the ER-positive breast cancers by using the one-step  $^{18}\text{F}$ -labeling method to simplify the radiosynthesis procedure. The new tracer [ $^{18}\text{F}$ ] $\text{AmBF}_3$ -TEG-ES was prepared by conjugation of  $\text{AmBF}_3$  and estradiol with a  $\text{PEG}_4$  spacer. This new tracer could be easily prepared through one-step  $^{18}\text{F}$ -labeling method and simple purification in a short time. The in vitro stability, cytotoxicity, lipophilicity, and tumor cell uptake of the radiotracer were also investigated systematically. In addition, in vivo micro-PET imaging of breast cancer-bearing mice was also carried out and the results indicated that the tracer [ $^{18}\text{F}$ ] $\text{AmBF}_3$ -TEG-ES would be a potential PET imaging agent for the diagnosis of estrogen-dependent tumors.

## 2. Materials and Methods

**2.1. General.** All the materials were purchased from Energy Chemical and were all of reagent grade or analytical grade without further purification. Fluoride-18 was obtained from a medical cyclotron (HM7, Sumitomo Heavy Industries) through a bombardment of  $^{18}\text{O}$ -enriched water. Human breast cancer cell lines T47D and MCF-7 were purchased from the Cell Bank of Chinese Academy of Sciences (Shanghai, China) and cultured in the 1640 medium and  $\alpha$ -MEM medium (Biological Industries, Israel) with 10% (v/v) fetal bovine serum (Biological Industries, Israel) in a  $37^\circ\text{C}$  incubator under 5%  $\text{CO}_2$ , respectively. A 1470 Wizard  $\gamma$  counter (Perkin-Elmer Corporation, USA) was employed in the studies of cellular uptake.

The semi-prep HPLC (Waters, USA) with a Waters 2998 photodiode array detector (PDA) and C18 HPLC column ( $5\ \mu\text{m}$ ,  $250 \times 19\ \text{mm}$ , Phenomenex) was employed for purification of compounds. The flow rate of semi-prep HPLC was 3 mL/min. The semi-prep HPLC method for the purification of  $\text{AmBF}_3$ -TEG-ES has been listed in Table 1.

The analytical HPLC equipped with a C18 column ( $5\ \mu\text{m}$ ,  $250 \times 4.6\ \text{mm}$ , Phenomenex) and a Waters 2487 dual  $\lambda$  absorbance detector was used for purity identification of the precursor on a Waters Breeze system. A Radiomatic 610TR flow scintillation analyzer (Perkin-Elmer) was necessary for the quality control analysis of radiolabeled compounds in this system. The flow rate of analytical HPLC was 1 mL/min. The analytical HPLC method for quality control has been listed in Table 2.

**Animals.** BALB/c nude mice (18–20 g; 4–6 weeks old; SLAC Laboratory Animal Co. Ltd., Shanghai, China) were used for

TABLE 1: The gradient elution condition for semi-prep HPLC analysis of  $\text{AmBF}_3$ -TEG-ES.

Time (min)	Flow (mL/min)	% A	% B
0.01	3.00	80.0	20.0
3.00	3.00	80.0	20.0
15.00	3.00	65.0	35.0
20.00	3.00	65.0	35.0
25.00	3.00	50.0	50.0
30.00	3.00	30.0	70.0
35.00	3.00	10.0	90.0
40.00	3.00	80.0	20.0

TABLE 2: The gradient elution condition of analytical HPLC.

Time (min)	Flow	% A	% B
0.01	1.00	80.0	20.0
3.00	1.00	80.0	20.0
25.00	1.00	30.0	70.0
30.00	1.00	80.0	20.0

animal experiments. Mice were housed with free access to food and water and allowed ample time to acclimatize before the experiments. The tumor-bearing mice were established by subcutaneous injection of MCF-7 cells ( $5 \times 10^6$ ) suspended in PBS ( $100\ \mu\text{L}$ ) in the right shoulder of each nude mouse. The tumors were allowed to grow for around 3–4 weeks to reach the size of 0.5–1.0 cm in diameter for in vivo studies. All procedures and animal protocols were approved by the Animal Care and Ethics Committee of Jiangsu Institute of Nuclear Medicine.

Nuclear magnetic resonance spectrometers ( $^1\text{H}$ -NMR,  $^{13}\text{C}$ -NMR, and  $^{19}\text{F}$ -NMR, Bruker DRX-400, Bruker, Germany) were used to obtain spectra of samples dissolved in  $d_6$ -DMSO, and the chemical shifts were referenced to tetramethylsilane (TMS). Electrospray ionization mass spectrometry (ESI-MS) was obtained on a Waters Platform ZMD4000 quadrupole tandem mass spectrometer. A Perkin-Elmer 240C Elemental Analyzer was employed for the elemental analysis (C, H, and N). FT-IR spectra of the cold compound  $\text{AmBF}_3$ -TEG-ES was obtained using a FT-IR spectrometer (SENSOR27, Bruker) in the range of  $400$ – $4000\ \text{cm}^{-1}$ .

### 2.2. Chemical Synthesis

**2.2.1. Synthesis of Compound 1.** Compound 1 was synthesized according to the method reported previously [12]. Tetraethylene glycol (4.51 g, 23 mmol) was first dissolved in THF (20 mL) at room temperature, and then KOH (2.06 g, 36 mmol) dissolved in  $\text{H}_2\text{O}$  (3 mL) was added to the solution. Subsequently, *p*-toluenesulfonyl chloride (4.37 g, 23 mmol) was dissolved in THF and added drop-wise to the solution. The reaction mixture was stirred under ice-bath. The reaction solution was diluted with NaCl saturated solution (50 mL) and extracted with  $\text{CH}_2\text{Cl}_2$  ( $3 \times 50\ \text{mL}$ ). The combined organic layer was dried over anhydrous sodium sulfate and

the solvent was evaporated under reduced pressure. Then, the crude product was purified by column chromatography using  $\text{CH}_2\text{Cl}_2/\text{CH}_3\text{OH}$  (30:1 v/v) to obtain the compound **1**. Yield: 61%, 5.23 g. ESI-MS:  $m/z$  349.23  $[\text{M} + \text{H}]^+$ .

**2.2.2. Synthesis of Compound 2.** Compound **1** (5.23 g, 15 mmol) and  $\text{NaN}_3$  (2.90 g, 45 mmol) were dissolved in  $\text{CH}_3\text{CN}$  (20 mL) and refluxed at  $95^\circ\text{C}$  for 16 h. Then the solution of the reaction mixture was cooled down to room temperature and  $\text{NaCl}$  saturated solution (50 mL) was added. After being extracted with  $\text{CH}_2\text{Cl}_2$ , the combined organic layer was dried with anhydrous sodium sulfate and the solvent was evaporated under reduced pressure to obtain the compound **2**. Yield: 89%, 2.93 g. ESI-MS:  $m/z$  242.22  $[\text{M} + \text{Na}]^+$ .

**2.2.3. Synthesis of Compound 3.** Compound **2** (2.93 g, 13 mmol) was dissolved in  $\text{CH}_2\text{Cl}_2$  (20 mL), and then DMAP (0.35 g, 2.9 mmol) and TEA (8.9 mL, 67 mmol) were added. When the reaction mixture was stirred under ice-bath, *p*-toluenesulfonyl chloride (2.47 g, 13 mmol) in  $\text{CH}_2\text{Cl}_2$  was added drop-wise to the solution. Then the reaction mixture was stirred at room temperature overnight. Subsequently, the solution of reaction mixture was washed with  $\text{HCl}$  aqueous solution (1 M,  $3 \times 50$  mL) and  $\text{NaCl}$  saturated solution ( $3 \times 50$  mL). Then, the organic layer was dried with anhydrous sodium sulfate and the solvent was evaporated under reduced pressure. The crude product was purified by flash column chromatography hexane/acetone (2:1 v/v) to provide compound **3**. Yield: 66%, 3.20 g. ESI-MS:  $m/z$  396.25  $[\text{M} + \text{Na}]^+$ .

**2.2.4. Synthesis of Compound 4.** The suspension of compound **3** (3.20 g, 8.6 mmol), *N,N*-dimethylethanolamine (772  $\mu\text{L}$ , 7.5 mmol), and  $\text{KOH}$  (1.62 g, 29 mmol) in THF (50 mL) was refluxed at  $70^\circ\text{C}$  for 12 h. The reaction mixture was filtered and the filtrate was collected. The solvent was evaporated under reduced pressure and then  $\text{H}_2\text{O}$  (50 mL) was added and extracted with  $\text{CH}_2\text{Cl}_2$  ( $3 \times 50$  mL). The combined organic layer was dried over hydrous sodium sulfate and then evaporated under reduced pressure. The crude product was purified through flash column chromatography  $\text{CH}_2\text{Cl}_2/\text{CH}_3\text{OH}$  (10:1 v/v). Yield: 45%, 1.12 g. ESI-MS:  $m/z$  291.31  $[\text{M} + \text{H}]^+$ .

**2.2.5. Synthesis of Compound 5.** Compound **4** (480 mg, 1.6 mmol) was dissolved in anhydrous THF (10 mL). 2-(Bromomethyl)-4,4,5,5-teramethyl-1,3,2-dioxaboralane (900  $\mu\text{L}$ , 4.92 mmol) was added drop-wise to the above solution at room temperature under nitrogen atmosphere. Then the reaction mixture was stirred for 3 h. The solvent was evaporated under reduced pressure to obtain compound **5**. Compound **5** was used without any purification. Yield: 67%, 478 mg. ESI-MS:  $m/z$  431.49  $[\text{M}]^+$ .

**2.2.6. Synthesis of Compound 6.** Compound **5** (478 mg, 1.1 mmol) was dissolved in DMF (1 mL).  $\text{KHF}_2$  (3 M, 1 mL) and  $\text{HCl}$  (4 M, 1 mL) were added to the above solution. The reaction was stirred at  $45^\circ\text{C}$  for 2 h. Then the reaction was

quenched by  $\text{NH}_4\text{OH}$  (20  $\mu\text{L}$ ). Crude product was purified through silica gel  $\text{CH}_2\text{Cl}_2/\text{CH}_3\text{OH}$  (20:1 v/v) to give compound **6**. Yield: 16%, 66 mg. ESI-MS:  $m/z$  395.34  $[\text{M} + \text{Na}]^+$ .

**2.2.7. Synthesis of Compound 7 (AmBF<sub>3</sub>-TEG-ES).** Click chemistry was used for the synthesis of compound **7** (AmBF<sub>3</sub>-TEG-ES). Briefly, compound **6** (66 mg, 0.18 mmol), ethinylestradiol (64 mg, 0.22 mmol), tris(2-benzimidazolylmethyl)amine (7.2 mg, 0.018 mmol), sodium ascorbate (71 mg, 0.36 mmol), and  $\text{CuSO}_4 \cdot 5\text{H}_2\text{O}$  (9.1 mg, 0.036 mmol) were reacted in 4 mL DMF/ $\text{H}_2\text{O}$  (1:1) at  $45^\circ\text{C}$  for 1 h. Then, semi-prep HPLC was used for the purification of the crude product (Table 1). Then it was lyophilized to give the final product **7** (AmBF<sub>3</sub>-TEG-ES). The compound AmBF<sub>3</sub>-TEG-ES was analyzed by an analytical HPLC (Table 2). Yield: 73%, 88 mg. ESI-MS:  $m/z$  691.57  $[\text{M} + \text{Na}]^+$ . <sup>1</sup>H-NMR (*d*<sub>6</sub>-DMSO, 400 MHz,  $\delta$ : ppm):  $\delta$  7.84 (s, 1H), 6.96 (d, 1H,  $J = 8.0$  Hz), 6.48 (d, 1H,  $J = 12.0$  Hz), 6.42 (s, 1H), 4.50 (t, 2H,  $J = 4.0$  Hz), 3.79~3.83 (m, 4H), 3.42~3.52 (m, 14H), 3.00 (s, 6H), 2.70 (t, 2H,  $J = 4.0$  Hz), 2.35 (m, 3H), 1.24~2.09 (m, 12H), 0.93 (s, 3H); <sup>13</sup>C-NMR (*d*<sub>6</sub>-DMSO, 101 MHz,  $\delta$ : ppm):  $\delta$  155.3, 154.3, 137.6, 130.9, 126.4, 123.5, 115.4, 113.1, 81.5, 70.3, 70.2, 70.1, 70.0, 69.9, 69.9, 69.3, 65.1, 64.9, 53.8, 49.7, 48.0, 47.2, 43.7, 37.6, 33.1, 29.7, 29.5, 27.7, 26.5, 24.0, 14.8; <sup>19</sup>F-NMR (*d*<sub>6</sub>-DMSO, 376 MHz,  $\delta$ : ppm):  $\delta$  -135.5. Anal. Elem. Anal. Calc. for  $\text{C}_{33}\text{H}_{52}\text{BF}_3\text{N}_4\text{O}_6$ : C, 59.28; H, 7.84; N, 8.38. Found: C, 59.77; H, 7.63; N, 8.48. IR (KBr): 3391 (w), 2930 (m), 1611 (m), 1454 (s), 1352 (m), 971 (m).

**2.3. Stability of AmBF<sub>3</sub>-TEG-ES.** The stability of the cold compound AmBF<sub>3</sub>-TEG-ES was studied in pyridazine-HCl buffer (1.0 M, pH 2.0–2.5) at different temperatures. Briefly, AmBF<sub>3</sub>-TEG-ES was dissolved in pyridazine-HCl buffer and then incubated at various temperature (50, 60, 70, 80, 90, or  $100^\circ\text{C}$ ) for 30 min, respectively. After incubation, a little sample was taken out for stability assay using HPLC analysis (Table 1).

**2.4. Cytotoxicity Assay of AmBF<sub>3</sub>-TEG-ES.** Traditional 3-(4,5-dimethyl-thiazol-2-yl)-2,5-diphenyltetrazolium bromide (MTT) assay was used to assess the cytotoxicity of AmBF<sub>3</sub>-TEG-ES against ER<sup>+</sup> human breast cancer cell lines T47D and MCF-7. Briefly, the cells were seeded into 96-well plates with 100  $\mu\text{L}$  medium at a density of  $5 \times 10^3$  cells per well. Then the cells were incubated in a  $37^\circ\text{C}$  incubator with 5%  $\text{CO}_2$  for 12 h. Subsequently, the medium in each well was replaced by different concentrations (12.5, 25, 50, and 100  $\mu\text{M}$ ) of the cold compound AmBF<sub>3</sub>-TEG-ES (200  $\mu\text{L}$ /well), which were diluted with the culture medium. Then, the plates were incubated for 3, 6, 12, and 24 h, respectively. After treatment with AmBF<sub>3</sub>-TEG-ES, MTT solution (20  $\mu\text{L}$ , 5 mg/mL) was added to each well and all the plates were incubated for another 4 h. After that, medium in each well was removed and replaced by DMSO (150  $\mu\text{L}$ ). After the culture plates were shaken for 10 min, the optical density (OD) values were measured on a microplate reader (BioTek Instruments, Inc. Vermont, USA) at 490 nm. All tests were carried out in 6 repeats for at least three independent experiments.

**2.5. Radiosynthesis of [ $^{18}\text{F}$ ]AmBF<sub>3</sub>-TEG-ES.** Fluoride-18 (100–300 mCi) produced by cyclotron was trapped on an anion-exchange resin and then eluted with pyridazine-HCl buffer (200  $\mu\text{L}$ ) into the reaction polypropylene tube. The precursor AmBF<sub>3</sub>-TEG-ES (10  $\mu\text{L}$ , 25 mM in pyridazine-HCl buffer) was added to the tube. Then the mixture was heated at different temperature for 30 min, respectively. After reaction, the reaction mixture was loaded on a C18 light cartridge when diluted with water (10 mL). Then, the C18 light cartridge was washed with water (3  $\times$  10 mL). The pure tracer [ $^{18}\text{F}$ ]AmBF<sub>3</sub>-TEG-ES was obtained after being eluted with ethanol/saline (0.5 mL) into a glass vial. The target product [ $^{18}\text{F}$ ]AmBF<sub>3</sub>-TEG-ES should be diluted with saline for further biological evaluation. A small sample was taken out for radio-HPLC analysis using the condition listed in Table 2.

**2.6. Determination of Octanol-Water Partition Coefficient.** Octanol (50 mL) and distilled water (50 mL, pH 7.0) were mixed by oscillation at 25°C for 24 h. After standing, a separatory funnel was used to separate the two layers. The tracer (30  $\mu\text{Ci}$ ) in distilled water (500  $\mu\text{L}$ ) was added to a polypropylene tube. Octanol (500  $\mu\text{L}$ ) was also added to the tube and then oscillated on a vortex mixer for 5 min. Next, the tube was centrifuged for 5 min at 4000 g to separate the two layers. In each layer, the radioactivity of samples (100  $\mu\text{L}$ ) in triplicate was measured by a  $\gamma$ -counter. The partition coefficient ( $\log P$ ) value was calculated using the equation  $\log P = \log(C_o/C_w)$ , where  $C_o$  is the radioactivity of the tracer in the n-octanol layer and  $C_w$  is the radioactivity in the water layer. The result was the average of three independent experiments.

**2.7. Cell Uptake and Block Studies of [ $^{18}\text{F}$ ]AmBF<sub>3</sub>-TEG-ES.** The cell uptake and block studies of the radiotracer [ $^{18}\text{F}$ ]AmBF<sub>3</sub>-TEG-ES were conducted on human breast cancer cell lines MCF-7 and T47D, respectively. Firstly, MCF-7 or T47D cells (500  $\mu\text{L}$ /well,  $4 \times 10^5$  cells/mL) were seeded in 24-well culture plates and incubated overnight. Then the medium was replaced by fresh serum-free medium (500  $\mu\text{L}$ ) containing [ $^{18}\text{F}$ ]AmBF<sub>3</sub>-TEG-ES (0.5  $\mu\text{Ci}$ ). The plates were incubated in a 37°C incubator for 15, 30, 60, and 120 min, respectively. For the block study, the cells were pretreated with excess of estradiol for 30 min. At each time point, the supernatant in each well was removed and then the cells were washed with ice-cold PBS (500  $\mu\text{L}$ /well) twice. Next, NaOH solution (0.1 M) was added to lyse the cells. The cell lysates were collected and the following eluents of PBS were combined. The radioactivity of cell lysates was determined using a  $\gamma$ -counter. The cell uptake rate was expressed as the percentage of the total added radioactive dose (%AD).

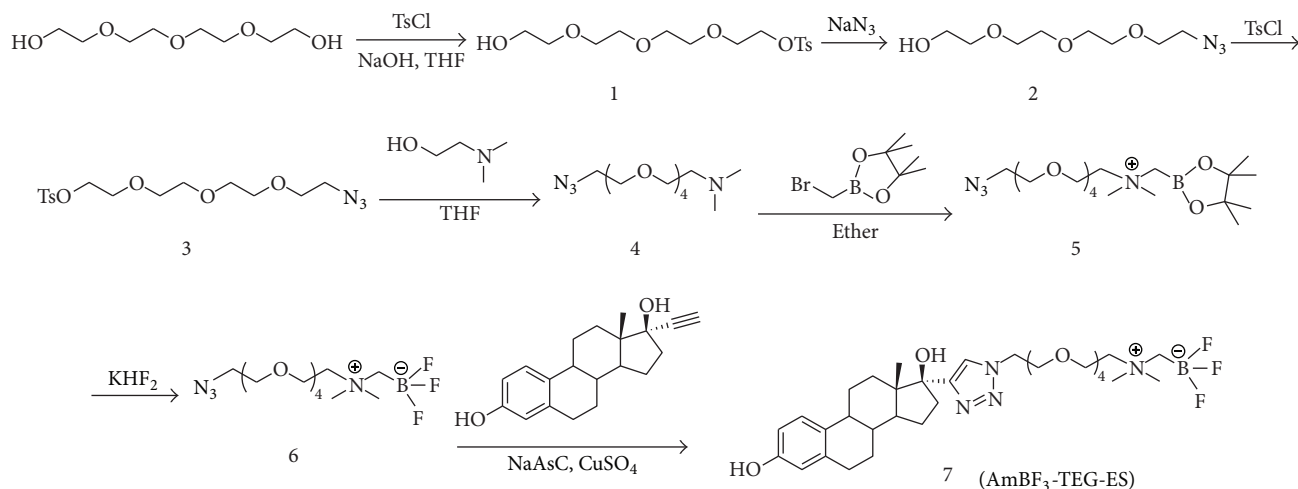
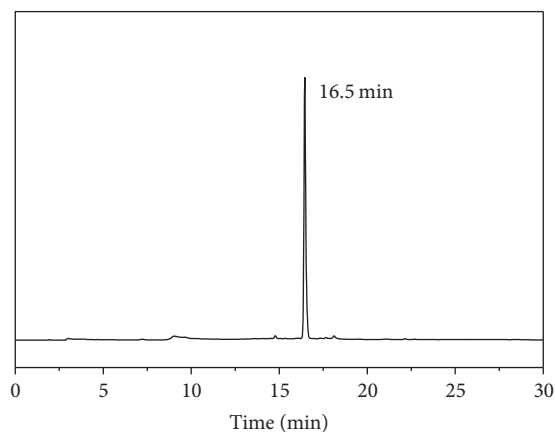
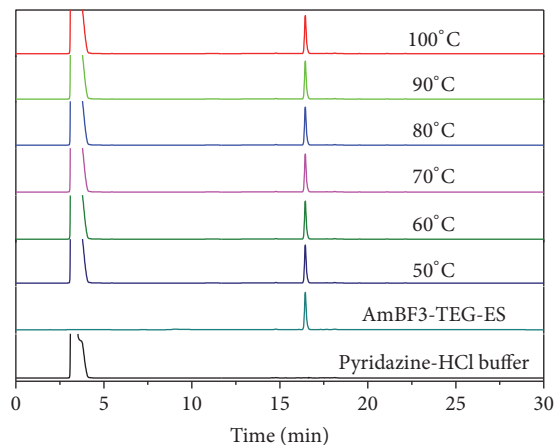
**2.8. PET Imaging.** Small animal PET imaging was performed on an Inveon micro-PET scanner (Siemens Medical Solutions, Germany). Imaging studies were carried out on female Balb/c nude mice bearing the human breast cancer cell line MCF-7. The mice were anesthetized with 1.5%–2% isoflurane,

positioned prone, immobilized, injected with [ $^{18}\text{F}$ ]AmBF<sub>3</sub>-TEG-ES (150  $\mu\text{Ci}$ ) via the tail vein, and imaged dynamically for the first hour. Then, static scanning images were collected immediately at 0.5, 1, and 2 h after injection. The obtained images were reconstructed using 3D ordered subset expectation maximization (OSEM 3D/SP-MAP) and then processed using the Siemens Inveon Research Workplace (IRW2.0.0.1050). Regions of interest (ROIs) were drawn over tumors and main organs, and average signal levels in the ROIs were measured. The %ID/g was also calculated.

### 3. Results and Discussion

**3.1. Design and Synthesis of AmBF<sub>3</sub>-TEG-ES.** The harsh radiosynthesis conditions and purification procedure limit the clinical applications of the estradiol-based PET imaging agents. Thus, development of new radiolabeling method is imperative. In our previous work, a novel PET tracer [ $^{18}\text{F}$ ]AmBF<sub>3</sub>-ES was reported, which was synthesized by conjugating the estradiol with the AmBF<sub>3</sub> directly [13]. Excitedly, the radiotracer [ $^{18}\text{F}$ ]AmBF<sub>3</sub>-ES was obtained in high yield within 30 min obviating HPLC purification through one-step  $^{18}\text{F}$ -labeling approach, and it also showed high serum stability and cellular uptakes. However, the following in vivo tumor imaging studies were disappointing as the tumor tissues showed no uptakes. In order to further develop the simple one-step  $^{18}\text{F}$ -labeling method and improve the in vivo imaging effect of  $^{18}\text{F}$ -labeled estradiol derivatives, the new tracer [ $^{18}\text{F}$ ]AmBF<sub>3</sub>-TEG-ES was designed and prepared by conjugation of AmBF<sub>3</sub> and estradiol with a PEG<sub>4</sub> spacer. Notably, the embedding of PEG<sub>4</sub> spacer between AmBF<sub>3</sub> and estradiol was to adjust the solubility of the tracer in saline, to reduce the steric hindrance for the estradiol-estrogen receptor binding, and to improve the in vivo pharmacokinetics of the tracer [ $^{18}\text{F}$ ]AmBF<sub>3</sub>-TEG-ES, which might overcome the disadvantages of the tracer [ $^{18}\text{F}$ ]AmBF<sub>3</sub>-ES reported previously.

The synthetic route of AmBF<sub>3</sub>-TEG-ES has been shown in Scheme 1. Compound **3** was obtained with high yield by three steps from tetraethylene glycol, which further reacted with N,N'-dimethylethanolamine to generate compound **4**. And then compound **6** was prepared according to the method by Liu et al. [9, 14]. Finally, AmBF<sub>3</sub>-TEG-ES was obtained through a click reaction of compound **6** and ethinylestradiol. Then the precursor was purified on a semi-prep HPLC with a high yield of 73%. The purity of AmBF<sub>3</sub>-TEG-ES was confirmed by HPLC analysis. As shown in Figure 1, the single peak recorded at 280 nm demonstrates high chemical purity of the precursor. All the intermediates were characterized by ESI-MS, and the corresponding molecular ion peaks ( $[\text{M} + \text{H}]^+$  or  $[\text{M} + \text{Na}]^+$ ) indicated the successful synthesis of the compounds. As shown in Figure S1, the peaks 669.5 and 691.5 were assigned to the molecular ion peaks  $[\text{M} + \text{H}]^+$  and  $[\text{M} + \text{Na}]^+$  of the cold compound AmBF<sub>3</sub>-TEG-ES, respectively. Then  $^1\text{H}$ -,  $^{13}\text{C}$ -, and  $^{19}\text{F}$ -NMR spectra further confirmed the structure of AmBF<sub>3</sub>-TEG-ES. The peaks at  $\delta$  6.42 ppm (hydrogen atom of triazole) of  $^1\text{H}$ -NMR spectrum and those at  $\delta$  126.4 and 123.5 ppm (carbon atoms of

SCHEME 1: Synthesis route of **AmBF<sub>3</sub>-TEG-ES**.FIGURE 1: HPLC chromatogram of the precursor **AmBF<sub>3</sub>-TEG-ES**.FIGURE 2: Stability of **AmBF<sub>3</sub>-TEG-ES** in pyridazine-HCl buffer at various temperatures.

triazole) of <sup>13</sup>C-NMR spectrum as well as the disappearance of alkynyl peaks in the <sup>1</sup>H-NMR and <sup>13</sup>C-NMR spectra demonstrated the successful occurrence of the click reaction (Figures S2 and S3). The peak at -75.7 ppm of <sup>19</sup>F-NMR spectrum was assigned to TFA in the final compound and the single peak at -135.5 ppm also indicated the purity of the compound **AmBF<sub>3</sub>-TEG-ES** (Figure S4). All of these results indicated that the compound **AmBF<sub>3</sub>-TEG-ES** was successfully synthesized with a high chemical purity.

**3.2. Stability of AmBF<sub>3</sub>-TEG-ES.** Since the one-step <sup>18</sup>F-<sup>19</sup>F isotope exchange labeling reaction was performed in the pyridazine-HCl buffer (pH = 2.0–2.5) around 80°C, the stability of **AmBF<sub>3</sub>-TEG-ES** in the pyridazine-HCl buffer was studied by HPLC analysis at the temperature range of 50–100°C. As shown in Figure 2, the peak at 3.35 min corresponded to the buffer while **AmBF<sub>3</sub>-TEG-ES** showed a single peak at 16.5 min. After incubation at different temperatures, the HPLC analysis of **AmBF<sub>3</sub>-TEG-ES** in pyridazine-HCl buffer showed a single peak at 16.5 min. This indicated that

**AmBF<sub>3</sub>-TEG-ES** was stable enough in the pyridazine-HCl buffer after incubation even up to 100°C for 30 min and the <sup>18</sup>F-labeling reaction can be carried out in the pyridazine-HCl buffer.

**3.3. Cytotoxicity of AmBF<sub>3</sub>-TEG-ES.** The good biocompatibility is essential for the application of a PET imaging agent [15]. Therefore, the cytotoxicity of **AmBF<sub>3</sub>-TEG-ES** against the human breast cancer cells T47D and MCF-7 was assessed by MTT assay. As can be seen from Figures 3(a) and 3(b), the cell viability of T47D and MCF-7 did not change significantly after incubation for different time with **AmBF<sub>3</sub>-TEG-ES** at the concentration ranging from 12.5 to 100 μM. In fact, more than 87% of both cells still survived after treatment with **AmBF<sub>3</sub>-TEG-ES** at the high concentration of 100 μM for 24 h. Hence, it is inferred that **AmBF<sub>3</sub>-TEG-ES** possesses negligible cytotoxicity and good biocompatibility. Compared with the compound **AmBF<sub>3</sub>-ES** reported by our group previously [13], the cytotoxicity of

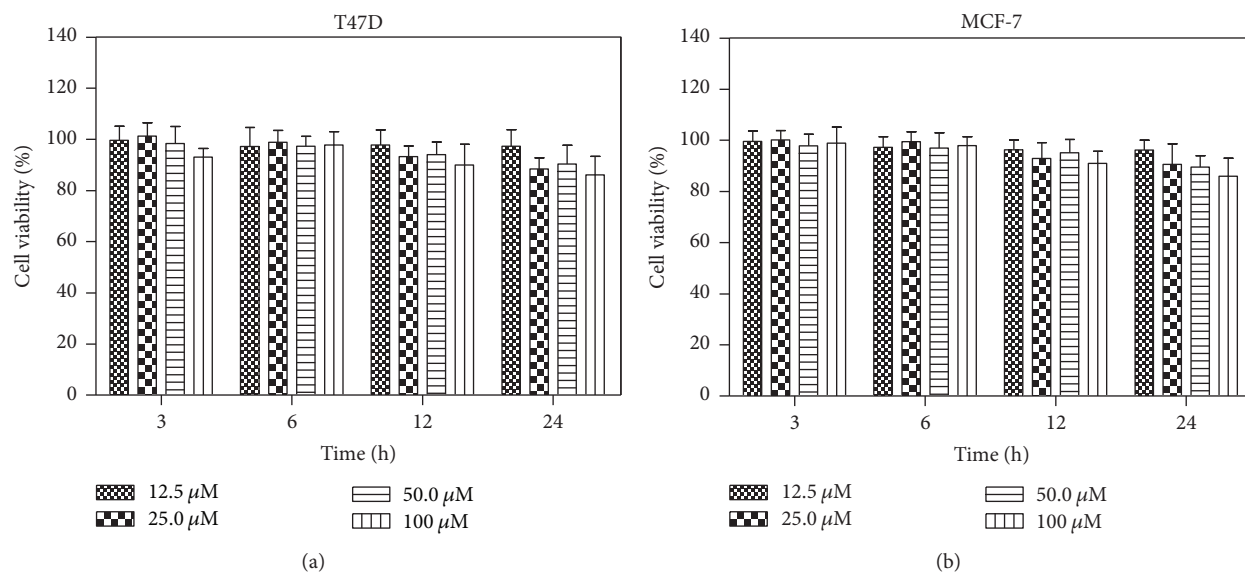


FIGURE 3: Cytotoxicity of  $\text{AmBF}_3\text{-TEG-ES}$  against breast cancer cells T47D (a) and MCF-7 (b).

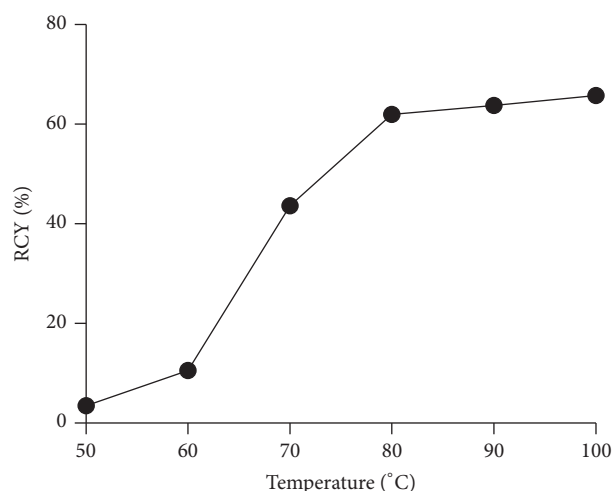


FIGURE 4: Radiochemical yield (RCY) of  $[^{18}\text{F}]\text{AmBF}_3\text{-TEG-ES}$  in pyridazine-HCl buffer (1.0 M, pH 2.0–2.5) at different incubation temperature.

$\text{AmBF}_3\text{-TEG-ES}$  against MCF-7 and T47D cells showed no significant difference, indicating that the short PEG linker had almost no influence on the cytotoxicity of  $\text{AmBF}_3\text{-TEG-ES}$ .

**3.4. Radiosynthesis of  $[^{18}\text{F}]\text{AmBF}_3\text{-TEG-ES}$ .**  $^{18}\text{F}$ -labeling of the precursor  $\text{AmBF}_3\text{-TEG-ES}$  was performed using the one-step  $^{18}\text{F}$ - $^{19}\text{F}$  isotope exchange approach. To optimize the condition of  $^{18}\text{F}$ -labeling, the precursor  $\text{AmBF}_3\text{-TEG-ES}$  was heated with  $^{18}\text{F}$ -fluoride in the pyridazine-HCl buffer (pH = 2.0–2.5) at different temperatures. As shown in Figure 4, the RCYs of  $[^{18}\text{F}]\text{AmBF}_3\text{-TEG-ES}$  increased significantly with the increasing temperature within 30 min. Especially at 80°C, the RCY reached 61% and the RCP was over 98% after C18

purification (Figure 5), but further increasing the reaction temperature did not produce a higher RCY. Therefore, the optimum radiolabeling condition (80°C, 30 min) was selected for further experiments. It was worth mentioning that the radiosynthesis process of the ER imaging agent was significantly simplified in comparison with that of  $^{18}\text{F}$ -FES [16–18]. For the radiosynthesis of the widely studied ER imaging agent  $^{18}\text{F}$ -FES, two reaction steps and semi-prep were required which resulted in a long synthesis time [16–18]. However,  $^{18}\text{F}$ -labeling of the ER imaging agent through the one-step  $^{18}\text{F}$ - $^{19}\text{F}$  isotope exchange approach remarkably shortened the synthesis time and improved the radiolabeling efficiency, which obviated drying of fluoride-18 ion and HPLC purification with the total radiosynthesis time of 40 min. Moreover, the C18 column instead of HPLC purification also led to a high RCY with a satisfactory RCP. All the results indicated that the one-step  $^{18}\text{F}$ - $^{19}\text{F}$  isotope exchange could offer a more convenient method for the  $^{18}\text{F}$ -labeling process and it was more suitable for clinical application.

In order to evaluate the stability of  $[^{18}\text{F}]\text{AmBF}_3\text{-TEG-ES}$  in vitro,  $[^{18}\text{F}]\text{AmBF}_3\text{-TEG-ES}$  was incubated in PBS (pH = 7.4) for 4 h at 37°C. As shown in Figure 6, the probe showed high stability (>95%) in PBS for up to 4 h. The high stability of  $[^{18}\text{F}]\text{AmBF}_3\text{-TEG-ES}$  indicated that this probe was suitable for further biological studies.

**3.5. Octanol-Water Partition Coefficient.** The octanol-water partition coefficient ( $\log P$ ) of a compound always reflects its lipid solubility and correlates with its pharmacokinetics, such as cell membrane permeability and tissue distribution, according to the studies of quantitative structure-activity relationship [19]. The  $\log P$  value for  $[^{18}\text{F}]\text{AmBF}_3\text{-TEG-ES}$  was determined to be  $-0.17 \pm 0.03$ , which displayed better hydrophilicity than  $[^{18}\text{F}]\text{AmBF}_3\text{-ES}$  ( $0.52 \pm 0.09$ ) as expected. The lipophilicity of  $[^{18}\text{F}]\text{AmBF}_3\text{-TEG-ES}$  may

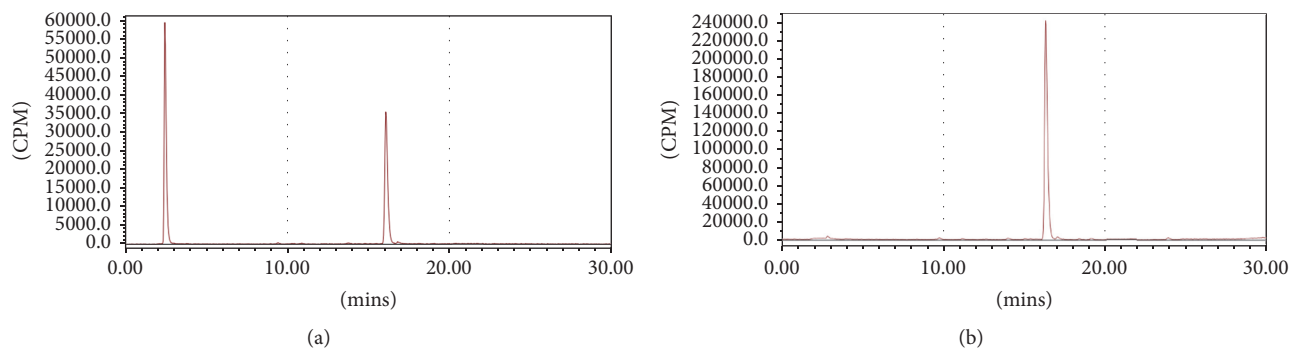


FIGURE 5: Radio-HPLC analysis of [ $^{18}\text{F}$ ]AmBF $_3$ -TEG-ES ( $t_R = 16.3$  min) before purification (a) and after C18 purification (b).

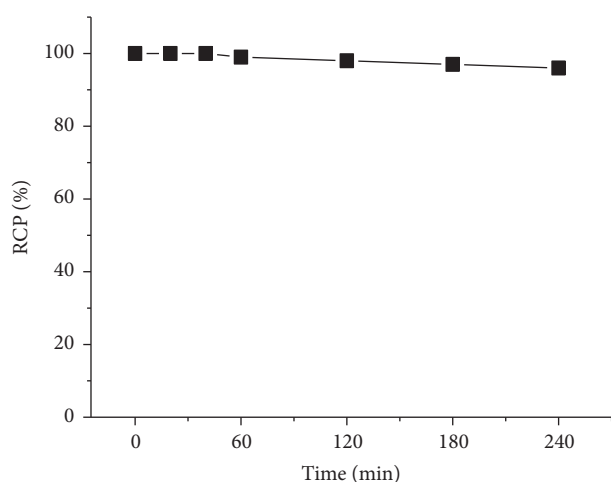


FIGURE 6: In vitro stability test of [ $^{18}\text{F}$ ]AmBF $_3$ -TEG-ES after incubation in PBS at 37°C for different periods of time.

endow it with suitable pharmacokinetics in vivo for tumor imaging. The hydrophilicity of [ $^{18}\text{F}$ ]AmBF $_3$ -TEG-ES may endow it with a suitable pharmacokinetics in vivo for tumor imaging.

### 3.6. Cell Uptake and Blocking Assay of [ $^{18}\text{F}$ ]AmBF $_3$ -TEG-ES.

Since estrogen receptor is overexpressed in human breast cancer cell lines MCF-7 and T47D, cell uptake and block studies of [ $^{18}\text{F}$ ]AmBF $_3$ -TEG-ES were performed on these two kinds of cells, respectively. As shown in Figure 7(a), the cell uptake rate of [ $^{18}\text{F}$ ]AmBF $_3$ -TEG-ES approached a plateau of  $\sim 2.7\%$  after incubation at 37°C for 60 min and remained at a similar uptake level to 120 min, indicating that the radiotracer could bind quickly to the ER $^+$  MCF-7 cells. Similarly, approximately 2.8% cell uptake of [ $^{18}\text{F}$ ]AmBF $_3$ -TEG-ES in T47D cells was determined at 60 min and almost no change up to 120 min, which was consistent with that of MCF-7 cell lines (Figure 7(b)). For the blocking study, the cell uptake rate in MCF-7 cells decreased from 2.7% to 1.3% at presence of excess estradiol at 60 min, which decreased about 52% compared with the total cell uptake. In T47D cells, the

cell uptake rate was only 1.2% at presence of excess estradiol at 60 min. These data showed that the cell uptake in ER $^+$  breast cancer cells could be effectively blocked by estradiol and further demonstrated the specificity of [ $^{18}\text{F}$ ]AmBF $_3$ -TEG-ES to ER.

**3.7. Micro-PET Imaging.** In vivo micro-PET imaging was also carried out to investigate the specificity of [ $^{18}\text{F}$ ]AmBF $_3$ -TEG-ES to localize in ER-positive tumor. The MCF-7 tumor-bearing nude mice were used for imaging at different time periods varying from 40 to 120 min. As shown in Figures 8(a) and 8(b), [ $^{18}\text{F}$ ]AmBF $_3$ -TEG-ES accumulated in ER $^+$  MCF-7 tumors with an uptake of 1.4 to 2.3%D/g, showing visualization of the ER-positive tumors. The highest uptake in tumor was observed at 40–50 min after injection, and then the uptake decreased slightly with the time prolonging. However, the tumor/muscle ratio increased with the increase of time, which was about 4 at the initial time point of 40 min (Figure 8(c)) and then increased to about 6 at 70 min and remained 6 at 110 min. Noteworthy is that the previously reported compound [ $^{18}\text{F}$ ]AmBF $_3$ -ES showed no uptake in the same tumor tissues, but the compound [ $^{18}\text{F}$ ]AmBF $_3$ -TEG-ES showed an improvement, which may be attributed to the introduction of the PEG spacer [20]. Hence, the results of micro-PET imaging further indicate that [ $^{18}\text{F}$ ]AmBF $_3$ -TEG-ES has potential application for the ER-positive tumor imaging.

## 4. Conclusions

In summary, a novel estradiol-based PET imaging agent [ $^{18}\text{F}$ ]AmBF $_3$ -TEG-ES was synthesized and characterized, and its in vitro and in vivo biological performance was also evaluated. The radiosynthesis of this compound was quite applicable in clinic by using the one-step  $^{18}\text{F}$ - $^{19}\text{F}$  isotope exchange reaction within 40 min, which obviated the drying of fluoride-18 ion and the HPLC purification. The high RCY, excellent RCP, good biocompatibility, high stability, and specific ER-targeting ability suggested that the radiotracer [ $^{18}\text{F}$ ]AmBF $_3$ -TEG-ES might be a promising PET imaging agent for diagnosis of ER $^+$  breast cancers.

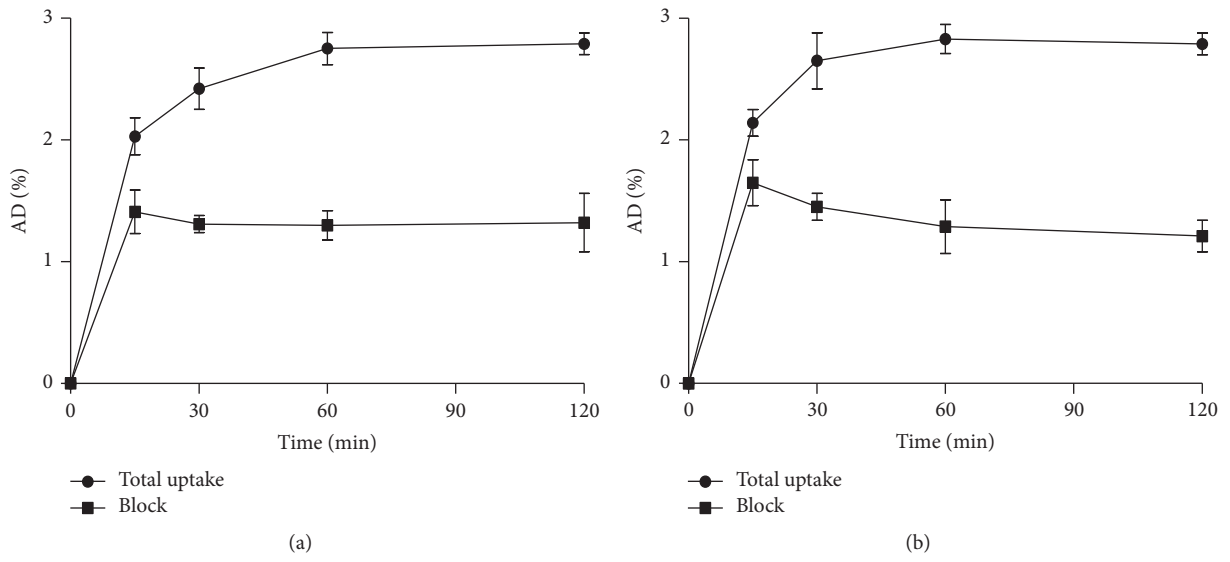


FIGURE 7: Cell uptake and block studies of  $[^{18}\text{F}]\text{AmBF}_3\text{-TEG-ES}$  in MCF-7 (a) and T47D cells (b).

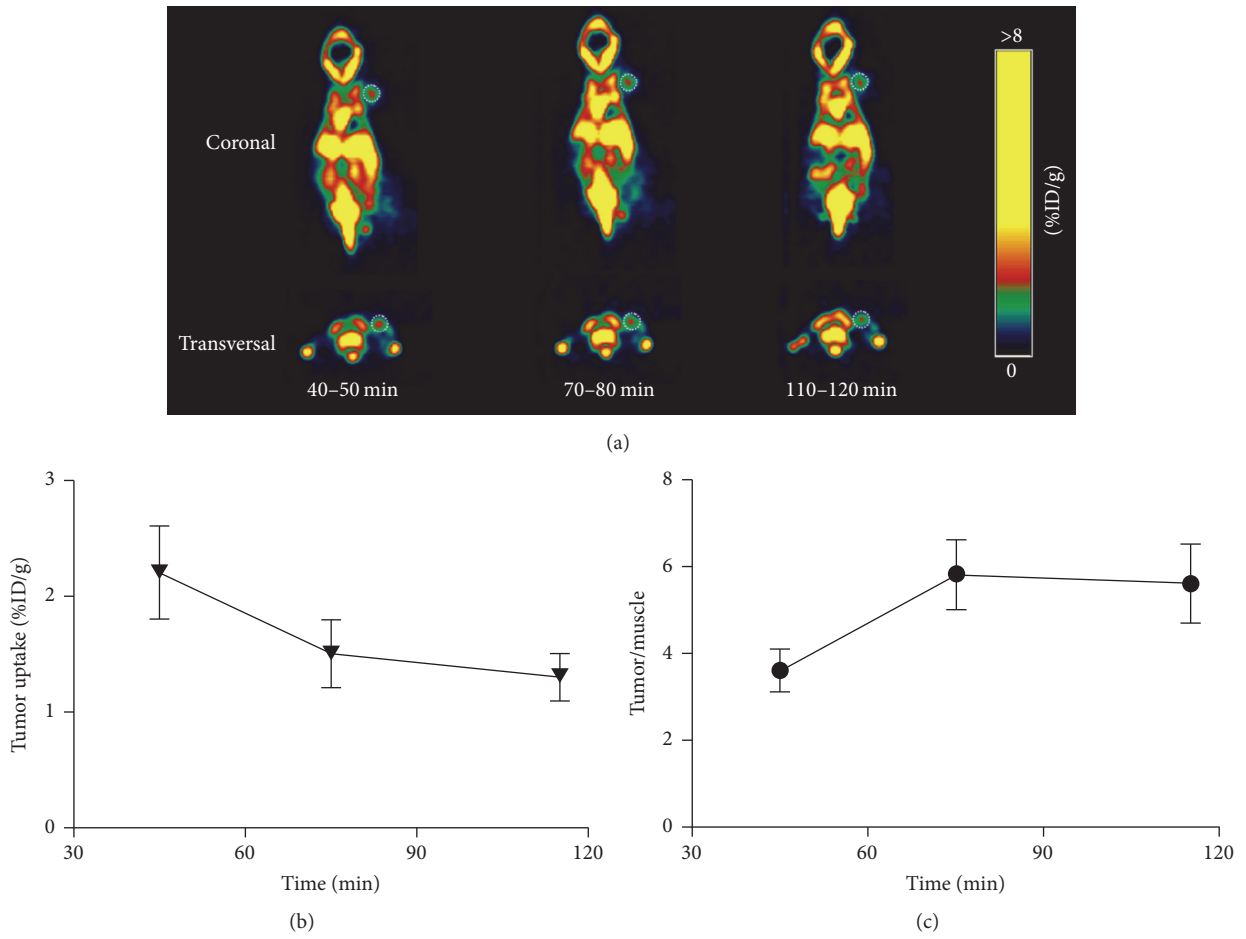


FIGURE 8: (a) Micro-PET imaging of  $[^{18}\text{F}]\text{AmBF}_3\text{-TEG-ES}$  in MCF-7 tumor-bearing nude mice. (b) Tumor uptake at different time. (c) Tumor/muscle uptake ratio at different time.

## Conflicts of Interest

The authors declare that there are no conflicts of interest regarding the publication of this paper.

## Authors' Contributions

Hongbo Huang and Ke Li contributed equally to this work.

## Acknowledgments

This work was financially supported by Natural Science Foundation of China (21371082), Natural Science Foundation of Jiangsu Province (BK20151118), 333 Project of Jiangsu Province (BRA2016518), and Key Youth Medical Talent Project of Jiangsu Province (QNRC20162016626 and QNRC20162016629).

## Supplementary Materials

Supplementary data available: ESI-MS and NMR spectra. Figure S1: ESI-MS of compound **AmBF<sub>3</sub>-TEG-ES**. Figure S2: <sup>1</sup>H-NMR of compound **AmBF<sub>3</sub>-TEG-ES**. Figure S3: <sup>13</sup>C-NMR of compound **AmBF<sub>3</sub>-TEG-ES**. Figure S4: <sup>19</sup>F-NMR of compound **AmBF<sub>3</sub>-TEG-ES**. (*Supplementary Materials*)

## References

- [1] L. A. Torre, F. Bray, R. L. Siegel, J. Ferlay, and J. Lortet-Tieulent, "Global cancer statistics, 2012," *CA: A Cancer Journal for Clinicians*, vol. 65, no. 2, pp. 87–108, 2015.
- [2] K. Chauhan, A. Arun, S. Singh et al., "Bivalent Approach for Homodimeric Estradiol Based Ligand: Synthesis and Evaluation for Targeted Theranosis of ER(+) Breast Carcinomas," *Bioconjugate Chemistry*, vol. 27, no. 4, pp. 961–972, 2016.
- [3] J. N. Bharti, P. Rani, V. Kamal, and P. N. Agarwal, "Angiogenesis in breast cancer and its correlation with estrogen, Progesterone receptors and other prognostic factors," *Journal of Clinical and Diagnostic Research*, vol. 9, no. 1, pp. EC05–EC07, 2015.
- [4] H. M. Linden and F. Dehdashti, "Novel methods and tracers for breast cancer imaging," *Seminars in Nuclear Medicine*, vol. 43, pp. 324–329, 2013.
- [5] A. C. Tecalco-Cruz, I. A. Pérez-Alvarado, J. O. Ramírez-Jarquín, and L. Rocha-Zavaleta, "Nucleo-cytoplasmic transport of estrogen receptor alpha in breast cancer cells," *Cellular Signalling*, vol. 34, pp. 121–132, 2017.
- [6] A. Losurdo, S. Rota, G. Gullo et al., "Controversies in clinicopathological characteristics and treatment strategies of male breast cancer: A review of the literature," *Critical Review in Oncology/Hematology*, vol. 113, pp. 283–291, 2017.
- [7] X. Xia, H. Feng, C. Li, C. Qin, Y. Song, Y. Zhang et al., "99mTc-labeled estradiol as an estrogen receptor probe: Preparation and preclinical evaluation," *Nuclear Medicine and Biology*, vol. 43, pp. 89–96, 2016.
- [8] C. S. Kue, A. Kamkaew, K. Burgess, L. V. Kiew, L. Y. Chung, and H. B. Lee, "Small Molecules for Active Targeting in Cancer," *Medicinal Research Reviews*, vol. 36, no. 3, pp. 494–575, 2016.
- [9] Z. Liu, K.-S. Lin, F. Bénard et al., "One-step 18 F labeling of biomolecules using organotrifluoroborates," *Nature Protocols*, vol. 10, no. 9, pp. 1423–1432, 2015.
- [10] Z. Liu, M. Pourghiasian, M. A. Radtke et al., "An organotrifluoroborate for broadly applicable one-step 18F-labeling," *Angewandte Chemie International Edition*, vol. 53, no. 44, pp. 11876–11880, 2014.
- [11] J. Lin, W. Wang, K. Li et al., "Development of a kit-like radiofluorinated biomolecule leading to a controlled self-assembly of 18F nanoparticles for a smart PET imaging application," *Chemical Communications*, vol. 53, no. 48, pp. 6476–6479, 2017.
- [12] B. Shen, J. Jeon, M. Palner et al., "Positron emission tomography imaging of drug-induced tumor apoptosis with a caspase-triggered nanoaggregation probe," *Angewandte Chemie International Edition*, vol. 52, no. 40, pp. 10511–10514, 2013.
- [13] G. Liu, W. Wang, J. Lin, K. Li, G. Lv, and X. Zhao, "Kit-like 18F-labeling of an estradiol derivative as a potential PET imaging agent for estrogen receptor-positive breast cancer," *Journal of Radioanalytical and Nuclear Chemistry*, pp. 1–9, 2017.
- [14] Z. Liu, Y. Li, J. Lozada et al., "Kit-like 18F-labeling of RGD-19F-Arytrifluoroborate in high yield and at extraordinarily high specific activity with preliminary in vivo tumor imaging," *Nuclear Medicine and Biology*, vol. 40, no. 6, pp. 841–849, 2013.
- [15] F. F. An, H. Kommidi, N. Chen, and R. Ting, "A conjugate of pentamethine cyanine and 18F as a positron emission tomography/near-infrared fluorescence probe for multimodality tumor imaging," *International Journal of Molecular Sciences*, vol. 18, no. 6, article no. 1214, 2017.
- [16] J. Yoo, C. S. Dence, T. L. Sharp, J. A. Katzenellenbogen, and M. J. Welch, "Synthesis of an estrogen receptor  $\beta$ -selective radioligand: 5-[<sup>18</sup>F]fluoro-(2R\*,3S\*)-2,3-bis(4-hydroxyphenyl) pentanenitrile and comparison of in vivo distribution with 16 $\alpha$ -[<sup>18</sup>F]fluoro-17 $\beta$ -estradiol," *Journal of Medicinal Chemistry*, vol. 48, no. 20, pp. 6366–6378, 2005.
- [17] Z. Zhao, Y. Yoshida, T. Kurokawa, Y. Kiyono, T. Mori, and H. Okazawa, "18F-FES and 18F-FDG PET for differential diagnosis and quantitative evaluation of mesenchymal uterine tumors: Correlation with immunohistochemical analysis," *Journal of Nuclear Medicine*, vol. 54, no. 4, pp. 499–506, 2013.
- [18] T. Mori, S. Kasamatsu, C. Mosdzianowski, M. J. Welch, Y. Yonekura, and Y. Fujibayashi, "Automatic synthesis of 16 $\alpha$ -[<sup>18</sup>F]fluoro-17 $\beta$ -estradiol using a cassette-type [<sup>18</sup>F]fluorodeoxyglucose synthesizer," *Nuclear Medicine and Biology*, vol. 33, no. 2, pp. 281–286, 2006.
- [19] Y. N. Nosova, L. S. Foteeva, and I. V. Zenin, "Enhancing the Cytotoxic Activity of Anticancer PtIV Complexes by Introduction of Lonidamine as an Axial Ligand," *European Journal of Inorganic Chemistry*, vol. 12, pp. 1785–1791, 2017.
- [20] C. Dong, S. Yang, J. Shi et al., "SPECT/NIRF Dual Modality Imaging for Detection of Intraperitoneal Colon Tumor with an Avidin/Biotin Pretargeting System," *Scientific Reports*, vol. 6, Article ID 18905, 2016.

## Clinical Study

# Comparing the Differential Diagnostic Values of $^{18}\text{F}$ -Alfatide II PET/CT between Tuberculosis and Lung Cancer Patients

Xiaoqing Du,<sup>1</sup> Yu Zhang,<sup>1</sup> Liping Chen,<sup>1</sup> Baoming Mi,<sup>1</sup> Qingjun You,<sup>1</sup> Yuping Xu,<sup>2</sup>  
Donghui Pan,<sup>2</sup> Weixing Wan,<sup>1</sup> Min Yang,<sup>2</sup> and Chunjing Yu <sup>1</sup>

<sup>1</sup>Department of Nuclear Medicine, Affiliated Hospital of Jiangnan University (Wuxi No. 4 People's Hospital), Wuxi, China

<sup>2</sup>Key Laboratory of Nuclear Medicine, Ministry of Health, Jiangsu Institute of Nuclear Medicine, Wuxi, China

Correspondence should be addressed to Chunjing Yu; ycj\_wxd1978@163.com

Received 31 October 2017; Revised 27 December 2017; Accepted 31 December 2017; Published 19 February 2018

Academic Editor: Yuebing Wang

Copyright © 2018 Xiaoqing Du et al. This is an open access article distributed under the Creative Commons Attribution License, which permits unrestricted use, distribution, and reproduction in any medium, provided the original work is properly cited.

**Purpose.** To compare the differential diagnostic values of  $^{18}\text{F}$ -Alfatide II PET/CT between tuberculosis and lung cancer patients and in patients with sarcoidosis and common inflammation. **Methods.** Nine inflammation patients (4 tuberculosis, 3 sarcoidosis, and 2 common inflammation) and 11 lung cancer patients were included in this study. All patients underwent  $^{18}\text{F}$ -FDG and  $^{18}\text{F}$ -Alfatide II PET/CT within 2 weeks, followed by biopsy and surgery. The maximized standard uptake value (SUVmax) and the mean standard uptake value (SUVmean) were evaluated. **Results.** The active tuberculosis lesions showed a high accumulation of  $^{18}\text{F}$ -FDG, but varying degrees of accumulation of  $^{18}\text{F}$ -Alfatide II, including negative results. The SUVmax of  $^{18}\text{F}$ -Alfatide II in malignant lesions was significantly higher than that in tuberculosis ( $4.08 \pm 1.51$  versus  $2.63 \pm 1.34$ ,  $P = 0.0078$ ). Three patients with sarcoidosis showed negative results in  $^{18}\text{F}$ -Alfatide II PET/CT. **Conclusions.** The expression of  $\alpha_V\beta_3$  is much lower in tuberculosis as compared to that in lung cancer, and accumulation of  $^{18}\text{F}$ -Alfatide II varied even in lesions of the same patient. The negative results of sarcoidosis patients led to the speculation that  $\alpha_V\beta_3$  was not expressed in those lesions.

## 1. Introduction

Lung cancer is one of the largest malignant tumors with fast-growing morbidity and mortality.  $^{18}\text{F}$ -FDG PET/CT has been verified as a crucial tool for detecting, identifying, and staging lung cancer. However, the specificity of  $^{18}\text{F}$ -FDG PET/CT in lung cancer is controversial as some benign lesions such as tuberculosis and sarcoidosis also show a high accumulation of  $^{18}\text{F}$ -FDG. Thus, a new tracer with higher specificity in differentiating lung cancer and inflammation is essential.

The expression of integrin  $\alpha_V\beta_3$  on the surface of cancer cells and neovascularization endothelial cells is upregulated in cancer, inflammation, and wound [1].  $^{18}\text{F}$ -Alfatide II is an annular dimer RGD (Arg-Gly-Asp) tracer targeting integrin  $\alpha_V\beta_3$ . Previous studies reported that the uptake of Alfatide in lung cancer and tuberculosis lesions is markedly different [2, 3]. Thus, additional clinical data is needed to illustrate whether this new tracer is beneficial for the differentiation of tuberculosis from lung cancer.

The present study investigated the differential diagnostic value of  $^{18}\text{F}$ -Alfatide II PET/CT between tuberculosis and lung cancer patients. Also, the angiogenesis in sarcoidosis and chronic inflammations was investigated.

## 2. Materials and Methods

**2.1. Radiopharmaceutical Preparation.** The kit was provided by Jiangsu Institute of Nuclear Medicine. Synthesis of  $^{18}\text{F}$ -Alfatide II has been described previously [4].

**2.2. Patients.** The local institutional review board approved the  $^{18}\text{F}$ -Alfatide II PET/CT complement protocol. Written informed consent was obtained from each patient. The cohort consisted of 9 patients [5 men and 4 women; aged 25–71 ( $55 \pm 16$ ) years] with suspected inflammations and 11 patients [10 men, 1 woman; aged 48–78 ( $66 \pm 9$ ) years] with suspected lung cancer.

TABLE 1: Patient demographics (inflammation group).

Patient number	Age (years)	Sex	Histology
1	69	M	Thoracic tuberculosis
2	71	M	Lung tuberculosis
3	25	F	Lymph node tuberculosis
4	63	M	Lung tuberculosis + tuberculous pleurisy
5	66	F	Sarcoidosis
6	56	F	Sarcoidosis
7	32	F	Sarcoidosis
8	67	M	Chronic-inflammation with fibrosis
9	66	M	Common inflammation

TABLE 2: Patient demographics (malignancy group).

Patient number	Age (years)	Sex	Histology
1	65	M	Squamous cell carcinoma (SCC)
2	75	M	Adenocarcinoma
3	78	M	Squamous cell carcinoma (SCC)
4	72	M	Squamous cell carcinoma (SCC)
5	58	M	Squamous cell carcinoma (SCC)
6	57	M	Squamous cell carcinoma (SCC)
7	67	M	Squamous cell carcinoma (SCC)
8	48	M	Squamous cell carcinoma (SCC)
9	57	F	Adenocarcinoma
10	75	M	Adenocarcinoma
11	74	M	Adenocarcinoma

2.3. *PET/CT Acquisition and Image Analysis.*  $^{18}\text{F}$ -FDG and  $^{18}\text{F}$ -Alfatide II PET/CT were performed at an interval of 2 weeks. Patients were required to fast at least 6 h before  $^{18}\text{F}$ -FDG (5.55 MBq/kg) intravenous injection. The acquisitions were conducted at 60 min after the injection. The patients were placed in a supine position on the scanner bed. Imaging data were acquired from the skull to the thigh, using PET/CT scanner, at 1.5 min/bed position. Low-dose CT was performed for attenuation correction and lesion localization.  $^{18}\text{F}$ -Alfatide II PET/CT was performed on the next day without any specific preparation before the examination.  $^{18}\text{F}$ -Alfatide II ( $248.27 \pm 45.14$  MBq) was injected intravenously in all patients. The acquisition procedure and parameters were identical to that as  $^{18}\text{F}$ -FDG PET/CT. Regions of interest (ROIs) were drawn manually on the site of lesions based on the corresponding CT images.

PET/CT Scanner was from Siemens (Biograph True Point PET/CT).

Visual analysis was used to evaluate the preliminary accumulation of  $^{18}\text{F}$ -Alfatide II and  $^{18}\text{F}$ -FDG in tuberculosis and lung cancer. Maximum standard uptake value (SUV<sub>max</sub>), mean standard uptake value (SUV<sub>mean</sub>), and lesion/muscle (L/M) ratio recorded the uptake of the lesions in this study. The uptake of the right hip muscle was selected as a reference for lesions. All lesions were divided into different regions of head-neck, chest, abdomen, and pelvis. The largest lesion of each region was chosen to measure the uncountable lesions.

Two physicians evaluated the images independently, and the discrepancies were resolved by consultation.

#### 2.4. Pathological Analysis and Follow-Up

*Inflammation Group.* Number 1 patient was confirmed as thoracic tuberculosis by biopsy. Number 2–4 patients, receiving PPD test, T-SPOT test, and antituberculosis treatment, were followed up for 16, 17, and 33 months, respectively; they were confirmed as lung tuberculosis, lymph node tuberculosis, and lung tuberculosis mixed with tuberculous pleurisy. Number 5 patient was confirmed as sarcoidosis by bronchoscope puncture biopsy. Number 6–7 patients, receiving no treatment and followed up for 17 and 28 months, respectively, were diagnosed as sarcoidosis. Number 8 patient was shown to have chronic inflammation accompanied by fibrosis as assessed by percutaneous lung biopsy. Number 9 patient was diagnosed with inflammation caused by common infection after 20 months' follow-up based on CT (Table 1).

*Malignancy Group.* Eight patients received surgery. One patient did not undergo surgery since the pulmonary trunk was invaded by cancer, and two patients were not recommended surgery as distant metastasis detected by PET/CT and MRI. All patients were confirmed by pathology; one distant metastasis patient received bronchoscopy biopsy, while the other underwent clavicle lymph node excision (Table 2).

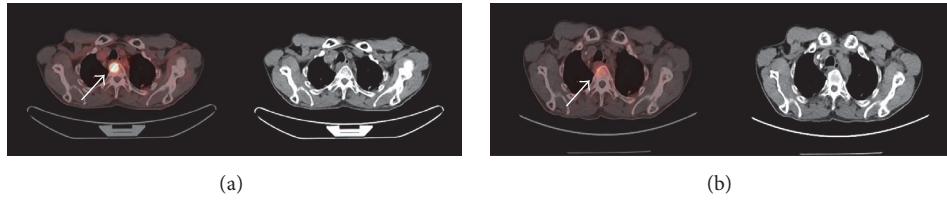


FIGURE 1:  $^{18}\text{F}$ -FDG (a) and  $^{18}\text{F}$ -Alfatide II (b) PET/CT images of a thoracic tuberculosis patient. T2, T3, and T4 showed intense  $^{18}\text{F}$ -FDG uptake and mild  $^{18}\text{F}$ -Alfatide II uptake. The white arrows indicate tuberculosis lesions in T4.

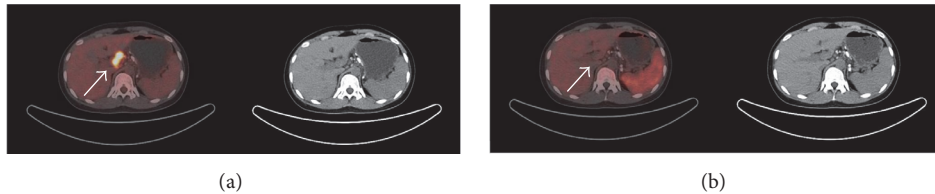


FIGURE 2:  $^{18}\text{F}$ -FDG (a) and  $^{18}\text{F}$ -Alfatide II (b) PET/CT images of a lymph node tuberculosis patient. Lymph nodes tuberculosis lesions showed intense  $^{18}\text{F}$ -FDG uptake and no  $^{18}\text{F}$ -Alfatide II uptake. The white arrows indicate tuberculosis lesions in porta hepatis lymph nodes.

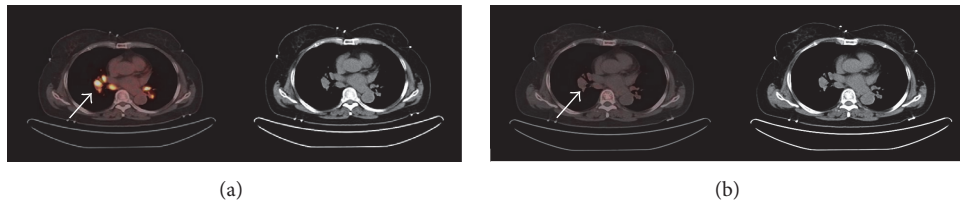


FIGURE 3:  $^{18}\text{F}$ -FDG (a) and  $^{18}\text{F}$ -Alfatide II (b) PET/CT images of a sarcoidosis patient. All lesions showed intense  $^{18}\text{F}$ -FDG uptake and no  $^{18}\text{F}$ -Alfatide II uptake. The white arrows indicate sarcoidosis lesions in mediastinum and hilus pulmonis.

2.5. *Statistical Analysis.* Mean  $\pm$  standard deviation (m  $\pm$  SD) was used to express all quantitative data. Differences in SUVmax/SUVmean between patients with different diseases were compared and assessed by *t*-test or Mann-Whitney *U* test. All statistical analyses were carried out using SAS 9.2.  $P < 0.05$  indicated statistical significance.

### 3. Results

3.1. *Safety.* Patients did not report any subjective effects following the injected dose of  $^{18}\text{F}$ -Alfatide II. No adverse events were noted during the examination of  $^{18}\text{F}$ -Alfatide II PET/CT or follow-up (at least 6 months).

3.2. *Visual Analysis Results.* The accumulation of  $^{18}\text{F}$ -Alfatide II in tuberculosis was much lower than that of  $^{18}\text{F}$ -FDG (Figures 1 and 2), while no accumulation was observed in sarcoidosis lesions (Figure 3). Additionally, 2 chronic inflammations showed a high accumulation of  $^{18}\text{F}$ -Alfatide II.

All lung cancer patients in this study showed a high accumulation of  $^{18}\text{F}$ -Alfatide II, including brain and bone metastasis. The results were similar to that in the previous reports [5].

3.3. *Preliminary Diagnostic Value of  $^{18}\text{F}$ -FDG PET/CT and  $^{18}\text{F}$ -Alfatide II PET/CT in Tuberculosis.* The SUVmax of

tuberculosis was calculated as  $7.53 \pm 2.88$  and  $2.63 \pm 1.34$  for  $^{18}\text{F}$ -FDG and  $^{18}\text{F}$ -Alfatide II, respectively. The SUVmean of tuberculosis was  $4.58 \pm 1.73$  and  $1.86 \pm 1.0$ , respectively.

3.4. *Preliminary Diagnostic Value of  $^{18}\text{F}$ -FDG PET/CT and  $^{18}\text{F}$ -Alfatide II PET/CT in Chronic Inflammation.* The SUVmax of two patients with chronic inflammation was 10.80 and 1.62 for  $^{18}\text{F}$ -FDG and 9.13 and 5.75 for  $^{18}\text{F}$ -Alfatide II, respectively. The SUVmean was 5.33, 0.99 and 5.12, 2.65, respectively.

3.5. *Preliminary Diagnostic Value of  $^{18}\text{F}$ -FDG PET/CT and  $^{18}\text{F}$ -Alfatide II PET/CT in Sarcoidosis.* The SUVmax of  $^{18}\text{F}$ -FDG and  $^{18}\text{F}$ -Alfatide II in sarcoidosis was calculated as  $8.82 \pm 5.17$  and  $1.77 \pm 0.69$ , respectively, while SUVmean was  $5.34 \pm 3.08$  and  $1.28 \pm 0.63$ , respectively.

3.6. *Preliminary Diagnostic Value of  $^{18}\text{F}$ -FDG PET/CT and  $^{18}\text{F}$ -Alfatide II PET/CT in Lung Cancer.* The SUVmax of  $^{18}\text{F}$ -FDG and  $^{18}\text{F}$ -Alfatide II in lung cancer was  $12.04 \pm 4.67$  and  $4.08 \pm 1.51$ , respectively, while SUVmean was  $4.55 \pm 1.98$  and  $1.99 \pm 0.81$ , respectively.

3.7. *Difference between the SUVmax of Malignant Lesions and Tuberculosis Lesions.* The lesion-to-lesion analysis showed that the SUVmax of  $^{18}\text{F}$ -Alfatide II in malignant lesions

TABLE 3: SUVmax and SUVmean of lesions.

	<sup>18</sup> F-FDG SUVmax	<sup>18</sup> F-Alfatide II SUVmax	<sup>18</sup> F-FDG SUVmean	<sup>18</sup> F-Alfatide II SUVmean
Tuberculosis	7.53 ± 2.88	2.63 ± 1.34	4.58 ± 1.73	1.86 ± 1.0
Lung cancer	12.04 ± 4.67	4.08 ± 1.51	4.55 ± 1.98	1.99 ± 0.81
Sarcoidosis	8.82 ± 5.17	1.77 ± 0.69	5.34 ± 3.08	1.28 ± 0.63
Chronic inflammation 1	10.80	9.13	5.33	5.12
Chronic inflammation 2	1.62	5.75	0.99	2.65

was  $4.08 \pm 1.51$ , which was significantly higher than that in tuberculosis ( $2.63 \pm 1.34$ ,  $P = 0.0078$ ).

**3.8. Difference between the SUVmean of Malignant Lesions and Tuberculosis Lesions.** The SUVmean of <sup>18</sup>F-Alfatide II in malignant lesions was  $1.99 \pm 0.81$  without any statistically significant difference from that of tuberculosis ( $1.86 \pm 1.0$ ,  $P = 0.3820$ ).

**3.9. Preliminary Diagnostic Value of <sup>18</sup>F-FDG and <sup>18</sup>F-Alfatide II PET/CT in Inflammations (Active TB, Chronic Inflammation, and Sarcoidosis) and Lung Cancer.** See Table 3.

#### 4. Discussion

Integrin  $\alpha_V\beta_3$  is overexpressed not only in various tumor cells and tumor neovasculature [6] but also in chronic inflammatory diseases, such as inflammatory bowel disease (IBD) and rheumatoid arthritis (RA) [7, 8]. Previous studies reported that angiogenesis and chronic inflammation are interrelated [7, 9]. Jackson et al. [10] suggested that several resident cells (fibroblasts, monocytes-macrophages, neutrophils, and lymphocytes) can promote angiogenesis when the microenvironment becomes hypoxic or inflammatory, thereby facilitating the migration of inflammatory cells to inflammatory sites and the supply of nutrients and oxygen to the proliferating tissue. The frequent dual functionality of angiogenic factors such as  $\alpha_V\beta_3$  and VEGF reflects the close relationship between angiogenesis and inflammation [11]. Cao et al. [12] demonstrated specific uptake of  $\alpha_V\beta_3$  in the chronic inflammation of mouse ear using <sup>64</sup>Cu-DOTA-RGD tetramer PET imaging.

Chin et al. [13] carried out a PET imaging study with <sup>18</sup>F-FPP(RGD)<sub>2</sub> in a healthy woman volunteer, and no unusual or adverse patient symptoms were found on the day of imaging as well as during follow-up. Wan et al. [2] did not record any adverse events associated with <sup>18</sup>F-Alfatide in the first subject during the study, in which nine lung cancer patients were investigated. No adverse events occurred in all patients during or after the <sup>18</sup>F-Alfatide II PET/CT imaging in the current study. All these investigations revealed that using RGD tracers labeled by <sup>18</sup>F is safe for patients.

Tuberculosis is a major global health problem with an estimated 8.6 million new cases worldwide in 2012 [14]. The tuberculous granuloma is an organized collection of differentiated macrophages surrounded by T-lymphocytes, B-lymphocytes, dendritic cells, fibroblasts, and extracellular

matrix components [15]. Some studies demonstrated  $\alpha_V\beta_1$  expression in lung granulomas and lymph nodes of sarcoid patients [16]. Rojas et al. [17] found that the mycobacterial glycolipid phosphatidylinositol mannoside interacts directly with  $\alpha_V\beta_1$  integrin VLA-5 on CD4<sup>+</sup> T-lymphocytes, resulting in fibronectin binding and T-cell migration. Several studies have reported increased levels of VEGF in granulomatous disease, such as pulmonary tuberculosis [18–21] and Crohn's disease [22]. Hur et al. [23] reported that median concentration of serum VEGF-A was significantly higher in tuberculosis patients than that in the latent tuberculosis infection and control groups. Four patients with active tuberculosis showed varying degree of accumulation of <sup>18</sup>F-Alfatide II in this study, including negative results, and even the positive lesions showed a low accumulation of <sup>18</sup>F-Alfatide II than that of <sup>18</sup>F-FDG. Kang et al. [3] reported that tuberculosis granuloma and the surrounding vasculature epithelium showed baseline  $\alpha_V\beta_3$  expression as assessed by immunohistochemistry. The diversity in the current study revealed different expression of  $\alpha_V\beta_3$  in all tuberculosis lesions.

All lung cancer lesions and the metastases in the brain and bone showed an increased RGD uptake. A significant difference was noted in SUVmax between the lung cancer and tuberculosis groups, which indicated that RGD PET/CT might differentiate lung cancer from tuberculosis.

Sarcoidosis is an immunological, granulomatous disorder affecting multiple systems. The presence of noncaseating granulomas in involved organs is a pathological feature [24]. The common sites of the disease are lung, mediastinum, and hilus pulmonis lymph node [25, 26]. The precise pathogenesis is yet unknown, which might include various factors: environmental, occupational exposure, the presence of infectious agents, and genetic susceptibility [27–29]. Various studies suggested that angiogenic factors contribute to the pathogenesis of sarcoidosis [30, 31]. Agostini et al. [32] and Antoniou et al. [31] indicated the presence of angiogenesis in the pathogenesis of granulomatous and pulmonary fibrosis. Tzouveleakis et al. [33] revealed an abundant expression of VEGF and ING4 within the granulomatous tissue, localized in the epithelioid and giant cells. Three sarcoidosis patients, in this study, showed negative results in <sup>18</sup>F-Alfatide II PET/CT, thereby indicating the lack of  $\alpha_V\beta_3$  expression in sarcoidosis. Kambouchner et al. [34] proposed the presence of an avascular microenvironment within sarcoid lesions. Tzouveleakis et al. [33] speculated that abundant expression of VEGF might be implicated in the inflammatory than the angiogenic cascade of sarcoidosis. Murdoch et al. supported

this speculation with respect to the pleiotropic properties of VEGF in promoting the Th1-dependent immunity via facilitation of monocyte recruitment and T-cell migration to sites of ongoing inflammation [35]. The results from the current study were in agreement with the theory by Kambouchner et al. and Tzouveleakis et al.

Furthermore, the present study comprised 2 common infection patients: one patient showed high accumulation of  $^{18}\text{F}$ -Alfatide II as well as  $^{18}\text{F}$ -FDG, while the other showed a high accumulation of  $^{18}\text{F}$ -Alfatide II compared to  $^{18}\text{F}$ -FDG. Winter et al. [36] speculated that integrin  $\alpha_V\beta_3$  was a potential marker of inflammation and angiogenesis in atherosclerotic lesions. Srivatsa et al. and Hansson both observed persistently high levels of  $\alpha_V\beta_3$  expression between 7 and 21 days following injury in the neointima, media, and adventitia [37, 38]. Other studies demonstrated the expression of integrin  $\alpha_V\beta_3$  on activated macrophages by different methods [39–41]. When acute inflammation transforms into subacute and chronic inflammation, macrophages are gradually increased in number in lesions than the neutrophils. Thus, the high accumulation of  $^{18}\text{F}$ -Alfatide II in the 2 patients in this study indicated the chronic inflammatory stage, which was confirmed by fibrosis tested by percutaneous lung biopsy in one lesion. Storgard et al. [42] reported that the treatment with cyclic RGD peptide c(RGDfV), an integrin  $\alpha_V\beta_3$  antagonist, significantly inhibited the disease progression in an experimental RA model. Taken together,  $^{18}\text{F}$ -Alfatide II PET/CT may not only detect chronic inflammation but also allow the evaluation of angiogenesis and neovascularization during chronic inflammation and guide the selection of patients for antiangiogenesis therapy.

Nevertheless, the present study has some deficiencies. (1) Early experimental design was not perfect; for example, we did not recruit lymphoma patients to compare with sarcoidosis in  $^{18}\text{F}$ -Alfatide II PET/CT. (2) The number of patients was small. (3) Further investigations are essential.

## 5. Conclusion

The accumulation of lung cancer and tuberculosis exhibits distinct difference, which might be valuable in differentiating the two diseases. Three sarcoidoses showed negative results, and thus, we speculated the lack of  $\alpha_V\beta_3$  expression within sarcoidosis.  $^{18}\text{F}$ -Alfatide II might be valuable in the evaluation of angiogenesis and neovascularization during chronic inflammation, which could guide the selection of patients for antiangiogenesis therapy and evaluate the clinical effect of the treatment.

## Conflicts of Interest

The authors declare that they have no conflicts of interest.

## Acknowledgments

This work was supported by the Natural Science Foundation of China (81471691).

## References

- [1] J. A. Varner and D. A. Cheresh, "Integrins and cancer," *Current Opinion in Cell Biology*, vol. 8, no. 5, pp. 724–730, 1996.
- [2] W. Wan, N. Guo, D. Pan et al., "First experience of  $^{18}\text{F}$ -alfatide in lung cancer patients using a new lyophilized kit for rapid radiofluorination," *Journal of Nuclear Medicine*, vol. 54, no. 5, pp. 691–698, 2013.
- [3] F. Kang, S. Wang, F. Tian et al., "Comparing the diagnostic potential of  $^{68}\text{Ga}$ -Alfatide II and  $^{18}\text{F}$ -FDG in differentiating between non-small cell lung cancer and tuberculosis," *Journal of Nuclear Medicine*, vol. 57, no. 5, pp. 672–677, 2016.
- [4] L. Lang, Y. Ma, D. O. Kiesewetter, and X. Chen, "Stability analysis of glutamic acid linked peptides coupled to NOTA through different chemical linkages," *Molecular Pharmaceutics*, vol. 11, no. 11, pp. 3867–3874, 2014.
- [5] S. Gao, H. Wu, W. Li et al., "A pilot study imaging integrin  $\alpha_V\beta_3$  with RGD PET/CT in suspected lung cancer patients," *European Journal of Nuclear Medicine and Molecular Imaging*, vol. 42, no. 13, pp. 2029–2037, 2015.
- [6] W. Cai and X. Chen, "Anti-angiogenic cancer therapy based on integrin  $\alpha_V\beta_3$  antagonism," *Anti-Cancer Agents in Medicinal Chemistry*, vol. 6, no. 5, pp. 407–428, 2006.
- [7] S. Danese, M. Sans, C. de la Motte et al., "Angiogenesis as a novel component of inflammatory bowel disease pathogenesis," *Gastroenterology*, vol. 130, no. 7, pp. 2060–2073, 2006.
- [8] R. L. Wilder, "Integrin alpha V beta 3 as a target for treatment of rheumatoid arthritis and related rheumatic diseases," *Annals of the Rheumatic Diseases*, vol. 61, supplement 2, pp. ii96–ii99, 2002.
- [9] I. E. Koutroubakis, G. Tsiolakidou, K. Karmiris, and E. A. Kouroumalis, "Role of angiogenesis in inflammatory bowel disease," *Inflammatory Bowel Diseases*, vol. 12, no. 6, pp. 515–523, 2006.
- [10] J. R. Jackson, M. P. Seed, C. H. Kircher, D. A. Willoughby, and J. D. Winkler, "The codependence of angiogenesis and chronic inflammation," *The FASEB Journal*, vol. 11, no. 6, pp. 457–465, 1997.
- [11] D. A. Walsh, "Angiogenesis and arthritis," *Rheumatology*, vol. 38, no. 2, pp. 103–112, 1999.
- [12] Q. Cao, W. Cai, Z.-B. Li et al., "PET imaging of acute and chronic inflammation in living mice," *European Journal of Nuclear Medicine and Molecular Imaging*, vol. 34, no. 11, pp. 1832–1842, 2007.
- [13] F. T. Chin, B. Shen, S. Liu et al., "First experience with clinical-grade  $^{18}\text{F}$ -FPP (RGD) $_2$ : An automated multi-step radiosynthesis for clinical PET studies," *Molecular Imaging and Biology*, vol. 14, no. 1, pp. 88–95, 2012.
- [14] Eurosurveillance editorial, "WHO publishes global tuberculosis report 2013," *Euro Surveill*, vol. 18, no. 43, 2013.
- [15] C. L. Cosma, D. R. Sherman, and L. Ramakrishnan, "The secret lives of the pathogenic mycobacteria," *Annual Review of Microbiology*, vol. 57, pp. 641–676, 2003.
- [16] K. Shigehara, N. Shijubo, M. Hirasawa, S. Abe, and T. Uede, "Immunolocalization of extracellular matrix proteins and integrins in sarcoid lymph nodes," *Virchows Archiv*, vol. 433, no. 1, pp. 55–61, 1998.
- [17] R. E. Rojas, J. J. Thomas, A. J. Gehring et al., "Phosphatidylinositol mannoside from mycobacterium tuberculosis binds  $\alpha_V\beta_1$  integrin (VLA-5) on CD4+ T cells and induces adhesion to fibronectin," *The Journal of Immunology*, vol. 177, no. 5, pp. 2959–2968, 2006.

- [18] W. Matsuyama, T. Hashiguchi, K. Matsumuro et al., "Increased serum level of vascular endothelial growth factor in pulmonary tuberculosis," *American Journal of Respiratory and Critical Care Medicine*, vol. 162, no. 3 I, pp. 1120–1122, 2000.
- [19] S. W. Ra, J. Lyu, C.-M. Choi et al., "Distinguishing tuberculosis from Mycobacterium avium complex disease using an interferon-gamma release assay," *The International Journal of Tuberculosis and Lung Disease*, vol. 15, no. 5, pp. 635–640, 2011.
- [20] Y. Nishigaki, S. Fujiuchi, Y. Fujita et al., "Increased serum level of vascular endothelial growth factor in Mycobacterium avium complex infection," *Respirology*, vol. 11, no. 4, pp. 407–413, 2006.
- [21] C. Riou, B. Perez Peixoto, L. Roberts et al., "Effect of standard tuberculosis treatment on plasma cytokine levels in patients with active pulmonary tuberculosis," *PLoS ONE*, vol. 7, no. 5, Article ID e36886, 2012.
- [22] I. D. Pousa, J. Maté, X. Salcedo-Mora, M. T. Abreu, R. Moreno-Otero, and J. P. Gisbert, "Role of vascular endothelial growth factor and angiopoietin systems in serum of Crohn's disease patients," *Inflammatory Bowel Diseases*, vol. 14, no. 1, pp. 61–67, 2008.
- [23] Y.-G. Hur, Y. A. Kang, S.-H. Jang et al., "Adjunctive biomarkers for improving diagnosis of tuberculosis and monitoring therapeutic effects," *Infection*, vol. 70, no. 4, pp. 346–355, 2015.
- [24] R. P. Baughman, E. E. Lower, and R. M. Du Bois, "Sarcoidosis," *The Lancet*, vol. 361, no. 9363, pp. 1111–1118, 2003.
- [25] R. P. Baughman, S. Nagai, M. Balter et al., "Defining the clinical outcome status (COS) in sarcoidosis: results of WASOG task force," *Sarcoidosis, Vasculitis and Diffuse Lung Diseases*, vol. 28, pp. 56–64, 2011.
- [26] G. W. Hunninghake, U. Costabel, M. Ando et al., "American thoracic society/european respiratory society/world association of sarcoidosis and other granulomatous disorders," *Sarcoidosis, Vasculitis and Diffuse Lung Diseases*, vol. 16, pp. 149–173, 1999.
- [27] A. Lazarus, "Sarcoidosis: epidemiology, etiology, pathogenesis, and genetics," *Disease-a-Month*, vol. 55, no. 11, pp. 649–660, 2009.
- [28] K. W. Thomas and G. W. Hunninghake, "Sarcoidosis," *Journal of the American Medical Association*, vol. 289, no. 24, pp. 3300–3303, 2003.
- [29] M. C. Iannuzzi, B. A. Rybicki, and A. S. Tierstein, "Sarcoidosis," *The New England Journal of Medicine*, vol. 357, pp. 2153–2165, 2007.
- [30] A. Cui, O. Anhenn, D. Theegarten et al., "Angiogenic and angiostatic chemokines in idiopathic pulmonary fibrosis and granulomatous lung disease," *Respiration*, vol. 80, no. 5, pp. 372–378, 2010.
- [31] K. M. Antoniou, A. Tzouveleakis, M. G. Alexandrakis et al., "Different angiogenic activity in pulmonary sarcoidosis and idiopathic pulmonary fibrosis," *CHEST*, vol. 130, no. 4, pp. 982–988, 2006.
- [32] C. Agostini, M. Facco, M. Siviero et al., "CXC chemokines IP-10 and Mig expression and direct migration of pulmonary CD8+/CXCR3+ T cells in the lungs of patients with HIV infection and T-cell alveolitis," *American Journal of Respiratory and Critical Care Medicine*, vol. 162, no. 4 I, pp. 1466–1473, 2000.
- [33] A. Tzouveleakis, P. Ntoliou, A. Karameris et al., "Expression of hypoxia-inducible factor (HIF)-1 $\alpha$ -vascular endothelial growth factor (VEGF)-inhibitory growth factor (ING)-4- axis in sarcoidosis patients," *BMC Research Notes*, vol. 5, article 654, 2012.
- [34] M. Kambouchner, D. Pirici, J.-F. Uhl, L. Mogoanta, D. Valeyre, and J.-F. Bernaudin, "Lymphatic and blood microvasculature organisation in pulmonary sarcoid granulomas," *European Respiratory Journal*, vol. 37, no. 4, pp. 835–840, 2011.
- [35] C. Murdoch, A. Giannoudis, and C. E. Lewis, "Mechanisms regulating the recruitment of macrophages into hypoxic areas of tumors and other ischemic tissues," *Blood*, vol. 104, no. 8, pp. 2224–2234, 2004.
- [36] P. M. Winter, A. M. Morawski, S. D. Caruthers et al., "Molecular imaging of angiogenesis in early-stage atherosclerosis with  $\alpha$ V $\beta$ 3-integrin-targeted nanoparticles," *Circulation*, vol. 108, no. 18, pp. 2270–2274, 2003.
- [37] S. S. Srivatsa, L. A. Fitzpatrick, P. W. Tsao et al., "Selective  $\alpha$ V $\beta$ 3 integrin blockade potently limits neointimal hyperplasia and lumen stenosis following deep coronary arterial stent injury: evidence for the functional importance of integrin  $\alpha$ V $\beta$ 3 and osteopontin expression during neointima formation," *Cardiovascular Research*, vol. 36, no. 3, pp. 408–428, 1997.
- [38] G. K. Hansson, "Inflammation, atherosclerosis, and coronary artery disease," *The New England Journal of Medicine*, vol. 352, pp. 1685–1695, 2005.
- [39] A. S. Antonov, F. D. Kolodgie, D. H. Munn et al., "Regulation of macrophage foam cell formation by  $\alpha$ V $\beta$ 3 integrin: potential role in human atherosclerosis," *The American Journal of Pathology*, vol. 165, pp. 247–258, 2004.
- [40] J. Waldeck, F. Häger, C. Höltke et al., "Fluorescence reflectance imaging of macrophage-rich atherosclerotic plaques using an  $\alpha$ V $\beta$ 3 integrin-targeted fluorochrome," *Journal of Nuclear Medicine*, vol. 49, no. 11, pp. 1845–1851, 2008.
- [41] Y. Yao, Y. Jiang, Z. Sheng et al., "Analysis of in situ and ex vivo  $\alpha$ V $\beta$ 3 integrin expression during experimental carotid atherogenesis," *International Journal of Nanomedicine*, vol. 7, pp. 641–649, 2012.
- [42] C. M. Storgard, D. G. Stupack, A. Jonczyk, S. L. Goodman, R. I. Fox, and D. A. Cheresh, "Decreased angiogenesis and arthritic disease in rabbits treated with an  $\alpha$ V $\beta$ 3 antagonist," *The Journal of Clinical Investigation*, vol. 103, no. 1, pp. 47–54, 1999.

## Research Article

# Synthesis and Bioevaluation of Iodine-131 Directly Labeled Cyclic RGD-PEGylated Gold Nanorods for Tumor-Targeted Imaging

Yingying Zhang,<sup>1,2</sup> Yongxue Zhang,<sup>1,2</sup> Lianglan Yin,<sup>1,2</sup> Xiaotian Xia,<sup>1,2</sup> Fan Hu,<sup>1,2</sup> Qingyao Liu,<sup>1,2</sup> Chunxia Qin,<sup>1,2</sup> and Xiaoli Lan<sup>1,2</sup>

<sup>1</sup>Department of Nuclear Medicine, Union Hospital, Tongji Medical College, Huazhong University of Science and Technology, Wuhan 430022, China

<sup>2</sup>Hubei Key Laboratory of Molecular Imaging, Union Hospital, Tongji Medical College, Huazhong University of Science and Technology, Wuhan 430022, China

Correspondence should be addressed to Chunxia Qin; [qin\\_chunxia@hust.edu.cn](mailto:qin_chunxia@hust.edu.cn) and Xiaoli Lan; [lxl730724@hotmail.com](mailto:lxl730724@hotmail.com)

Received 6 September 2017; Accepted 4 December 2017; Published 24 December 2017

Academic Editor: Yuebing Wang

Copyright © 2017 Yingying Zhang et al. This is an open access article distributed under the Creative Commons Attribution License, which permits unrestricted use, distribution, and reproduction in any medium, provided the original work is properly cited.

**Introduction.** Radiolabeled gold nanoparticles play an important role in biomedical application. The aim of this study was to prepare iodine-131 (<sup>131</sup>I)-labeled gold nanorods (GNRs) conjugated with cyclic RGD and evaluate its biological characteristics for targeted imaging of integrin  $\alpha_v\beta_3$ -expressing tumors. **Methods.** HS-PEG<sub>(5000)</sub>-COOH molecules were applied to replace CTAB covering the surface of bare GNRs for better biocompatibility, and c(RGDfK) peptides were conjugated onto the carboxyl terminal of GNR-PEG-COOH via EDC/NHS coupling reactions. The nanoconjugate was characterized, and <sup>131</sup>I was directly tagged on the surface of GNRs via AuI bonds for SPECT/CT imaging. We preliminarily studied the characteristics of the probe and its feasibility for tumor-targeting SPECT/CT imaging. **Results.** The [<sup>131</sup>I]GNR-PEG-cRGD probe was prepared in a simple and rapid manner and was stable in both PBS and fetal bovine serum. It targeted selectively and could be taken up by tumor cells mainly via integrin  $\alpha_v\beta_3$ -receptor-mediated endocytosis. In vivo imaging, biodistribution, and autoradiography results showed evident tumor uptake in integrin  $\alpha_v\beta_3$ -expressing tumors. **Conclusions.** These promising results showed that this smart nanoprobe can be used for angiogenesis-targeted SPECT/CT imaging. Furthermore, the nanoprobe possesses a remarkable capacity for highly efficient photothermal conversion in the near-infrared region, suggesting its potential as a multifunctional theranostic agent.

## 1. Introduction

Ideal physicochemical properties, a high binding affinity for selected molecules with thiol terminal groups, and remarkable photoacoustic features provide gold nanoparticles (GNPs) with significant capabilities for biomedical applications [1, 2]. Different forms of gold nanostructures, such as GNPs [3], gold nanorods (GNRs) [4], gold nanocages [5], gold nanospheres [6], and gold nanoshells [7], have been investigated for molecular imaging and therapy. As a representative GNP, GNRs have attracted considerable attention in recent years because of their small size, ease of preparation and bioconjugation, strong absorption and scattering properties, and well-characterized biocompatibility [8]. The long surface plasmon resonance (LSPR) of GNRs can be finely

tuned by the aspect ratio [9], which gives rise to many exciting possibilities for biosensing, optical imaging, photothermal therapy, and drug delivery. With a proper aspect ratio, the LSPR of GNRs can be located in the near-infrared region (NIR; 650–900 nm) that is particularly suitable for in vivo imaging and photothermal therapy [9–11].

The high reaction activity of the surface in the crystal structure of GNRs allows multiple functionalizations including target ligands (e.g., peptides [12], folic acid [13], and antibodies [14]) and imaging agents (e.g., fluorescent, radionuclide, and contrast reagents) [15, 16]. Cetyltrimethylammonium bromide (CTAB), a kind of cationic surfactant stabilizer, is essential for the synthesis of GNRs. However, CTAB molecules exhibit strong cytotoxicity that can induce cell apoptosis and autophagy by damaging mitochondria and generating

intracellular reactive oxygen species [17]. Fortunately, CTAB can be replaced or conjugated with many functional groups [2]. Introducing polyethylene glycol (PEG) to the surface of nanoparticles achieves better biocompatibility and lower cytotoxicity by decreasing the opsonization effect and minimizing nonspecific uptake by the reticuloendothelial system *in vivo* for a longer blood circulation time [8]. In addition, it has been shown that halide ions chemisorb onto the gold surface with Au-X, and its binding strength varies as  $I > Br > Cl$  [18]. Iodine-131 ( $^{131}\text{I}$ ;  $t_{1/2} = 8.01$  days), a radionuclide with gamma emission of 364 keV and beta emission of 0.608 keV, provides imaging feasibility and a beta-emitting therapeutic effect, which makes it the optimal choice for application as a theranostic agent [19].

Extensive angiogenesis exists in solid tumors, which can be used as a diagnostic and therapeutic target. Integrin  $\alpha_v\beta_3$  is a cell adhesion molecule overexpressed on most tumor cells for regulation of angiogenesis and plays important roles in various stages, such as malignant transformation, tumor growth, progression, invasion, and metastasis [20]. An Arg-Gly-Asp- (RGD-) based strategy to target integrin  $\alpha_v\beta_3$  is one of the most promising and best studied in oncological research [20], especially cyclic RGD (cRGD) peptides, which have higher affinity, selectivity, and stability than linear peptides [16]. Furthermore, hypervascularity, a defective vascular architecture, poor lymphatic drainage, or recovery system, and greatly increased production of a number of permeability mediators facilitate nanosized particle extravasation from the blood pool, which can be retained in solid tumors, known as the enhanced permeability and retention (EPR) effect [21]. Therefore, cRGD-conjugated nanodrugs can accumulate in tumor tissues actively through target molecules and passively because of the EPR effect, resulting in increased curative efficacy and reduced side effects [22, 23].

Based on the above theoretical fundamentals, we synthesized a smart multifunctional nanoprobe,  $^{131}\text{I}$ -labeled, cRGD-conjugated PEG-modified GNRs and evaluated the feasibility of the nanoprobe for tumor-targeted imaging by *in vitro* cell experiments and *in vivo* tumor-bearing mouse imaging.

## 2. Materials and Methods

**2.1. Chemicals and Materials.** The chemicals and materials included a gold colloid solution (GNR-PEG) (Xi'an Ruixi Biological Tech. Co., Ltd., Xi'an, China), N-(3-dimethylaminopropyl)-N'-ethylcarbodiimide hydrochloride (EDC-HCl) (Aladdin Bio-Chem Tech. Co., Ltd, Shanghai, China), N-hydroxysuccinimide (NHS) (Sinopharm Chemical Reagent Co., Ltd., Shanghai, China), cyclo (Arg-Gly-Asp-d-Phe-Lys) [c(RGDfK)] (GL Biochem Ltd., Shanghai, China), sodium iodide-131 ( $^{131}\text{I}$ NaI) (Atom High Tech., Beijing, China), and instant thin-layer chromatography-silica gel (iTLC-SG) (Agilent Tech, Santa Clara, CA, USA).

**2.2. Synthesis of  $^{131}\text{I}$ GNR-PEG-cRGD.** A scheme of the  $^{131}\text{I}$ GNR-PEG-cRGD preparation procedure is shown in Figure 1.

First, EDC-HCl ( $5.88 \times 10^{-2}$  mmol) and NHS ( $5.88 \times 10^{-2}$  mmol) were individually dissolved in 500  $\mu\text{L}$  ultrapure deionized (DI) water, added to 1 mL of a GNR-PEG solution (0.59 mg Au/mL), and allowed to react overnight in the dark at room temperature. Subsequently, 500  $\mu\text{L}$  c(RGDfK) peptide ( $5.89 \times 10^{-3}$  mmol) was added to the reaction mixture, followed by stirring for 12 h in the dark at room temperature. Sonication was conducted discontinuously during the reaction process to avoid formation of precipitates or aggregates. The final product was purified by centrifugation (8000 rpm for 15 min at 4°C), redispersed in 1 mL DI water, and stored at 4°C in the dark.

Radiolabeling was performed before use. Briefly,  $^{131}\text{I}$ NaI (1111 MBq/mL) was added to the GNR-PEG-cRGD solution (118  $\mu\text{g}/\text{mL}$ ) and allowed to react for 15 min at room temperature, followed by centrifugation (8000 rpm for 15 min at 4°C), and then redispersed in 1 mL phosphate-buffered saline (PBS).

**2.3. Characterization of GNRs.** The morphology and size of GNRs were characterized by transmission electron microscopy (TEM). Optical absorption spectra were measured on a UV-Vis-NIR spectrophotometer (722S, Jinghua Instrument, Shanghai, China). The hydrodynamic diameter and zeta potential were measured by ZetaPALS zeta potential analyzer (Brookhaven Instrument Corp., Holtsville, NY, USA). The *in vitro* stability of  $^{131}\text{I}$ GNR-PEG-cRGD in PBS and fetal bovine serum (FBS) was determined by mixing 0.1 mL  $^{131}\text{I}$ GNR-PEG-cRGD with an equal volume of PBS/FBS and incubating at 37°C for 48 h. Radiochemical stability was monitored by iTLC-SG with a 0.9% sodium chloride solution as the solvent on a radioactive chromatography scanner (Zhongcheng, Hefei, China) at 6, 12, 24, and 48 h.

**2.4. Cell Culture and Analysis of Integrin  $\alpha_v\beta_3$  Expression.** Integrin  $\alpha_v\beta_3$ -positive B16F10 mouse malignant melanoma cells and integrin  $\alpha_v\beta_3$ -negative MCF-7 human breast cancer cells (American Type Culture Collection, Manassas, VA, USA) were cultured in Dulbecco's modified Eagle's medium (Gibco, Carlsbad, CA, USA) containing 10% (v/v) FBS (Gibco) and 1% antibiotics (100 U/ml penicillin and 100 U/ml streptomycin; Beyotime, Shanghai, China) at 37°C with 5%  $\text{CO}_2$ . The expression of integrin  $\alpha_v\beta_3$  was confirmed by immunofluorescence with a primary anti-integrin  $\alpha_v\beta_3$  antibody (1:100, Bioss, Beijing, China) and Cy3-conjugated goat anti-rabbit secondary antibody (1:50, Aspen, Wuhan, China) as described previously [24]. Anti-rabbit IgG (Cell Signaling Technology, Inc., USA) instead of the primary antibody was used as the control.

**2.5. In Vitro Cell Binding Assay.** B16F10 and MCF-7 cells were seeded in 24-well plates at a density of  $2 \times 10^5$  cells per well, incubated at 37°C overnight, and then treated with 0.8 mL  $^{131}\text{I}$ GNR-PEG-cRGD (0.074 MBq/well) at 37°C for 30, 60, 120, and 240 min. The medium was then removed, and the cells were collected and washed twice with PBS. The cell pellet was lysed with 1N NaOH and then washed twice

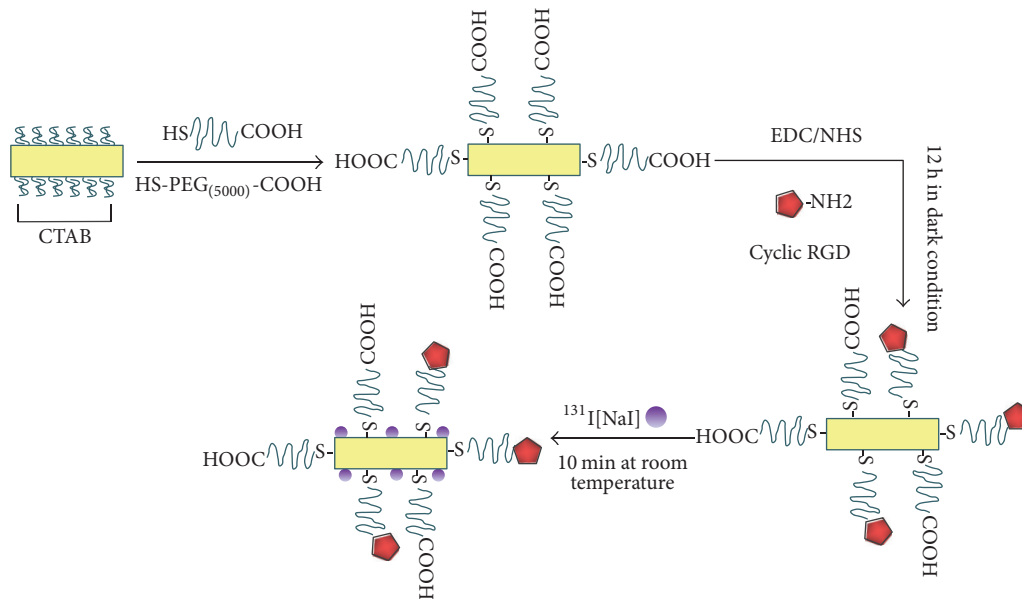


FIGURE 1: Scheme of the [ $^{131}\text{I}$ ]GNR-PEG-cRGD preparation procedure.

with PBS. Radioactivity was measured with a WIZARD  $\gamma$ -counter (PerkinElmer, MA, USA). The percentage of cellular uptake activity was calculated. Nonspecific binding was tested in parallel using B16F10 cells preincubated with excess free c(RGDfK) peptide for 1 h.

**2.6. Animal Model, In Vivo Imaging, and Biodistribution Analyses.** All animal experiments were performed in compliance with the Institutional Animal Care and Use Committee of Huazhong University of Science and Technology. MCF-7 cells ( $7 \times 10^6$ ) suspended in  $100 \mu\text{L}$  PBS were subcutaneously injected into the right shoulder flank of BALB/C-nu/nu mice (female, 3-4 weeks old, Beijing HFK Bioscience Co., Ltd, China), and  $2 \times 10^5$  B16F10 cells were implanted in C57BL/6 mice (female, 5-6 weeks, Wuhan Centers for Disease Prevention & Control, China).

When the tumor diameter reached about 10 mm, [ $^{131}\text{I}$ ]GNR-PEG-cRGD (5.55–7.4 MBq,  $100 \mu\text{L}$ ) was injected via the tail vein. Static images were acquired using a Symbia T6 SPECT/CT scanner (Siemens, Germany) under 2% pentobarbital sodium (Boster, Wuhan, China) anesthesia at 1, 3, 6, 9, and 12 h after injection. For blocking experiments, 6 mg c(RGDfK) was administered at 1 h before injection of [ $^{131}\text{I}$ ]GNR-PEG-cRGD into B16F10 tumor-bearing mice.

For biodistribution analysis, 1.48–1.85 MBq [ $^{131}\text{I}$ ]GNR-PEG-cRGD was intravenously injected into tumor-bearing mice, and then tissue dissection was carried out at 1, 3, and 6 h after injection. Tumors and organs of interest (blood, brain, heart, lung, liver, spleen, kidney, stomach, intestine, muscle, bone, and thyroid) were collected, weighed, and analyzed using the  $\gamma$ -counter. Tissue radioactivity was expressed as the percentage of injected dose per gram of tissue (% ID/g).

**2.7. Autoradiography and Immunofluorescence.** Tumors, muscles, lungs, livers, spleens, and kidneys were excised and

fixed in 4% paraformaldehyde. Frozen sections ( $20 \mu\text{m}$  thick) were prepared and placed on a phosphor screen for 40 min and then analyzed on a Cyclone Plus Phosphor Scanning System (PerkinElmer, USA). Regions of interest (ROIs) were drawn to quantify the radioactivity.

Immunofluorescence staining of tumors was performed as described above.

**2.8. Statistical Analysis.** Data are shown as the mean  $\pm$  standard deviation. Comparisons between groups were made using the Student's *t*-test.  $p < 0.05$  was considered to be statistically significant.

### 3. Results

**3.1. Synthesis of [ $^{131}\text{I}$ ]GNR-PEG-cRGD.** TEM images showed that PEGylated GNRs were well dispersed with a narrow size distribution and exhibited a rod shape with an average aspect ratio of 3.8 (93.4 nm in length and 24.8 nm in width) (Figure 2(a)). The successful modification of GNRs with PEG and conjugation of c(RGDfK) peptides were confirmed by zeta potentials (Figure 2(b)) and the hydrodynamic diameter (Figure 2(c)). Cetyltrimethylammonium bromide (CTAB) is a cationic surfactant, so the zeta potential of GNR coated with CTAB was  $28.13 \pm 0.59$  mV. When CTAB was replaced with a long chain structure HS-PEG-COOH molecule, the zeta potential of GNR-PEG shifted in negative direction to  $-5.17 \pm 0.60$  mV due to the carboxyl end group of HS-PEG-COOH molecule dissociated in aqueous solution and showed negative potential. On conjugation with c(RGDfK) zeta potential of GNR-PEG-RGD shifted a little in positive direction due to slight positive charge of c(RGDfK). After modification with PEG and cRGD, the size of the nanostructure became bigger, so hydrodynamic diameter was increased. The shift in the zeta potential and hydrodynamic diameter indicated

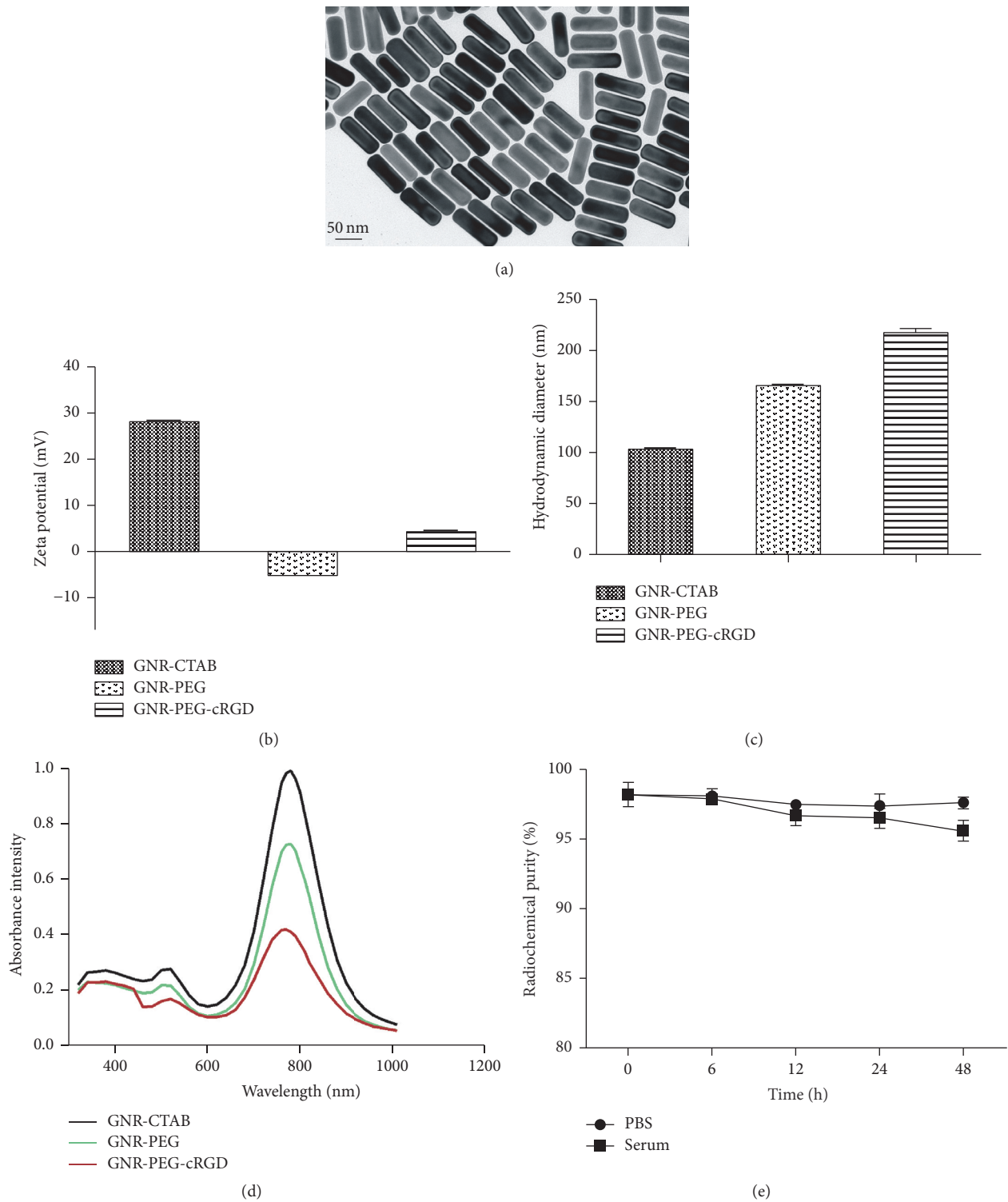


FIGURE 2: Characterization of GNR-PEG-cRGD. (a) TEM of GNR-PEG. Zeta potentials (b), hydrodynamic diameter (c), and UV-vis spectra (d) of GNR-CTAB, GNR-PEG, and GNR-PEG-cRGD. (e) In vitro stability of  $^{131}\text{I}$ GNR-PEG-cRGD in PBS and FBS at 6, 12, 24, and 48 h after labeling.



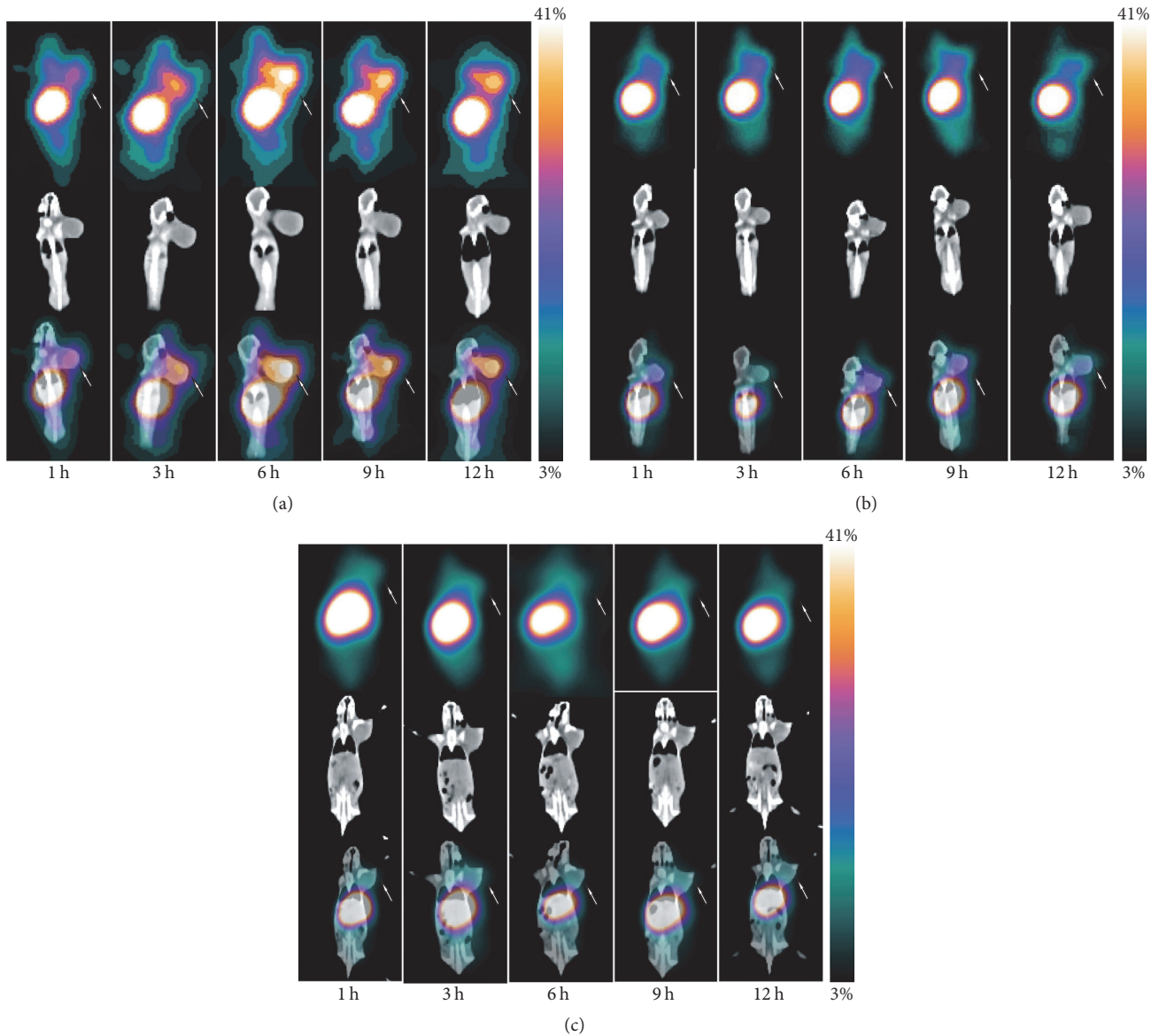


FIGURE 4: Representative whole body SPECT/CT images of B16F10 (a), blocked B16F10 (b), and MCF-7 (c) tumor-bearing mice at 1, 3, 6, 9, and 12 h after intravenous injection of [ $^{131}\text{I}$ ]GNR-PEG-cRGD. Arrows indicate tumor sites.

**3.3. In Vivo Analyses.** SPECT/CT images (Figure 4) and biodistribution analyses (Table 1) showed evident specific tumor uptake. [ $^{131}\text{I}$ ]GNR-PEG-cRGD had accumulated in B16F10 tumors quickly and effectively at 1 h after injection. Remarkably, the tumor uptake increased gradually over time and reached the peak value at about 6 h, and tumors were clearly visualized at 12 h after injection. However, nanoprobe in MCF-7 tumors were almost undetectable at all time points. In blocking experiments, B16F10 tumor uptake was clearly reduced. Biodistribution results revealed that B16F10 tumor uptake of [ $^{131}\text{I}$ ]GNR-PEG-cRGD was gradually increased to  $5.09 \pm 0.68$  % ID/g ( $n = 4$ ) at 6 h after injection, which was significantly higher compared with MCF-7 tumors ( $1.59 \pm 0.39$  % ID/g,  $n = 4$ ,  $p < 0.05$ ) and the blocked group ( $2.21 \pm 0.52$  % ID/g,  $n = 4$ ,  $p < 0.05$ ). Tumor/muscle ratios were  $9.99 \pm 2.98$  (B16F10),  $3.67 \pm 0.92$  (MCF-7), and  $3.87 \pm 0.93$  (blocked)

at 6 h. Liver, spleen, and lungs had remarkable radioactivity uptake. The kidneys showed low uptake of about 2 % ID/g.

**3.4. Autoradiography and Immunofluorescence.** Autoradiography also revealed abundant radioactivity accumulation in B16F10 tumors and little radioactivity accumulation in MCF-7 tumors (ROIs:  $3.73 \pm 0.75$  versus  $1.27 \pm 0.47$ ,  $n = 4$ ,  $p < 0.05$ ), which demonstrated specific targeting of the nanoprobe. High radioactivity had accumulated in samples of the lungs, liver, and spleen, while radioactivity distribution in muscles was sparse (Figure 5(a)). These ex vivo results were consistent with in vivo analyses.

Immunofluorescence staining of integrin  $\alpha_v\beta_3$  in B16F10 sections revealed intense fluorescence, but little fluorescence in MCF-7 sections (Figure 5(b)), which validated abundant

TABLE 1: Biodistribution of [ $^{131}\text{I}$ ]GNR-PEG-cRGD in C57BL/6 mice with B16F10 tumors and athymic mice with MCF-7 tumors at 1, 3, and 6 h after intravenous administration ( $n = 4$ ).

Tissue	B16F10			B16F10 blocking		MCF-7	
	1h	3h	6h	6h	1h	3h	6h
Blood	3.53 ± 1.31	4.53 ± 1.58	3.19 ± 0.35	3.97 ± 1.25	3.14 ± 2.10	3.1 ± 0.31	2.44 ± 0.28
Brain	0.20 ± 0.09	0.18 ± 0.03	0.17 ± 0.02	0.15 ± 0.09	0.18 ± 0.09	0.15 ± 0.03	0.10 ± 0.02
Heart	1.14 ± 0.44	1.45 ± 0.27	0.85 ± 0.19	0.78 ± 0.17	0.45 ± 0.16	0.93 ± 0.17	0.47 ± 0.17
Lung	19.25 ± 4.59	11.74 ± 1.97	7.07 ± 0.25	6.93 ± 0.24	20.56 ± 9.24	17.41 ± 1.04	3.31 ± 1.87
Liver	32.05 ± 5.37	28.83 ± 7.17	26.51 ± 4.93	27.59 ± 5.01	30.18 ± 4.87	31.51 ± 5.71	27.60 ± 3.34
Spleen	11.28 ± 0.63	9.86 ± 1.05	5.55 ± 0.69	6.32 ± 1.01	15.99 ± 1.74	8.57 ± 0.70	6.20 ± 1.18
Kidney	2.34 ± 0.75	2.60 ± 1.04	2.29 ± 0.21	3.01 ± 0.91	2.29 ± 1.51	2.00 ± 0.36	1.50 ± 0.37
Stomach	3.59 ± 1.81	6.12 ± 2.28	3.43 ± 0.44	4.02 ± 0.59	3.49 ± 2.69	5.44 ± 2.75	4.70 ± 1.37
Intestine	1.52 ± 0.55	1.60 ± 0.57	1.23 ± 0.48	1.04 ± 0.29	1.15 ± 0.77	1.35 ± 0.25	0.89 ± 0.47
Muscle	0.47 ± 0.19	0.59 ± 0.08	0.51 ± 0.08	0.57 ± 0.12	0.54 ± 0.22	0.58 ± 0.23	0.42 ± 0.07
Bone	2.59 ± 0.78	3.29 ± 1.47	1.69 ± 0.13	1.70 ± 0.21	2.02 ± 0.85	2.72 ± 0.68	1.26 ± 0.71
Thyroid	2.88 ± 0.37	2.25 ± 1.09	2.93 ± 0.75	3.01 ± 0.92	3.26 ± 2.15	2.93 ± 0.26	3.59 ± 2.68
Tumor	3.57 ± 1.25	4.02 ± 1.45	5.09 ± 0.68	2.21 ± 0.52	1.31 ± 0.88	1.75 ± 0.26	1.59 ± 0.39
Uptake ratio							
Tumor/blood	1.01 ± 0.11	0.80 ± 0.29	1.58 ± 0.13	0.56 ± 0.22	0.52 ± 0.07	0.57 ± 0.04	0.63 ± 0.19
Tumor/muscle	7.06 ± 2.53	6.89 ± 2.37	9.99 ± 2.98	3.87 ± 0.93	2.17 ± 1.06	3.26 ± 0.98	3.67 ± 0.92

integrin  $\alpha_v\beta_3$  expression in B16F10 tumors, but low expression in MCF-7 tumors.

#### 4. Discussion

An  $^{131}\text{I}$ -labeled, cRGD-conjugated PEG-modified GNR probe was synthesized successfully. Compared with a reported spherical gold nanoprobe with single surface plasma resonance in visible light [12], which limits certain applications in the medical field, the probe we designed and synthesized possesses distinct advantages in the field of optical biological applications. Excellent surface plasma resonances in the NIR region confer GNRs with minimal light absorption by hemoglobin and water, maximal penetration [25], and highly efficient photothermal conversion [9], making them particularly attractive for optoacoustic imaging [13] and photothermal therapy [26].

There has been increasing use of radioisotopes to label nanoparticles, such as positron emitters copper-64 [26], gallium-67 [27], and zirconium-89 [28], and single photon emitters Technetium-99m [3] and radioiodine (e.g., iodine-125 [29], iodine-123, and iodine-131 [30]). In most conditions, a bifunctional chelator, such as DOTA or HYNIC, must be conjugated to the nanoparticle for radiolabeling. Therefore, modification of nanoparticles is required before labeling. It has been shown that iodide ions have high affinity and strong binding to the surface of GNRs [8, 29, 31, 32]. Iodide ions absorb preferentially onto facets of GNRs and form the strongest bonds with Au, which probably leads to the formation of a surface of AuI [18]. Such simple chemistry between iodine and GNRs allows straightforward and efficient labeling of radioiodine to GNRs without iodination reagents or iodine-accepting functional groups such as a phenol residue [29]. Iodine-125 has been reported to directly label GNRs in

a simple and rapid manner [8, 29]. Here, we first report the in vitro and in vivo behaviors of directly  $^{131}\text{I}$ -labeled GNRs by simply mixing a GNR colloid with [ $^{131}\text{I}$ ]NaI at room temperature for a short time. This reaction takes place fairly rapidly and completely, which agrees well with the previous reports of high affinity and strong binding of iodide ions to the surface of GNRs [18]. The labeling method is characterized by simplicity, a short reaction time, mild reaction conditions, and high yield. Another advantage is that purification is simple by centrifugation to remove free [ $^{131}\text{I}$ ]iodide ions. Furthermore, this nanoprobe has excellent stability with radiochemistry purity greater than 95% after incubation in PBS or FBS for 48 h.  $^{131}\text{I}$  is widely used in clinics and easy to obtain. The properties of  $\beta$ -emitters are used for radiotherapy. Passing through tissue, the ejected  $\beta$ -particles (i.e., electrons) interact with atoms, mainly in water molecules, and lose their energy, leading to the generation of excited and ionized atoms and free radicals that are responsible for DNA damage in cells by inducing single-strand breaks in DNA [33], making  $^{131}\text{I}$  the optimal choice for application as a theranostic agent [19]. Our ultimate goal is to use this probe for both imaging and therapy, so  $^{131}\text{I}$  was chosen.

The significant difference in cellular uptake of [ $^{131}\text{I}$ ]GNR-PEG-cRGD by B16F10 and MCF-7 cells confirmed receptor-specific internalization of the probes, suggesting that the probes were taken up by tumor cells via receptor-mediated endocytosis. However, [ $^{131}\text{I}$ ]GNR-PEG-cRGD accumulation in MCF-7 cells and blocked B16F10 cells was up to about 20% because of passive uptake, which may be explained by the following three reasons. First, the nanometric size of the probe is known to be taken up by all mammalian cell types [34]. Second, serum proteins in the cell culture may be absorbed onto the surface of nanoparticles or targeted c(RGDfK) peptides, which can be taken up by cells and can

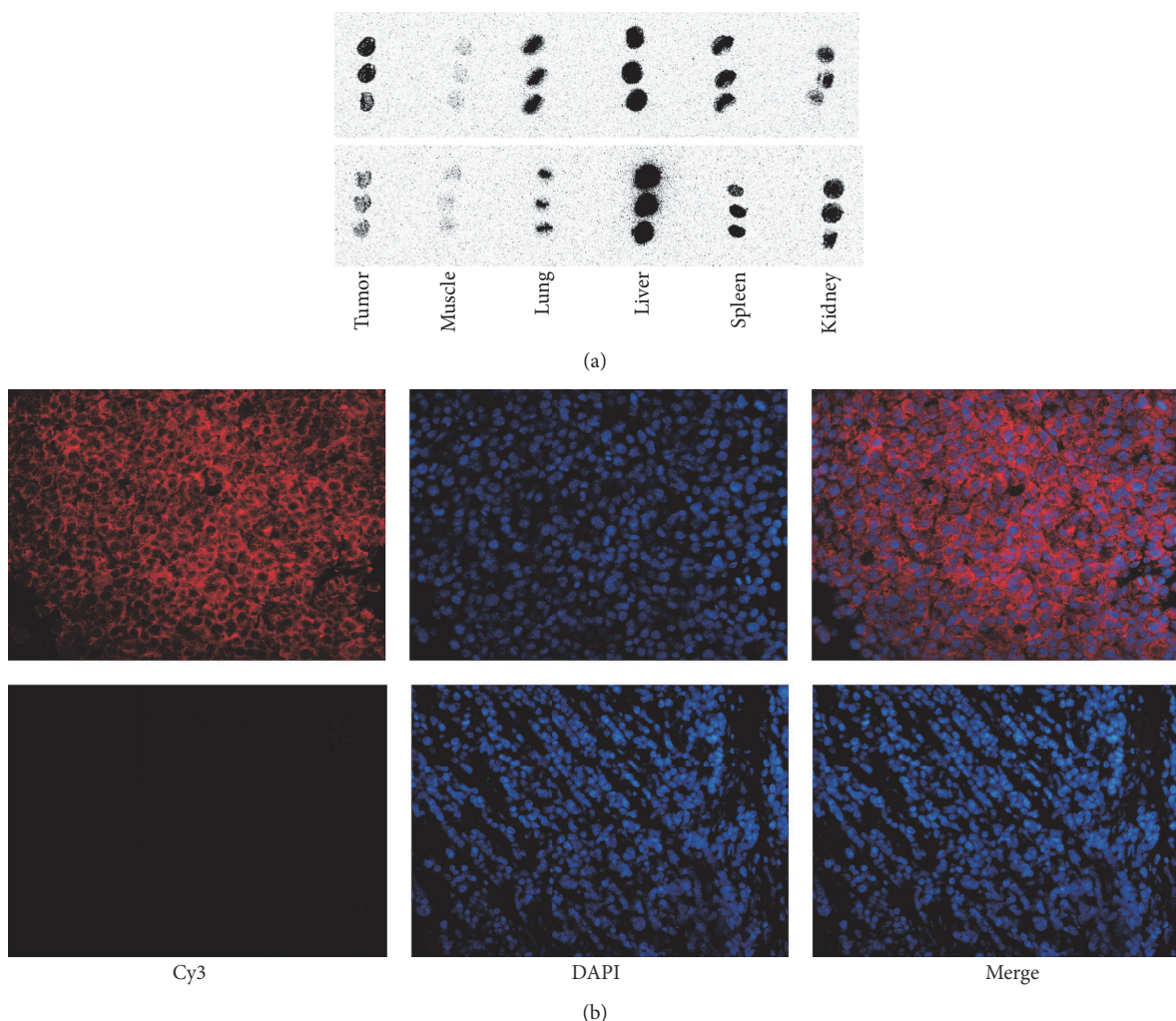


FIGURE 5: (a) Autoradiography of tumor tissue and organs. B16F10 tumor-bearing mice (upper row) and MCF-7 tumor-bearing mice (lower row). (b) Immunofluorescence staining of integrin  $\alpha_v\beta_3$  in B16F10 (upper row) and MCF-7 (lower row) tumors ( $\times 200$ ).

mediate uptake of nanoparticles into cells nonspecifically via the mechanism of receptor-mediated endocytosis [34]. Third, tumor cell membranes have a predominant negative charge, whereas the zeta potential of [ $^{131}\text{I}$ ]GNR-PEG-cRGD was positive, which can bind efficiently to the surface of tumor cells by electrostatic attraction and then promote nonspecific uptake via clathrin-mediated endocytosis [35].

SPECT/CT imaging results revealed high [ $^{131}\text{I}$ ]GNR-PEG-cRGD accumulation in B16F10 tumors; the tumors of blocked B16F10 mice and MCF-7 mice are also visible although they are not very clear. In biodistribution study, tumor uptake values were  $5.09 \pm 0.68$ ,  $2.21 \pm 0.52$ , and  $1.59 \pm 0.39$  % ID/g at 6 h p.i. in B16F10, blocked B16F10 and MCF-7 mice, with tumor/muscle ratio of  $9.99 \pm 2.98$ ,  $3.87 \pm 0.93$ , and  $3.67 \pm 0.92$ , respectively. These results indicate that low EPR effects existed in B16F10/MCF-7 bearing mouse due to the characteristics of nanoparticles and solid tumor, and tracer accumulation in B16F10 can be explained by both integrin  $\alpha_v\beta_3$ -specific endocytosis and EPR effect, in which active targeting plays a vital role.

Theoretically, due to the large size of these nanoparticles, usually optimal uptake would be observed at late time points.

Actually, our *in vitro* cell binding results were  $28.52 \pm 1.00\%$ ,  $36.02 \pm 1.20\%$ ,  $38.2 \pm 1.48\%$ , and  $39.11 \pm 1.80\%$  at 30, 60, 120, and 240 min and nearly reached a platform at 120 min; our *in vivo* imaging also revealed highest tumor uptake present at 6 h and decreased overtime. In addition, significant thyroid uptake is also observed which increased overtime in our studies; thyroid uptake was also observed in reported 125I-Labeled Gold Nanorods papers as expected [8, 29]. One possible explanation of short blood circulation (dropped at 6 h p.i.) and rapid thyroid accumulation (e.g., 1 h p.i.) was *in vivo* deiodination from nanoparticles. Our *in vitro* stability results may not reflect real condition, because iTLC might not be able to identify the disassociated [ $^{131}\text{I}$ ] that might also be absorbed by protein(s) in blood. We will use FPLC to further assess the serum and *in vivo* stability of [ $^{131}\text{I}$ ]GNR-PEG-cRGD, and late time points will be included in our therapy study.

Compared with other radiotherapeutic systems such as those based on Lu-177-gold nanoparticles-RGD, one study compared 177Lu-labeled monomeric, dimeric, and multimeric RGD peptides for the therapy of tumors expressing a(n)b(3) integrins; 177Lu-AuNP-c(RGDfK)C was demonstrated

as the best one for targeted radionuclide therapy of tumors expressing  $\alpha(n)\beta(3)$  integrins; with highest tumor uptake of  $6.42 \pm 0.71$  % ID/g at 6 h [36], our [ $^{131}\text{I}$ ]GNR-PEG-cRGD system has similar in vivo stability ( $5.09 \pm 0.68$ % ID/g at 6 h). Another study reports that the mean tumor residence times of  $^{177}\text{Lu}$ -AuNP-RGD were  $61.6 \pm 5.8$  h [37]. And we will get the data in our therapy study.

Although CTAB was replaced with HS-PEG<sub>(5000)</sub>-COOH for better stability and biocompatibility, significant uptake was still observed in the liver and spleen because of abundant macrophages in the reticuloendothelial system of the liver and spleen and the colloidal nature of the probe, which have been well documented in previous reports of radiolabeled nanoparticles [3, 4]. Efforts have been made to understand and minimize uptake by the liver and spleen as much as possible. One study reported that targeting ligands on the surface of nanoparticles might even be detrimental because their exposure can accelerate nanoparticle opsonization and blood clearance by the immune system, resulting in high uptake in the liver and spleen [35]. Morales-Avila et al. [3] studied the biodistribution of GNPs using various administration methods. Their results showed that intravenous administration resulted in higher liver and spleen accumulation than intraperitoneal administration, because intravenous administration leads to opsonization followed by substantial uptake by macrophages located in the liver and spleen. Our results revealed that [ $^{131}\text{I}$ ]GNR-PEG-cRGD had accumulated in the liver and spleen at an early time point and gradually declined over time; the reason may be due to the radiolabeled nanosystem accumulation by reticuloendothelial system (RES), metabolized by the hepatobiliary system; it is also possible that the activity eliminated by the hepatobiliary system corresponds to the free iodide and not to the radiolabeled nanosystem.

However, the detailed metabolism mechanism in vivo is still not understood. The size of a nanoparticle may be another influencing factor. It has been reported that GNPs of less than 5–6 nm in size can be removed from the body via the kidney which can minimize nonspecific accumulation by RES [29]. In addition, the final metabolic pattern of larger sized nanoparticles is associated with the shape and surface chemistry [38]. Our results also demonstrated that the in vivo environment is far more complex than in vitro model systems.

In summary, a stable and tumor-specific SPECT imaging nanoparticle probe was successfully prepared in this study. The probe can specifically target integrin  $\alpha_v\beta_3$ -expressing tumor cells both in vitro and in vivo mainly by receptor-mediated endocytosis. Importantly, the radiolabeling method is simple and fast with a high yield and high stability. These promising results demonstrate that our [ $^{131}\text{I}$ ]GNR-PEG-cRGD probe can be used as an angiogenesis-targeted SPECT imaging probe. Currently, more detailed studies to improve the in vivo fate of the [ $^{131}\text{I}$ ]GNR-PEG-cRGD probe and the use of this multifunctional probe as a theranostic agent are ongoing.

## 5. Conclusion

In this study, a smart nanoprobe, [ $^{131}\text{I}$ ]GNR-PEG-cRGD, was successfully developed, and it showed specific binding ability

with integrin  $\alpha_v\beta_3$ , indicating its potential as a multifunctional theranostic agent for tumors.

## Conflicts of Interest

The authors declare that there are no conflicts of interest regarding the publication of this paper.

## Acknowledgments

This study was supported by the National Natural Science Foundation of China (no. 81401444) and the Independent Innovation Research Fund of Huazhong University of Science (no. 2014QN038).

## References

- [1] E. C. Dreaden, A. M. Alkilany, X. Huang, C. J. Murphy, and M. A. El-Sayed, "The golden age: gold nanoparticles for biomedicine," *Chemical Society Reviews*, vol. 41, no. 7, pp. 2740–2779, 2012.
- [2] S. Same, A. Aghanejad, S. A. Nakhjavani, J. Barar, and Y. Omid, "Radiolabeled theranostics: Magnetic and gold nanoparticles," *BioImpacts*, vol. 6, no. 3, pp. 169–181, 2016.
- [3] E. Morales-Avila, G. Ferro-Flores, B. E. Ocampo-García et al., "Multimeric system of  $^{99m}\text{Tc}$ -labeled gold nanoparticles conjugated to c[RGDfK(C)] for molecular imaging of tumor  $\alpha(v)\beta(3)$  expression," *Bioconjugate Chemistry*, vol. 22, no. 5, pp. 913–922, 2011.
- [4] Y. Xiao, H. Hong, V. Z. Matson et al., "Gold nanorods conjugated with doxorubicin and cRGD for combined anti-cancer drug delivery and PET imaging," *Theranostics*, vol. 2, no. 8, pp. 757–768, 2012.
- [5] L. Au, D. Zheng, F. Zhou, Z.-Y. Li, X. Li, and Y. Xia, "A quantitative study on the photothermal effect of immuno gold nanocages targeted to breast cancer cells," *ACS Nano*, vol. 2, no. 8, pp. 1645–1652, 2008.
- [6] M. Tian, W. Lu, R. Zhang et al., "Tumor uptake of hollow gold nanospheres after intravenous and intra-arterial injection: PET/CT study in a rabbit VX2 liver cancer model," *Molecular Imaging and Biology*, vol. 15, no. 5, pp. 614–624, 2013.
- [7] H. Xie, Z. J. Wang, A. Bao, B. Goins, and W. T. Phillips, "In vivo PET imaging and biodistribution of radiolabeled gold nanoshells in rats with tumor xenografts," *International Journal of Pharmaceutics*, vol. 395, no. 1–2, pp. 324–330, 2010.
- [8] X. Shao, A. Agarwal, J. R. Rajian, N. A. Kotov, and X. Wang, "Synthesis and bioevaluation of  $^{125}\text{I}$ -labeled gold nanorods," *Nanotechnology*, vol. 22, no. 13, Article ID 135102, 2011.
- [9] C.-H. Chou, C.-D. Chen, and C. R. C. Wang, "Highly efficient, wavelength-tunable, gold nanoparticle based photothermal nanoconvertors," *The Journal of Physical Chemistry B*, vol. 109, no. 22, pp. 11135–11138, 2005.
- [10] C. Wang, C. Bao, S. Liang et al., "RGD-conjugated silica-coated gold nanorods on the surface of carbon nanotubes for targeted photoacoustic imaging of gastric cancer," *Nanoscale Research Letters*, vol. 9, no. 1, article 264, 2014.
- [11] Z. Heidari, M. Salouti, and R. Sariri, "Breast cancer photothermal therapy based on gold nanorods targeted by covalently-coupled bombesin peptide," *Nanotechnology*, vol. 26, no. 19, Article ID 195101, 2015.

- [12] N. Su, Y. Dang, G. Liang, and G. Liu, "Iodine-125-labeled cRGD-gold nanoparticles as tumor-targeted radiosensitizer and imaging agent," *Nanoscale Research Letters*, vol. 10, article 160, 2015.
- [13] J. Zhong, L. Wen, S. Yang, L. Xiang, Q. Chen, and D. Xing, "Imaging-guided high-efficient photoacoustic tumor therapy with targeting gold nanorods," *Nanomedicine: Nanotechnology, Biology and Medicine*, vol. 11, no. 6, pp. 1499–1509, 2015.
- [14] P. P. Joshi, S. J. Yoon, W. G. Hardin, S. Emelianov, and K. V. Sokolov, "Conjugation of antibodies to gold nanorods through Fc portion: synthesis and molecular specific imaging," *Bioconjugate Chemistry*, vol. 24, no. 6, pp. 878–888, 2013.
- [15] L. Vigdeman, B. P. Khanal, and E. R. Zubarev, "Functional gold nanorods: synthesis, self-assembly, and sensing applications," *Advanced Materials*, vol. 24, no. 36, pp. 4811–4841, 2012.
- [16] R. Haubner, F. Bruchertseifer, M. Bock, H. Kessler, M. Schwai-ger, and H.-J. Wester, "Synthesis and biological evaluation of a  $^{99m}\text{Tc}$ -labelled cyclic RGD peptide for imaging the  $\alpha\beta_3$  expression," *Nuklearmedizin*, vol. 43, no. 1, pp. 26–32, 2004.
- [17] J. Wan, J.-H. Wang, T. Liu, Z. Xie, X.-F. Yu, and W. Li, "Surface chemistry but not aspect ratio mediates the biological toxicity of gold nanorods in vitro and in vivo," *Scientific Reports*, vol. 5, Article ID 11398, 2015.
- [18] S. Singh, R. Pasricha, U. M. Bhatta, P. V. Satyam, M. Sastry, and B. L. V. Prasad, "Effect of halogen addition to monolayer protected gold nanoparticles," *Journal of Materials Chemistry*, vol. 17, no. 16, pp. 1614–1619, 2007.
- [19] S. V. Gudkov, N. Y. Shilyagina, V. A. Vodeneev, and A. V. Zvyagin, "Targeted radionuclide therapy of human tumors," *International Journal of Molecular Sciences*, vol. 17, no. 1, article 33, 2015.
- [20] M. A. Dechantsreiter, E. Planker, B. Mathä et al., "*N*-methylated cyclic RGD peptides as highly active and selective  $\alpha_v\beta_3$  integrin antagonists," *Journal of Medicinal Chemistry*, vol. 42, no. 16, pp. 3033–3040, 1999.
- [21] H. Maeda, J. Wu, T. Sawa, Y. Matsumura, and K. Hori, "Tumor vascular permeability and the EPR effect in macromolecular therapeutics: a review," *Journal of Controlled Release*, vol. 65, no. 1-2, pp. 271–284, 2000.
- [22] V. Torchilin, "Tumor delivery of macromolecular drugs based on the EPR effect," *Advanced Drug Delivery Reviews*, vol. 63, no. 3, pp. 131–135, 2011.
- [23] J. Fang, H. Nakamura, and H. Maeda, "The EPR effect: unique features of tumor blood vessels for drug delivery, factors involved, and limitations and augmentation of the effect," *Advanced Drug Delivery Reviews*, vol. 63, no. 3, pp. 136–151, 2011.
- [24] C. Qin, X. Lan, J. He et al., "An in vitro and in vivo evaluation of a reporter gene/probe system hERL/18F-FES," *PLoS ONE*, vol. 8, no. 4, Article ID e61911, 2013.
- [25] R. Weissleder, "A clearer vision for in vivo imaging," *Nature Biotechnology*, vol. 19, no. 4, pp. 316–317, 2001.
- [26] X. Sun, X. Huang, X. Yan et al., "Chelator-free  $^{64}\text{Cu}$ -integrated gold nanomaterials for positron emission tomography imaging guided photothermal cancer therapy," *ACS Nano*, vol. 8, no. 8, pp. 8438–8446, 2014.
- [27] C. Tsoukalas, G. Laurent, G. Jiménez Sánchez et al., "Initial in vitro and in vivo assessment of Au@DTDTPA-RGD nanoparticles for Gd-MRI and  $^{68}\text{Ga}$ -PET dual modality imaging," *EJNMMI Physics*, vol. 2, no. 1, article A89, 2015.
- [28] L. Karmani, V. Bouchat, C. Bouzin et al., " $^{89}\text{Zr}$ -labeled anti-endoglin antibody-targeted gold nanoparticles for imaging cancer: implications for future cancer therapy," *Nanomedicine*, vol. 9, no. 13, pp. 1923–1937, 2014.
- [29] Y.-H. Kim, J. Jeon, S. H. Hong et al., "Tumor targeting and imaging using cyclic RGD-PEGylated gold nanoparticle probes with directly conjugated iodine-125," *Small*, vol. 7, no. 14, pp. 2052–2060, 2011.
- [30] H.-W. Kao, Y.-Y. Lin, C.-C. Chen et al., "Evaluation of EGFR-targeted radioimmuno-gold-nanoparticles as a theranostic agent in a tumor animal model," *Bioorganic & Medicinal Chemistry Letters*, vol. 23, no. 11, pp. 3180–3185, 2013.
- [31] D. K. Smith, N. R. Miller, and B. A. Korgel, "Iodide in CTAB prevents gold nanorod formation," *Langmuir*, vol. 25, no. 16, pp. 9518–9524, 2009.
- [32] W. Cheng, S. Dong, and E. Wang, "Iodine-induced gold-nanoparticle fusion/fragmentation/aggregation and iodine-linked nanostructured assemblies on a glass substrate," *Angewandte Chemie International Edition*, vol. 42, no. 4, pp. 449–452, 2003.
- [33] H. Hong, Y. Zhang, J. Sun, and W. Cai, "Molecular imaging and therapy of cancer with radiolabeled nanoparticles," *Nano Today*, vol. 4, no. 5, pp. 399–413, 2009.
- [34] B. D. Chithrani, A. A. Ghazani, and W. C. W. Chan, "Determining the size and shape dependence of gold nanoparticle uptake into mammalian cells," *Nano Letters*, vol. 6, no. 4, pp. 662–668, 2006.
- [35] O. Harush-Frenkel, E. Rozentur, S. Benita, and Y. Altschuler, "Surface charge of nanoparticles determines their endocytic and transcytotic pathway in polarized MDCK cells," *Biomacromolecules*, vol. 9, no. 2, pp. 435–443, 2008.
- [36] M. Luna-Gutiérrez, G. Ferro-Flores, B. Ocampo-García et al., " $^{177}\text{Lu}$ -labeled monomeric, dimeric and multimeric RGD peptides for the therapy of tumors expressing  $\alpha(\nu)\beta(3)$  integrins," *Journal of Labelled Compounds and Radiopharmaceuticals*, vol. 55, no. 4, pp. 140–148, 2012.
- [37] A. Vilchis-Juárez, G. Ferro-Flores, C. Santos-Cuevas et al., "Molecular targeting radiotherapy with Cyclo-RGDfK(C) peptides conjugated to  $^{177}\text{Lu}$ -labeled gold nanoparticles in tumor-bearing mice," *Journal of Biomedical Nanotechnology*, vol. 10, no. 3, pp. 393–404, 2014.
- [38] X. Huang, X. Peng, Y. Wang et al., "A reexamination of active and passive tumor targeting by using rod-shaped gold nanocrystals and covalently conjugated peptide ligands," *ACS Nano*, vol. 4, no. 10, pp. 5887–5896, 2010.